

WASM: Minerals, Energy and Chemical Engineering

Photocatalytic performance of nanocatalysts

Qiaoran Liu

0000-0002-7864-3343

**This thesis is presented for the Degree of
Doctor of Philosophy
of
Curtin University**

June 2021

Declaration

To the best of my knowledge and belief this thesis contains no material previously published by any other person except where due acknowledgment has been made.

This thesis contains no material which has been accepted for the award of any other degree or diploma in any university.

Signature:

Date: 02 / 07 / 2021

Dedication

To my beloved family

Abstract

Organic contaminants, dyes and antibiotics, discharged in wastewater systems, have posed great threats to the sustainability of the ecosystem. The photocatalytic oxidation technology has advantages of simple structure of equipment, mild reaction conditions, easy control of operation and strong oxidizing ability. Photocatalytic oxidation technology is a new type of water treatment technology with broad application prospects. Metals or metal oxides are widely used as photo/electro catalysts for environmental remediation or clean energy production. However, there are many issues related to these metal-based catalysts for practical applications, such as high cost, poor stability and detrimental environmental impact. Unlike the metal-containing photocatalysts that need expensive metal salts for preparation, carbon-based metal-free catalysts such as graphitic carbon nitride (GCN) have the potential to overcome these limitations. This study centered on the strategies for metal-free photocatalytic towards increasing photocatalytic performance. The resultant photocatalysts revealed prominent performances for total photodegradation of organic contaminants. The physicochemical properties are investigated using a set of characterizations ranging from XRD, XPS, FTIR, BET to SEM and TEM. The photochemical performance is evaluated by UV-vis DRS and photoluminescence. The degradation processes were investigated by in situ electron paramagnetic resonance (EPR). The mechanistic studies on the enhanced photoelectrochemical and photocatalytic performances were also conducted.

In the first part of the thesis, graphitic carbon nitride (GCN) nanocomposites modified by four kinds of nanocarbons were successfully fabricated by straight forward one-pot

method. The resultant photocatalysts revealed prominent performances for total photodegradation of organic contaminants. The photocatalytic degradation difference is mainly stemmed from the higher contents of COOH and C=O functional groups. The intimate contact or interaction between the two phases of GCN and nanocarbon in the nanocomposites may further improve the activity.

In the second part of my thesis, monodisperse nitrogen-doped carbon nanospheres (NC) were synthesized and loaded onto graphitic carbon nitride (g-C₃N₄, GCN) via a facile hydrothermal method for photocatalytic removal of sulfachloropyridazine (SCP). The nitrogen content in NC critically influences the physicochemical properties and performances of the resultant hybrids. The mechanism of the improved photocatalytic performance and band structure alternation were further investigated by density functional theory (DFT) calculations, which confirmed the high capability of the GCN-NC hybrids to activate the electron-hole pairs by reducing the band-gap energy and efficiently separating electron/hole pairs.

Thirdly, ZnO microflower cores were partially wrapped with Fe₃O₄ nanoparticles via a layer-by-layer self-assembly process. The degradation was triggered with in-situ photocatalytic formation of hydrogen peroxide over Fe₃O₄@ZnO. We explored possible mechanisms of the enhanced photocatalysis by quenching and radical trapping experiments. The magnetic separation was also performed to recover and reuse the spent catalysts.

Lastly, a novel two-dimensional CdS@Ti₃C₂@TiO₂ nano hybrids was developed by facile calcination and a subsequent hydrothermal process. The charge carrier sinking function of Ti₃C₂ in this three-phase Z-scheme catalyst was proposed based on UV-visible spectroscopy band gap calculation, photoluminescence measurement and photoelectrochemical analysis. The electron paramagnetic resonance assay verified that both superoxide ions and hydroxyl radicals played crucial roles in the removal of

contaminants.

In summary, this thesis shows a series of highly selective photocatalysts and provides insight in the design of highly efficient metal-free photocatalysts to better utilize the clean and free solar energy for environmental remediation.

Acknowledgements

Firstly, I would like to express my deepest and most sincere thanks to my supervisor Prof. Shaomin Liu, for offering me this precious opportunity to pursue my study in his group and for his instructive guidance during my research work. His kindness, patience and professional advice helped me get through many problems during this journey. The discussions on my research topic were always enthusiastic and fruitful. During the past four years, I have learned a lot from him, especially his serious attitude towards research and this will inspire me to pursue a meaning career in the future.

Equally, I am grateful to my co-supervisor, Prof. Shaobin Wang, for his generous help and professional suggestions on my experiments. His dedication and commitment work have had great influence on my career. No matter what I plan to do for my research, both of my supervisors always provided me with adequate guidance and support, then encouraged me to make attempts to the experiments. I am lucky and proud to be one of their students.

Also, I owe special thanks to Dr Lihong Liu, who helped me so much for my research work. She is very patient and supportive. Without her help and company, my study cannot be completed smoothly. I am also very grateful to Prof. Hongqi Sun for professional help and advice on my writing skills.

I would like to offer my sincere thanks to my colleagues and friends, Zhangfeng Shen, Xiaoguang Duan, Li Zhou, Jiaquan Li, Kai Wang, Zhengxin Yao, Xiaojie Li, Ning Han, and many others. They are always willing to share their experiences and give me kind suggestions about both experiments and life. Thank you very much for all your help and support during my PhD study. My life would be boring and tough without you!

Here, I would also like to extend my gratitude to all Curtin Chemical Engineering lab

technicians, Mr Jason Wright, Mr Jimmy Hua, Mr Araya Abera Mr Andrew Chan, Ms Roshanak Doroushi, and Ms Jennifer Wang for their professional help and technical support in the lab.

Last but not the least, I would like to express my deepest gratitude to my beloved parents, my husband Xiao Hua. I can never go so far without your understanding and encouragement. I love you all!

List of Publications

Publications by the author:

1. **Qiaoran Liu**, Li Zhou, Jun Gao, Shaobin Wang, Lihong Liu and Shaomin Liu. “Surface chemistry-dependent activity and comparative investigation on the enhanced photocatalytic performance of graphitic carbon nitride modified with various nanocarbons”. *J. Colloid Interface Sci.* 2020, 569,12-21.
2. **Qiaoran Liu**, Hao Tian, Zhenghua Dai, Hongqi Sun, Jian Liu, Zhimin Ao, Shaobin Wang, Chen Han and Shaomin Liu. “Nitrogen-doped Carbon Nanospheres Modified Graphitic Carbon Nitride for Enhanced Photocatalytic Performances”. *Nano-micro Lett.* 2020, 12, 24.
3. **Qiaoran Liu**, Li Zhou, Lihong Liu, Jiaquan Li, Shaobin Wang, Hussein Znad and Shaomin Liu. “Magnetic ZnO@Fe₃O₄ composite for self-generated H₂O₂ toward photo-Fenton-like oxidation of nitrophenol”. *Compos. B. Eng.* 2020, 200, 108345.
4. **Qiaoran Liu**, Xiaoyao Tan, Shaobin Wang, Fang Ma, Hussin Znad, Zhangfeng Shen, Lihong Liu and Shaomin Liu. “MXene as non-metal charge mediator in 2D layered CdS@Ti₃C₂@TiO₂ composites with superior Z-scheme visible light-driven photocatalytic activity”. *Environ. Sci.: Nano*, 2019, 6, 3158.

Table of Contents

Declaration	I
Dedication	I
Abstract	III
Acknowledgements.....	III
List of Publications.....	V
Table of Contents.....	VI
Chapter 1. Introduction	1
1.1 Current issues and developing methods for environmental remediation	1
1.2 Research objectives.....	3
1.3 Thesis organization	5
References.....	6
Chapter 2. Literature review	9
2.1 Introduction	9
2.2 Applications of advanced oxidation processes (AOPs) in degradation of pollutants	10
2.3 Photocatalysis	13
2.3.1 Classifications of semiconductor photocatalysis.....	15
2.4 Metal-based semiconductors.....	17
2.4.1 Noble metal-based photocatalysts.....	17
2.4.2 Metallic oxides.....	19
2.4.3 Metal sulfides, nitrides (or oxynitrides) and carbide.....	24
2.5 Metal-free photocatalyst.....	27
2.5.1 Graphitic carbon nitride (g-C ₃ N ₄).....	28
2.5.2 Nanocarbon material	34
2.5.2.1 Graphene	35
2.5.2.2 Graphene oxide (GO) and reduced GO (rGO).....	40
2.5.2.3 Carbon quantum dots (CQDs).....	42
2.6 Summary and perspectives.....	45
Reference.....	48
Chapter 3. Surface chemistry-dependent activity and comparative investigation on the enhanced photocatalytic performance of graphitic carbon nitride modified with various nanocarbons	78
3.1. Introduction.....	80
3.2 Experimental	82
3.2.1. Materials	82

3.2.2. Synthesis of nanocarbon modified GCN	82
3.3. Photocatalytic activity testing.....	83
3.4. Results and discussion.....	84
3.4.1 Physical properties of the different nanocarbon modified graphitic carbon nitride (GCN)	84
3.4.2. Optical properties of graphitic carbon nitride (GCN) and nanocarbon composites	90
3. 4. 3. Photocatalytic activities of graphitic carbon nitride (GCN) and nanocarbon composites.....	92
3.5. Conclusions.....	102
References.....	104

Chapter 4. Nitrogen-doped Carbon Nanospheres Modified Graphitic Carbon Nitride for Enhanced Photocatalytic Performances 111

4.1. Introduction.....	113
4.2. Experimental.....	115
4.2.1 Materials	115
4.2.2 Synthesis of graphitic carbon nitride (GCN).....	115
4.2.3 Synthesis of carbon nanospheres (C) and nitrogen-doped carbon nanospheres (NC)	115
4.2.4 Preparation of GCN-NC and GCN-C.....	116
4.2.5 Characterizations.....	117
4.2.6 Photocatalytic activity testing.....	118
4.2.7 DFT calculations.....	118
4.3 Results and Discussion	119
4.3.1 Physiochemical property of pre-pared samples	119
4.3.2 Photocatalytic property of pre-pared samples	123
4.4. Conclusions.....	137
References.....	139

Chapter 5. Magnetic ZnO@Fe₃O₄ composite for self-generated H₂O₂ toward photo-Fenton-like oxidation of nitrophenol.....146

5.1. Introduction.....	147
5.2. Experimental	149
5.2.1. Materials	149
5.2.2. Preparation of Fe ₃ O ₄ nano powder	149
5.2.3. Preparation of flower-like ZnO micro-powder	149
5.2.4. Preparation of ZnO@Fe ₃ O ₄ composites (ZFCMs).....	150
5.2.5. Characterisation techniques	150
5.2.6. Photocatalytic activity assessment.....	151
5.3. Results and discussion.....	152
5. 4. Conclusions.....	166
References.....	167

Chapter 6. MXene as non-metal charge mediator in 2D layered CdS@Ti₃C₂@TiO₂

composites with superior Z-scheme visible light-driven photocatalytic activity174

6.1 Introduction.....	175
6.2. Material and Methods.....	176
6.2.1. Material preparation.....	176
6.2.2. Material characterizations.....	178
6.2.3. Photocatalytic activity evaluations.....	178
6.2.4. Reactive oxygen species (ROS) capturing experiment.....	179
6.3. Results and discussion.....	179
6.3.1. Structures, morphologies and textural properties of as-prepared samples.....	179
6.3.2. Organic pollutants removal studies.....	185
6.3.3 Proposed photocatalytic degradation mechanism.....	188
6. 4. Conclusions.....	193
References.....	194

Chapter 7. Conclusions and Perspectives200

7.1 Conclusions.....	200
7.1.1 Surface chemistry-dependent activity and comparative investigation on the enhanced photocatalytic performance of graphitic carbon nitride modified with various nanocarbons.	201
7.1.2 Nitrogen-doped Carbon Nanospheres Modified Graphitic Carbon Nitride for Enhanced Photocatalytic Performances.....	202
7.1.3 Efficient photo-Fenton oxidation of nitrophenol driven by self-generated H ₂ O ₂ from ZnO@Fe ₃ O ₄ composite.	203
7.1.4 MXene as non-metal charge mediator in 2D layered CdS@Ti ₃ C ₂ @TiO ₂ composites with superior Z-scheme visible light-driven photocatalytic activity.....	204
7.2 Perspectives for Future Research.....	204

APPENDIX I: ATTRIBUTION TABLES206

APPENDIX II: Copyright Permission Statements.....212

Chapter 1. Introduction

1.1 Current issues and developing methods for environmental remediation

The best estimates currently available suggest that the planet that we live on owns around 332.5 million cubic miles of water, however the proportion of freshwater that we can use directly for household and industrial consumption is quite limited (less than 1%) [1]. Although Arctic and Antarctic pack an abundant and wide variety of freshwater ecosystems, almost all of them in polar regions are in limbo, which is impossible for practical application [2].

In the past a few decades, attending all the boons brought about by high-tech wonders have come some sufferings; and the extensive deterioration of the Earth's ecosystem is manifest among them. Rampant deforestation has engendered vast soil erosion; worse yet, a multitude of chemical works, sewage disposal plants and textile factories discharge their toxic waste into streams, rivers or lakes. Approximately 80% of wastewater was endangered by the discharged sewage containing pharmaceutical compounds and pesticides which is far beyond the eco self-purification capacity[3]. Moreover, even tiny amount of organic pollutants such as dyes in water may cause knotty issue to the ecosystem [4]. Purification of sewage is indeed a growing concern all over the world, and thus it is necessary to develop effective way for sustainable development of human water issues [5, 6].

Chlorination, bio-flocculation and membrane technologies used to be employed to

combat this crisis. Nevertheless, the cons of multiple-stage processes, higher cost and halfway settlement of these technologies have become issues open to debate[7-9]. For example, flocculation and coagulation such as inorganic metal salts have been utilized as the most common measure to treat sewage from factories, but the secondary pollution to the water system will ensue due to introducing metal ions [10, 11].

Up to now, advanced oxidation processes (AOPs) have regarded as more effective technique comparing to traditional methods. There is no denying that the objective of AOP is to generate commonly superoxide ($\bullet\text{O}_2^-$) and superhydroxyl ($\bullet\text{OH}$) radicals for oxidation of contaminants. The hydroxyl radical has high oxidation potential (2.8V), which makes it easier for producing in natural water condition. Moreover, the short shelf life of these generated radicals within nanoseconds enables it to be self-eliminated during AOPs treatment. There are four main pathways for organic degradation using hydroxyl radicals: radical addition, hydrogen abstraction, electron transfer and radical combination [12].

Generally, AOPs can be divided into three pathways: Ozone based AOP, Fenton based AOP and Photocatalysis based AOP [12]. Ozone is a strong oxidant with high oxidation potential of 2.07 V. The $\text{OH}\cdot$ can be significantly increased with the participation of these additional oxidants. To date, the ozone based AOP can be classified to three types including ozonation, $\text{O}_3/\text{H}_2\text{O}_2$ and photolysis of H_2O_2 . However, direct O_3 oxidation is a selective reaction, which demands ionized and dissociated form of organic compounds rather than natural form. Moreover, the limited pH value restricts the application of ozone degradation. Meanwhile, it is reported that iron is one of the most popular metals in activated generation of $\text{OH}\cdot$ from H_2O_2 , which is called Fenton process. Three extended processes are exhibited on the base of classical Fenton process, they are Fenton-like, photo-Fenton and electro-Fenton reactions [5]. The only blemish exists that Fenton reaction needs to be carried out under acidic condition. On the other hand, the main step in photocatalysis based AOP is that the light energy induced electron of substrate transfers to molecular oxygen with ground state to produce highly

reactive oxidant species, which is an integral part of sewage treatment. Photocatalysis has been deemed as the most promising technology owing to its relative simple reaction process and through treatment of the persistent organic without introduction of secondary contaminate [13].

1.2 Research objectives

Our present work involves the development of efficient, economical and re-usable materials for decomposing dyes, phenol and antibiotics in water system utilizing solar energy. Numerous materials have been considered as photo driven catalysts. The materials chosen in this study including carbon materials because of its highly inert nature, large specific surface area diverse morphologies and easy modification of band gap. Modification of absorption spectrum of carbon materials from UV to visible region has been the major challenge. Fenton reaction and the photochemically enhanced or assisted Fenton reactions are widely considered to be efficient processes for removing pollutants in aqueous solution, which based on the generation of highly oxidizing species from hydrogen peroxide and Fe ions. In addition, a two-dimensional (2D) transition metal carbides/nitrides material named MXenes has been targeted toward various applications due to the outstanding electronic properties. MXenes can be employed as co-catalyst in combination with certain photocatalysts in photocatalytic systems to enhance photogenerated charge separation, suppress rapid charge recombination, and convert solar energy into chemical energy or use it in the degradation of organics.

Meanwhile, this work studies the intrinsic mechanisms for photocatalytic activation and radical evolution. Comprehensive studies integrating deliberate materials design were implemented, including morphology characterization, optical performance, electron paramagnetic resonance (EPR) and density functional theory (DFT) calculation.

Several objectives were set to develop novel photocatalytic materials or active device in visible region of light as follows:

1. To optimize various parameters pertaining to synthesize materials with appropriate size and morphology. Experiment conditions such as sample concentrations, reaction times and temperatures will be studied and optimized. The morphology of materials will be studied using scanning electron microscope (SEM) and transmission electron microscope (TEM). X-Ray Diffraction (XRD) and X-ray photoelectron spectroscopy (XPS) can be employed to qualitative and quantitative analysis of samples.
2. To establish suitable and reproducible methods for the preparation of semiconductor material using appropriate chemical routes. Hybridize the surface of semiconductor materials such as graphitic carbon nitride doped with nanocarbons.
3. To compare the effects of the properties before and after modification and carry out studies of band gap energy. The extension of the absorption spectrum from UV region to the UV-visible region will be studied.
4. To investigate the effects of heteroatom doping on carbon or MXenes materials for photocatalytic degradation with deliberate materials design and theoretical calculations.
5. To probe the mechanisms unveiling the intrinsic active sites and identify the pathways of modified catalysts with mechanistic studies.
6. To study the recyclability by using the photocatalytic system repeatedly on fresh contaminant solutions. The evaluation of the degradation rate will be carried out to estimate the stability of the obtained photocatalysts.

1.3 Thesis organization

This thesis consists of seven chapters. Chapter 2 introduces latest progress of wastewater treatment. Chapters 3-6 details experimental studies that have been published. Chapter 7 concludes the thesis and presents future perspectives of this research.

Chapter 1 — Introduction — Introduces the background and topic of this study that related to environmental pollution and sewage treatment in present-day society. Research objectives and thesis organization are conducted in this chapter.

Chapter 2 — Literature review — provides a comprehensive review of recent progress in wastewater treatment, including various advanced oxidation processes (AOPs), classification of photocatalysts, synthesis methods and applications of photocatalysis.

Chapter 3 — Surface chemistry-dependent activity and comparative investigation on the enhanced photocatalytic performance of graphitic carbon nitride modified with various nanocarbons. *J. Colloid Interface Sci.* 2020; 1(569):12-21— goes about to prepare graphitic carbon nitride (GCN) nanocomposites modified by nanocarbons that revealed great performances for total photodegradation of organic contaminants.

Chapter 4 — Nitrogen-doped Carbon Nanospheres Modified Graphitic Carbon Nitride for Enhanced Photocatalytic Performances. *Nanomicro Lett.* 2020; 24(12): 1886— unravels a facile hydrothermal method to synthesize a metal-free material for photocatalytic removal of sulfachloropyridazine (SCP) remarkably. The nitrogen content in NC critically influences the physicochemical properties and performances of the resultant hybrids. The mechanisms are further investigated by density functional

theory (DFT) calculations.

Chapter 5 — *Efficient photo-Fenton oxidation of nitrophenol driven by self-generated H₂O₂ from ZnO@Fe₃O₄ composite. Compos. Part B-Eng. 2020; 1(200): 108345*— reports in situ generation of H₂O₂ for efficient nitrophenol oxidation by simply reversing the prototypical Fe₃O₄-ZnO core-shell structure to provide inexhaustable Fe²⁺ and Fe³⁺ Fenton-active species on Fe₃O₄ shell.

Chapter 6 — *MXene as non-metal charge mediator in 2D layered CdS@Ti₃C₂@TiO₂ composites with superior Z-scheme visible light-driven photocatalytic activity. Environ. Sci.: Nano 2019; 6: 3158-3169*— synthesizes two-dimensional CdS@Ti₃C₂@TiO₂ nano-hybrids. The effect of CdS loading on the photocatalytic performance is elucidated. A charge carrier sinking function of Ti₃C₂ is first time fabricated and three-phase Z-scheme catalyst was proposed.

Chapter 7 — *Conclusions and perspectives* — highlights the meaningful findings in this study and proposes suggestions for further research in the field. discusses the remaining challenges and suggestions for further research in photocatalysis.

References

1. O. Haq, D. Choi, J. Choi and Y. Lee, Carbon electrodes with ionic functional groups for enhanced capacitive deionization performance. J. Ind. Eng. Chem., 2020. 83, 136-144.
2. M. Brusseau, Ecosystems and Ecosystem Services, Environ. Sci. Pollut. Res., 2019, 89-102.
3. P. Puijenbroek, A. Beusen and A. Bouwman, Global nitrogen and phosphorus in

- urban waste water based on the Shared Socio-economic pathways. *J. Environ. Manage.*, 2019. 231, 446-456.
4. J. Ren, X. Wang, C. Wang, P. Gong, X. Wang and T Yao, Biomagnification of persistent organic pollutants along a high-altitude aquatic food chain in the Tibetan Plateau: Processes and mechanisms. *Environ. Pollut.*, 2017. 220, 636-643.
 5. Q. Liu, X. Duan, H. Sun, Y. Wang, M. Tade and S. Wang, Size-tailored porous spheres of manganese oxides for catalytic oxidation via peroxymonosulfate activation. *J. Phys. Chem. C*, 2016. 120(30), 16871-16878.
 6. E. Saputra, H. Zhang, Q. Liu, H. Sun and S. Wang, Egg-shaped core/shell α -Mn₂O₃@ α -MnO₂ as heterogeneous catalysts for decomposition of phenolics in aqueous solutions. *Chemosphere*, 2016. 159, 351-358.
 7. K. Kosaka, K. Ohkubo and M. Akiba, Occurrence and formation of haloacetamides from chlorination at water purification plants across Japan. *Water Res.*, 2016. 106, 470-476.
 8. A. Pugazhendhi, S. Shobana, P. Bakonyi, N. Nemest'othy, A. Xia, R. Banu J and G. Kumar, A review on chemical mechanism of microalgae flocculation via polymers. *Biotechnol, Rep.*, 2019. 21, e00302.
 9. I. Tlili, T. Alkanhal, and Desalination, Nanotechnology for water purification: electrospun nanofibrous membrane in water and wastewater treatment. *J. Water Reuse Desalination*, 2019. 9(3), 232-248.
 10. L. Chao, H. Chao, X. Wei, J. Li, C. Ji and X. Qi, Design of SiO₂-TiO₂-P (AM-DMC) cationic composite flocculant and optimization of the flocculation process using response surface methodology. *J. Dispersion Sci. Technol.*, 2020, 1-14.
 11. J. Xiong, C. Zhang, X. Yang, T. Zhou and S. Yang, Combining chemical coagulation with activated coke adsorption to remove organic matters and retain nitrogen compounds in mature landfill leachate. *Environ. Technol.*, 2020, 1-9.

12. S. Jiménez, M. Andreozzi, M. Micó, M. Álvarez and S. Contreras, Produced water treatment by advanced oxidation processes. *Sci. Total Environ.*, 2019. 666, 12-21.
13. Y. Zhang, J. Zhou, X. Chen, L. Wang and W. Cai, Coupling of heterogeneous advanced oxidation processes and photocatalysis in efficient degradation of tetracycline hydrochloride by Fe-based MOFs: Synergistic effect and degradation pathway. *Chem. Eng., J.*, 2019. 369, 745-757.

Chapter 2. Literature review

2.1 Introduction

Environmental challenges, ranging from the smog in cities to toxic groundwater, have been emerged with our civilization advancement. Fresh water has been closely associated with lives, not only the life of human beings, but also the lives of all kinds of plants and animals. Aquatic ecosystem has been largely ruined by agriculture and industry activities, especially unrestricted drainage of sewages, which cause irreversible damage to our plants. Numerous traditional techniques have been developed to address these environmental concerns, including coagulation, filtration, sedimentation, adsorption, reverse osmosis, and biological methods; but most of which have deficiency of low efficiency, incomplete purification, high energy consumption or causing secondary pollution. Therefore, an environmentally friendly technology with highly efficiency is urgently required. Photocatalytic degradation has shown great potential as a low cost and environmentally sustainable technology for water purification compared to conventional methods [1].

Since Prof. Fujishima and Honda discovered that the single crystal titanium dioxide could generate hydrogen by splitting water under ultraviolet irradiation, the potential of solar energy utilization has been revealed in photocatalysis area, which provides a novel way in solving the problems of energy crises and environmental pollution [2]. However, given the low efficiency of solar energy conversion and high recombination rate between photoelectrons and holes, photocatalysis techniques still has a long way to go in large-scale industrial applications.

Photocatalysis blossomed in the past decades and several different types of

photocatalysts have been raised. Primarily, combinations of metal nanoparticles on the surface plasmon resonance have been investigated for degrading organic pollutants and carcinogenic materials [3]. The application of plasma metals as photocatalysts has flourished since the early 20th century and noble metal nanoparticles were deemed as the materials with strong localized surface plasmon resonance (LSPR) property. This kind of material has shown great potential in treatment of a wide range of organic pollutants under irradiation of solar light. Nevertheless, the noble metal nanoparticles are not earth-abundant and they suffer from high cost issues, which limit their widespread applications in industry [4].

In contrast, semiconductor photocatalysts attract a great deal of attention as generally economical materials; however, their low photoactivity seriously restricts the practical applications in aspect of photocatalysis. Various strategies have been developed to enhance the photocatalytic performance of semiconductor photocatalysts [5].

2.2 Applications of advanced oxidation processes (AOPs) in degradation of pollutants

Recently, AOPs draw close attention to purify polluted water because of the ability in the degradation of a wide range of organics through oxidation and reduction reactions. AOP is suitable for specific impurities treatment, including removal of heavy metals, degradation of specific contaminants, sludge treatment, and reduction of color or odor. In addition, pollutants can be removed without disinfection in AOPs.

Basically, AOPs are based on electricity activation, light scattering, and catalysts (or oxidants) to generate free radicals with high reactivity (such as OH) during the reaction. After combination, substitution, electron transfer or breaking bonds, the

macromolecular organic substances can be oxidative degraded into low-toxic or non-toxic substances with small molecule, or even be directly mineralized into CO₂ and H₂O. As one of the physicochemical treatment technologies, AOPs have advantages of high efficiency and thorough decomposition of organic substances. Various AOPs have been invented and studied for a couple of years and can be classified mainly into five different types, including chemical oxidation, electrochemical oxidation, wet oxidation, supercritical water oxidation and photocatalytic oxidation.

The methods of chemical oxidation include Fenton oxidation, Fenton-like oxidation and ozone oxidation. Fenton technology was originated in the mid-1990s, proposed by a French scientist H. J. Fenton who found that tartaric acid could be effectively oxidized by H₂O₂ with catalysis of ferrous ions. The default Fenton principle is producing hydroxyl radicals from hydrogen peroxide with adding Fe²⁺: $\text{Fe}^{2+} + \text{H}_2\text{O}_2 \rightarrow \text{Fe}^{3+} + \text{OH}^- + \bullet\text{OH}$. Fenton method shows superiority in treatment of some refractory organics such as phenols and anilines. However, it has limitations that most of these reactions must be performed under acidic conditions. The Fenton-like reaction is carried out utilizing Fe³⁺, iron-containing minerals or other transition metals (Co, Cd, Cu, Ag, Mn, Ni, etc.) to accelerate or replace Fe²⁺ in H₂O₂ catalysis. However, complexing agents (EDTA etc.) need to be introduced for enhancing catalytic activity. The ozone oxidation system owns high oxidation-reduction potential which can oxidize most organic pollutants. However, the ozone reaction is restricted by the target selectivity, and the outcomes of carboxylic acid organic substance express an incompletely degradation. Since ozone is extremely unstable in non-pure water, some strengthening means such as photocatalytic ozonation, alkali-catalyzed ozonation and ozone/ultrasonic methods have been developed to improve the efficiency.

The electrochemical catalytic oxidation method was originated in 940s, which has advantages of wide range of applications, high efficiency of degradation, automatic operation, and flexible use scenarios. The strong electrochemical oxidation method has

been favored by researchers in dealing with high concentration and toxic phenol-containing wastewater. However, limitations still exist and affect the wide-scale promotion of this method, such as high-power consumption, high cost of precious metals on electrodes, anodic corrosion, micro-kinetics, and thermodynamics research that needs perfecting.

Wet Air Oxidation (WAO) needs to be carried out under high temperature and pressure conditions. To make the condition milder and shorten the oxidation time, catalysts (metal salts, oxides, and composite oxides) are brought into the reactions, which can be called Catalytic Wet Air Oxidation (CWAO). CWAO can be divided into homogeneous CWAO and heterogeneous CWAO, according to the form of catalysts. The catalyst exists as ions in homogeneous CWAO, which is difficult to recycle thus causes secondary pollution. Although insoluble solid catalyst in heterogeneous CWAO has overcome the deficiency in homogeneous CWAO, the degradation rate is dependent on the specific surface area of catalysts, which is the main limitation in heterogeneous CWAO.

Supercritical water oxidation technology has made strengthening and improvement of CWAO, which employs supercritical water as medium to oxidize and decompose organic matters. Sourcing a proper catalyst with broad-spectrum catalytic performance is a key determinant of the development of this technique.

The photocatalytic oxidation technology has a host of boons, including simple structure of equipment, mild reaction conditions, easy control of operation and strong oxidizing ability. Therefore, photocatalytic oxidation technology is a new type of water treatment technology with broad application prospects. Photocatalytic technology has received tremendous attention due to its potential application because it can mineralize various organic pollutants at room temperature and pressure without secondary pollution. In recent years, more and more researchers focus on substantive

works and explorations in the field of semiconductor photocatalysis. In this paper, we will present various strategies for heterogeneous photocatalysts employing metal oxides, chalcogenides, carbonaceous and polymers. In addition, we will include the latest research and development progress in all aspects of heterogeneous photocatalysts.

2.3 Photocatalysis

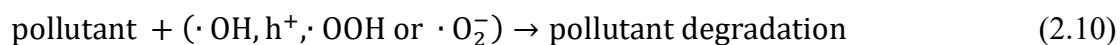
Typically, the semiconductor materials are widely employed as photocatalysts, which can be divided into 5 categories as shown in Table 2.1.

Table 2. 1 Typical semiconductive photocatalytic materials

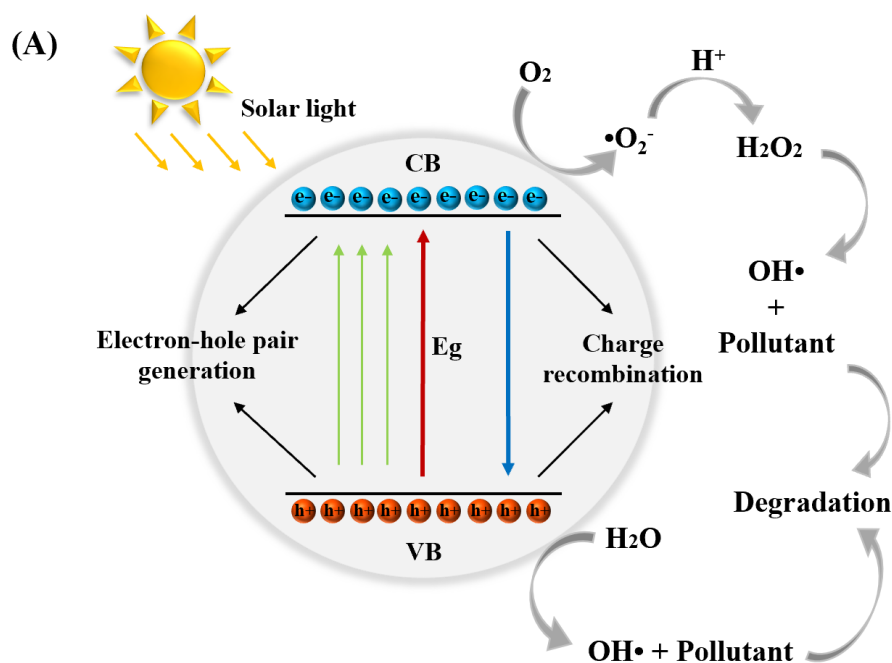
Semiconductor photocatalysts	
Nano metal oxide	TiO ₂ , Fe ₂ O ₃ , WO ₃ , SnO ₂ , CuO, Al ₂ O ₃ , ZnO
Noble metal loaded on nano metal oxides	Au, Pt, Rh, Ag, Co
Surface-coupled nano-semiconductors	CdS-ZnO, CdS-SnO, CdS-TiO ₂ , CdSe-TiO ₂ and SnO-TiO ₂
Perovskite-type photocatalysts	BaTiO ₃ , SrTiO ₃ , LaFeO ₃
Supported metal oxide catalysts	loading TiO ₂ or ZnO on adsorbent carrier (silica, zeolite, alumina, activated carbon)

Generally speaking, main steps of the activation of semiconductor photocatalyst are summarized in Fig.2.1 (A). (1) Upon light irradiation, e⁻/h⁺ pairs are produced through migration of photo-generated electrons from valence band (VB) to conduction band (CB). (2) The photogenerated electrons and holes are separated and migrate to catalytical active sites, imitating oxidation and reduction reactions on the surface of photocatalysts. (3) The photogenerated electrons and holes, producing reactive oxygen species including superoxide and hydroxyl radicals, which decompose

complex macromolecular organics into less hazardous organics or inorganic substances as following:



Many publications have focused on the mechanisms of semiconductor-based photocatalytic processes. The band-edge positions and potentials for different redox couples are summarized and exhibited in Fig.2.1 (B).



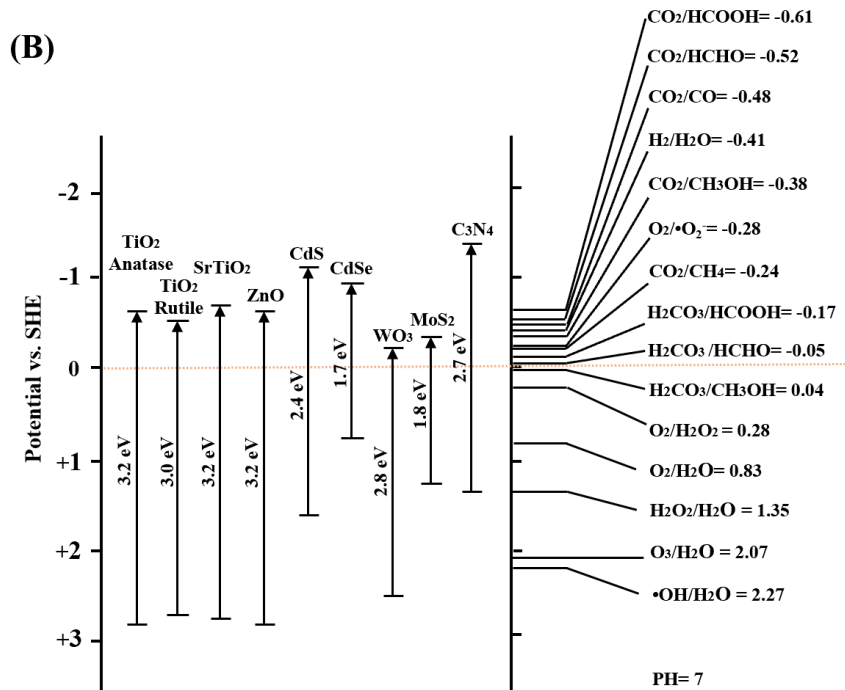


Fig. 2. 1 (A) Schematic illustration of semiconductor photocatalysts in degrading organic pollutants. (B) Band-edge positions and potentials for different redox couples of semiconductor photocatalysts.

2.3.1 Classifications of semiconductor photocatalysis.

To design a highly active photocatalyst, a lot of work is focusing on the design of heterojunction photocatalysts. Basically, inverse heterojunction (p-n) and homogeneous heterojunction (n-n) are two main categories of heterojunction structures according to the conductivity type of materials. Vast of studies have proved that both of p-n and n-n photocatalysts have outstanding performances in water splitting and contaminants degradation (Table 2.1).

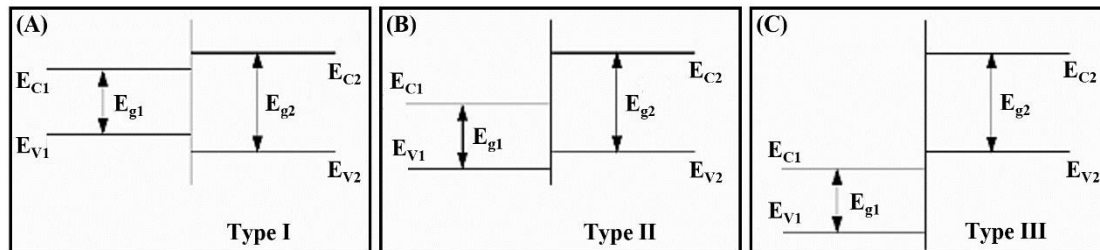


Fig. 2. 2. (A)Type I, (B)Type II and (C)Type III heterojunctions depending on the relative position of the energy bands.

Three types can be classified according to the relative positions of the energy bands of the semiconductors. The band diagrams of three types are shown in Fig.2.2. For type I, the band gap energy of one semiconductor material completely overlaps with the other one and produces discontinuity at the interface. For type II, parts of the band gap energies of the two semiconductors are overlapped. For type III, the forbidden bands of two semiconductors are completely staggered.

In a single crystal semiconductor combined with P-type and N-type semiconductors, p–n junction can be found at the interface. When a p–n junction forms, a stronger electric field is generated between the semiconductors, which accelerates the charge separation and reduces the charge recombination rate. Homojunction is a junction on the interface of alike semiconductor materials, which have similar band gaps but typically have diverse doping.

Table 2. 2 summarizes different types of heterojunctions reported in literatures, illustrating that heterojunctions in photocatalysts can improve the reaction activity effectively.

Table 2. 2. Different types of heterojunction

	Photocatalysts	Ref.
Type I	Bi _x O _y I _z /g-C ₃ N ₄ , V ₂ O ₅ /BiVO ₄	[6, 7]

Type II	graphene/g-C ₃ N ₄ , Au/g-C ₃ N ₄ , and WO ₃ /g-C ₃ N ₄ .	[8]
Type III	H ₃ PW ₁₂ O ₄₀ /TiO ₂ -In ₂ S ₃	[9]
p-n junction	Bi ₂ O ₃ /ZnO, NiO/ZnO	[7, 10]
Homojunction	g-C ₃ N ₄ , Cd _{1-x} Zn _x S	[11, 12]

2.4 Metal-based semiconductors

It is revealed that loading metal related nanoparticles on the surface of semiconductor nanoparticles can overcome some limitations of semiconductor. For example: (1) it suppresses probability of recombination of photogenerated charge carrier by serving passive electron sinks and facilitating charges' separation; (2) it promotes rapid dioxygen reduction to generate reactive free radicals; (3) it enlarges the response range of photocatalysts in the UV and visible ranges; (4) it acts as a trapping center to increase the longevity of carriers; (5) it can be directly activated under irradiation of visible light [13].

2.4.1 Noble metal-based photocatalysts

The existing problems of semiconductor photocatalysts are low utilization rates of solar energy and high rates of photo-generated carrier recombination, which can be effectively solved by noble metal doping, i.e. from gold (Au), silver (Ag), palladium (Pd) and platinum (Pt). When doped with metals, Schottky barrier (Φ_B) could be formed on the interface of the semiconductors, which will establish an internal electric field to promote charge separation. Noble metal doping can increase the concentration of surface electrons and decrease the resistance of n-type semiconductors (i.e. SnO₂, ZnO and TiO₂). While for p-type semiconductors, it will decrease the concentration of holes and increase the resistance [14-16].

In 1979, Kiwi and Gratezl observed that Pt nanoparticles could be photo-excited in water splitting. Since then, Kiwi's group has attempted to dope Pt nanoparticles on the surface

of TiO₂ nanoparticles and a significant enhancement of hydrogen production (300ml/h) was observed compared to the pure Pt and TiO₂ nanoparticles. Charge separation can occur when electrons are transferred from Pt nanoparticles to the conduction band of TiO₂, and therefore the induced photocatalysis can split water.

Ag has many advantages including low-cost, strong LSPR effect and controllable morphology. In 2008, Awazu et al. proposed that the photocatalytic activity of TiO₂ might be enhanced by the assistance of Ag nanoparticles [17]. Many investigations indicated that Ag/semiconductors (Ag/TiO₂, Ag/ZnO, Ag/AgBr, Ag/AgCl) showed efficient degradation of organics and hydrogen production under sunlight activation, which was ascribed to the strong LSPR of metallic Ag components that increased the absorption of visible light [18-21]. Shen et al. reported a green synthesis of Ag modified ZnO catalyst via simplified hydrothermal method toward degradation of methylene blue (MB) under UV irradiation. The excellent performance is attributed to the separation of charge carriers and reaction space resulting in an effective degradation result. Under UV irradiation, generated photoelectrons in ZnO are captured by Ag because of efficient light absorption and charge transportation/separation, and these electrons produced hydroxyl radical for further degradation mechanism [22].

Au nanoparticle has a transformable LSPR performance by controlling the morphology of particles, which accordingly acquires the light in different optical bands. Tian and Tatsuma reported that Au played a pivotal role in controlling the rapid charge separation in the photocatalytic system, which offered new opportunities in treatment of organic/inorganic dyes [23].

More prominently, it is possible to further expand the absorption range of Au doping by adjusting the size and morphology, which greatly improves the photocatalytic performance of the composites. It is found that, based on the variable LSPR effect of Au particles, an egg yolk-like hollow composite material could be synthetically tailored

across a broad spectrum from visible to near-infrared region, thereby significantly improved the performance of catalytic oxidation of benzyl alcohol [24]. Similarly, in the study by Ye et al., the synthesized Au@TiO₂ core-shell composites could strongly enhance the photocatalytic oxidation activity because of their ability to absorb more solar energy.

2.4.2 Metallic oxides

2.4.2.1 TiO₂ and modified TiO₂ counterparts

Titanium dioxide (TiO₂) has been widely utilized as a typical semiconductor, which can be divided into three main crystalline structures including brookite, anatase and rutile. Anatase TiO₂, with band-gap energy of 3.2 eV, possesses great photo response activity among these structures.

The anatase TiO₂ catalysts have been intensively studied in the past few years. Five typical steps are ascertained on the surface of TiO₂ during a photocatalytic process: (1) photoexcitation (light absorption and charge-carriers generation), (2) diffusion, (3) trapping, (4) recombination, and (5) oxidation [25]. Therefore, a variety of modification methods have been undertaken to control each step to improve the activity of TiO₂ photocatalysts.

Surface modification has been generally considered as an effective method to achieve photocatalytic promotion via changing the distribution of electrons and the surface properties of TiO₂. Impregnation reduction method or photoreduction deposition method can be employed to deposit an appropriate amount of noble metal (Pt, Au, Pd, Rh, Ag and Nb) on the surface of TiO₂, bringing about broaden response range of TiO₂. The photo induced electrons will concentrate on noble metals, leading to a reduction density on TiO₂ surface.

When TiO_2 combined with another material owning different energy levels, the photogenerated electrons will rapidly inject to the lower energy conduction band through the contact interface, which can reduce the recombination rate of the photogenerated carriers, thus broadening the response area of TiO_2 to visible region. Metallic oxides and metallic sulfide with narrow energy gaps (i.e. Co_3O_4 , Cu_2O , WO_3 , ZnO/ZrO_2 and ZnS/CdS) are extensively used in TiO_2 compositional modification. Whereas these dopants are still subject to the insufficiencies including low thermal stability and poor quantum efficiencies.

Dye sensitizations introduce organic sensitizers on the surface of TiO_2 to absorb more photons for activating and injecting more electrons to the conduction band of TiO_2 , which broadens the excitation wavelength of TiO_2 , thus harvest visible light for photocatalysis. Phthalocyanine, eosin, chlorophyll copper trisodium, heteropoly blue, erythrosin B, porphyrin compounds and its derivatives can be used as effective sensitizers to improve the photoactivity of TiO_2 .

Ion doping is to introduce metal or non-metal ions into the TiO_2 lattices during the preparation of TiO_2 , therefore changing the charges and types of crystal lattices, which affects the movement of photogenerated carriers and the distribution in the system. The change of the valence band or the conduction band potential structure ultimately brings about an increasing photocatalytic activity of TiO_2 .

Non-metal doped TiO_2 has attracted extensive attentions because researchers found that doped TiO_2 with non-metallic elements (P, N, S, C, B, F, etc.) can extend the response range to the visible light region, consequently obtain enhanced solar energy utilization. A comparison of typical modification methods of TiO_2 is summarized in Table 2.3.

Table 2. 3. Comparison of typical modification methods to enhance the photocatalytic properties of TiO_2 .

Modification methods	Catalyst	Preparation method	Activity	Disadvantages	Ref.
Noble metal doping	Pd/TiO ₂ -CS	Impregnation method	99.5% MB	Toxic and expensive	[26]
	PdPt/TiO ₂	Chemical deposition	96% CO		[27]
	Ag-TiO ₂	Photodeposition method	74.7% nitrate		[28]
Composite semiconductor	WO ₃ -TiO ₂	Sol-gel method	98.8% MO	Toxic, unstable and	[29]
	CdS/Pt/TiO ₂ nanotubes	Chemical deposition	91.9% MO	photocorrosive	
Dye sensitization	Porphyrin sensitized TiO ₂ /rGO	Impregnation method	85% MB	Competitive adsorption	[30]
Metal ion doping	Co/TiO ₂	Sol-gel method	97% RhB	Narrow range of	[31]
	Fe/TiO ₂	hydrothermal method	60% para quate	doping concentration	[32]
Nonmetallic ion doping	Graphene/N /TiO ₂	Sol-gel method	96.2% MO	Narrow range of	[33]
	rGO/ TiO ₂	Hydrothermal method	90% MB	concentration	[34]

2.4.2.2 Iron oxide

It is difficult to recycle photocatalysts in particular in nanosize from reaction mixtures, which restricts the usage of heterogeneous photocatalysts in wastewater treatment. UV light only accounts for small proportion in solar spectrum (5-7%), while visible and infrared lights constitute 46% and 47% [8, 35], respectively. To resolve the

above problems, iron oxide nanoparticles including Fe_3O_4 [36-39], $\alpha\text{-Fe}_2\text{O}_3$ [40], $\beta\text{-Fe}_2\text{O}_3$ [41], $\gamma\text{-Fe}_2\text{O}_3$ [42], FeO and MFe_2O_4 [43, 44], have been employed as rational materials due to the paramagnetism/ferrimagnetism, environmental-friendly nature and great stability [45]. Applications of magnetic iron oxide integrated photocatalysts are summarized in Table 2. 4.

Table 2. 4. Applications of magnetic iron oxide integrated photocatalysts.

Photocatalyst	Preparation method	Saturation magnetization	Activity	Ref
$\text{Fe}_3\text{O}_4@\text{TiO}_2$	Hydrothermal method	32.9 emu/g	94% RhB in 60 min	[38]
g-$\text{C}_3\text{N}_4@\text{Fe}_3\text{O}_4@$ BiOI	Hydrothermal method	8.7 emu/g	98% RhB in 240 min	[46]
$\text{Fe}_3\text{O}_4@\text{ZnO}$	Hydrothermal method	60.7 emu/g	94.8% phosphate in 5 min	[39]
$\text{Fe}_3\text{O}_4@\text{TiO}_2$	Precipitation titration	52.6 emu/g	100% FCF in 60 min	[47]
rGO@$\text{Fe}_3\text{O}_4@$ TiO₂	Sol-gel and assembling method		100% MB in 9 min	[37]
$\gamma\text{-Fe}_2\text{O}_3@$ TiO₂	Hydrothermal method	75 emu/g	94% MO in 120 min	[42]
$\text{ZnO}@\text{Fe}_3\text{O}_4$	One-step synthesis route		100% RhB, 100% Ag^+ , 80% Co^{2+} , 89.7% Cu^{2+} and 91.6% Ni^{2+} in 40 min	[36]
$\text{Fe}_3\text{O}_4@\text{ZnO}$	Surfactant-free method	2.81 emu/g	73.9 % Phenol in 180 min, E. coli	[48]

				inactivation in 30 min
Fe₃O₄@C@ZnO	One-pot method			99% MB in 60 min [49]
γ-Fe₂O₃@ZnO	Atomic layer deposition	5.2 emu/g		90.3% ciprofloxacin in 60 min [40]
MFe₂O₄-Ag₂O (M = Zn, Co, & Ni)	hydrothermal method	16.48, 22.71 and 19.62 emu/g		95%, 80% and 95% MO in 5, 14 and 6 min, respectively [44]
Fe₂O₃-MFe₂O₄	Laterite leach liquors	9.0 emu/g		90.0% RhB in 90 min [50]

2.4.2.3 ZnO and other metal oxide/ complex metal oxides photocatalysts

ZnO nanoparticles have been effectively used in numerous fields, such as aser [51], sensor [52], solar cell [53] and field-emission device [54], due to its non-hazardous nature, low cost and high photoactivity [36]. ZnO is a n-type semiconductor possessing a direct and wide band gap (3.37 eV) and a big excitation binding energy (60 meV), which are close to anatase TiO₂, the mostly used and classical photocatalytic material, so ZnO theoretically has similar photocatalytic ability as TiO₂ [55]. In fact, ZnO owns a higher photocatalytic activity than TiO₂, yet worse stability, because photocorrosion and unsatisfactory utilization efficiency of visible light often limit its photocatalytic activity [56-58]. Therefore, considerable amount of research efforts has been employed towards ZnO band gap engineering to improve charge separation and extend its response into the visible light region.

In general, doping metallic elements (Na, Cu, and Fe) [59-61], non-metallic elements (N and C) [62, 63] and noble metals (Au, Ag, and Pt) [64-66] can effectively improve the visible-light response of ZnO. And coupling with other semiconductors is a preferable approach to enhance the photoactivity of ZnO. Binary (ZnO/Fe₂O₃, ZnO/CuO, ZnO/Bi₂O₃, ZnO/BiOI, ZnO/NiO, ZnO/Ag₃VO₄ and ZnO/CeO₂) [67-73] and ternary

ZnO-based nanocomposites have been confirmed to have higher light absorption, better suppression of photoinduced electron-hole pairs recombination and increased charge separation than the original materials.

In addition, further studies showed that some other metal-oxide semiconductors are promising photocatalysts for water splitting and organics degradation due to the lower band-gap energy and the more negative conduction band positions, including WO_3 [74], In_2O_3 [75], CuO [76], SnO_2 [77], Ta_2O_5 [78] and Bi_2O_3 [79].

Involving two or more metals in semiconductors would make it easier to modulate the band structures, eg. band-gap energies and the positions of the VB and CB, therefore achieving the desired photocatalysis. The ideal perovskite type oxide has structure of cubic symmetry with general formula of ABO_x , wherein A refers to rare-earth metals, and B refers to transition metal ions. Partial replacement of A or B with other metal ions will result in ionic defects, accordingly improving the photoactivity of the catalysts. Some compounds, such as KBiO_3 [80], Ag_3PO_4 [81], $\text{CaBi}_6\text{O}_{10}$ [82], CuBi_2O_4 [83], Bi_2WO_6 [84], BiTaO_4 [85], InTaO_4 [86], SrSnO_3 [87], $\text{Bi}_4\text{Ti}_3\text{O}_{12}$ [88], LaTaON_2 [89] and Zn_2GeO_4 [90] have been proven to have strong absorption properties in the visible light region.

2.4.3 Metal sulfides, nitrides (or oxynitrides) and carbide

There have been several studies in literature reporting metal sulfides. In 1983, CdS was found to be able to produce hydrogen from water under visible-light photocatalysis [91]. With proper modification or hybridization, CdS has been frequently applied in photodegradation of organic pollutants in water system [92-94] and hydrogen production [95]. ZnS has been widely investigated as a good photocatalyst owing to the rapid generation of electron-hole pairs and the excellent reduction potential for the photodegradation of contaminants, hydrogen production [95, 96] and CO_2 conversion [97]. Other metal sulfides, such as Bi_2S_3 [98, 99], CuS [100], In_2S_3 [101], Co_3S_4 [102], Ag_2S [103] MoS_2 [101], WS_2 [99], NiS [104] have merited close attention due to their excellent photocatalytic performance under visible light irradiation and are widely used

for the wastewater treatment. Metal nitrides such as TiN [105], Mo₂N [106], Ta₃N₅ [107], and Ge₃N₄ [108] are widely investigated as visible-light photocatalysts. In addition, metal oxynitrides, such as TaON [109] and TiON [110] have also been regarded as a promising visible-light-driven photocatalyst for water splitting and organic degradation.

2.4.3.1 Transition metal carbide/nitride materials

Nowadays, two-dimensional (2D) materials have been consolidating their status as the chief means of photo driven materials, such as graphene, graphite carbon nitride, and molybdenum disulfide [111, 112]. Graphene with two-dimensional honeycomb structure has been most widely studied, which is composed of carbon atoms with sp² hybrid orbitals and confirmed to have high theoretical specific surface area of 2630 m²g⁻¹ and high electron mobility of 200,000 cm²v⁻¹s⁻¹. However, the weak van der Waals force between the interlayers and the complicated preparation process are the biggest obstacle for the further application of the graphene. MXene is a new two-dimensional material with composition of metal carbide or carbonitride. In 2011, Naguib with his team successfully synthesized two-dimensional Ti₃C₂ MXene for the first time [113]. They selectively etched the metal Al atoms using hydrofluoric acid at room temperature to form layered hexagonal ternary carbide (Ti₃AlC₂).

The MXene is generally prepared from M_{n+1}AX_n, where M represents an early transition metal (Sc, Ti, Zr, Hf, V, Nb, Ta, Mo); while A is mainly from group III or IV elements and X indicates C or N; n usually refers to 1, 2, 3 [114-116]. Owing to their unique structure, superior photoelectronic conductivity and storage capacity, graphene-like MXenes with layer structure show various potential applications in different areas, such as energy storage, electromagnetic interference shielding [116, 117], gas sensors [118], biological probe, wireless communication [119], water treatment [120, 121], solar cells [122-124], and catalysis [111, 125-128]. The general formula of MXenes is M_{n+1}X_nT_x, where T_x denotes surface functional groups from

etching process (–O, –OH, –F, or a mixture of several groups), the existing of which shows great chemical property in MXenes. Generally, wet chemical HF etching and in situ HF etching methods are most commonly used in MXenes preparation [129]. Meanwhile, other processes employing tetramethylammonium hydroxide (TMAOH) [130, 131], electrochemical [132], or etching with NaOH [132] and ZnCl₂ [127] have also been reported.

It is worth emphasizing that enormous potential of MXenes can be seen in aspect of catalytic applications, including electrocatalysis, photocatalysis and traditional heterogeneous catalysis, because of the rich compositions and surface chemistry, tunable structures, and outstanding thermal stability. Some representative MXene-based materials are summarized in table 2. 5.

Table 2. 5. Summary of representative MXene-based materials for applications in catalysis.

Catalytic reaction	Catalyst	Photocatalytic activity	Ref.
HER	MoS ₂ /Ti ₃ C ₂ @C	Overpotential of 135 mV @ 10 mA cm ⁻² in acid solution.	[125]
	Mo ₂ CTx	Overpotential of 283 mV in 0.5 m H ₂ SO ₄ .	[133]
OER	Co-P/Ti ₃ C ₂	Overpotential of 298 mV @ 10 mA cm ⁻² alkaline electrolyte.	[134]
	Ni _{0.7} Fe _{0.3} PS ₃ @Ti ₃ C ₂ Tx	overpotential of 282 mV @ 10 mA cm ⁻² in 1 m KOH.	[135]
Photocatalytic CO₂ reduction	TiO ₂ /Ti ₃ C ₂	0.22 μmol h ⁻¹ for CH ₄ production	[136]
	Ti ₃ C ₂ /Bi ₂ WO ₆	0.069 mmol/g CO ₂ adsorption	[137]
Photocatalytic H₂ production	CdS/Ti ₃ C ₂ Tx	hydrogen production of 14 342 μmol h ⁻¹ g ⁻¹	[138]

	Cu/TiO ₂ @Ti ₃ C ₂ T _x	hydrogen production of 860 $\mu\text{mol h}^{-1} \text{g}^{-1}$	[139]
	Ti ₃ C ₂ /g-C ₃ N ₄	hydrogen production of 72.3 $\mu\text{mol h}^{-1} \text{g}^{-1}$	[140]
	ZnS/ Ti ₃ C ₂	hydrogen production of 124.6 $\mu\text{mol h}^{-1} \text{g}^{-1}$	[141]
Photocatalytic degradation	CdS@Ti ₃ C ₂ @TiO ₂	Remove RhB, MB, SCP and phenol in 60, 88, 88 and 150 min	[111]
	Ti ₃ C ₂ -OH/CdS	Remove 97% RhB in 100 min	[142]
	g-C ₃ N ₄ /Ti ₃ C ₂	Remove ciprofloxacin in 150 min	[121]
	a-Fe ₂ O ₃ / Ti ₃ C ₂	Remove 98% RhB in 120 min	[143]

2.5 Metal-free photocatalyst

In the past decades, the metal-based photocatalysts have attracted a surge in attention in aspect of the application of solar energy for water purification, but the shortcomings of high cost, source scarcity, low selectivity, poor durability and environmentally toxicity cannot be ignored. In recent years, researchers have turned their focus on metal-free materials. Unlike the metal-containing photocatalysts which need expensive metal salts for preparation, metal-free photocatalysts have unique advantages of earth abundance, low cost, simple structure, simple synthesis and environmental friendliness.

In 2009, Dai and his colleagues developed a brand new kind of carbon nanotube material with high-efficiency ORR catalysis, which showed better performance than commercial Pt/C [144].

According to the classification of the metal-free photocatalysts, it comprises three major parts, graphitic carbon nitride (g-C₃N₄)-based photocatalysts, graphene-based photocatalysts and elemental metal-free photocatalysts made of one single element

[145-149].

2.5.1 Graphitic carbon nitride (g-C₃N₄)

Carbon nitride (g-C₃N₄) is the most extensively studied material among metal-free photocatalysts. It is a polymeric layered material, structurally analogous to graphene. The van der Waals forces between layers bring about good thermal and chemical stabilities of g-C₃N₄ and it is insoluble in water, ethanol, acetone, dichloro carbon, N, and N-dimethylformamide. It can remain unchanged after heated to 600°C in air. g-C₃N₄ is a medium band gap semiconductor with band gap of 2.7 eV. Pertaining to its yellow color, the light absorption of g-C₃N₄ lies around 460 nm, resulting in a promising ability to harvest solar energy. Traditionally, g-C₃N₄ is generally synthesized by thermal condensation of N-rich precursors, such as urea, dicyandiamide and melamine. However, the popularization and application of g-C₃N₄ is restricted by the ineffective utilization of solar energy due to low specific surface, serious recombination of photogenerated electron–hole pairs, low quantum efficiency and broad band gap. It is imperative to develop optimized and modified methods to enhance photocatalytic efficiency of g-C₃N₄ [149].

2.5.1.1 Structural modification of g-C₃N₄

Although great progresses have been made in studies of g-C₃N₄, designing and preparing porous g-C₃N₄ materials with large surface area and pore volume are still challenges for researchers [150, 151]. Among various synthesis methods, the hard-templating method is the most effective one. It can easily adjust the porosity, structure, morphology, surface area and the size of the samples, which provides more active sites on the surface of g-C₃N₄ [152, 153].

The main steps of the hard templating method include: (1) immersing the nitrogen-rich

precursor in the mesoporous template; (2) calcining the powder after drying, the framework structure of g-C₃N₄ is condensed in the template channel; (3) employing NH₄HF₂ or HF to remove the hard template then obtaining g-C₃N₄ with ordered nanoporous structure. The mostly used agents are silica particles, porous alumina film and calcium carbonate particles. Cyanamide, dicyandiamide, melamine, urea, thiourea and other nitrogen-rich materials can be utilized as precursors, but most of the precursor molecules have cons of poor solubility in water, toxicity and high-cost. Therefore, the selection of suitable templates and precursors is crucial for the synthesis of g-C₃N₄ with various morphologies and carbon-nitrogen ratios.

Liquid phase surfactant can be used as the soft template, which shows merits of shorter cycle, lower cost, and more environmentally friendly comparing with the hard templating.

Zhang et al. prepared nanopores g-C₃N₄ via soft-templating using P123, F127, Triton X-100, Brij-30 and CTAB as surfactants. The obtained g-C₃N₄ had a high BET surface area (112 m² g⁻¹), but a nonuniformed and unordered pore distribution [154]. However, GCN intermediate polymer would inevitably decompose during the decomposition process of surfactant and the total yield was only 20%-30%, which was lower than that of hard templating.

In 2013, Zhu et al. developed g-C₃N₄ with mesoporous structure by changing the calcining atmosphere. The obtained g-C₃N₄ had a high specific surface area of 201-209 m²g⁻¹ and pore volume of 0.50-0.52 cm³g⁻¹, endowing high catalytic activity in photodegradation of methyl orange [155]. Additionally, the ultrasonic stripping [156, 157], chemical stripping [158], gas loosening [159] and secondary calcining [160] were also widely used in pore-forming of block g-C₃N₄ or synthesized graphene-like g-C₃N₄ nanosheets. Shanker et al. obtained the block nonporous g-C₃N₄ via direct calcining of melamine, and the specific surface area and pore volume were 8m²g⁻¹ and 0.08cm³g⁻¹.

Afterwards, the block g-C₃N₄ was placed in ethanol solution with 33Hz ultrasonic waves at room temperature for 5 hours. g-C₃N₄ with mesoporous structure was obtained after subsequent separation and drying. Both of specific surface area and pore volume increased to 121 m²g⁻¹ and 0.39 cm³g⁻¹. Meanwhile, the pore size was 3.9nm, and the distribution was relatively concentrated [161]. From the aspects of the cost, preparation cycle and environmental impact, the template-free method is naturally the most ideal for preparing mesoporous g-C₃N₄. However, the meso-porosity on g-C₃N₄ synthesized by soft templating and template-free methods is basically composed of disordered pores, and the distributions of pore sizes are relatively wide. Nevertheless, if high values of texture properties and ordered pores are not required (such as photocatalysis and fuel cells), the soft templating and template-free methods are undoubtedly preferred.

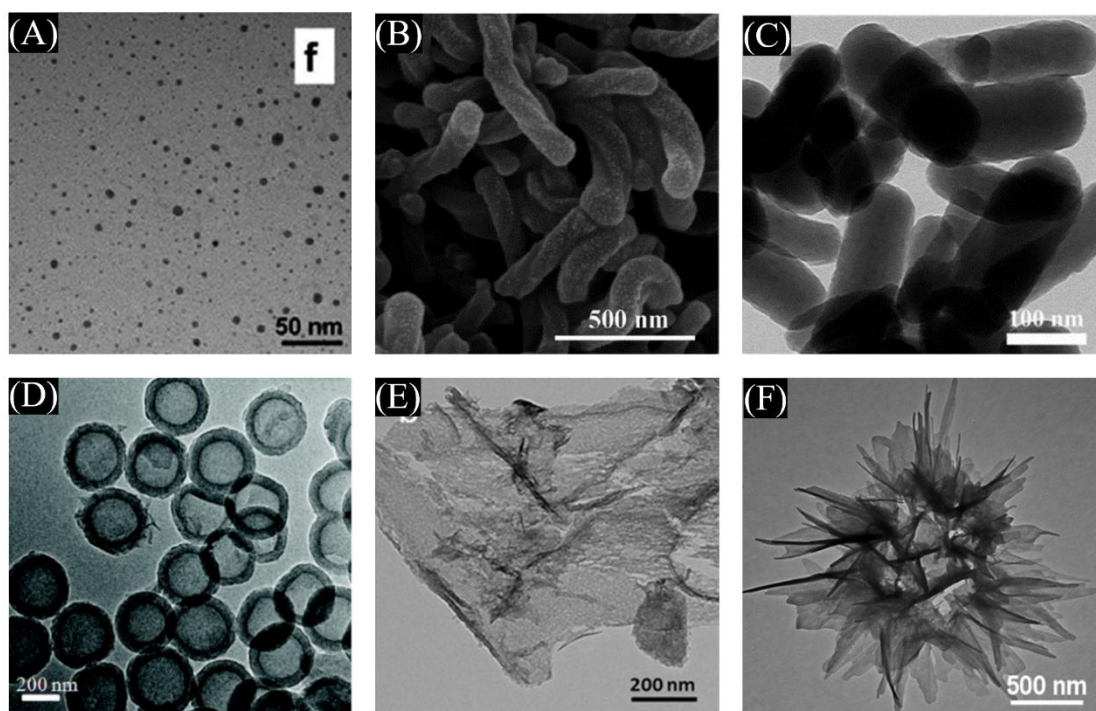


Fig. 2. 2 Different dimensional g-C₃N₄ materials

Fig. 2. 2 shows six different shapes of g-C₃N₄ photocatalysts: quantum dots, twisted nanorods, nanorods, nanospheres, nanosheets and nanostructured flowers. Wang et al. reported that the bulk g-C₃N₄ could be exfoliated into 2D nanosheets, 1D nanoribbons

and finally 0D quantum dots via directly thermal-chemical etching [162]. The obtained quantum dots exhibited blue emission and charge recombination with visible light activation. Zheng et al. synthesized g-C₃N₄ with twisted hexagonal rod-like morphology (diameter of 100–200 nm and length of 0.5–2.0 mm) via nanocasting technique [163]. This especial nanoarchitecture promoted charge separation and mass transfer of semiconductors, which showed efficient photocatalytic potential for water splitting and CO₂ reduction. Antonietti fabricated uniform graphitic carbon nitride nanorods (CNR) by templating a chiral mesostructured silica nanorod [164]. The prepared CNR demonstrated excellent photocatalytic capability in H₂ generation, although the BET surface area of CNR was 52 m²g⁻¹ that was much smaller than the 230 m²g⁻¹ for mesoporous g-C₃N₄. Niu et al. synthesized graphene-like g-C₃N₄ nanosheets with a thickness of around 2 nm, which could be easily obtained by thermal oxidation etching of bulk g-C₃N₄ in air [165]. A higher BET surface area of 306 m²g⁻¹ was obtained, compared to the bulk g-C₃N₄. Excellent photocatalytic hydrogen productivity could be observed owing to the increased band gap and better electron transport ability originating from the quantum confinement effect. Zheng et al. reported a hollow g-C₃N₄ nanosphere (HCNS) by incorporating aromatic motifs into the nanosized shells of hollow structure of g-C₃N₄, which resulted in an extension of π -conjugation and a red-shift of optical absorption [166]. Therefore, an enhancement of photocatalytic hydrogen evolution could be found under visible light irradiation.

Recently, Wang et al. designed a single or few-layered polymeric carbon nitride (PCN) nanosheets via a facile and green one-step carbon/nitrogen steam reforming approach from precursors including urea, melamine, dicyandiamide and thiourea [167]. The obtained PCN exposed more active sites on the enlarged surface area and prolonged charge lifetime, which resulted in a great enhancement in hydrogen generation (261.1 mmol h⁻¹). Such a delamination method could be applied to other carbon-based 2D materials for advanced applications.

Zhu et al. reported a P-doped g-C₃N₄ nanostructured flowers of in-plane mesopores by a co-condensation method without templates, which promoted light trapping, mass transfer and charge separation [168]. The open-up surface and well-defined mesopores enabled to enhance the catalytic activity in hydrogen production under visible light irradiation.

2.5.1.2 Modification of g-C₃N₄

Heteroatom doping is an efficient method to narrow the bandgap of g-C₃N₄. Several heteroatom elements doping of g-C₃N₄ have been demonstrated to narrow the bandgap. Both cations and anions, including metal ions (Fe [169-172], Zn [173, 174], Bi [175], Co [176, 177], Mn [178], Cu [179, 180], Na [181]) and nonmetal ions (C [182-184], N [185], O [186], S [187], P [188], F[189], I[190, 191]) have been extensively investigated. However, the doped heteroatoms are distributed on the surface of g-C₃N₄ layers, which limited extension of the light-absorbing edge and improvement of photocatalytic activity. Combinations of g-C₃N₄ with some semiconductors, including Cu₂O [192], Ni complex [193-195], Bi complex [6, 196, 197], red phosphor [198], graphene [199], TiO₂ [200], and CdS [200] have emerged as one of the most fascinating and exciting research directions in the past 10 years especially in arenas of environmental remediation, energy conversion, and energy storage. The moderate performances were attributed to the insufficient light harvesting and inefficient charge separation. Thus, more research efforts have been dedicated to further improve the efficiency.

As we all know, organic dyes have been widely applied as a visible light harvesting molecule for taking advantage of solar energy effectively. In such a photoexcitation process, the photoinduced electrons were generated from dye molecules rather than g-C₃N₄, which were injected into the conduction band of g-C₃N₄, thus suppressing the charge carrier recombination [201]. Over the past a few years, dyes have been gradually used as a visible

light harvesting molecule to extend the possibility of the reaction. Currently, eosin-Y [202], fluorescein [203] and perylene [204] dyes have proven to be efficient sensitizers during photocatalytic processes and they can significantly boost the photoactivity over the g-C₃N₄ photocatalyst. Table 2. 6 compares typical modification methods above-mentioned.

Table 2. 6. Comparison of typical modification methods to enhance the photocatalytic properties of g-C₃N₄.

Modification methods	Catalyst	Preparation method	Photocatalytic activity	Ref.
Metal ion doping	Fe@ g-C ₃ N ₄	one-step pyrolysis process	75% MB in 3h; H ₂ 536 $\mu\text{mol h}^{-1} \text{g}^{-1}$	[172]
	Na@ g-C ₃ N ₄	one-pot, solid-state route	98% EE2 in 2h	[181]
	Co@ g-C ₃ N ₄	one-step thermal polycondensation	H ₂ 560 $\mu\text{mol h}^{-1} \text{g}^{-1}$	[177]
Nonmetallic ion doping	C@ g-C ₃ N ₄	hydrothermal method	97% MB in 2h	[184]
	P-S@ g-C ₃ N ₄	in situ thermal condensation	100% MB in 3h	[188]
	I-K@ g-C ₃ N ₄	simple pyrolysis method	100% SMX in 40 min	[189]
Composite semiconductor	g-C ₃ N ₄ @ Cu ₂ O	chemical precipitation method	92% E. coli in 120 min	[6]
	CdS@ g-C ₃ N ₄	In situ fabrication	100% MO in 40 min	[200]
Dye sensitization	Fluorescein/ Ag@ g-C ₃ N ₄		H ₂ 2014.20 $\mu\text{mol h}^{-1} \text{g}^{-1}$	[205]

Eosin Y /g-	12.50 mmol g ⁻¹ h ⁻¹ [206]
C ₃ N ₄ /NiCoP	

2.5.2 Nanocarbon material

Numerous researchers have demonstrated that nanocarbon material can be classified to graphite, diamond, fullerene, carbon nanotubes and graphene, depending on the hybridization (sp, sp², or sp³) of carbon atoms. Graphite is a kind of black, soft and stable conductor with strong covalent bonds in the carbon layers and weak van der Waals forces between the carbon layers. As a tough transparent material with 3D network structure, each crystal lattice of diamond is consisted of four carbon atoms (sp³ hybridized). C₆₀ produces a major branch of carbon material as a cage-shaped spherical material. Carbon nanotubes open a new space of material science and nanotechnology, which possess a unique 1 D coaxial tube with diameter of 2-20 nm and consist of hexagonal arrangement of carbon atoms. It has the peculiarities of strong elasticity, high strength, good quantitative, great thermal insulation, excellent stealth and strong infrared absorption. Fig. 2. 3 illustrates 2D graphene family nanomaterials with various morphologies and characteristics, including graphene, few-layer graphene, graphite, reduced graphene oxide and graphene oxide [207]. Carbon quantum dots (CQDs), new kind of zero-dimensional (0D) carbon nanomaterial (less than 10 nm in size), have been suggested to be promising photocatalytic candidate. CQDs' capabilities of harvesting long wavelength light and exchanging energy with solution species endow them feasibilities to function as photocatalysts in organic syntheses. Different from spherical, tubular or nanosheets of carbon, CQDs exhibit distinctive electronic and optical properties because of their large edge effects and quantum confinement, which result in better peroxidase-like activities than others

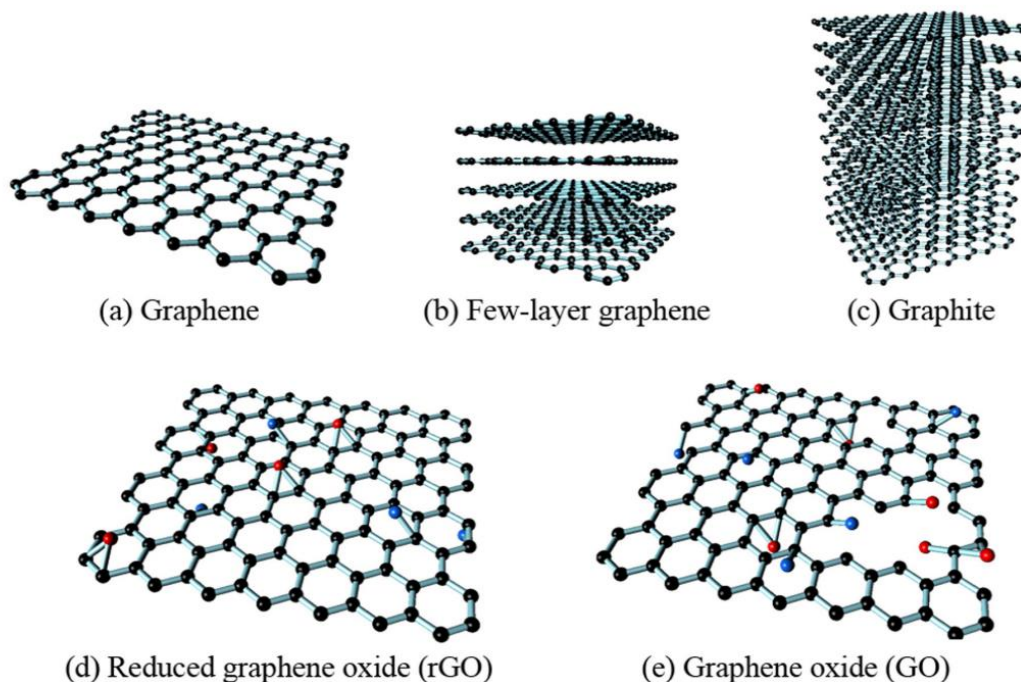


Fig. 2. 3. 2D graphene family nanomaterials.

2.5.2.1 Graphene

Since graphene was first fabricated through mechanical exfoliation in 2004, researchers invested intensively in studying this “dream material” [208]. Graphene, a flat single-atom-thick sheet of sp^2 hybridized carbon atoms, is arranged in a hexagonal lattice with a distance of 0.142 nm between two carbon atoms [26], which can be classified into four types: zero-dimensional (0D) fullerenes [209]; one-dimensional (1D) nanotubes; two-dimensional (2D) honeycomb lattice structure [210] and three-dimensional (3D) graphite [211]. Among these types, 2D structure brings about the best photocatalytic effect. The mechanism of 2D graphene in photocatalysis can be attributed to three main aspects: 1. serving as the collectors and transmitters of photo excited electrons; 2. broadening the range of light absorption; 3. enhancing the adsorption ability. Recently, tremendous progresses have been achieved in development of 2D graphene family nanomaterials including graphene, few-layer graphene, graphite, reduced graphene and graphene oxide.

Since the conduction band energy of the Fermi level of graphene are lower than most of the semiconductors, photogenerated electrons can be easily transferred from the semiconductor to the graphene through the interface. Graphene involves a giant π -conjugated system, which results in extraordinary mobility of charge carrier (up to $1.5 \times 10^4 \text{ cm}^2/(\text{V}\cdot\text{s})$) transferring to the target reactant, accordingly forming superoxide radicals (hydroxyl radicals and peroxy radicals), then achieving non-selective oxidization of organic pollutants, photocatalytic sterilization, water splitting and CO_2 reduction. When graphene is combined with semiconductors, M-C or M-O-C (M represents metal) bonds may be formed on the surfaces or in a certain depth of graphene, causing a certain degree of red shift, thereby expanding the response to visible light range. Graphene involving π -conjugation and the single-atomic with two-dimensional planar has the largest specific surface area ($2630 \text{ m}^2/\text{g}$), thereby it exhibits higher photocatalytic efficiency compared to other carbon nanomaterials (graphite, carbon black, activated carbon, carbon fiber, carbon nanotubes, fullerenes, etc.) [208].

Non-metal doping methods can be divided in two categories: in-situ and post-processing methods. In-situ method includes vapor deposition and ball milling, while post-processing method includes thermal decomposition and wet chemical method. Each method has its respective advantages and disadvantages as shown in Table. 2. 7.

Table. 2. 7 Advantages and disadvantages of various preparation methods of non-metal doping graphene.

Preparation method	Advantages	Disadvantages	Ref.
vapour deposition method	Good controllability and uniform doping	Complex procedures, low output, harsh conditions and tedious processes	[212, 213]

Wet chemical method	Low cost, simple process, easy industrialization	Long preparation cycle, low product purity and large particle radius	[214, 215]
Thermal annealing method	Low cost and environmentally friendly	Poor uniformity, poor controllability, and low doping rate	[216, 217]

Nitrogen atoms can be easily embedded in the graphene lattice, because of a similar size with carbon atoms. Compared to carbon atoms, one more electron can be found in the nitrogen atoms in the conduction band, which opens the band gap of graphene to obtain an n-type graphene semiconductor with nitrogen doped [217, 218]. Yang and colleagues [218] synthesized small-sized nitrogen doped graphene (S-NGR) via one-step alkali-assisted hydrothermal method. Under visible light irradiation (wavelength of 405 ± 15 nm) for 6 h, 96% rhodamine B could be degraded, and the effect of the size of catalyst was further discussed in this work. Jiang [219] prepared N-doped graphene hydrogels (NGHs) with varying doping densities by one-pot hydrothermal method and used ammonium hydroxide as N precursor. NGHs were verified to have higher surface area, porous structure, better mechanical strength and lower weight. It was also found that NGHs could effectively degrade 70% of acridine orange (AO) solution within 5 h under visible light irradiation. Mohamed et al. [220] synthesized nitrogen-hybridized graphene (NG) via heating the mixture of GO and urea and at 900 °C for 10 h. The obtained NG photocatalyst was tested under visible light ($\lambda > 420$ nm, 160 W). The TOC removal rate reached 75% and 5% of methylene blue (MB) and phenol, respectively. Doping nitrogen into graphene sheets can vary the conductivity and the concentration of charge carriers, which developed a novel area to study photocatalysis.

The composites of graphene and semiconductor can effectively reduce the recombination of photogenerated electrons and holes, which is a key determinant of the efficiency of photocatalytic reactions. The most prominent characteristic of graphene is

the staggering speed of electrons movement (1/300 of the light), which outdistance other conductors. Therefore, compounding can make it easier to separate the electron-hole pairs, thus improving the efficiency of the photocatalyst. In addition, the large specific surface area of graphene brings about an improvement of adsorption capacity of target pollutants in the photocatalytic degradation reaction.

TiO₂ is a classic material in the field of photocatalysis due to its great performance of stability, non-toxicity, environmental-friendliness, chemical resistance, and photo-corrosion resistance. Compared with graphene, the absorption range of TiO₂ can be extended to the visible light region, which improves the photocatalytic efficiency effectively.

The synthesis of graphene/TiO₂ composites can be achieved by solvothermal, hydrothermal, sol-gel, electrospinning or in situ growth methods [221, 222]. Table 2. 8 summaries the preparation methods and applications of graphene photocatalysts.

Chemically bonded graphene/TiO₂ nanorod hybrid composites with superior dispersity were prepared via a one-step in situ method using graphene oxide (GO) and TiO₂ (P25) as starting materials [223]. Zhang et al. adopted hydrothermal method to obtain graphene TiO₂ nanocomposites [224]. The photocatalytic degradation of sodium pentachlorophenol (PCP-Na) was investigated and exhibited 18.34 times higher activity than P25.

Compared with titanium-based catalysts, tungsten-based catalysts have better response in the range of visible light. Introducing graphene into tungsten-based catalysts can promote the separation of photogenerated e⁻ and h⁺, thereby improving the photocatalytic efficiency.

Zhu et al. [225] prepared Bi₂WO₆ via a hydrothermal method, and subsequently

synthesized graphene-Bi₂WO₆ composite via a two-step method. A study of methylene blue degradation showed that the introduction of graphene increased the photocatalytic activity of Bi₂WO₆ effectively. The highest activity was observed when the graphene content was 1.5%, which was 5 times higher than that of the original Bi₂WO₆.

ZnO has advantages of low price and non-toxicity, but it is unable to be band gap-photoexcited and has photochemical corrosion inclination during photocatalytic reaction. As a macromolecular photosensitizer for ZnO semiconductors, the special interfacial interaction between graphene and ZnO plays a pivotal role in widening the band gap. The involvement of graphene can enhance the photocatalytic performance of ZnO and inhibits the occurrence of ZnO photocorrosion during reactions [226, 227].

Table 2. 8. Applications of graphene photocatalysts.

Photocatalyst	Preparation method	degradati on object	Activity	Ref.
TiO₂/graphene	sol-gel method	MB	0.201 mmol g _{cat} ⁻¹ h ⁻¹	[221]
graphene/TiO₂	in situ growth method	MB	85% in 100 min	[223]
graphene/TiO₂	hydrothermal method	PCP-Na	97% in 120 min	[224]
Bi₂WO₆/graphene	Hydrothermal method	MB	88.1% in 2 h.	[225]
graphene-ZnO	in situ wet chemistry process	Cr(VI)	82% in 2 h.	[226]
graphene-ZnO	Two-step Electrochemical Route	MB	100% in 30–35 min	[227]
Graphene/ BiVO₄	facile sol-gel method	MB	95% in 210 min.	[228]
Bi/BiOBr/	One-pot synthesis	RhB	100% in 90	[229]

graphene	min
-----------------	------------

Researchers have combined bismuth-based compound and graphene to prepare effective photocatalysts [229].

Gawande et al. [228] synthesized graphene wrapped BiVO₄ photocatalyst via facile sol–gel method. The wrapping of graphene sheets in this composite showed a prominent enhancement of photocatalytic performance under visible light, which is attributed to the effective quenching of the photogenerated electron–hole pairs which was confirmed by photoluminescence spectra.

Non-metal atom doped graphitic material has been regarded a promising non-metallic redox catalyst, which can be divided to two main types (surface transfer and substitute doping). Surface transfer doping is based on grafting of functional groups on the surface of graphene, which depends on the electrons provided or absorbed from graphene itself; thereby forming n-type or p-type doping. Substitute doping is achieved by replacing carbon atoms with heteroatoms in the graphene lattice. In general, introducing electron donor or electron atom into honeycomb lattices of graphene sheet is quite difficult, because the carbon atom with sp² hybrid has great stability. Therefore, additional free charge carriers are usually introduced by adding dopant in substitute doping [230]. Chemical doping can also convert graphene into semiconductors via breaking the band gap. Meanwhile, the symmetry of the graphene lattice is broken by extraneous atoms, which forms the gap between π bond and anti- π bond, therefore consequently improving the photocatalytic activity of the graphene-based photocatalytic system.

2.5.2.2 Graphene oxide (GO) and reduced GO (rGO)

As an analog of graphene with many functional groups, graphene oxide (GO) has attracted a great deal of scientific interest, probably because of unique 2D structure and small lateral size [231]. Graphene oxide (GO) has a similar structure to pristine

graphene with some important functional groups (hydroxyl, carboxyl and epoxy groups) which can be seen on the surface (Fig. 2. 3) [207]. Important characteristics of GO include great hydrophilicity, intercalation performance and adsorption capacity. The band gap of GO is about 2.4~4.3 eV and the corresponding absorption wavelength is 288 ~516 nm, therefore it can be excited under visible light illumination. GO and its composites have been proved as a promising photo-sensitive material for water splitting, water purification, and removal of air pollutants.

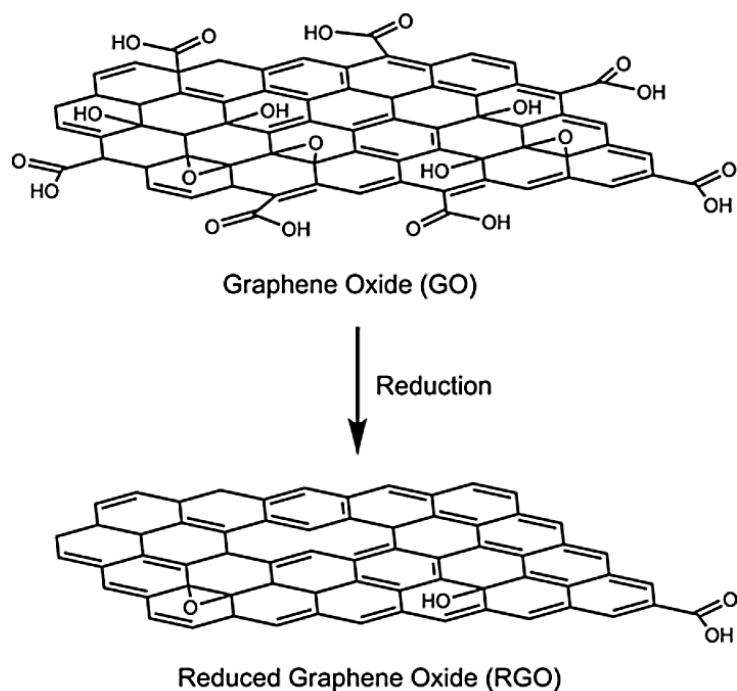


Fig. 2. 4 Schematic illustration of the reduction of graphene oxide (GO) to reduced graphene oxide (RGO).

Single-layered graphene oxide can be prepared by the oxidation of graphite using strong acid and oxidizing agent, then peeling it utilizing ultrasound treatment [232]. The GO sheet can be modified with oxygen-containing functional groups such as carboxyl, hydroxyl and epoxidized groups, thus GO sp^{2-} and sp^{3-} hybridized carbon atoms can be found on GO sheet. However, the oxygen-containing groups in GO can be cleared and the defects of conjugated π -electron can be repaired during the reduction process to greatly increase the capacity of light absorption as illustrated in Fig. 2. 4. Currently, GO

and rGO photocatalysts are favored by researchers in various fields as they can provide mechanical support and electric charge carrier for photocatalysts. Thus, the composite of GO/rGO with semiconductors such as TiO₂, CdS, MoS₂, α -Fe₂O₃, ZnO, WO₃ and graphitic-C₃N₄ have attracted many attentions owing to their particular characteristics from hybridization. The catalytic activities of GO/rGO integrated photocatalysts heavily depend on the structure and interaction, and the preparation method of compounds is of paramount importance [233-235]. Up to now, hydrothermal method, solvothermal method, co-precipitation method and sol-gel method have been employed to prepare GO/rGO based photocatalysts, as summarizes in table 2. 9 [236].

Table 2. 9. Applications of GO and rGO integrated photocatalysts.

Photocatalyst	Preparation method	degradation object	Activity	Ref.
N-ZnO/CdS/GO	Hydrothermal	ciprofloxacin	86% of CIP in 60 min	[235]
GO/TiO₂	Hydrothermal	methyl orange	85.73% MO in 4 h	[237]
GO/g-C₃N₄/MoS₂	solvothermal	MB, RhB and CV	100%MB, 77.2%RhB and 70.3%CV in 60 min	[233]
Ag₃PO₄/GO/g-C₃N₄	co-precipitation	RhB	94.8% RhB in 50 min,	[238]
ZnO-g-C₃N₄/GO	co-precipitation	MB	99.5% MB in 15 min	[234]
Fe₃O₄@SiO₂@TiO₂-Co/rGO	sol-gel	MB	98.87% MB in 160 min	[239]

2.5.2.3 Carbon quantum dots (CQDs)

Carbon quantum dots (GQDs), new kind of zero-dimensional (0D) carbon nanomaterial

(less than 10 nm in size), have been suggested to be promising photocatalytic candidate. CQDs' capabilities of harvesting long wavelength light and exchanging energy with solution species endow them feasibilities to function as photocatalysts in organic syntheses [240]. Different from spherical, tubular or nanosheets of carbon, CQDs exhibit distinctive electronic and optical properties because of their large edge effects and quantum confinement, which result in better peroxidase-like activities than others [241].

Two more obvious features of CQDs are the strong absorption peaks in the ultraviolet region and the long tails in the visible region. Most of the absorption peaks are concentrated in the range of 260-320 nm, which usually show the maximum fluorescence emission wavelength and dependence of excitation wavelength [242]. Absorption shoulders also appear in some spectra, which are probably due to the $\pi \rightarrow \pi^*$ transition of C=C bond and the $n \rightarrow \pi^*$ transition of C=O bond.

Furthermore, another outstanding feature of CQDs is the characteristics of photoluminescence. In general, CQDs with good water solubility can emit bright fluorescence under light irradiation and exhibit excellent optical stability [242]. Scientists believe that this photoluminescence phenomenon may be caused by the great storage capacity of energy via holes on the surface. Recent studies show that the photoluminescence spectrum of CQDs is related to the wavelength and intensity of emission spectrums, possibly due to the optical selectivity of nanoscale quantum effects on the surface of CQDs [243].

In addition, up-conversion photoluminescence (UCPL) is another CQDs' favorable property, which suggests a potential for the fabrication of multi-functional composite materials [242]. Generally speaking, CQDs could only be excited by high-energy (short-wavelength and high-frequency) light and emitted low-energy (long-wavelength and low-frequency) light. Later some materials discovered could achieve the opposite

effect to above-mentioned law, which is called UCPL. Some scholars believed that CQDs absorbed two or more photons at the same time so that it could absorb light at shorter wavelength and generate up-conversion fluorescence [244]. The UCPL property of CQDs has great prospects in applications of light microscope for cell imaging, efficient catalyst design, biological science and energy technology.

In another aspect, traditional quantum dots are generally extracted from a mixture of plumbum, cadmium and silicon, but they have the issues of severe contamination of the ecosystem due to toxicity. Therefore, extracting quantum dots from benign compounds has been a focus of research to prevent the involvement of heavy metals in the preparation process of CQDs. Some studies even have directly extracted CQDs from food and beverages, such as egg white and winter melon. In addition, CQDs are chemically inert, because carbon is stable in nature and also has a high content in living organisms. At the same time, hydrophilic functional groups (such as carboxyl groups) on the surface of CQDs have excellent solubility in water. Therefore, compared with metallic quantum dot materials, CQDs are better choices in photocatalysis [245].

Over the past ten years, scientists have developed various methods for synthesizing CQDs. Depending on the carbon sources, methods can be divided into "top-down" and "bottom-up" synthesis [241]. The "top-down" synthesis method refers to physically or chemically stripping for a large-sized carbon source to a small-sized carbon quantum dot, carbon nanotubes, carbon fibers, graphite rods, carbon ash and activated carbon are generally used as carbon sources. Arc discharge, laser pin erosion and electrochemical synthesis are often employed to prepare CQDs by decomposing these carbon-rich substances. "Bottom-up" method is opposite to "top-down" method, which uses carbon materials in smaller size (such as molecular or ionic states) to synthesize CQDs. Organic molecules or oligomers are commonly used as carbon sources, such as citric acid, glucose, polyethylene glycol, urea and ionic liquids. Chemical oxidation, combustion, hydrothermal method, solvothermal method, microwave synthesis, and

template method are usually utilized as the "bottom-up" methods.

2.6 Summary and perspectives

With the global population swelling and the deterioration of environment, our hunger for energy has reached unprecedented levels, thus abundant and clean solar energy has been believed to be an excellent energy source to replace fossil fuels. Under this context, photocatalysis is a promising technology to decompose toxic organic pollutants such as textiles, dyeing and large amounts of synthetic organic effluents discharged by various industries.

To date, researchers have focused on semiconductor materials as photocatalysts of energy and environmental applications. More than 150 kinds of semiconductor materials are probed for the solar energy conversion, including metal oxides/ sulfides/ carbides, sulfides/ nitrides and non-metal materials. Among various materials, metal-based materials have been widely employed owing the outstanding photocatalytic activity. TiO_2 has been proven its value as one of the most popular photocatalytic materials. Besides the structure engineering, noble metal doping and coating with other methods, multiple phase compositing has been also investigated for the improvement in light harvesting, charge transporting and suppressing charge recombination. Moreover, various metal oxides have been evaluated as potential photocatalysts. The most prominent materials are zinc oxide, iron oxide and tin oxide, which show great ability in fabricating electrodes.

However, the secondary contamination caused by metal leaching has become a disturbed and alarmed issue to the environment. Therefore, researchers have dedicated efforts to fabricate clean, safe and economical photocatalysts for wastewater treatment process. In order to alleviate these problems, metal-free materials, as green catalysts, have been demonstrated as effective photocatalysts for water purification. Carbon

materials, particularly nanocarbon materials, are very promising materials to be adsorbents. Numerous studies have investigated the efficiency of organic pollutant removal from wastewater using nanocarbon as photocatalysts [145, 246].

Among these metal-free semiconductor materials, graphitic carbon nitride (GCN), has been deemed as a promising photocatalytic material due to economical-efficiency, its layered graphite-like structure, electronic structure for solar energy conversion and the simplicity of material synthesis [247-249]. But the relatively large bandgap energy of pure GCN causes poor absorption capacity and fast recombination of photo-introduced electron hole pairs. Hybridization with co-catalysts is conducive to improve the charge separation and prolong the lifetime of electrons on the surface. Carbon quantum dots (CQDs) reveal great visible light-excitable ability in degradation of organics, due to the wide light absorption at short and long wavelengths and light emission at both long and short wavelengths [250, 251]. As one of the most popular materials, reduced graphene oxide (rGO) composite materials obtained via the modified Hummers' method are usually used as a modifier since the presence of abundant oxygen functional groups and the unique porous structure. Carbon nanotube (CNT) has demonstrated as an excellent catalytic oxidation activity due to the unique surface properties, superior electronic conductivity and charge transfer [252]. Carbon nanospheres (CNP) have also attracted intensive attention as a promising promoter to improve photo activity of carbon nitride in photocatalytic performance [253].

Herein, this chapter highlights the recent development reported in the literature that can provide the insights on the modification of metal and metal free catalysts. Up to now, many works have been conducted on developing new photocatalytic materials to absorb visible light as a main part of solar spectrum. The applications for the degradation of organic pollutants and water splitting are also discussed.

In recent years, great progress and breakthroughs have been made

in the field of photocatalysis. Despite of significant achievement, there are still many problems such as low solar energy utilization, low quantum yield, deficient separation of photogenerated electrons and holes, and poor stability. So far, all these studies about photocatalytic materials are limited in the laboratory stage, in-depth exploration to achieve greater breakthroughs for large scale applications in environmental conservation.

The modification methods applied in these photocatalytic material systems share a certain similarity and each of these individual methods has its respective limitations. In another word, some common challenges are still facing the research community of the field. Element doping and noble metal deposition require precise control of the dosage; dye sensitization is limited by insufficient stability. Desirable morphology control is still difficult from nano-scale to micro-size. Some naked catalysts have displayed sufficiently high activity, but such a high efficiency could not be maintained once being prepared in supported form. The consensus of the reaction mechanism still has not been reached, such as N-type hybrid materials. In this regard, the Z-type semiconductor provides sufficient space for the catalyst modification strategy due to its unique structure.

A careful comparison of the previous researches indicates the deficiency of single-component material thus the multi-component composite materials should be developed in the future. In addition, the contamination of natural water system is complex with heavy metals and various organic pollutants, thus future research should be focused on the synergistic mechanisms of the substances in the reaction processes and environmental conditions.

Reference

1. Q. Liu, X. Duan, H. Sun, Y. Wang, M. O. Tade, and S. Wang, Size-tailored porous spheres of manganese oxides for catalytic oxidation via peroxymonosulfate activation. *J. Phys. Chem. C*, 2016.120(30), 16871-16878.
2. A. Fujishima and K. Honda. Electrochemical photolysis of water at a semiconductor electrode. *Nature*, 1972. 238(5358), 37-38.
3. P. Jain, X. Huang and I. Sayed , Review of some interesting surface plasmon resonance-enhanced properties of noble metal nanoparticles and their applications to biosystems. *Plasmonics*, 2007. 2(3), 107-118.
4. B. You , N. Jiang, X. Liu and Y. Sun , Simultaneous H₂ Generation and Biomass Upgrading in Water by an Efficient Noble-Metal-Free Bifunctional Electrocatalyst. *Angew. Chem. Int. Ed. Engl.*, 2016. 128(34), 10067-10071.
5. D. Zhu and Q. Zhou, Action and mechanism of semiconductor photocatalysis on degradation of organic pollutants in water treatment: A review. *Environ. Nanotechnol. Monit. Manag.*, 2019. 12, 100255.
6. H. Huang, C. Liu, H. Ou, T. Ma and Y. Zhang, Self-sacrifice transformation for fabrication of type-I and type-II heterojunctions in hierarchical Bi₂O₃/g-C₃N₄ for efficient visible-light photocatalysis. *Appl. Surf. Sci.*, 2019. 470, 1101-1110.
7. S.Yi, X. Yue, D. Xu, Z. Liu, F.i Zhao, D. Wang and Y. Lin, Study on photogenerated charge transfer properties and enhanced visible-light photocatalytic activity of p-type Bi₂O₃/n-type ZnO heterojunctions. *New J. Chem.*, 2015. 39, 2917-2924.
8. Y. Wang, Q. Wang, X. Zhan, F. Wang, M. Safdar and J. He, Visible light driven type II heterostructures and their enhanced photocatalysis properties: A review. *Nanoscale*, 2013. 5(4), 8326-8339.
9. H. Heng, Q. Gan, P. Meng and X. Liu, The visible-light-driven type III

heterojunction $\text{H}_3\text{PW}_{12}\text{O}_{40}/\text{TiO}_2\text{-In}_2\text{S}_3$: a photocatalysis composite with enhanced photocatalytic activity. *RSC Adv.*, 2017. 696, 51-59.

10. O. Hiromichi and H. Masahiro, Fabrication and photoresponse of a pn-heterojunction diode composed of transparent oxide semiconductors, p-NiO and n-ZnO. *Appl. Phys. Lett.*, 2003. 83, 1029-1031.

11. S. Martha, S. Mansingh, K. Parida and A. Thirumurugan, Exfoliated metal free homojunction photocatalyst prepared by a biomediated route for enhanced hydrogen evolution and Rhodamine B degradation. *Appl. Phys. Lett.*, 2017. 1, 1641-1653.

12. W. Dong, Y. Liu, G. Zeng, S. Zhang, T. Cai, J. Yuan, H. Chen, J. Gao and C. Liu, Regionalized and vectorial charges transferring of $\text{Cd}_{1-x}\text{Zn}_x\text{S}$ twin nanocrystal homojunctions for visible-light driven photocatalytic applications. *J. Colloid Interface Sci.*, 2018. 518, 156-164.

13. L. Devi and R. Kavitha, A review on plasmonic metal TiO_2 composite for generation, trapping, storing and dynamic vectorial transfer of photogenerated electrons across the Schottky junction in a photocatalytic system. *Appl. Surf. Sci.*, 2016. 360, 601-622.

14. L. Xiao, S. Shu and S. Liu, A facile synthesis of Pd-doped SnO_2 hollow microcubes with enhanced sensing performance. *Sens. Actuators B Chem.*, 2015. 221, 120-126.

15. J. Choi, I. Hwang, S. Kim, J. Park, S. Park, U. Jeong, Y. Kang, Jong and H. Lee, Design of selective gas sensors using electrospun Pd-doped SnO_2 hollow nanofibers. *Sens. Actuators B Chem.*, 2010. 150, 191-199.

16. L. Bagal, J. Patil, M. Vaishampayan, I. Mulla and S. Suryavanshi, Effect of Pd and Ce on the enhancement of ethanol vapor response of SnO_2 thick films. *Sens. Actuators B Chem.*, 2015. 207, 383-390.

17. K. Awazu, M. Fujimaki, C. Rockstuhl, J. Tominaga, H. Murakami, Y. Ohki, N. Yoshida and T. Watanabe, A plasmonic photocatalyst consisting of silver nanoparticles embedded in titanium dioxide. *J. Am. Chem. Soc.*, 2008. 130, 1676.

18. Rajaboopathi, S. and S. Thambidurai, Enhanced photocatalytic activity of Ag-ZnO nanoparticles synthesized by using Padina gymnospora seaweed extract. *J. Mol. Liq.*, 2018. 262, 148-160.
19. H. Liu , X. Dong , G. Li , X. Su , Z. Zhu Synthesis of C, Ag co-modified TiO₂ photocatalyst and its application in waste water purification. *Appl. Surf. Sci.*, 2013. 271, 276-283.
20. Y. Che, Q. Liu, B. Lu, J. Zhai, K. Wang and Z. Liu, A plasmonic photocatalyst of Ag/AgBr nanoparticles coupled with g-C₃N₄ with enhanced visible-light photocatalytic ability. *Colloids Surf. A Physicochem. Eng. Asp.*, 2013. 436, 474-483.
21. Z. Shen, B. Liu, V. Pareek, S. Wang, X. Li, L. Liu and S. Liu, Sustainable synthesis of highly efficient sunlight-driven Ag embedded AgCl photocatalysts. *RSC Adv.*, 2015, 5, 80488-80495.
22. Z. Shen, P. Liang, S. Wang, L. Liu and S. Liu, Green Synthesis of Carbon- and Silver-Modified Hierarchical ZnO with Excellent Solar Light Driven Photocatalytic Performance. *ACS Sustain. Chem. Eng.*, 2015. 3, 1010-1016.
23. Y. Tian and T. Tatsuma, Mechanisms and Applications of Plasmon-Induced Charge Separation at TiO₂ Films Loaded with Gold Nanoparticles. *J. Am. Chem. Soc.*, 2005. 127, 7632-7637.
24. A. Li, P. Zhang, X. Chang, W. Cai, T. Wang and J. Gong, Gold Nanorod@TiO₂ Yolk-Shell Nanostructures for Visible-Light-Driven Photocatalytic Oxidation of Benzyl Alcohol. *Small*, 2015. 11, 1892-1899.
25. K. Foo, and B. Hameed, Detoxification of pesticide waste via activated carbon adsorption process. *J. Hazard. Mater.*, 2010. 175, 1-11.
26. M Abdelaal and R. Mohamed, Novel Pd/TiO₂ nanocomposite prepared by modified sol-gel method for photocatalytic degradation of methylene blue dye under visible light irradiation. *J. Alloys Compd.*, 2013. 576, 201-207.

27. O. Rosseler, C. Ulhaq-Bouillet, A. Bonnefont, S. Pronkin, E. Savinova, A. Louvet, V. Keller and N. Keller, Structural and electronic effects in bimetallic PdPt nanoparticles on TiO₂ for improved photocatalytic oxidation of CO in the presence of humidity. *Appl. Catal. B*, 2015. 166-167, 381-392.
28. A. Sowmya and S. Meenakshi, Photocatalytic reduction of nitrate over Ag–TiO₂ in the presence of oxalic acid. *J. Water Process. Eng.*, 2015. 8, 23-30.
29. H. Sun, B. Dong, G. Su, R. Gao, W. Liu, L. Song and L. Cao, Towards TiO₂ nanotubes modified by WO₃ species: influence of ex situ crystallization of precursor on the photocatalytic activities of WO₃/TiO₂ composites. *J. Phys. D: Appl. Phys.*, 2015. 48, 35.
30. C. Ruan, L. Zhang, Y. Qin, C. Xu, X. Zhang, J. Wan, Z. Peng, J. Shi, X. Li and L. Wang, Synthesis of porphyrin sensitized TiO₂/graphene and its photocatalytic property under visible light. *Mater. Lett.*, 2015. 141, 362-365.
31. D. Yang, H. Liu, Z. Zheng, Y. Yuan, J. Zhao, E. Waclawik, X. Ke and H. Zhu, The highly efficient photocatalysts of Co/TiO₂: Photogenerated charge-transfer properties and their applications in photocatalysis. *Chem. Phys. Lett.*, 2014. 615, 111-116.
32. S. Kruanetr and R. Wanchanthuek, Studies on preparation and characterization of Fe/TiO₂ catalyst in photocatalysis applications. *Mater. Res. Express*, 2017. 4, 076507.
33. F. Azizi, Synthesis and characterization of graphene-N-doped TiO₂ nanocomposites by sol-gel method and investigation of photocatalytic activity. *J. Mater. Sci. Mater. Electron.*, 2017. 28, 11222-11229.
34. J. Hu, H. Li, Q. Wu, Y. Zhao and Q. Jiao, Synthesis of TiO₂ nanowire/reduced graphene oxide nanocomposites and their photocatalytic performances. *Chem. Eng. J.*, 2015. 263, 144-150.
35. D. Jamwal, G. Kaur, P. Raizada, P. Singh, D. Pathak and P. Thakur, Twin-tail surfactant peculiarity in superficial fabrication of semiconductor quantum dots: Toward structural, optical, and electrical features. *J. Phys. Chem. C*, 2015. 119, 5062-5073.

36. M. Xu, Q. Li and H. Fan, Monodisperse nanostructured Fe₃O₄/ZnO microrods using for waste water treatment. *Adv. Powder Technol.*, 2014. 25, 1715-1720.
37. S. Banerjee, P. Benjwal, M. Singh and K. Kar, Graphene oxide (rGO)-metal oxide (TiO₂/Fe₃O₄) based nanocomposites for the removal of methylene blue. *Appl. Surf. Sci.*, 2018. 439, 560-568.
38. L. Shi, Y. He, X. Wang and Y. Hu, Recyclable photo-thermal conversion and purification systems via Fe₃O₄@TiO₂ nanoparticles. *Energy Convers. Manag.* 2018. 171, 272-278.
39. N. Li, Y. Tian, J. Zhao, W. Zhan, J. Du, L. Kong, J. Zhang and W. Zuo, Ultrafast selective capture of phosphorus from sewage by 3D Fe₃O₄@ZnO via weak magnetic field enhanced adsorption. *Chem. Eng. J.*, 2018. 341, 289-297.
40. N. Li, J. Zhang, Y. Tian, J. Zhao, J. Zhang and W. Zuo, Precisely controlled fabrication of magnetic 3D γ -Fe₂O₃@ZnO core-shell photocatalyst with enhanced activity: Ciprofloxacin degradation and mechanism insight. *Chem. Eng. J.*, 2017. 308, 377-385.
41. K. Christoforidis, T. Montini, E. Bontempi, S. Zafeiratos, J. Jaén and P. Fornasiero, Synthesis and photocatalytic application of visible-light active β -Fe₂O₃/g-C₃N₄ hybrid nanocomposites. *Appl. Catal. B: Environ.*, 2016. 187, 171-180.
42. X. Lu, Y. Li, W. Jiang and Y. Huang, Porous γ -Fe₂O₃ microspheres decorated with TiO₂ nanocrystals as highly recyclable photocatalysts and potential highly efficient magnetic hyperthermia agents. *J. Mater. Sci. Mater. Electron.*, 2018. 29, 20856-20865.
43. K. Tezuka, M. Kogure and Y. Shan, Photocatalytic degradation of acetic acid on spinel ferrites MFe₂O₄ (M=Mg, Zn, and Cd). *Catal. Commun.*, 2014. 48, 11-14.
44. F. Sun, Q. Zeng, W. Tian, Y. Zhu and W. Jiang, Magnetic MFe₂O₄-Ag₂O (M = Zn, Co, & Ni) composite photocatalysts and their application for dye wastewater treatment. *J. Environ. Chem. Eng.*, 2019. 7, 103011-103023.

45. S. Laurent, D. Forge, M. Port, A. Roch, C. Robic, L. Elst and R. Muller, Magnetic iron oxide nanoparticles: synthesis, stabilization, vectorization, physicochemical characterizations, and biological applications. *Chem. Rev.*, 2008. 108, 2064-2110.
46. M. Mousavi and A. Habibi-Yangjeh, Ternary g-C₃N₄/Fe₃O₄/Ag₃VO₄ nanocomposites: Novel magnetically separable visible-light-driven photocatalysts for efficiently degradation of dye pollutants. *Mater. Chem. Phys.*, 2015. 163, 421-430.
47. M. Zazouli, F. Ghanbari, M. Yousefi and S. Madihi-Bidgoli, Photocatalytic degradation of food dye by Fe₃O₄-TiO₂ nanoparticles in presence of peroxymonosulfate: The effect of UV sources. *J. Environ. Chem. Eng.*, 2017. 5, 2459-2468.
48. J. Sin, S. Tan, J. Quek and S. Lam, A. Mohamed, Facile fabrication of hierarchical porous ZnO/Fe₃O₄ composites with enhanced magnetic, photocatalytic and antibacterial properties. *Mater. Lett.*, 2018. 228, 207-211.
49. L. Tian, Y. Hu, Y. Guo and Q. Pan, Dual effect of lignin amine on fabrication of magnetic Fe₃O₄/C/ZnO nanocomposite in situ and photocatalytic property. *Ceram. Int.*, 2018. 44, 14480-14486.
50. J. Gao and F. Cheng, Facile Synthesis of Magnetically Recyclable Fe₂O₃-MFe₂O₄ Photocatalyst from Saproelite-Limonite Laterite Leach Liquors. *J. Supercond. Nov. Magn.*, 2017. 30, 3339-3343.
51. M. Huang, S. Mao, H. Feick, H. Yan, Y. Wu, H. Kind, E. Weber, R. Russo and P. Yang, Room-temperature ultraviolet nanowire nanolasers. *Science*, 2001. 292, 1897-1899.
52. C. Lee, C. Chen and Y. Chiu, Versatile function of nanostructured-ZnO sensors using photo-assisted method. *AIP Adv.*, 2016. 6, 015104.
53. M. Mahmud, N. Elumalai, M. Upama, D. Wang, K. Chan, M. Wright, C. Xu, F. Haque and A. Uddin, Low temperature processed ZnO thin film as electron transport layer for efficient perovskite solar cells. *Sol. Energy Mater Sol. Cells.*, 2017. 159, 251-264.

54. Z. Zulkifli , S. Shinde , T. Suguira , G. Kalita and M. Tanemura , Fabrication of graphene and ZnO nanocones hybrid structure for transparent field emission device. *Appl. Surf. Sci.*, 2015. 356, 674-678.
55. M. Pirhashemi, A. Habibi-Yangjeh and S. Pouran, Review on the criteria anticipated for the fabrication of highly efficient ZnO-based visible-light-driven photocatalysts. *J. Ind. Eng. Chem.*, 2018. 62, 1-25.
56. N. Huang, J. Shu, Z. Wang and M. Chen , One-step pyrolytic synthesis of ZnO nanorods with enhanced photocatalytic activity and high photostability under visible light and UV light irradiation. *J. Alloys Compd.*, 2015. 648, 919-929.
57. G. Lee and J. Wu, Recent developments in ZnS photocatalysts from synthesis to photocatalytic applications - A review. *Powder Technol.*, 2017. 318, 8-22.
58. X. Chen, Y. Dai and X. Wang, Methods and mechanism for improvement of photocatalytic activity and stability of Ag₃PO₄: A review. *J. Alloys Compd.*, 2015. 649, 910-932.
59. T. Asma, B. Wiem. S. Brigitte, A. Ahmed, E. Habib, F. Mokhtar and B. Rabah, Structural and optical properties of Na doped ZnO nanocrystals: Application to solar photocatalysis. *Appl. Surf. Sci.*, 2017. 396, 1528-1538.
60. A. Kadam, T Kim, D Shin, K. Garadkar and J. Park, Morphological evolution of Cu doped ZnO for enhancement of photocatalytic activity. *J. Alloys Compd.*, 2017. 710, 102-113.
61. C. Han, L. Duan, X. Zhao, Z. Hu, Y. Niu and W. Geng, Effect of Fe doping on structural and optical properties of ZnO films and nanorods. *J. Alloys Compd.*, 2019. 770, 854-863.
62. S. Kumar, N. Reddy, A. Kumar, M. Shankar, V. Krishnan, Two dimensional N-doped ZnO-graphitic carbon nitride nanosheets heterojunctions with enhanced photocatalytic hydrogen evolution. *Int. J. Hydrog. Energy.*, 2018. 43, 3988-4002.

63. S. Sharma, S Mehta and S. Kansal, N doped ZnO/C-dots nanoflowers as visible light driven photocatalyst for the degradation of malachite green dye in aqueous phase. *J. Alloys Compd.*, 2017. 699, 323-333.
64. Y. Cheng W. Jiao, Q. Li, Y. Zhang, S. Li, D. Li and R. Che, Two hybrid Au-ZnO aggregates with different hierarchical structures: A comparable study in photocatalysis. *J. Colloid Interface Sci.*, 2018. 509, 58-67.
65. M. Pérez-González, S. Tomás, J. Santoyo-Salazar, S. Gallardo-Hernández, M. Tellez-Cruz and O. Solorza-Feria, Sol-gel synthesis of Ag-loaded TiO₂-ZnO thin films with enhanced photocatalytic activity. *J. Alloys Compd.*, 2019. 779, 908-917.
66. J. Fernando, M. Shortell, K. Firestein, C. Zhang, K. Larionov, Z. Popov, P. Sorokin, L. Bourgeois, E. Waclawik and D. Golberg, Photocatalysis with Pt-Au-ZnO and Au-ZnO Hybrids: Effect of Charge Accumulation and Discharge Properties of Metal Nanoparticles. *Langmuir*, 2018. 34, 7334-7366.
67. Y. Yang, X. Li, R. Zhao, J. Yang, Q. Sun, X. Chen and X. Wu, The Study on Degradation and Separation of RhB Under UV Light by Magnetically ZnO/Fe₂O₃ Nanoparticles. *Phys. Status Solidi*, 2018. 215, 1800416-1800422.
68. K. Szostak and M. Banach, Sorption and photocatalytic degradation of methylene blue on bentonite-ZnO-CuO nanocomposite. *J. Mol. Liq.*, 2019. 286, 110859-110874.
69. J. C. Medina, N. S. Portillo-Vélez and S. E. Rodil, Synergistic effect of supported ZnO/Bi₂O₃ heterojunctions for photocatalysis under visible light. *Dyes Pigm.*, 2018. 153, 106-116.
70. J. Liu, S. Zou, B. Lou, C. Chen, L. Xiao and J. Fan, Interfacial Electronic Interaction Induced Engineering of ZnO-BiOI Heterostructures for Efficient Visible-Light Photocatalysis. *Inorg. Chem.*, 2019. 58, 8525-8532.
71. S. Periyannan, L. Manceri, N. D. Nguyen, A. Klein, W. Jaegermann and P. Colson, Influence of ZnO Surface Modification on the Photocatalytic Performance of ZnO/NiO

Thin Films. Catal. Lett., 2019. 149, 1813-1824.

72. F. Kiantazh and A. Habibi-Yangjeh, Ultrasonic-assisted one-pot preparation of ZnO/Ag₃VO₄ nanocomposites for efficiently degradation of organic pollutants under visible-light irradiation. Solid State Sci., 2015. 49, 68-77.

73. L. Zhu, H. Li, P. Xia, Z. Liu and D. Xiong, Hierarchical ZnO Decorated with CeO₂ Nanoparticles as the Direct Z-Scheme Heterojunction for Enhanced Photocatalytic Activity. ACS Appl. Mater. Interfaces, 2018. 10, 39679-39687.

74. S. Adhikari, K. S. Chandra and D. Sarkar, Understanding the morphological effects of WO₃ photocatalysts for the degradation of organic pollutants. Adv. Powder Technol, 2018. 29, 1591-1600.

75. Y. Chao, P. Zhou, N. Li, J. Lai, Y. Yang, Y. Zhang, Y. Tang, W. Yang, Y. Du, D. Su, Y. Tan and S. Guo, Ultrathin Visible-Light-Driven Mo Incorporating In₂O₃-ZnIn₂Se₄ Z-Scheme Nanosheet Photocatalysts. Adv. Mater., 2019. 31, 1807226.

76. S. Jafarirad, I. Rasoulpour, B. Divband, I. H. Torghabe and M. Kosari-Nasab, Innovative biocapped CuO nano-photocatalysts: a rapid and green method for photocatalytic degradation of 4-nitrophenol. Mater. Res. Innovations, 2018. 22, 415-421.

77. D. Zhao, and X. Wu, Nanoparticles assembled SnO₂ nanosheet photocatalysts for wastewater purification. Mater. Lett., 2018. 210, 354-357.

78. A. Kohlsdorf, D. H. Taffa, and M. Wark, Microwave assisted synthesis of Ta₂O₅ nanostructures for photocatalytic hydrogen production. J. Photochem. Photobiol. A, 2018. 366, 41-47.

79. J. Ke, C. Zhao, H. Zhou, X. Duan and S. Wang, Enhanced solar light driven activity of p-n heterojunction for water oxidation induced by deposition of Cu₂O on Bi₂O₃ microplates. SM&T, 2018. 17, e00088- e00097.

80. T. Montalvo-Herrera, D. Sánchez-Martínez, D. B. Hernandez-Uresti and L. M.

Torres-Martínez, The role of the reactive oxygen species and the influence of KBiO_3 synthesis method in the photodegradation of methylene blue and ciprofloxacin. *React. Kinet. Mech. Catal.*, 2019. 126, 561-573.

81. Q. Wang, J. Cai, and L. Zhang, In situ synthesis of Ag_3PO_4 /cellulose nanocomposites with photocatalytic activities under sunlight. *Cellulose*, 2014. 21, 3371-3382.

82. Z. Liu, X. Wang, Q. Cai, C. Ma and Z. Tong, $\text{CaBi}_6\text{O}_{10}$: a novel promising photoanode for photoelectrochemical water oxidation. *J. Mater. Chem. A*, 2017. 5, 8545-8554.

83. L. Zhao, X. Wang, and Z. Liu, Efficient photoelectrochemical performances of the novel honeycomb network-like CuBi_2O_4 films. *Mater. Sci. Proc.*, 2018. 124, 1-7.

84. Y. Wang, Y. Zeng, X. Chen, Q. Wang, L. Guo, S. Zhang and Q. Zhong, One-step hydrothermal synthesis of a novel 3D $\text{BiFeWO}_x/\text{Bi}_2\text{WO}_6$ composite with superior visible-light photocatalytic activity. *Green Chem.*, 2018. 20, 3014-3023.

85. J. Nisar, L. A. Silva, C. G. Almeida, A. J. S. Mascarenhas, B. Wang, C. M. Araújo, R. Ahuja, I. Pepe, J. S. Almeida and A. F. Silva, Study of electronic and optical properties of BiTaO_4 for photocatalysis. *Phys. status solidi (c)*, 2012. 9, 1593-1596.

86. F. Rechberger, E. Tervoort, and M. Niederberger, Nonaqueous sol-gel synthesis of InTaO_4 nanoparticles and their assembly into macroscopic aerogels. *J. Am. Ceram. Soc.*, 2017. 100, 4483-4490.

87. M. Osugi, Toxicological study of the degradation products of antineoplastic agent etoposide in commercial formulation treated by heterogeneous photocatalysis using SrSnO_3 . *Environ. Sci. Pollut. Res.*, 2018. 26, 1-10.

88. S. Tu, H. Huang, T. Zhang and Y. Zhang, Controllable synthesis of multi-responsive ferroelectric layered perovskite-like $\text{Bi}_4\text{Ti}_3\text{O}_{12}$: Photocatalysis and piezoelectric-catalysis and mechanism insight. *Appl. Catal. B-Environ.*, 2017. 219, 550-562.

89. X. Wang , T. Hisatomi , Z. Wang , J. Song , J. Qu , T. Takata and K. Domen, Core–Shell-Structured LaTaON₂ Transformed from LaKNaTaO₅ Plates for Enhanced Photocatalytic H₂ Evolution. *Angew. Chem.*, 2019. 58, 10666-10670.
90. H. Zhang ,Y. Chen , H. Zhou , Y. Yao and X. Li, Mn²⁺-doped Zn₂GeO₄ for photocatalysis hydrogen generation. *Int. J. Engine. Res.*, 2019. 43, 5013-5019.
91. T. Aruga, K. Domen, S. Naito, T. Onishi and K. Tamaru, The role of sulfite anion as a hole scavenger in the photocatalytic hydrogen formation from water on CdS semiconductor under illumination of visible light. *Chem. Lett*, 1983. 12(7), 1037-1040.
92. J. Yang, C. Hu, Y. Jin, H. Chen, W. Zhu and X. Zhou, Fabrication of TiO₂ mesoporous microspheres sensitized with CdS nanoparticles and application in photodegradation of organic dye. *Res. Chem. Intermediat*, 2018. 1-16.
93. Q. Chen, T. Wang, B. Wang, X. Yang, F. Li and Y. Wang, Construction of CuO/CdS composite nanostructure for photodegradation of pollutants in sewage. *J. Mater. Sci.: Mater. Electron.*, 2019. 30(17), 15989-15999.
94. D. Ayodhya and G. Veerabhadram, Ultrasonic synthesis of g-C₃N₄/CdS composites and their photodegradation, catalytic reduction, antioxidant and antimicrobial studies. *Mater. Res. Innov*, 2019. 24, 210-228
95. W. Chen, Y. Wang, M. Liu, L. Gao, Z. Fan and W. Shangguan, In situ photodeposition of cobalt on CdS nanorod for promoting photocatalytic hydrogen production under visible light irradiation. *Appl. Surf. Sci.*, 2018. 444, 485-490.
96. C-J. Chang, K-L. Huang, J-K. Chen, K-W. Chu and M-H. Hsu, Improved photocatalytic hydrogen production of ZnO/ZnS based photocatalysts by Ce doping. *J.Tai. Wan. Inst. Chem.*, 2015. 55, 82-89.
97. M. Akbari, and S. Sharifnia, Synthesis of ZnS/ZnO nanocomposite through solution combustion method for high rate photocatalytic conversion of CO₂ and CH₄. *Materials Letters*, 2017. 194, 110-113.

98. D. Chen, J. Fang, S. Lu, GY. Zhou, W. Feng, F. Yang, Y.Chen and ZQ. Fang, Fabrication of Bi modified Bi_2S_3 pillared $\text{g-C}_3\text{N}_4$ photocatalyst and its efficient photocatalytic reduction and oxidation performances. *Appl. Surf. Sci.*, 2017. 426, 427-436.
99. SVP. Vattikuti, J. Shim, and C. Byon, 1D Bi_2S_3 nanorod/2D e- WS_2 nanosheet heterojunction photocatalyst for enhanced photocatalytic activity. *J. Solid.State.Chem.*, 2018. 258, 526-535.
100. J. Wu, B. Liu, Z. Ren, M. Ni, C. Li, Y. Gong, W. Qin, Y. Huang, C. Sun and X. Liu, CuS/RGO hybrid photocatalyst for full solar spectrum photoreduction from UV/Vis to near-infrared light. *J. Colloid. Interf. Sci.*, 2018. 517, 80-85.
101. Z. Li, Z. Zhou, J. Ma, Y. Li, W. Peng, G. Zhang, F. Zhang and X. Fan, Hierarchical photocatalyst of In_2S_3 on exfoliated MoS_2 nanosheets for enhanced visible-light-driven Aza-Henry reaction. *Appl. Catal. B-Environ*, 2018. 237, 288-294.
102. Y. Li, N. Wang, J. Xu, Z. Liu and H. Yu, Significant effect of advanced catalysts Co_3S_4 modified $\text{CuWO}_4 \cdot 2\text{H}_2\text{O}$ under visible light condition photocatalytic hydrogen production. *J Nanopart Res.*, 2019. 21(4), 1-13.
103. X. Li, D. Shen, C. Liu, J. Li and Y. Yan, Fabricated rGO-modified Ag_2S nanoparticles/ $\text{g-C}_3\text{N}_4$ nanosheets photocatalyst for enhancing photocatalytic activity. *J. Colloid. Interf. Sci.*, 2019. 554, 468-478.
104. D-T. Nguyen, CC. Nguyen, M. St-Jean, S. Chabot, S. Kaliaguine and TO. Do, All in One: Contributions of Ni Dopants and Ni/NiS Dual Cocatalysts to the Enhanced Efficiency of TiO_2 Photocatalyst for the Degradation of Organic Pollutants. *ACS Appl. Nano Mater*, 2018. 1(12), 6864-6873.
105. C. Li, W. Yang, and Q. Li, TiO_2 -based photocatalysts prepared by oxidation of TiN nanoparticles and their photocatalytic activities under visible light illumination. *J. Mater. Sci. Technol*, 2018. 34(6), 969-975.

106. B. Ma, Y. Liu, J. Li, K. Lin, W. Liu and H. Zhan, Mo₂N: An efficient non-noble metal cocatalyst on CdS for enhanced photocatalytic H₂ evolution under visible light irradiation. *Int. J. Hydrog. Energy*, 2016. 41(47), 22009-22016.
107. C. Zhou, J. Lu, L. Wang, J. Shi and Z. Bing, Surface electric field driven directional charge separation on Ta₃N₅ cuboids enhancing photocatalytic solar energy conversion. *Appl. Catal B-Environ*, 2018. 237, 742-752.
108. Y. Lee, T. Watanabe, T. Takata, M. Hara and K. Domen, Effect of high-pressure ammonia treatment on the activity of Ge₃N₄ photocatalyst for overall water splitting. *J. Phys. Chem B*, 2006. 110(35), 17563-9.
109. J. Liu, Y. Li, S. Arumugam, J. Tudor and S. Beeby, Investigation of low temperature processed titanium dioxide (TiO₂) films for printed dye sensitized solar cells (DSSCs) for large area flexible applications. *Mater. Today*, 2018. 5(5), 13846-13854.
110. L. Qi, R. Xie, KS. Jian and EA. Mintz, Effect of Precursor Ratio on Synthesis and Optical Absorption of TiON Photocatalytic Nanoparticles. *J. Am. Ceram. Soc.*, 2007. 90(4), 1045-1050.
111. Q. Liu, X. Tan, S. Wang, F. Ma, H. Znad, Z. Shen, L. Liu and S. Liu, MXene as a non-metal charge mediator in 2D layered CdS@Ti₃C₂@TiO₂ composites with superior Z-scheme visible light-driven photocatalytic activity. *Environ. Sci. Nano*, 2019. 6(10), 3158-3169.
112. M. Naguib, VN. Mochalin, MW. Barsoum and Y. Gogotsi, 25th Anniversary Article: MXenes: A New Family of Two-Dimensional Materials. *Adv.Mater*, 2014. 26(7), 992-1005.
113. M. Naguib, M. Kurtoglu, V. Presser, J. Lu, J. Niu, H. Min, L. Hultman, Y Gogotsi and MW. Barsoum, Two-dimensional nanocrystals produced by exfoliation of Ti₃AlC₂. *Adv.Mater*, 2011. 23(37), 4248-4253.
114. H. Jiang, Z. Wang, Q. Yang, L. Tan, L. Dong and M. Dong, Ultrathin Ti₃C₂Tx

- (MXene) Nanosheet-Wrapped NiSe₂ Octahedral Crystal for Enhanced Supercapacitor Performance and Synergetic Electrocatalytic Water Splitting. *NML*, 2019. 11(1), 1-14.
115. H. Liu, X. Zhang, Y. Zhu, B. Cao and R. Chen, Electrostatic Self-assembly of 0D–2D SnO₂ Quantum Dots/Ti₃C₂ TxMXene Hybrids as Anode for Lithium-Ion Batteries. *Nano-Micro Letters*, 2019. 11(1), (1-12)
116. L. Yu, L. Hu, A. Babak, Y.T. Liu, Q. Zhu, Z. Peng, G. Yury and B. Xu, MXene-Bonded Activated Carbon as a Flexible Electrode for High-Performance Supercapacitors. *ACS. Energy. Lett.*, 2018. 3(7), 1597-1603.
117. M. Han, X. Yin, X. Li, B. Anasori, L. Zhang, L. Cheng and Y. Gogotsi, Laminated and Two-Dimensional Carbon-Supported Microwave Absorbers Derived from MXenes. *ACS Appl. Mater. Interfaces*, 2017. 9(23), 20038-20045.
118. J. Zhu, E. Ha, G. Zhao, Y. Zhou, D. Huang, G. Yue, L. Hu, N. Sun, Y. Wang and LYS. Lee, Recent advance in MXenes: A promising 2D material for catalysis, sensor and chemical adsorption. *Coordin. Chem. Rev*, 2017. 352, 306-327.
119. J. Zhu, E. Ha, G. Zhao, Y. Zhou, D. Huang, G. Yue, L. Hu, N. Sun, Y. Wang and LYS Lee, 2D titanium carbide (MXene) for wireless communication. *Sci. Adv.*, 2018. 4(9), 306-327.
120. Y. Ying, Y. Liu, X. Wang, Y. Mao, W. Cao, P. Hu and X. Peng, Two-dimensional titanium carbide for efficiently reductive removal of highly toxic chromium(VI) from water. *ACS Appl. Mater. Interfaces*, 2015. 7(3), 1795-803.
121. N. Liu, N. Lu, Y. Su, P. Wang and X. Quan, Fabrication of g-C₃N₄/Ti₃C₂ composite and its visible-light photocatalytic capability for ciprofloxacin degradation. *Sep. Purif. Technol.*, 2019. 211, 782-789.
122. C. D. Agnese, Y. D. Agnese, B. Anasori, W. Sugimoto and S. Mori, Oxidized Ti₃C₂ MXene nanosheets for dye-sensitized solar cells. *New J. Chem.*, 2018. 42(20), 16446-16450.

123. L. Yang, Y. Dall'Agnese, K. Hantanasirisakul, C. Shuck and T. Miyasaka, SnO₂-Ti₃C₂ MXene electron transport layers for perovskite solar cells. *J. Mater. Chem. A*, 2019. 5625-5642.
124. HC. Fu, V. Ramalingam, H. Kim, CH. Lin, X. Fang, HN. Alshareef and JH. He, MXene-Contacted Silicon Solar Cells with 11.5% Efficiency. *Adv. Energy. Mater*, 2019. 9(22), 1900180.1-1900180.9.
125. X. Wu, Z. Wang, M. Yu, L. Xiu and J. Qiu, Stabilizing the MXenes by Carbon Nanoplatelet for Developing Hierarchical Nanohybrids with Efficient Lithium Storage and Hydrogen Evolution Capability. *Adv. Mater (Deerfield Beach, Fla.)*, 2017. 29(24), 1607017.
126. H. Wang, Y. Wu, X. Yuan, G. Zeng, J. Zhou, X. Wang and J. W. Chew, Clay-Inspired MXene-Based Electrochemical Devices and Photo-Electrocatalyst: State-of-the-Art Progresses and Challenges. *Adv. Mater*, 2018. 30, 1704561– 1704588.
127. M. Li, J. Lu, K. Luo, Y. Li, K. Chang, K. Chen, J. Zhou, J. Rosen, L. Hultman, P. Eklund, P. O. Å. Persson, S. Du, Z. Chai, Z. Huang and Q. Huang, Element Replacement Approach by Reaction with Lewis Acidic Molten Salts to Synthesize Nanolaminated MAX Phases and MXenes. *J. Am. Chem. Soc.*, 2019. 141, 4730–4737.
128. X. Lu, K. Xu, P. Chen, K. Jia, S. Liu and C. Wu, Facile one step method realizing scalable production of g-C₃N₄ nanosheets and study of their photocatalytic H₂ evolution activity. *J. Mater. Chem. A*, 2014. 2, 18924–18928.
129. M. Alhabeab, K. Maleski, B. Anasori, P. Lelyukh, L. Clark, S. Sin and Y. Gogotsi, Guidelines for Synthesis and Processing of Two-Dimensional Titanium Carbide (Ti₃C₂T_x MXene). *Chem. Mater*, 2017. 29, 7633–7644.
130. J. Xuan, Z. Wang, Y. Chen, D. Liang, L. Cheng, X. Yang, Z. Liu, R. Ma, T. Sasaki and F. Geng, Organic-Base-Driven Intercalation and Delamination for the Production of Functionalized Titanium Carbide Nanosheets with Superior Photothermal Therapeutic Performance. *Angew. Chem. Int. Ed.*, 2016. 55, 1–7.

131. S. Yang, P. Zhang, F. Wang, A. G. Ricciardulli, M. R. Lohe, P. W. M. Blom and X. Feng, Fluoride-Free Synthesis of Two-Dimensional Titanium Carbide (MXene) Using A Binary Aqueous System. *Angew. Chem. Int. Edit.*, 2018. 57, 15491-15495.
132. S.-Y. Pang, Y.-T. Wong, S. Yuan, Y. Liu, M.-K. Tsang, Z. Yang, H. Huang, W.-T. Wong and J. Hao, Universal Strategy for HF-Free Facile and Rapid Synthesis of Two-dimensional MXenes as Multifunctional Energy Materials. *J. Am. Chem. Soc.*, 2019. 141, 9610–9616.
133. Z. W. Seh, K. D. Fredrickson, B. Anasori, J. Kibsgaard, A. L. Strickler, M. R. Lukatskaya, Y. Gogotsi, T. F. Jaramillo and A. Vojvodic, Two-Dimensional Molybdenum Carbide (MXene) as an Efficient Electrocatalyst for Hydrogen Evolution. *ACS Energy Lett.*, 2016. 1, 589–594.
134. L. Xiu, Z. Wang, M. Yu, X. Wu and J. Qiu, Aggregation-Resistant 3D MXene-Based Architecture as Efficient Bifunctional Electrocatalyst for Overall Water Splitting. *ACS Nano*, 2018. 12, 8017–8028.
135. C.-F. Du, K. N. Dinh, Q. Liang, Y. Zheng, Y. Luo, J. Zhang and Q. Yan, Self-Assemble and In Situ Formation of Ni_{1-x}Fe_xPS₃ Nanomosaic-Decorated MXene Hybrids for Overall Water Splitting. *Adv. Energy Mater*, 2018. 8, 1801127–1801135.
136. Z. Zhang, H. Li, G. Zou, C. Fernandez, B. Liu, Q. Zhang, J. Hu and Q. Peng, Self-Reduction Synthesis of New MXene/Ag Composites with Unexpected Electrocatalytic Activity. *ACS Sustainable Chem. Eng.*, 2016. 4, 6763–677.
137. S. Cao, B. Shen, T. Tong, J. Fu and J. Yu, 2D/2D Heterojunction of Ultrathin MXene/Bi₂WO₆ Nanosheets for Improved Photocatalytic CO₂ Reduction. *Adv. Funct. Mater*, 2018. 28, 1800136–1800145.
138. J. Ran, G. Gao, F.-T. Li, T.-Y. Ma, A. Du and S.-Z. Qiao, Ti₃C₂ MXene co-catalyst on metal sulfide photo-absorbers for enhanced visible-light photocatalytic hydrogen production. *Nat. Commun*, 2017. 8, 13907–13916.
139. C. Peng, P. Wei, X. Li , Y. Liu, Y. Cao , H. Wang, H.Yu, F. Peng, L. Zhang, B.

Zhang and K. Lv, High efficiency photocatalytic hydrogen production over ternary Cu/TiO₂@Ti₃C₂Tx enabled by low-work-function 2D titanium carbide. *Nano Energy*, 2018. 53, 97–107.

140. T. Su, Z. D. Hood, M. Naguib, L. Bai, S. Luo, M. Rouleau, I. N. Ivanov, H. Ji, Z. Qin and Z. Wu, 2D/2D heterojunction of Ti₃C₂/g-C₃N₄ nanosheets for enhanced photocatalytic hydrogen evolution. *Nanoscale*, 2019. 11, 8138–8149.

141. L. Tie, S. Yang, C. Yu, H. Chen, Y. Liu, S. Dong, J. Sun and J. Sun, In situ decoration of ZnS nanoparticles with Ti₃C₂ MXene nanosheets for efficient photocatalytic hydrogen evolution. *J. Colloid Interf. Sci.*, 2019. 545, 63–70.

142. H. Fang, Y. Pan, M. Yin and C. Pan, Enhanced visible light photocatalytic activity of CdS with alkalized Ti₃C₂ nano-sheets as co-catalyst for degradation of rhodamine B. *J. Mater. Sci. - Mater. Electron*, 2019. 30, 14954–14966.

143. H. Zhang, M. Li, J. Cao, Q. Tang, P. Kang, C. Zhu and M. Ma, 2D α-Fe₂O₃ doped Ti₃C₂ MXene composite with enhanced visible light photocatalytic activity for degradation of Rhodamine B. *Ceram. Int.*, 2018. 44, 19958-19962.

144. K. Gong, F. Du, Z. Xia, M. Durstock and L. Dai, Nitrogen-doped carbon nanotube arrays with high electrocatalytic activity for oxygen reduction. *Science*, 2009. 323(5915), 760–764.

145. L. Zhou, H. Zhang, H. Sun, S. Liu, M. O. Tade and S. Wang, Recent advances in non-metal modification of graphitic carbon nitride for photocatalysis: a historic review. *Catal. Sci. Technol*, 2016. 6, 7002–7023.

146. V. Hasija, P. Raizad, A. Sudhaik, K. Sharma, A. Kumar, P. Singh, S. B. Jonnalagadda and V. K. Thakur, Recent advances in noble metal free doped graphitic carbon nitride based nanohybrids for photocatalysis of organic contaminants in water: A review. *Appl. Mater. Today*, 2019. 15, 494–524.

147. M. Z. Rahman, K. Davey and S.-Z. Qiao, Carbon, nitrogen and phosphorus containing metal-free photocatalysts for hydrogen production: progress and challenges.

- J. Mater. Chem. A, 2018. 6, 1305–1322.
148. J. Liu, H. Wang and M. Antonietti, Graphitic carbon nitride "reloaded": Emerging applications beyond (photo) catalysis. *Chem. Soc. Rev.*, 2016. 45, 2308–2326.
149. D. Masih, Y. Ma and S. Rohani, Graphitic C₃N₄ based noble-metal-free photocatalyst systems: A review. *Appl. Catal. B*, 2017. 206, 556–588.
150. H. Yan, Soft-templating synthesis of mesoporous graphitic carbon nitride with enhanced photocatalytic H₂ evolution under visible light. *Chem. Commun*, 2012. 48, 3430–3432.
151. A. Savateev, Z. P. Chen and D. Dontsova, Baking ‘crumbly’ carbon nitrides with improved photocatalytic properties using ammonium chloride. *RSC Adv.*, 2016. 6, 2910–2913.
152. J. Huang, W. Ho and X. Wang, Metal-free disinfection effects induced by graphitic carbon nitride polymers under visible light illumination. *Chem. Commun*, 2014. 50, 4338–4340.
153. X. Li, A. F. Masters and T. Maschmeyer, Photocatalytic Hydrogen Evolution from Silica-Templated Polymeric Graphitic Carbon Nitride—Is the Surface Area Important?. *ChemCatChem*, 2015. 1(7), 121–126.
154. Y. Wang, X. Wang, M. Antonietti and Y. Zhang, Facile one-pot synthesis of nanoporous carbon nitride solids by using soft templates. *ChemSusChem*, 2010. 3, 435–439.
155. K. K. Han, C. C. Wang, Y. Y. Li, M. M. Wan, Y. Wang and J. H. Zhu, Facile template-free synthesis of porous g-C₃N₄ with high photocatalytic performance under visible light. *RSC Adv.*, 2013. 3(24), 9465–9469.
156. J. Ding, Q. Liu, Z. Zhang, X. Liu, J. Zhao, S. Cheng, B. Zong and W.-L. Dai, Carbon nitride nanosheets decorated with WO₃ nanorods: Ultrasonic-assisted facile synthesis and catalytic application in the green manufacture of dialdehydes. *Appl. Catal.*

B, 2015. 165, 511–518.

157. X. Zhang, X. Xie, H. Wang, J. Zhang, B. Pan and Y. Xie, Enhanced photoresponsive ultrathin graphitic-phase C_3N_4 nanosheets for bioimaging. *J. Am. Chem. Soc.*, 2013. 135, 18–21.

158. J. Xu, L. Zhang, R. Shi and Y. Zhu, Chemical exfoliation of graphitic carbon nitride for efficient heterogeneous photocatalysis. *J. Mater. Chem. A*, 2013. 46, 14766–14772.

159. Y. Xu, F. Ge, Z. Chen, S. Huang, W. Wei, M. Xie, H. Xu and H. Li, One-step synthesis of Fe-doped surface-alkalinized g- C_3N_4 and their improved visible-light photocatalytic performance. *Appl. Surf. Sci.*, 2019. 469, 739–746.

160. F. Dong, Y. Li, Z. Wang and W.-K. Ho, Enhanced visible light photocatalytic activity and oxidation ability of porous graphene-like g- C_3N_4 nanosheets via thermal exfoliation. *Appl. Surf. Sci.*, 2015. 358, 393–403.

161. S. Kumar, T. Surendar, B. Kumar, A. Baruah and V. Shanker, Synthesis of highly efficient and recyclable visible-light responsive mesoporous g- C_3N_4 photocatalyst via facile template-free sonochemical route. *RSC Adv.*, 2014. 4(16), 8132-8137.

162. W. Wang, J. C. Yu, Z. Shen, D. K. L. Chan and T. Gu, g- C_3N_4 quantum dots: direct synthesis, upconversion properties and photocatalytic application. *Chem. Commun.*, 2014. 50(70), 10148-10150.

163. Y. Zheng, L. Lin, X. Ye, F. Guo and X. Wang, Helical Graphitic Carbon Nitrides with Photocatalytic and Optical Activities. *Angew. Chem. Int. Ed.*, 2014. 53(44), 11926-11930.

164. J. Liu, J. Huang, H. Zhou and M. Antonietti, Uniform Graphitic Carbon Nitride Nanorod for Efficient Photocatalytic Hydrogen Evolution and Sustained Photoenzymatic Catalysis. *ACS Appl. Mater. Interfaces*, 2014. 6(11), 8434-8440.

165. P. Niu, L. Zhang, G. Liu and H.-M. Cheng, Graphene-Like Carbon Nitride Nanosheets for Improved Photocatalytic Activities. *Adv. Funct. Mater.*, 2012. 22(22),

4763-4770.

166. D. Zheng, C. Pang, Y. Liu and X. Wang, Shell-engineering of hollow g-C₃N₄ nanospheres via copolymerization for photocatalytic hydrogen evolution. *Chem. Commun.*, 2015. 51(47), 9706-9709.
167. P. Yang, H. Ou, Y. Fang, and X. Wang, A Facile Steam Reforming Strategy to Delaminate Layered Carbon Nitride Semiconductors for Photoredox Catalysis. *Angew. Chem., Int. Ed.*, 2017. 56(14), 3992-3996.
168. Y. Zhu, T. Ren, and Z. Yuan, Mesoporous Phosphorus-Doped g-C₃N₄ Nanostructured Flowers with Superior Photocatalytic Hydrogen Evolution Performance. *ACS Appl. Mater. Interfaces*, 2015. 7(30), 16850-16856.
169. Y. Feng, C. Liao, L. Kong, D. Wu, Y. Liu, and P. H. Lee, Facile synthesis of highly reactive and stable Fe-doped g-C₃N₄ composites for peroxymonosulfate activation: A novel nonradical oxidation process. *J. Hazard. Mater.*, 2018. 354, 63-71.
170. S. Hu, L. Ma, J. You, F. Li, Z. Fan and G. Lu, Enhanced visible light photocatalytic performance of g-C₃N₄ photocatalysts co-doped with iron and phosphorus. *Appl. Surf. Sci.*, 2014. 311, 164-171.
171. S. Liu, J. Ke, H. Sun, J. Liu, M. O. Tade and S. Wang, Size dependence of uniformed carbon spheres in promoting graphitic carbon nitride toward enhanced photocatalysis. *Appl. Catal. B, Environmental*, 2017. 204, 358-364.
172. J. Gao, Y. Wang, S. Zhou, W. Lin and Y. Kong, A Facile One-Step Synthesis of Fe-Doped g-C₃N₄ Nanosheets and Their Improved Visible-Light Photocatalytic Performance. *ChemCatChem*, 2017. 9(9), 1708-1715.
173. Z. Wang, J. Xu, H. Zhou and X. Zhang, Facile synthesis of Zn(II)-doped g-C₃N₄ and their enhanced photocatalytic activity under visible light irradiation. *Rare Metals*, 2019. 38(5), 1-9.
174. B. Yue, Q. Li, H. Iwai, T. Kako and J. Ye, Hydrogen production using zinc-doped

carbon nitride catalyst irradiated with visible light. *Sci Technol Adv Mat*, 2011. 12(3). 034401-034401.

175. Z. Wei, J. Liu, W. Fang, W. Guo, Y. Zhu and M. Xu, Photocatalytic hydrogen energy evolution from antibiotic wastewater via metallic bi nanosphere doped g-C₃N₄: performances and mechanisms. *Catal. Sci. Technol.*, 2019. 9(19), 5279-5291.

176. P. W. Chen, K. Li, Y. X. Yu and W. D. Zhang, Cobalt-doped graphitic carbon nitride photocatalysts with high activity for hydrogen evolution. *Appl. Surf. Sci.*, 2017. 392, 608-615.

177. Q. Liu, C. Zeng, Z. Xie, L. Ai, Y. Liu and Q. Zhou, Cobalt@nitrogen-doped bamboo-structured carbon nanotube to boost photocatalytic hydrogen evolution on carbon nitride. *Appl. Catal., B*, 2019. 254, 443-451.

178. J. C. Wang, C. X. Cui, Y. Li, L. Liu and Y. P. Zhang, Porous Mn doped g-C₃N₄ photocatalysts for enhanced synergetic degradation under visible-light illumination. *J. Hazard. Mater.*, 2017. 339, 43-53.

179. S. Le, T. Jiang, Q. Zhao, X. F. Liu and M. Gong, Cu-doped mesoporous graphitic carbon nitride for enhanced visible-light driven photocatalysis. *RSC Adv.*, 2016. 6(45), 38811-38819.

180. J. Gao, J. Wang, X. Qian, Y. Dong, H. Xu, R. Song, C. Yan, H. Zhu, Q. Zhong, G. Qian, and J. Yao, One-pot synthesis of copper-doped graphitic carbon nitride nanosheet by heating Cu-melamine supramolecular network and its enhanced visible-light-driven photocatalysis. *J. Solid State Chem.*, 2015. 228, 60-64.

181. H. Sudrajat, A one-pot, solid-state route for realizing highly visible light active Na-doped g-C₃N₄ photocatalysts. *J. Solid State Chem.*, 2018. 257, 26-33.

182. S. Panneri, P. Ganguly, M. Mohan, B. N. Nair, A. A. P. Mohamed, K. G. Warriar and U. S. Hareesh, Photoregenerable, bifunctional granules of carbon-doped g-C₃N₄ as adsorptive photocatalyst for the efficient removal of tetracycline antibiotic. *ACS Sustainable Chem. Eng.*, 2017, 1610–1618.

183. N. Bao, X. Hu, Q. Zhang, X. Miao, X. Jie and S. Zhou, Synthesis of porous carbon-doped g-C₃N₄ nanosheets with enhanced visible-light photocatalytic activity. *Appl. Surf. Sci.*, 2017. 403, 682-690.
184. Y. Li, S. Wu, L. Huang, J. Wang, H. Xu and H. Li, Synthesis of carbon-doped g-C₃N₄ composites with enhanced visible-light photocatalytic activity. *Mater. Lett.*, 2014. 137, 281-284.
185. Y. Gong, X. Zhao, H. Zhang, B. Yang, K. Xiao, T. Guo, and G. Yu, MOF-derived nitrogen doped carbon modified g-C₃N₄ heterostructure composite with enhanced photocatalytic activity for bisphenol A degradation with peroxymonosulfate under visible light irradiation. *Appl. Catal. B*, 2018. 233, 35-45.
186. Y. Zeng, X. Liu, C. Liu, L. Wang, Y. Xia and S. Zhang, Scalable one-step production of porous oxygen-doped g-C₃N₄ nanorods with effective electron separation for excellent visible-light photocatalytic activity. *Appl. Catal. B*, 2018. 224, 1-9.
187. K. Wu, D. Chen, J. Fang, S. Wu, F. Yang and X. Zhu, One-step synthesis of sulfur and tungstate co-doped porous g-C₃N₄ microrods with remarkably enhanced visible-light photocatalytic performances. *Appl. Surf. Sci.*, 2018. 462, 991-1001.
188. C. Hu, W.-Z. Hung, M.-S. Wang and P.-J. Lu, Phosphorus and sulfur codoped g-C₃N₄ as an efficient metal-free photocatalyst. *Carbon*, 2018. 127, 374-383.
189. Y. Wu, H. Wang, W. Tu, Y. Liu, S. Wu, Y. Z. Tan and J. W. Chew, Construction of hierarchical 2D-2D Zn₃In₂S₆/fluorinated polymeric carbon nitride nanosheets photocatalyst for boosting photocatalytic degradation and hydrogen production performance. *Appl. Catal. B*, 2018. 233, 58-69.
190. Y. Guo, Q. Liu, Z. Li, Z. Zhang and X. Fang, Enhanced photocatalytic hydrogen evolution performance of mesoporous graphitic carbon nitride co-doped with potassium and iodine. *Appl. Catal. B*, 2018. 221, 362-370.
191. L. K. B. Paragas, M. D. G. Luna, and R.-A. Doong, Rapid removal of sulfamethoxazole from simulated water matrix by visible-light responsive iodine and

- potassium co-doped graphitic carbon nitride photocatalysts. *Chemosphere*, 2018. 210, 1099-1107.
192. B. Liu, Y. Wu, J. Zhang, X. Han and H. Shi, Visible-light-driven g-C₃N₄/Cu₂O heterostructures with efficient photocatalytic activities for tetracycline degradation and microbial inactivation. *J. Photochem. Photobiol., A*, 2019. 378, 1-8
193. G. Tzvetkov, M. Tsvetkov, and T. Spassov, Ammonia-evaporation-induced construction of three-dimensional NiO/g-C₃N₄ composite with enhanced adsorption and visible light-driven photocatalytic performance. *Superlattices Microstruct.*, 2018. 119, 122-133.
194. J. Ge, Y. Liu, D. Jiang, L. Zhang and P. Du, Integrating non-precious-metal cocatalyst Ni₃N with g-C₃N₄ for enhanced photocatalytic H₂ production in water under visible-light irradiation. *Chin. J. Catal.*, 2019. 40(2), 160-167.
195. F. Chen, H. Yang, X. Wang and H. Yu, Facile synthesis and enhanced photocatalytic H₂-evolution performance of NiS₂-modified g-C₃N₄ photocatalysts. *Chin. J. Catal.*, 2017. 38(2), 296-304.
196. W. Feng, J. Fang, G. Zhou, L. Zhang, S. Lu, S. Wu, Y. Chen, Y. Ling and Z. Fang, Rationally designed Bi@BiOCl/g-C₃N₄ heterostructure with exceptional solar-driven photocatalytic activity. *Mol. Catal.*, 2017. 434, 69-79.
197. Y. Ma, Q. Han, X. Wang and J. Zhu, An in situ annealing route to [Bi₆O₆(OH)₂](NO₃)₄·2H₂O/ g-C₃N₄ heterojunction and its visible-light-driven photocatalytic performance. *Mater. Res. Bull.*, 2018. 101, 272-279.
198. Y.-P. Yuan, S.-W. Cao, Y.-S. Liao, L.-S. Yin and C. Xue, Red phosphor/ g-C₃N₄ heterojunction with enhanced photocatalytic activities for solar fuels production. *Appl. Catal. B*, 2013. 140-141(C), 164-168.
199. K. Santha kumara, B. Vellaichamy and T. Paulmony, Visible light active metal-free photocatalysis: N-doped graphene covalently grafted with g-C₃N₄ for highly robust degradation of methyl orange. *Solid State Sci.*, 2019. 94, 99-105.

200. Y. Wang, W. Yang, X. Chen, J. Wang and Y. Zhu, Photocatalytic activity enhancement of core-shell structure g-C₃N₄@TiO₂ via controlled ultrathin g-C₃N₄ layer. *Appl. Catal. B*, 2018. 220, 337-347.
201. S. Liu, H. Sun, H. M. Ang, M. O. Tade and S. Wang, Integrated oxygen-doping and dye sensitization of graphitic carbon nitride for enhanced visible light photodegradation. *J. Colloid Interface Sci.* 2016. 476, 193-199.
202. P. Wang, Z. Guan, Q. Li and J. Yang, Efficient visible-light-driven photocatalytic hydrogen production from water by using Eosin Y-sensitized novel g-C₃N₄/Pt/GO composites. *J. Mater. Sci.*, 2018. 53(1), 774-786.
203. X.-B. Qian, W. Peng and J.-H. Huang, Fluorescein-sensitized Au/g-C₃N₄ nanocomposite for enhanced photocatalytic hydrogen evolution under visible light. *Mater. Res. Bull.*, 2018. 102, 362-368.
204. F. Yua, Z. Wang, S. Zhang, K. Yun, H. Ye, X. Gong, J. Hua and H. Tian, N-Annulated perylene-based organic dyes sensitized graphitic carbon nitride to form an amide bond for efficient photocatalytic hydrogen production under visible-light irradiation. *Appl. Catal. B*, 2018. 237, 32-42.
205. J. Qin, J. Huo, P. Zhang, J. Zeng, T. Wang and H. Zeng, Improving the photocatalytic hydrogen production of Ag/g-C₃N₄ nanocomposites by dye-sensitization under visible light irradiation. *Nanoscale*, 2016. 8(4), 2249-2259.
206. J. Xu, Y. Qi, W. Wang and L. Wang, Montmorillonite-hybridized g-C₃N₄ composite modified by NiCoP cocatalyst for efficient visible-light-driven photocatalytic hydrogen evolution by dye-sensitization. *Int. J. Hydrogen Energy*, 2019. 44(8), 4114-4122.
207. S. F. Kiew, L. V. Kiew, H. B. Lee, T. Imae and L. Y. C. Kiew, Assessing biocompatibility of graphene oxide-based nanocarriers: A review. *J. Controlled Release*, 2016. 226, 217-228.
208. K. S. Novoselov, A. K. Geim, S. V. Morozov, D. Jiang, Y. Zhang, S. V. Dubonos,

- I. V. Grigorieva and A. A. Firsov, Electric Field Effect in Atomically Thin Carbon Films. AAAS, 2004. 306(5696), 666-669.
209. Z.-T. Hua, Y. N. Liang, J. Zhao, Y. Zhang, E.-H. Yang, J. Chen and T.-T. Li, Ultra-effective integrated technologies for water disinfection with a novel 0D-2D-3D nanostructured rGO-AgNP/Bi₂Fe₄O₉ composite. *Appl. Catal. B*, 2018. 227, 548-556.
210. N. N. Rosman, R. M. Yunus, L. J. Minggu, K. Arifin, M. N. I. Salehmin, M. A. Mohamed and M. B. Kassim, Photocatalytic properties of two-dimensional graphene and layered transition-metal dichalcogenides based photocatalyst for photoelectrochemical hydrogen generation: An overview. *Int. J. Hydrogen Energy*, 2018. 43(41), 18925-18945.
211. J. Park and M. Yan, Three-dimensional graphene-TiO₂ hybrid nanomaterial for high efficient photocatalysis. *Nanotechnol. Rev.*, 2016. 5(4), 417-423.
212. C. Li and G. Shi, Functional gels based on chemically modified graphenes. *Adv. Mater.*, 2014. 26(24), 3992-4012.
213. L. Yan, H. Kong and Z. Li, Synthesis and supercapacitor property of three-dimensional graphene/Ni-Al layered double hydroxide composite. *Acta Chim Sin*, 2013. 71(5), 822-828.
214. D. Long, W. Li, L. Ling, J. Miyawaki, I. Mochida and S.-H. Yoon, Preparation of nitrogen-doped graphene sheets by a combined chemical and hydrothermal reduction of graphene oxide. *Langmuir*, 2010. 26(20), 16096-16102.
215. L. Sun, L. Wang, C. Tian, T. Tan, Y. Xie, K. Shi, M. Li and H. Fu, Nitrogen-doped graphene with high nitrogen level via a one-step hydrothermal reaction of graphene oxide with urea for superior capacitive energy storage. *RSC Adv.*, 2012. 2(10), 4498-4506.
216. Z.-H. Sheng, H.-L. Gao, W.-J. Bao, F.-B. Wang and X.-H. Xia, Synthesis of boron doped graphene for oxygen reduction reaction in fuel cells. *J. Mater. Chem.*, 2012. 22(2), 390-395.

217. X. Wang, X. Li, L. Zhang, Y. Yoon, P. K. Weber, H. Wang, J. Guo and H. Dai, N-doping of graphene through electrothermal reactions with ammonia. *Science*, 2009. 324(5928), 768-771.
218. M.-L. Yang, N. Zhang, K.-Q. Lu and Y.-J. Xu, Insight into the role of size modulation on tuning the band gap and photocatalytic performance of semiconducting nitrogen-doped graphene. *Langmuir*, 2017. 33(13), 3161-3169.
219. Y. Jiang, S. Chowdhury and R. Balasubramanian, Nitrogen-doped graphene hydrogels as potential adsorbents and photocatalysts for environmental remediation. *Chem. Eng. J.*, 2017. 327, 751-763.
220. M. M. Mohamed, M. A. Mousa, M. Khairy and A. A. Amer, Nitrogen graphene: A new and exciting generation of visible light driven photocatalyst and energy storage application. *ACS Omega*, 2018. 3(2), 1801-1814.
221. N. N. T. Ton, A. T. N. Dao, K. Kato, T. Ikenaga, D. X. Trinh and T. Taniike, One-pot synthesis of TiO₂/graphene nanocomposites for excellent visible light photocatalysis based on chemical exfoliation method. *Carbon (New York)*, 2018. 133, 109-117.
222. L.-L. Tan, S.-P. Chai and A. R. Mohamed, Synthesis and Applications of Graphene-Based TiO₂ Photocatalysts. *ChemSusChem*, 2012. 5(10), 1868-1882.
223. M. Sun, W. Li, S. Sun, J. He, Q. Zhang and Y. Shi, One-step in situ synthesis of graphene-TiO₂ nanorod hybrid composites with enhanced photocatalytic activity. *Mater. Res. Bull.*, 2015. 61, 280-286.
224. Y. Zhang, Z. Zhou, T. Chen, H. Wang and W. Lu, Graphene TiO₂ nanocomposites with high photocatalytic activity for the degradation of sodium pentachlorophenol. *J. Environ. Sci.*, 2014. 26(10), 2114-2122.
225. F. Zhou and Y. Zhu, Significant photocatalytic enhancement in methylene blue degradation of Bi₂WO₆ photocatalysts via graphene hybridization. *J. Adv. Ceram.*, 2012. 1(1), 72-78.

226. M.-Q. Yang and Y.-J. Xu, Basic Principles for Observing the Photosensitizer Role of Graphene in the Graphene–Semiconductor Composite Photocatalyst from a Case Study on Graphene-ZnO. *J. Phys. Chem. C*, 2013. 117(42), 21724-21734.
227. A. R. Nanakkal and L. K. Alexander, Photocatalytic Activity of Graphene/ZnO Nanocomposite Fabricated by Two-step Electrochemical Route. *J. Chem. Sci.*, 2017. 129(1), 95-102.
228. S. B. Gawande and S. R. Thakare, Graphene wrapped BiVO₄ photocatalyst and its enhanced performance under visible light irradiation. *Int. Nano Lett.*, 2012. 2(1), 1-7.
229. Y. Yao, J. Liang, Y. Wei, X. Zheng, X. Xu, G. He and H. Chen, One-pot synthesis of visible-light-driven photocatalyst for degradation of Rhodamine B: Graphene based bismuth/bismuth(III) oxybromide. *Mater. Lett.*, 2019. 240, 246-249.
230. Y. Wang, Y. Shao, D. W. Matson, J. Li and Y. Lin, Nitrogen-doped graphene and its application in electrochemical biosensing. *ACS Nano*, 2010. 4(4), 1790-1798.
231. K. Toda, R. Furue and S. Hayami, Recent progress in applications of graphene oxide for gas sensing: A review. *Anal. Chim. Acta.*, 2015. 878, 43-53.
232. J. W. S. Hummers and R. E. Offeman, Preparation of graphitic oxide. *J. Am. Chem. Soc.*, 1958. 80(6), 1339-1339.
233. M. Wu, L. Li, Y. Xue, G. Xu, L. Tang, N. Liu and W. Huang, Fabrication of ternary GO/g-C₃N₄/MoS₂ flower-like heterojunctions with enhanced photocatalytic activity for water remediation. *Appl. Catal.*, 2018. 228, 103-112.
234. W.-K. Jo, and N.C.S. Selvam, Enhanced visible light-driven photocatalytic performance of ZnO–g-C₃N₄ coupled with graphene oxide as a novel ternary nanocomposite. *J. Hazard. Mater.*, 2015. 299, 462-470.
235. P. Huo, M. Zhou, Y. Tang, X. Liu, C. Ma, L. Yu and Y. Yan, Incorporation of N–ZnO/CdS/Graphene oxide composite photocatalyst for enhanced photocatalytic activity under visible light. *J. Alloys compd.*, 2016. 670, 198-209.

236. C. Prasad, Q. Liu, H. Tang, G. Yuvaraja, J. Long, A. Rammohan and G. V. Zyryanov, An overview of graphene oxide supported semiconductors based photocatalysts: Properties, synthesis and photocatalytic applications. *J. Mol. liq.*, 2020. 297, 111826.
237. C. Lin, Y. Gao, J. Zhang, D. Xue, H. Fang, J. Tian, C. Zhou, C. Zhang, Y. Li and H. Li, GO/TiO₂ composites as a highly active photocatalyst for the degradation of methyl orange. *J. Mater. Res.*, 2020. 35(10), 1307-1315.
238. J. Yan, Z. Song, X. Wang, Y. Xu, W. Pu, H. Xu, S. Yuan and H. Li, Enhanced photocatalytic activity of ternary Ag₃PO₄/GO/g-C₃N₄ photocatalysts for Rhodamine B degradation under visible light radiation. *Appl. Surf. Sci.*, 2019. 466, 70-77.
239. C. Fu, X. Liu, Y. Wang, L. Li and Z. Zhang, Preparation and characterization of Fe₃O₄@SiO₂@TiO₂-Co/rGO magnetic visible light photocatalyst for water treatment. *RSC adv.*, 2019. 9(35), 2256-2265.
240. X. Xu, R. Ray, Y. Gu, H. J. Ploehn, L. Gearheart, K. Raker and W. A. Scrivens, Electrophoretic analysis and purification of fluorescent single-walled carbon nanotube fragments. *JACS*, 2004. 126(40), 12736-12737.
241. Y. Wang and A. Hu, Carbon quantum dots: synthesis, properties and applications. *J. Mater. Chem. C*, 2014. 2(34), 6921-6939.
242. Y.-P. Sun, B. Zhou, Y. Lin, W. Wang, K. A. S. Fernando, P. Pathak, M. J. Meziani, B. A. Harruff, X. Wang, H. Wang, P.G. Luo, Hua Yang, M. E. Kose, B. Chen, L. M. Veca and S.-Y. Xie, Quantum-sized carbon dots for bright and colorful photoluminescence. *JACS*, 2006. 128(24), 7756-7757.
243. Q.-L. Zhao, Z.-L. Zhang, B.-H. Huang, J. Peng, M. Zhang and D.-W. Pang, Facile preparation of low cytotoxicity fluorescent carbon nanocrystals by electrooxidation of graphite. *Chem. Commun.*, 2008(41), 5116-5118.
244. X. Jia, J. Lia and E. Wang, One-pot green synthesis of optically pH-sensitive carbon dots with upconversion luminescence. *Nanoscale*, 2012. 4(18), 5572-5575.

245. Y. Wang, P. Anilkumar, L. Cao, J. -H. Liu, P. G. Luo, K. N. Tackett II, S. Sahu, P. Wang, X. Wang and Y. -P. Sun, Carbon dots of different composition and surface functionalization: cytotoxicity issues relevant to fluorescence cell imaging. *Exp Biol Med*, 2011. 236(11), 1231-1238.
246. P. Tiong, H. O. Lintang, S. Enduda and L. Yulianti, Improved interfacial charge transfer and visible light activity of reduced graphene oxide–graphitic carbon nitride photocatalysts. *RSC Adv.*, 2015. 5(114), 94029-94039.
247. H. Sun, G. Zhou, Y. Wang, A. Suvorova and S. Wang, A new metal-free carbon hybrid for enhanced photocatalysis. *ACS Appl. Mater. Interfaces*, 2014. 6(19), 16745-16754.
248. S. Liu, H. Sun, H. M. Ang, M. O. Tade, S. Wang, Integrated oxygen-doping and dye sensitization of graphitic carbon nitride for enhanced visible light photodegradation. *J. Colloid Interface Sci.*, 2016. 476, 193-9.
249. X.-H. Song, L. Feng, S.-L. Deng, S.-Y. Xie and L.-S. Zheng, Simultaneous Exfoliation and Modification of Graphitic Carbon Nitride Nanosheets. *Adv. Mater. Interfaces*, 2017. 4(15), 1700339.
250. H. Li, R. Liu, W. Kong, J. Liu, Y. Liu, L. Zhou, X. Zhang, S.-T. Lee and Z. Kang, Carbon quantum dots with photo-generated proton property as efficient visible light controlled acid catalyst. *Nanoscale*, 2014. 6(2), 867-873.
251. Y. Guo, P. Yao, D. Zhu, C. Gu, A novel method for the development of a carbon quantum dot/carbon nitride hybrid photocatalyst that responds to infrared light irradiation. *J. Mater. Chem. A*, 2015. 3(25), 13189-13192.
252. H. Zhang, Y. Huang, S. Hu, Q. Huang, C. Wei, W. Zhang, W. Yang, P. Dong and A. Hao, Self-assembly of graphitic carbon nitride nanosheets–carbon nanotube composite for electrochemical simultaneous determination of catechol and hydroquinone. *Electrochim. Acta*, 2015. 176, 28-35.
253. H. Sun, G. Zhou, Y. Wang, A. Suvorova and S. Wang, A new metal-free carbon

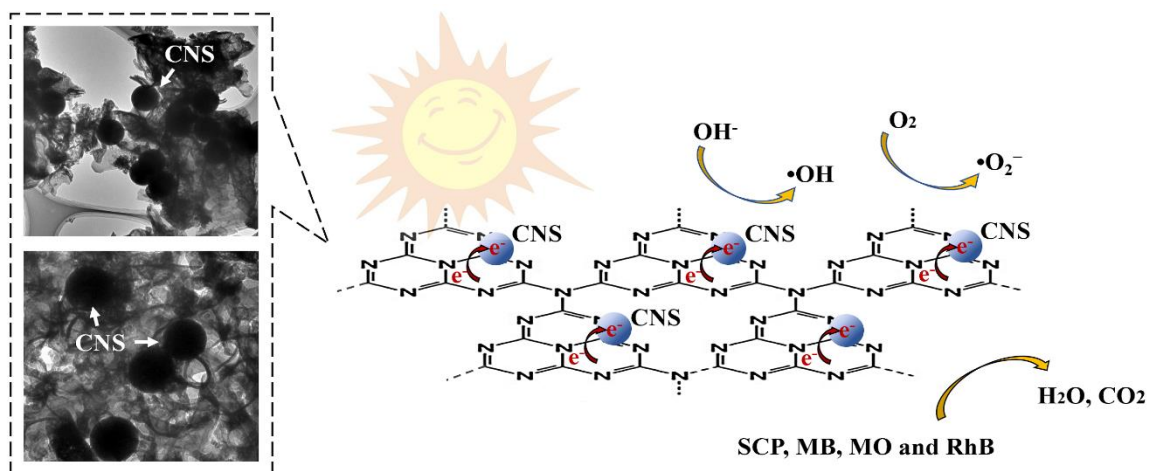
hybrid for enhanced photocatalysis. *ACS Appl. Mater. Interfaces*, 2014. 6(19), 16745-16754.

Chapter 3. Surface chemistry-dependent activity and comparative investigation on the enhanced photocatalytic performance of graphitic carbon nitride modified with various nanocarbons

Abstract

Organic contaminants, dyes and antibiotics, discharged in wastewater systems, have posed great threats to the sustainability of the ecosystem. This study was performed to prepare graphitic carbon nitride (GCN) nanocomposites modified by nanocarbons, including carbon quantum dots (CQD), carbon nanotube (CNT), reduced graphene oxide (rGO), and carbon nanospheres (CNS), by a straightforward one-pot method. The characterization results suggest that after the modification with nanocarbons, GCN demonstrated slight red shift and stronger light absorption. The resultant photocatalysts revealed prominent performances for total photodegradation of organic contaminants. The degradation processes were investigated by in situ electron paramagnetic resonance (EPR). The mechanistic studies on the enhanced photoelectrochemical and photocatalytic performances were also conducted. Results indicate that GCN modified by the nanocarbon spheres displayed a substantial improvement in the degradation of sulfachloropyridazine (SCP) and dyes, compared favourably with other GCN samples modified by carbon nanotubes, quantum dots and layered graphene oxide. The photocatalytic degradation difference is mainly stemmed from the higher contents of COOH and C=O functional groups. The intimate contact or interaction between the two phases of GCN and nanocarbon in the nanocomposites may further improve the activity. This work provides insight in the design of highly efficient metal-free photocatalysts to

better utilise the clean and free solar energy for environmental remediation.



The content of this chapter is published in J. Colloid Interface Sci. 2020, 569,12-21

3.1. Introduction

Water pollution has become a serious concern in the biodiversity and ecological balance of groundwater, surface waters and beyond, which attracts extensively the attention of authorities and environmental professionals [1, 2]. Among the various sources to water pollution, organic contaminants in wastewater become an inescapable problem to be solved. For example, antibiotic and organic dyes have a complex molecular structure, biotoxic benzene rings, and NH_2 functional groups, toward low biodegradability and good chemical stability in sewages [3]. Therefore, such artificial contaminants are arduous to be degraded by biological, physical and chemical treatments. Moreover, conventional chemical cleaning processes usually lead to the accumulation of concentrated sludge with excessive chemicals that creates a disposal issue and inevitably brings secondary contamination in the environment [4]. Recently, photocatalytic processes have emerged as a sustainable and efficient route for remediation of organic pollutants. Semiconductor materials, for example, TiO_2 , WO_3 , ZnO and CdS as UV or visible-light responsive photocatalysts, are effective for photodegradation of organics, but they are either of low visible light absorption or of secondary pollution via photocorrosion [5-8].

As a metal-free semiconductor material, graphitic carbon nitride (GCN) has been deemed as a promising photocatalyst material owing to its layered graphite-like structure, electronic structure for solar energy conversion, cost-effective and the simplicity of their production [9-11]. However, the band-gap energy of pristine GCN is relatively large, which leads to a poor absorption capacity and fast recombination of photo-introduced electron-hole pairs. Hybridization with another material helps to improve the charge separation and prolong the lifetime of photoinduced carriers. In order to avoid the high cost and dissolved toxic ions of transition metals or their oxides, metal-free materials as green catalysts have been used as effective co-catalysts for water purification. Carbon or nanocarbon materials, are promising to be applied as

adsorbents. A variety of nanocarbons have widely reported to be the co-catalysts for photocatalytic oxidation of organic pollutants in wastewater [12-15].

Carbon quantum dots (CQDs) have revealed a great visible light-excitability in degradation of organics, owing to the wide light absorption at short and long wavelengths and the light emitting of both wavelengths (up and down conversion photoluminescence) [16-19]. As one of the most popular materials, reduced graphene oxide (rGO) that can be obtained via the modified Hummers' method is usually used as a modifier because of the presence of abundant oxygen functional groups and the unique porous structure. As a result, rGO has been frequently applied as a co-catalyst with GCN for sustainable remediation of aqueous organics driven by sunlight irradiation [20]. Multi-walled carbon nanotube (CNT) has performed an excellent catalytic oxidation activity and fascinating up-conversion effect of GCN in photocatalysis, possibly due to the unique surface properties, superior electronic conductivity and charge transfer [21]. Carbon nanospheres (CNS) also have captured the imagination of researchers. These carbon spheres can be a promising promoter for improving photo activity on carbon nitride in photocatalytic performance [22, 23]. Depending on the applications, these different morphologies in CNT, CNS and CQD have their respective advantages. However, a systematic study of the morphological influence on one particular application has rarely been reported.

In this paper, we look at the effects of various nanocarbon materials with different morphologies on the photocatalytic property of GCN composites. Herein, a wide variety of typical nanocarbons, including CQDs, rGO, CNT and CNS, are employed to prepare modified GCN photocatalysts, for sulfachloropyridazine (SCP) removal under UV-visible light irradiations. SCP is one of the most widely used veterinary pharmaceuticals to treat animal infections. The highly mobile antibiotic discharged into water and soil can easily enter into the food chain and pose a challenge to public health. It is crucial to develop efficient catalysts to degrade SCP. Systematic

comparisons were made to acquire the advantageous properties of catalysts in photocatalytic degradation.

3.2 Experimental

3.2.1. Materials

All chemicals used were in analytical grade. Melamine (99.9%), ethanol ($\geq 99.9\%$), glucose ($\geq 99.0\%$), graphite ($\geq 99.0\%$), sulfuric acid (98%), nitric acid (68 wt.% in H₂O), sodium nitrate ($> 99.5\%$), potassium permanganate ($> 99.5\%$), resorcinol ($\geq 99.0\%$), formaldehyde (37% solution), 4-amino-3-nitrophenol ($\geq 99\%$), aqueous ammonia (25% solution) and commercial carbon nanotube (CNT) ($> 99.5\%$) were purchased from Sigma-Aldrich. Ultrapure water was used for all synthesis and reactions.

3.2.2. Synthesis of nanocarbon modified GCN

GCN was prepared by direct condensation of melamine. Briefly, melamine (10 g) was put in a 20 mL alumina crucible with 10 mL of methanol. After that, the crucible was transferred into an oven at 60 °C for 24 h to remove methanol. The powders were then moved into a muffle furnace, annealing at 550 °C for 2 h with a heating rate of 10 °C/min. Finally, yellow powders were harvested as GCN. A commercial CNT (1 g) sample was treated with diluted nitric acid (100 mL, 0.1 M) and stirring for 2 h at room temperature to remove residual impurities. CQDs were prepared following the method of Li et al. [24], and rGO was synthesized from graphite with Hummers' method [25]. Carbon nanospheres (CNS) were synthesized via a direct hydration treatment in a same way to the reported literature [26].

The nanocarbon modified GCN photocatalysts were prepared using the above

nanocarbon materials and GCN as the precursors by a hydrothermal treatment. Typically, 10 wt% nanocarbon materials were mixed with 1 g of the pristine GCN in 50 mL of deionized water. After 3 h ultrasonic treatment, the mixed solution was stirred for 3 h at room temperature to generate a homogenous suspension. Then the suspension was transferred into a 100 mL Teflon-lined autoclave for a hydrothermal treatment at 150 °C for 12 h. The products were dried at 60 °C and the obtained samples were referred to GCN/CQD, GCN/rGO, GCN/CNT and GCN/CNS, respectively.

3.3. Photocatalytic activity testing

The crystal structures were obtained on an Empyrean multipurpose research diffractometer (Panalytical Empyrean XRD) with a Cu K α irradiation ($\lambda=1.5418$ Å). The morphologies and structures of the samples were acquired by using a transmission electron microscope (HR-TEM, JEOL-2010). The Brunauer Emmette Teller (BET) specific surface areas and pore size distributions were observed in an automated nitrogen adsorption/desorption analyzer using a Micromeritics Tristar II Plus. X-ray photoelectron microscopy (XPS) analysis was evaluated using a Thermo Escalab 250 with the exciting source of Al K α radiation to investigate the surface chemical properties. The UV-vis diffused reflectance spectra (DRS) were conducted in a Cary 100 UV-vis Spectrophotometer. Photoluminescence (PL) spectra were recorded utilizing a Cary Eclipse Fluorescence Spectrophotometer (Agilent, US). Electrochemical experiments were carried out in a three-electrode cell with a Pt electrode served as a counter electrode, Ag/AgCl as a reference electrode and 0.1 M Na₂SO₄ as the electrolyte solution using an electrochemical analyzer. Electrochemical impedance spectroscopy (EIS) and transient photocurrent responses were conducted using an electrochemical workstation. Electron paramagnetic resonance (EPR) were carried out using a Bruker EMS-plus instrument with Xeon software (Bruker) and DMPO acted as a spin-trapping agent to capture the free radicals.

The performances of various photocatalysts were evaluated by photodegradation of sulfachloropyridazine (SCP, 20 mg/L), methylene blue (MB, 20 mg/L), methyl orange (MO, 20 mg/L) and Rhodamine B (RhB, 20 mg/L) in aqueous solutions under artificial sunlight irradiations.

In a typical run, a certain amount of catalyst (100 mg) was dispersed in a 100 mL of organic containing solution within a 500 mL double-jacket glass cylindrical reactor with a water circulating system at 25 °C. Prior to the irradiation, the suspension was kept stirring for 30 min to ensure the establishment of the adsorption equilibrium. The reactor was placed 30 cm away from the light source. Two light sources were employed in this study, including UV–vis light with an intensity at 300 mW/cm² with a cut-off filter (UV cut-off filter < 400 nm and visible light cut-off filter 400–700 nm). With turning on the light, 3 mL of solution was extracted with a pipette in a time interval and transferred to a centrifuge tube for centrifugation at 13,000 rpm for 15 min to remove the solid particles. SCP solutions were measured by a high performance liquid chromatography (HPLC, Thermo Scientific), and MB, MO and RhB solutions were analyzed by a UV-vis spectrometer (Perkin-Elmer Lambda 900UV/Vis/NIR).

3.4. Results and discussion

3.4.1 Physical properties of the different nanocarbon modified graphitic carbon nitride (GCN)

Fig. 3. 1 displays TEM images of GCN/CQD, GCN/rGO, GCN/CNS and GCN/CNT and GCN exhibits a thin layered, buckled and porous structure. As can be seen in Fig. 3. 1(A), the diameter of quantum dots in GCN/CQD is about 2 - 5 nm (marked by the dotted circles). According to Fig. 3. 1(B), the as-prepared rGO shows a thin-layered sheet-like and lapped structure, indicating a good exfoliation from the basal plane [27].

As for the GCN/CNS sample, the CNSs (~ 200 nm) display a homogeneous and uniform dispersion on the surface of GCN (Fig. 3. 1(C)). Moreover, the morphology and microstructure of GCN were not negatively impacted by the introduction of CNS. Fig. 3. 1(D) verifies a uniform distribution of CNTs and GCN, illustrating a well-connected porous network composed of CNTs coupled with GCN.

XRD was employed to study the crystalline structures of the as-prepared samples. As shown in Fig. 3. 2, there are two peaks at 13.1° and 27.4° of bulk GCN, corresponding to the (100) and (002) planes, respectively [28]. No additional peaks assigned to guest species were observed in the other four patterns, illustrating that the compounds exhibited graphite-like stacking structure similar to GCN. Further observation reveals that the (002) diffraction peak of nanocarbon-modified GCN samples was shifted toward a higher 2θ value at 27.4° than that of pure GCN, which can be ascribed to the electronic interaction between the nanocarbon materials and GCN that took place at an atomic level; and the gallery distance between the basic layers of GCN decreased because of the carbon vacancy [29, 30].

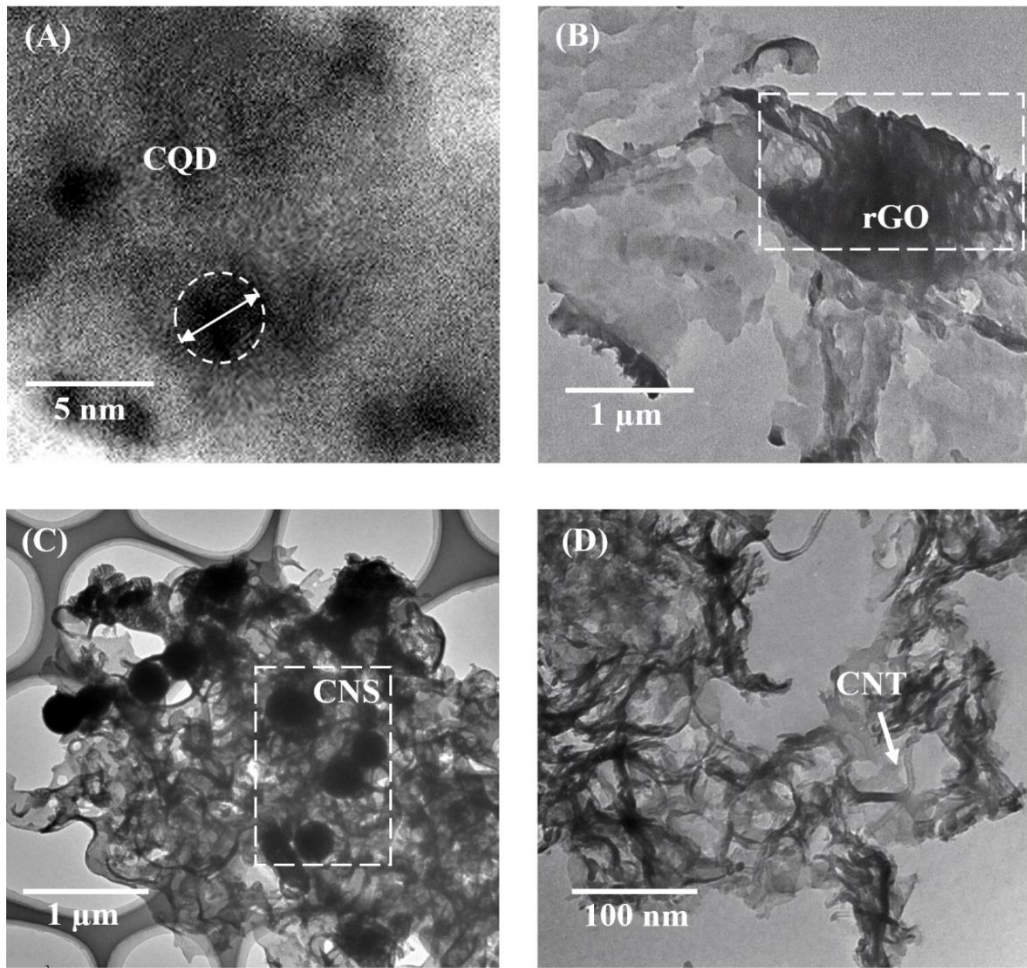


Fig. 3. 1. FETEM images of GCN/CQD (A), GCN/rGO (B), GCN/CNS (C) and GCN/CNT (D).

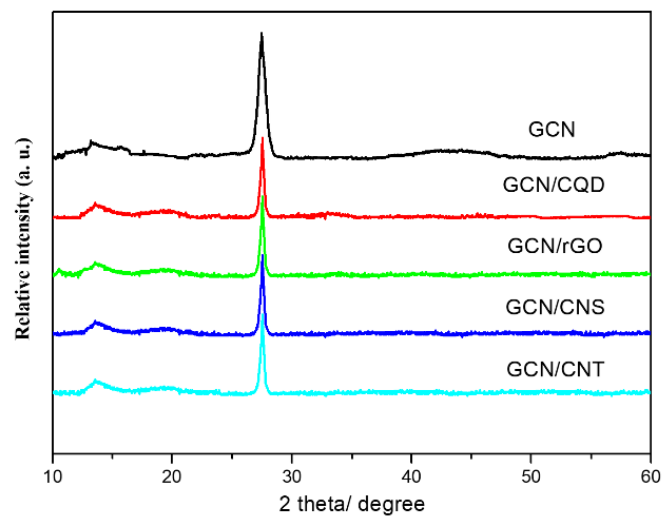


Fig. 3. 2. XRD patterns

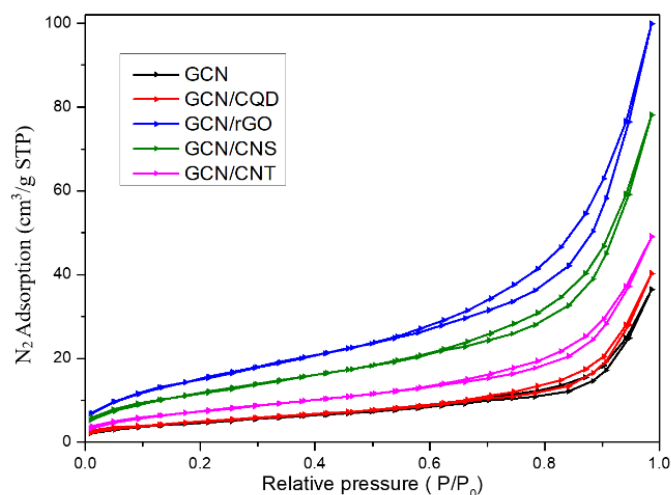


Fig. 3. 3. Nitrogen sorption isotherms

Fig. 3. 3. shows N_2 adsorption–desorption isotherms of the photocatalysts, which exhibit a type IV with a H3 hysteresis loop and characteristic features of the mesopores [31]. As listed in Table 3.1, the BET surface area of GCN/rGO is the largest, reaching $45.2 \text{ m}^2\text{g}^{-1}$, about three times higher than that of original GCN ($12.3 \text{ m}^2\text{g}^{-1}$) and GCN/CQD ($13.2 \text{ m}^2\text{g}^{-1}$), while over two times higher than that of GCN/CNT ($20.0 \text{ m}^2\text{g}^{-1}$) followed by GCN/CNS at $34.8 \text{ m}^2\text{g}^{-1}$. In comparison with the pore volume of GCN of $0.103 \text{ cm}^3\text{g}^{-1}$, the samples of GCN/CQD, GCN/rGO, GCN/CNS and GCN/CNT show a larger pore volume of 0.212, 0.317, 0.246 and $0.233 \text{ cm}^3\text{g}^{-1}$, respectively, as the hydrothermal treatment created porosity inside the particles [32]. The average size of pores was detected at around 24 nm on the nanocarbon modified GCN samples, while 12.5 nm pores were observed on the original GCN. We found that the open porous structure and relatively large surface area were beneficial to provide more active sites for organics adsorption. Accordingly, the SCP adsorption rates in the first 30 min followed the order of GCN (3.5%) < GCN/CNS (6.0%) < GCN/CQD (6.7%) < GCN/rGO (10.3%) < GCN/CNT (15.8%), which is in accordance with the specific surface areas.

Table 3. 1. Textural properties and SCP adsorption (in dark for 30 min) of various nanocarbons

Catalyst	S _{BET} (m ² /g)	V _{pore} (cm ³ /g)	Pore size (nm)	SCP adsorption (%)
GCN	12.3	0.103	12.5	3.5
GCN/CQD	13.2	0.212	24.3	6.7
GCN/rGO	45.2	0.317	25.5	13.3
GCN/CNS	34.8	0.246	23.0	12.8
GCN/CNT	20.0	0.233	24.7	8.0

The surface compositions and chemical states of the as-obtained samples were investigated by XPS, as displayed in Fig. 3. 4(A). Compared with the pristine GCN, the nanocarbon modified GCN samples show lower N contents but higher value of C, which follows the order of GCN/CNS (49.64%) < GCN/rGO (50.17%) < GCN/CNT (50.21%) < GCN/CQD (51.82%) < GCN (55.15%) for N1s, while GCN (44.87%) < GCN/CQD (46.43%) < GCN/rGO (47.91%) < GCN/CNT (48.02%) < GCN/CNS (48.50%) for C1s, respectively. The weak O1s signal in the hybrids might be ascribed to the adsorbed oxygen molecules or functional groups from the hydrothermal process. The C1s XPS spectra are presented in Fig. 3. 4(B-F). Four components of C1s XPS of GCN appear at 284.0, 284.9, 286.7 and 288.1 eV, respectively (Fig. 3. 4(B)), which can be attributed to aromatic C-NH-C, C=C, C-O and N-C=N linkages in the aromatic ring of typical GCN, respectively. Regarding to the GCN/CQD sample (Fig. 3. 4(C)), the C=O and COOH groups are detectable at 286.1 and 287.9 eV after the introduction of CQD. In Fig. 3. 4, the broad C1s peak of GCN/rGO or GCN/CNS can be observed at 284.9 eV (C=C), 286.1 eV (C=O), 287.4 or 288.0 eV (N-C=N) and 289.6 eV (COOH), respectively. Similarly, four peaks at 284.9, 286.2, 287.4 and 289.5 eV in the C1s spectrum of GCN/CNT can be also correlated to the functional groups of C=C, C=O, N-C=N and COOH [33-36], respectively. From above five spectra, N-C=N and C=C were determined as the main carbon species for GCN in the hybrid systems.

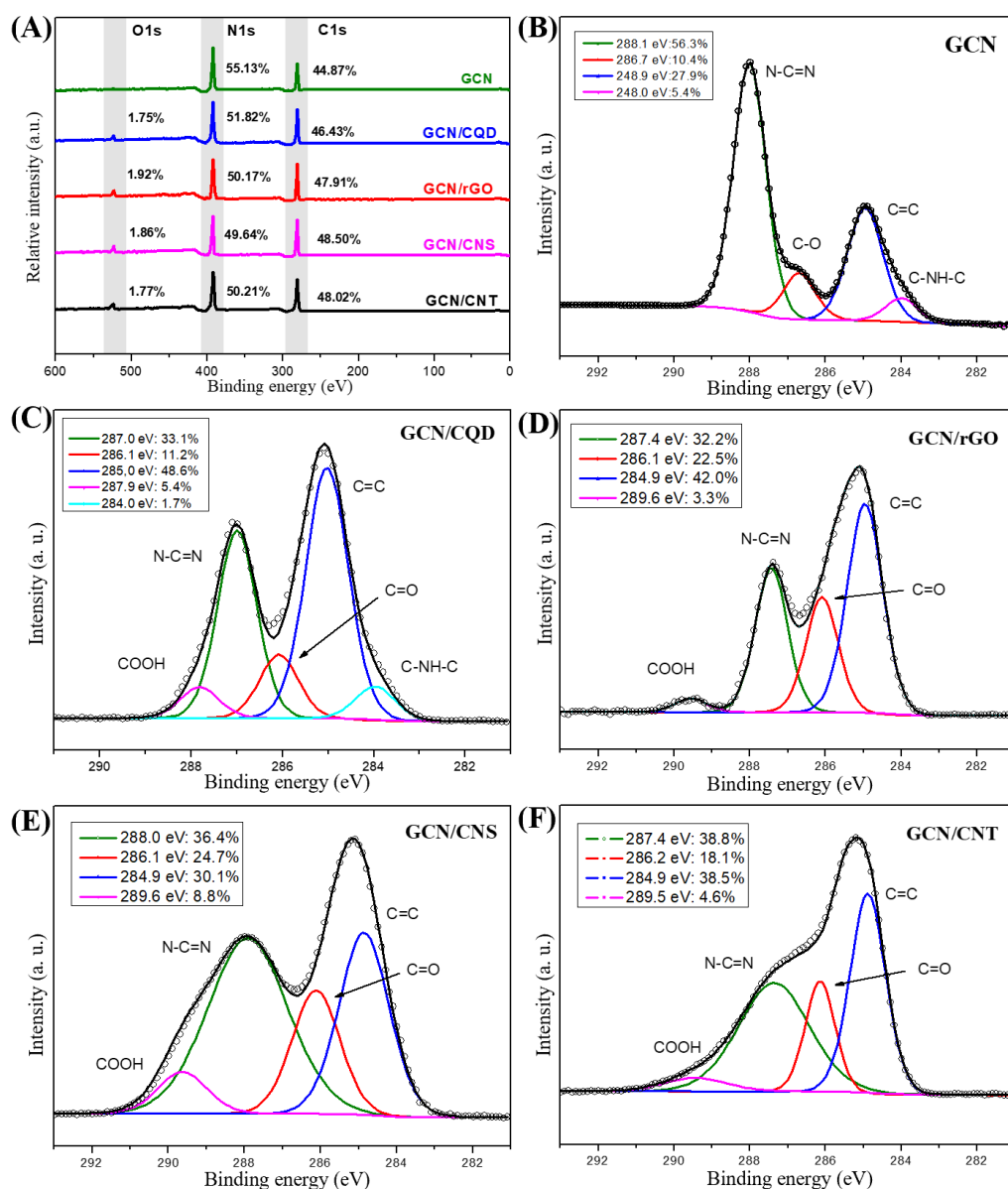


Fig. 3. 4. XPS survey spectra of nanocarbon modified GCN samples (A); XPS C1s spectra of GCN (B), GCN/CQD (C), GCN/rGO (D), GCN/CNS (E) and GCN/CNT (F).

The contents of elements in atomic percentage and the total contents of surface groups (COOH) and carboxyl carbonyl (C=O) are summarized in Table 3. 2. The surface COOH and C=O contents follows the order of GCN/CNS (16.2%) > GCN/rGO (12.4%) > GCN/CNT (10.9%) > GCN/CQD (7.7%) > GCN (~0), which is in agreement with the reported results that the catalytic oxidation activity can be improved by

introducing C=O [37, 38] or COOH [39, 40]. To further probe the effective species, the relative amounts of the surface groups that play a pivotal role in the photocatalysis process were determined. GCN/CNS possesses a larger amount of surface COOH and C=O (563.3) than that of GCN/rGO (560.1), GCN/CQD (438.6), GCN/CNT (218.4) and GCN (~0).

Table 3.2. Total content and relative amount of COOH/C=O on the surface of the catalyst samples.

Sample	Carbon content on the surface (at.%)	Molar ratio (at.%)		COOH/C=O content on the surface (at.%)	Relative amount of surface COOH/C=O ($S_{BET} \times$ surface content)
		COOH	C=O		
GCN	44.9	~0	~0	~0	~0
GCN/CQD	46.4	5.4	11.2	7.7	438.6
GCN/rGO	47.9	3.3	22.5	12.4	560.1
GCN/CNS	48.5	8.8	24.7	16.2	563.3
GCN/CNT	48.0	4.6	18.1	10.9	218.4

3.4.2. Optical properties of graphitic carbon nitride (GCN) and nanocarbon composites

The optical properties of GCN/CQD, GCN/rGO, GCN/CNS and GCN/CNT were investigated by ultraviolet-visible diffuse reflectance (UV-Vis) spectroscopy. In Fig. 3. 5(A), GCN exhibits a typical photosensitive semiconductor characteristics at 460 nm, corresponding to a bang gap energy of 2.68 eV for photo-excited electron. As shown in the inserted graph, the lone pair electrons in valance band jump from π to π^* at the C=N bonds in conductive band and from n to π^* at the terminal C-N groups [41-43]. It can be seen that carbon modification can extend the absorption edge of GCN to 475, 468,

480 and 470 nm by adding CQD, rGO, CNS and CNT, respectively. The band gap energies of the carbon modified GCN materials were estimated by the Kubelka–Munk equation to be 2.61, 2.45, 2.58 and 2.64 eV, respectively, as depicted from the inset of Fig. 3. 5(A) [44]. The enhancement of optical properties demonstrates that the composition of carbon materials changes the energy levels between the instinct valence and conduction bands of original GCN. To determine the energy levels of the samples, Mott–Schottky relationships were acquired, which feature the typical n-type Mott–Schottky plots of bulk GCN, GCN/CQD, GCN/rGO, GCN/CNS and GCN/CNT without light exciting. Importantly, flat-band potential was also measured here and the conduction band (CB) energies were determined to be -1.13, -1.28, -1.20, -1.19 and -1.31 V, versus the saturated calomel electrode (SCE), respectively.

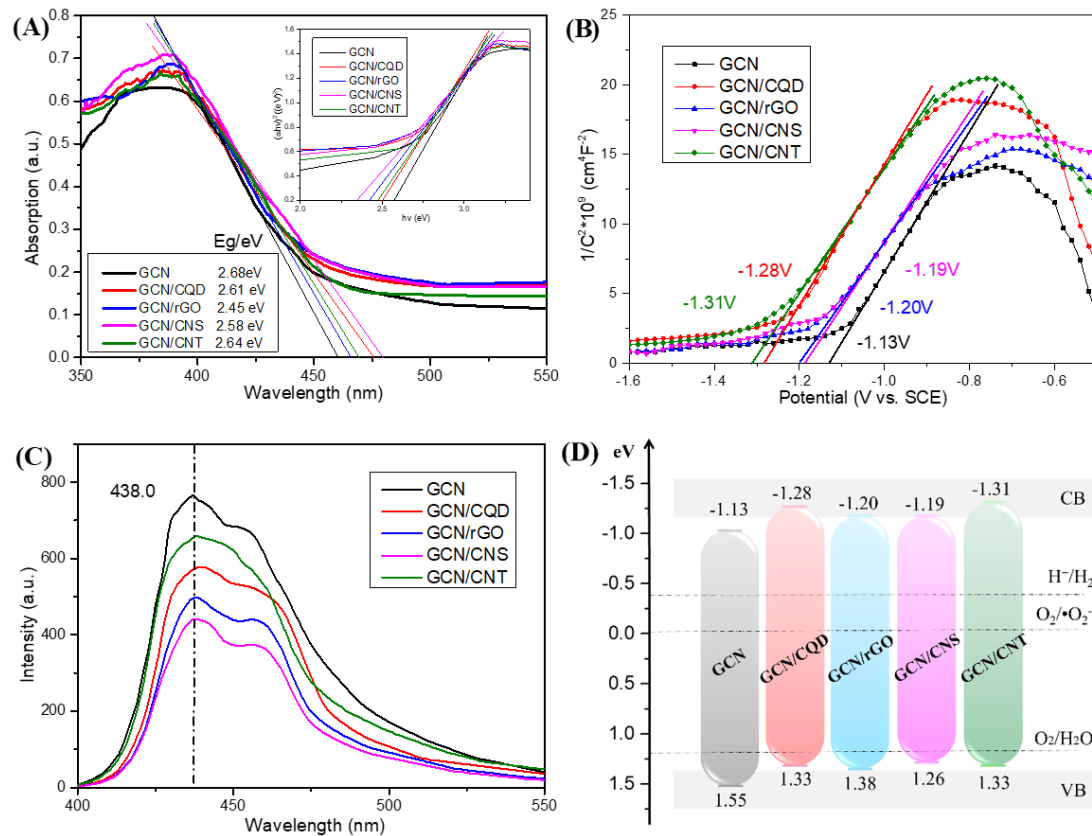


Fig. 3. 5. (A) UV-Vis spectra, the inset shows plots of $(\alpha h\nu)^2$ versus photon energy ($h\nu$) for the band gap energy; (B) Mott-Schottky measurements; (C) PL spectra; (D) Band

gap structures and degradation mechanism of SCP solutions.

As illustrated in Fig. 3. 5(C), the PL spectra show the fluorescence quenching by electron/hole pairs recombination. Along with an excitation wavelength of 325 nm, all the emission peaks of these five samples are at around 440 nm. GCN had the strongest PL emission, while GCN/CNS showed the weakest value. The results suggest that the GCN/CNS has a higher separation rate of the photoinduced carriers than other samples [45, 46]. Based on the E_g , the valence band (VB) positions were then calculated to be 1.55, 1.33, 1.38, 1.26 and 1.33 V for GCN, GCN/CQD, GCN/rGO, GCN/CNS and GCN/CNT, accordingly. As a result, the genuine effect of band structures on photocatalytic efficacy encompass the photocatalytic potential can be addressed and the band structure diagrams are presented in Fig. 3. 5(D). The band gaps of nanocarbon modified GCN are narrower than that of GCN, which ensures a continuous supply of electrons converted and empowered a high production of photo excited electrons under visible-light irradiations, hence maintained a decent photocatalytic efficiency, which is discussed subsequently.

3. 4. 3. Photocatalytic activities of graphitic carbon nitride (GCN) and nanocarbon composites

The photocatalytic activities of the pristine GCN and nanocarbon modified GCN samples were evaluated by degradation of SCP in water under UV-visible light irradiations. It can be seen from Fig. 3. 6(A) that there is about 20% degradation via self-photolysis after 180 min, which means a good stability of SCP under UV-visible light irradiations for a long time. Besides, the as-obtained GCN, GCN/CQD, GCN/rGO, GCN/CNS and GCN/CNT samples adsorbed 3.5%, 6.7%, 10.3%, 15.8% and 6.0% SCP in 30 min in darkness (Fig. 3. 7(A)).

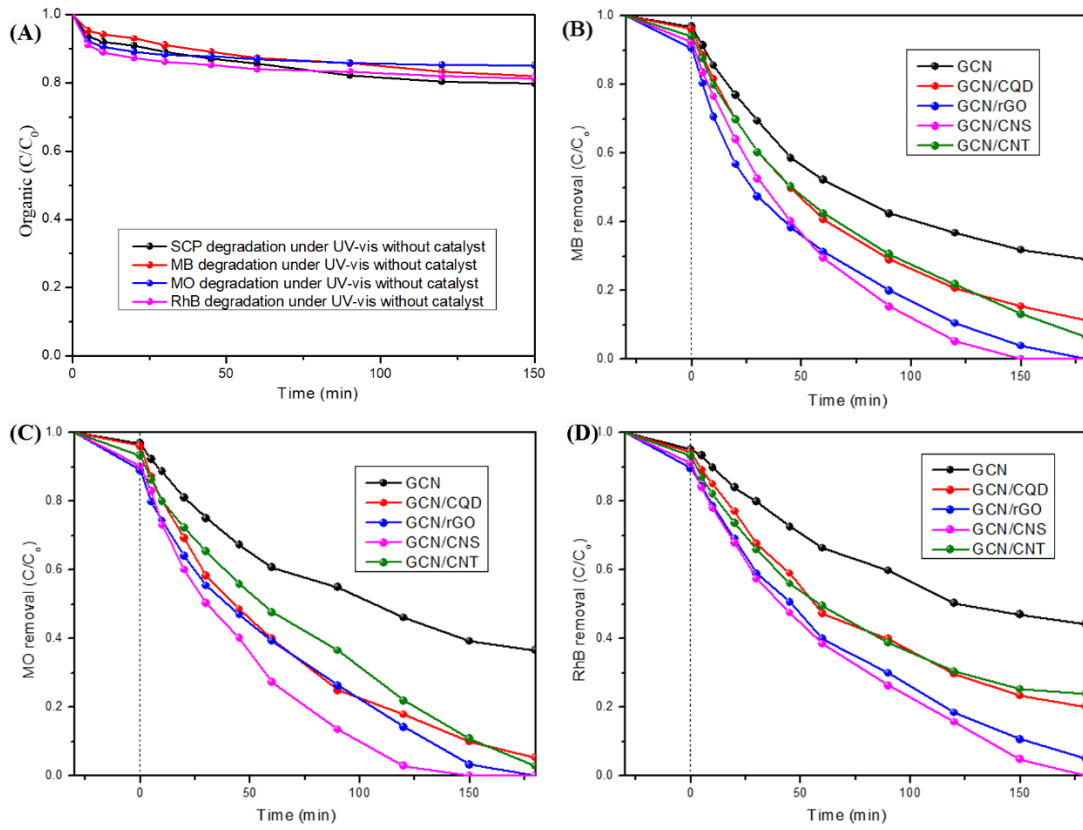


Fig. 3. 6. Control experiments of photolysis of organics under UV-visible light without catalyst (A); MB (B), MO (C) and RhB (D) removal profiles by the catalysts.

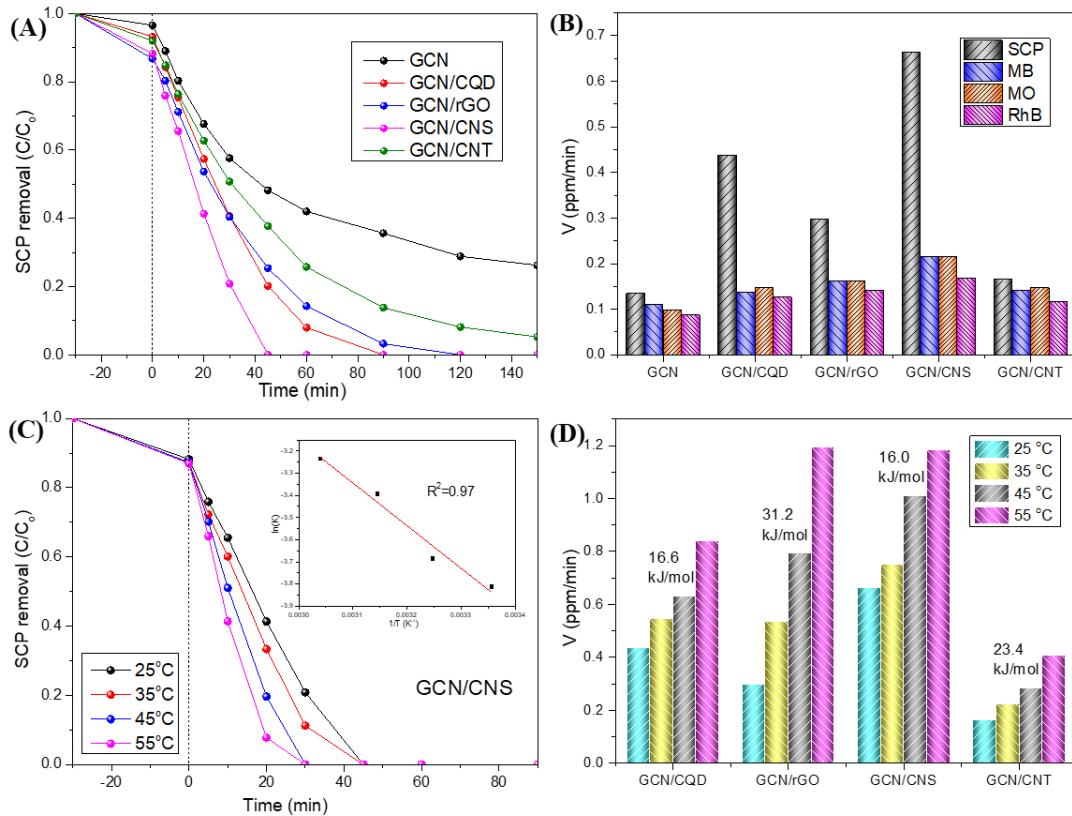


Fig. 3.7. (A) SCP removal profiles by GCN, GCN/CQD, GCN/rGO, GCN/CNS and GCN/CNT; (B) Comparison of the degradation rates of different organics by various photocatalysts; (C) Effects of reaction temperatures on SCP degradation and estimation of activation energy; (D) effect of reaction temperature on reaction rate and estimation of activation energy.

After the light was switched on, the photo-induced degradation efficiency was up to 74% in 150 min on GCN as the photocatalyst. For comparison, 95% SCP removal was observed on GCN/CNT, which confirms that the visible light response was enhanced by CNT's introduction. For an excellent photocatalytic efficiency of GCN/CNS composite, it took only 45 min for the complete removal of SCP, much quicker than that of GCN/CQD (90 min) and GCN/rGO (120 min) for the complete removal. It is hypothesized that some heterojunctions might be formed between CNS and GCN to play crucial roles in the transfer and separation of photogenerated carriers.

Table 3. 3. Kinetic parameters in organic degradation.

Organic	Catalyst	T (°C)	k (min ⁻¹)	v (ppm/min)	R ² of k	E _a (kJ/mol)	R ² of E _a
SCP	GCN	25	0.0045	0.135	0.83	—	—
	GCN/CQD	25	0.0146	0.438	0.98	16.6	0.98
		35	0.0182	0.546	0.98		
		45	0.021	0.63	0.98		
		55	0.028	0.84	0.99		
	GCN/rGO	25	0.0099	0.297	0.92	31.2	0.99
		35	0.0179	0.537	0.98		
		45	0.0264	0.792	0.98		
		55	0.0398	1.194	0.99		
	GCN/CNS	25	0.0221	0.663	0.99	16.0	0.97

		35	0.0251	0.753	0.99		
		45	0.0336	1.008	0.99		
		55	0.0394	1.182	0.99		
	GCN/CNT	25	0.0055	0.165	0.86	23.4	0.99
		35	0.0075	0.225	0.87		
		45	0.0095	0.285	0.87		
		55	0.0136	0.408	0.93		
MB	GCN	25	0.0037	0.111	0.89	—	—
	GCN/CQD	25	0.0046	0.138	0.89	—	—
	GCN/rGO	25	0.0054	0.162	0.89	—	—
	GCN/CNS	25	0.0072	0.216	0.94	—	—
	GCN/CNT	25	0.0047	0.141	0.93	—	—
MO	GCN	25	0.0033	0.099	0.93	—	—
	GCN/CQD	25	0.0049	0.147	0.91	—	—
	GCN/rGO	25	0.0054	0.162	0.96	—	—
	GCN/CNS	25	0.0072	0.216	0.94	—	—
	GCN/CNT	25	0.0049	0.147	0.97	—	—
RhB	GCN	25	0.0029	0.087	0.94	—	—
	GCN/CQD	25	0.0042	0.126	0.92	—	—
	GCN/rGO	25	0.0047	0.141	0.94	—	—
	GCN/CNS	25	0.0056	0.168	0.95	—	—
	GCN/CNT	25	0.0039	0.117	0.91	—	—

To further confirm the optimal photocatalysts, MB, MO and RhB were employed as the degradation targets in this study and the results are listed in Fig. 3. 6. Fig. 3. 6(A) shows the control photolysis experiments of MB, MO and RhB without a catalyst. As can be seen, these three dyes were hardly degraded by photolysis with UV–visible light. However, around 71% of MB was decomposed by pristine GCN after 180 min under

UV-vis irradiations. Meanwhile the removals of MB increased to 89%, 94% and 100% using GCN/CQD, GCN/CNT and GCN/rGO, respectively. Complete MB removal was achieved by GCN/CNS in 150 min (Fig. 3. 6(B)). Fig. 3. 6(C) shows that photodegradation efficiencies of MO in roughly 180 min are about 63%, 95%, 97% and 100% by GCN, GCN/CQD, GCN/CNT and GCN/rGO, respectively. Enhanced MO photodegradation was observed on GCN/CNS hybrids with complete degradation in 150 min. Fig. 3. 6(D) shows the effect of nanocarbon materials on photodegradation of RhB under UV-vis irradiations, and pristine GCN removed 56% of RhB only in 180 min. However, the photodegradation was substantially improved by introducing nanocarbon materials, with 80%, 95%, 100% and 77% removal efficiencies in 30 min by GCN/CQD, GCN/rGO, GCN/CNS and GCN/CNT, respectively. The first order kinetics (Eq (1)) was employed to evaluate the catalytic reaction rates (Table 3. 3).

$$\ln(C/C_0) = -kt \quad (1)$$

Where C_0 is the starting concentration of the organic pollutant and C is the concentration at the time (t), k is the first-order reaction rate constant. To compare more clearly and uprightly, the photodegradation rate constants of SCP, MB, MO and RhB by the five photocatalysts are provided in Fig. 3. 7(B). Based on the removal profiles, these five GCN based photocatalysts present better performance in SCP removal (0.135 min^{-1} for GCN, 0.438 min^{-1} for GCN/rGO, 0.663 min^{-1} for GCN/CNS and 0.165 min^{-1} for GCN/CNT) than degradation of the dyes. Not only for the SCP degradation, the GCN/CNS also demonstrated outstanding photocatalytic activities for the MB, MO and RhB degradation with reaction rates of 0.216 , 0.216 and 0.168 min^{-1} , respectively. The performances of the other photocatalysts in RhB removal under UV-visible light irradiations follow the order of GCN/rGO (0.141 min^{-1}) > GCN/CNT (0.141 min^{-1}) > GCN/CQD (0.126 min^{-1}) > GCN (0.087 min^{-1}). While, similar orders can be observed when the degraded targets become MB and MO: GCN/rGO (0.162 min^{-1}) > GCN/CNT (0.141 min^{-1}) > GCN/CQD (0.138 min^{-1}) > GCN (0.111 min^{-1}) for MB treatment and GCN/rGO (0.162 min^{-1}) > GCN/CNT (0.147 min^{-1}) = GCN/CQD (0.147 min^{-1}) > GCN

(0.099 min^{-1}) for MO treatment, respectively. The GCN/CNS exhibited better efficiency in degrading SCP than other dyes. The observation can be attributed to a combination of two factors. Firstly, as evidenced in Fig. 3. 5(A), SCP is more photosensitive than other dyes. Secondly, based on Fig. 3. 6 and Fig. 3. 7(A), we can see that GCN/CNS physically adsorbed 15.8 % SCP but $< 9 \%$ other dyes before starting the light irradiation. The amine groups contained in SCP molecules may interact strongly with the corresponding carboxyl groups of the catalyst through H-bonding. The intimate contact between the pollutant and catalyst will promote the degradation [47].

It can therefore be seen that GCN/CNS exhibited a much higher photocatalytic activity than the initial GCN and other nanocarbon modified GCN samples in all the degradation systems under UV-visible light irradiations, indicating that the intimate contact or interaction between CNS and GCN is crucial for the formation of a charge-separation heterojunction.

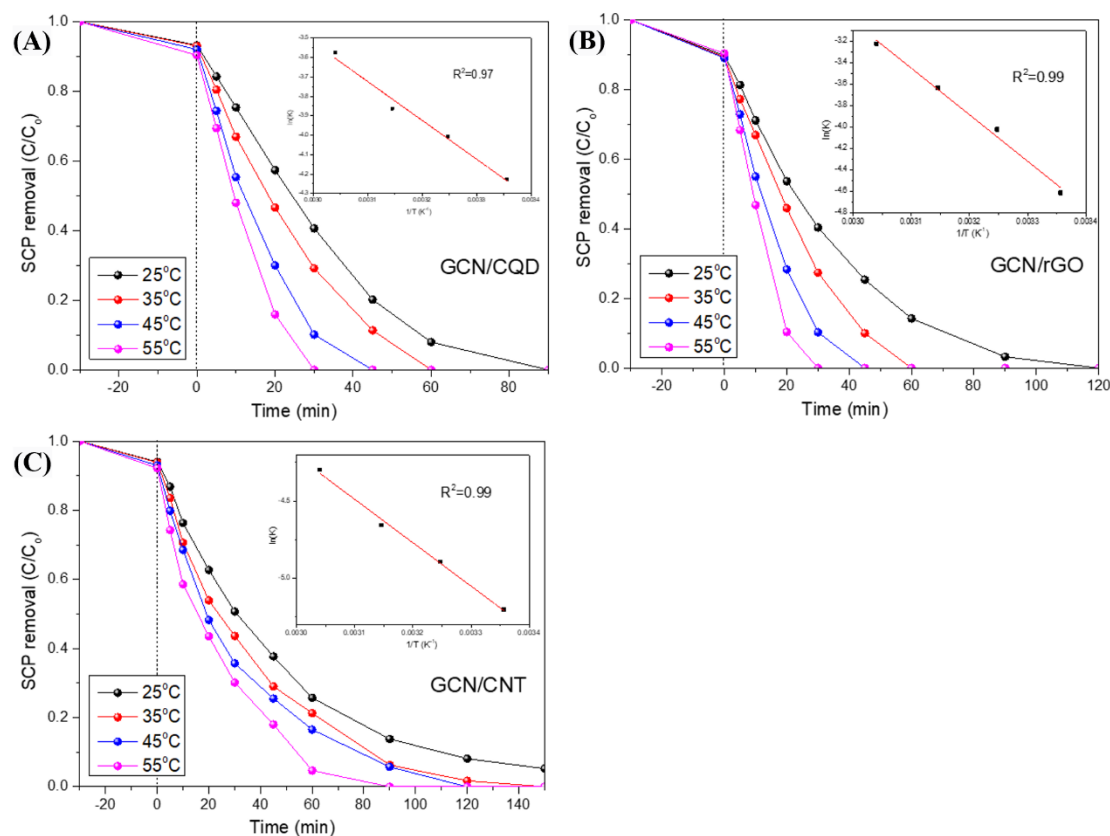


Fig. 3.8. Effect of reaction temperature on SCP degradation and estimation of activation energy for (A) GCN/CQD, (B) GCN/rGO, (C) GCN/CNT.

Fig. 3. 7(C) and Figs. 3. 8(A-C) reveal the effects of reaction temperatures on SCP degradation employing GCN/CNS, GCN/CQD, GCN/rGO and GCN/CNT as the photocatalysts, and the comparison of the degradation rates of the various photocatalysts are shown in Fig. 3. 7(D). It is a general trend that the degradation efficiencies are greatly impacted by reaction temperatures, and a higher temperature brings about better activities. According to the first-order kinetics, the reaction rate constants at the different temperatures are calculated and the relationship is found to follow the Arrhenius equation (Table 3. 3). The activation energies of GCN/CQD, GCN/rGO, GCN/CNS and GCN/CNT are calculated to be 16.6, 31.2, 16.0 and 23.4 kJ/mol, respectively. As observed, GCN/CNS presents the lowest activation energy than the others, which is easier for the photocatalytic reaction to take place.

The photoelectric properties are shown in Fig. 3. 9(A). The transient photocurrent during on-off cycles was measured at room temperature with the irradiation and darkness switching for every 20 seconds. GCN was able to produce a density of 0.45 μA photocurrent. GCN/CNS generated the highest photocurrent of 1.5 μA , due to the strong electron transfer from CNS into GCN, and that was stable in duration of 200 seconds. The photocurrent responses were 1.0, 0.8 and 0.7 μA for GCN/CQD, GCN/rGO and GCN/CNT, respectively, revealing that CNS contributes to enhancing the separation and transfer of photon-generated carriers, such as electrons and holes, producing a higher-strength photoelectric current than pristine GCN, consistent with the trends of their photocatalysis activity.

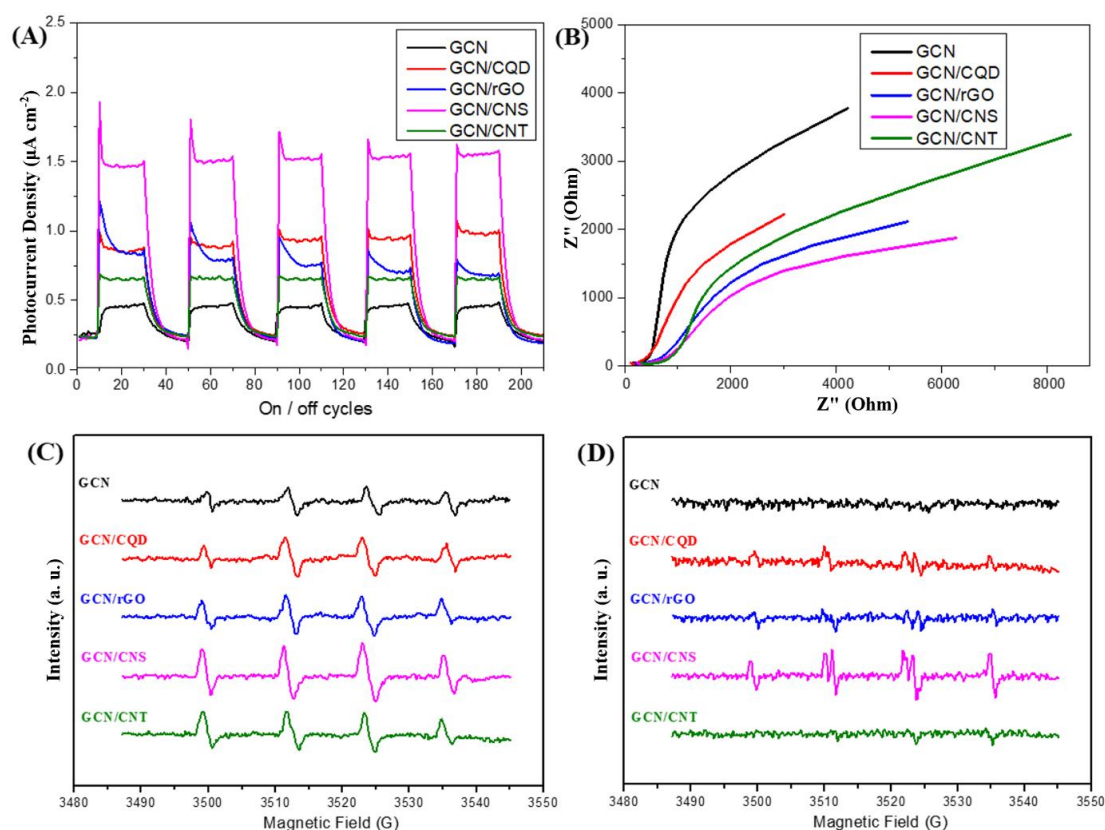


Fig. 3.9. (A) Transient photocurrent responses; (B) EIS investigations; EPR spectra for (C) DMPO –•OH radical species (with •O₂⁻ quenched by pBQ) and (D) DMPO–•O₂⁻ radical species (with •OH quenched by tBA).

EIS was performed to further verify the relationship between photoactivity and electrochemical properties [48]. In this study, we used a platinum foil as the counter electrode, Ag/AgCl as the reference electrode and 0.1M Na₂SO₄ solution as the electrolyte. EIS measurements were performed and recorded in a typical Nyquist diagram as shown in Fig. 3. 9(B). It was well known that the semicircle with a larger radius refers to a higher charge transfer resistance of the electrodes [49]. The charge transfer resistances of synthesized samples follow the order of GCN/CNS < GCN/rGO < GCN/CNT < GCN/CQD < GCN. Coupling with carbon materials lowered the EIS values than the pristine GCN due to the higher surface region and easier path for electrolyte ions to pass through, which successfully reduces the internal resistance and makes more contribution to the improvement of photocatalytic activity [50]. This result

is in general agreement with the enhancement of photocatalytic activity and the above PL results.

For further in-depth understanding of the photocatalytic reaction mechanism, electron paramagnetic resonance (EPR) study of the five samples was conducted using DMPO to trap radicals under full spectrum light illumination [51]. Two radical scavengers of tert-butanol (tBA) and p-benzoquinone (pBQ) were used to differentiate hydroxyl radicals ($\bullet\text{OH}$) and superoxide anions ($\bullet\text{O}_2^-$) [52]. As shown in Fig. 3. 9(C), obvious signals of $\bullet\text{OH}$ were observed on each sample, indicating that all of the carbon modified GCN could produce $\bullet\text{OH}$ during the photocatalytic reaction processes. From Fig. 3. 9(D), the characteristic signals of $\bullet\text{O}_2^-$ were easily observed when utilizing GCN/CNS as photocatalyst, while the signals were weaker on other catalysts. Combining with the degradation results, it is inferred that the $\bullet\text{OH}$ played a pivotal role in the photocatalytic degradation of SCP, while the generation of $\bullet\text{O}_2^-$ could further improve the photocatalytic ability.

Considering the band structure of these GCN based samples, $\bullet\text{O}_2^-$ radicals could be generated directly on the surface of these samples under visible light irradiations (-0.056 eV for $\text{O}_2/\bullet\text{O}_2^-$). The VB of these samples were lower than the electrode potentials of $\text{OH}^-/\bullet\text{OH}$ (1.99 eV) and $\text{H}_2\text{O}/\bullet\text{OH}$ (2.38 eV), therefore $\bullet\text{OH}$ could hardly be oxidized directly [53]. The $\bullet\text{OH}$ was derived from the further reaction of photogenerated electron with $\bullet\text{O}_2^-$ ($\bullet\text{O}_2^- \rightarrow \text{H}_2\text{O}_2 \rightarrow \bullet\text{OH}$) [54].

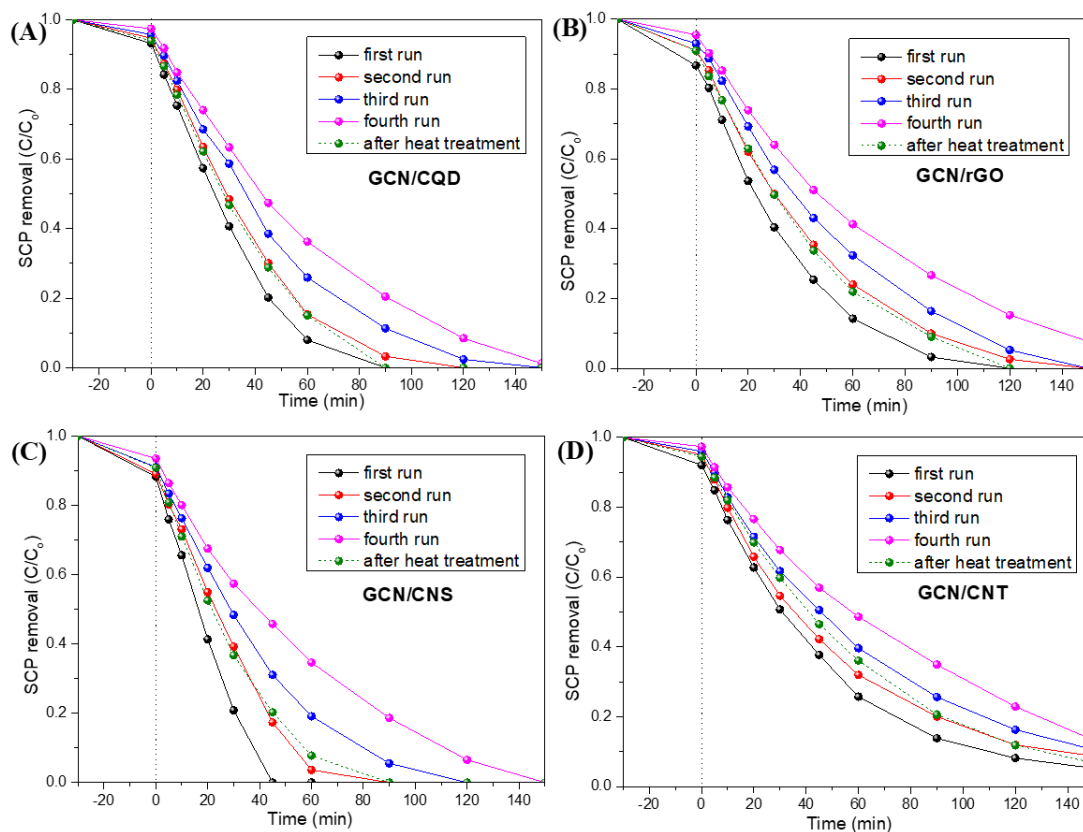


Fig. 3. 10. Stability studies with repeated uses of GCN/CQD (A), GCN/rGO (B), GCN/CNS (C) and GCN/CNT (D) in SCP removal.

Table 3. 4. Nitrogen sorption results of GCN/CNS after each reusability test

Catalyst	Reusability times	S_{BET} (m^2/g)	V_{pore} (cm^3/g)	Pore size (nm)
GCN/CNS	1 st run	32.33	0.272	21.4
	2 nd run	29.11	0.227	20.5
	3 rd run	26.79	0.213	18.9
	4 th run	23.40	0.198	18.5
	heat treatment	30.97	0.226	19.8

The stabilities of these nanocarbon modified GCN photocatalysts in SCP degradation were further evaluated (Fig. 3. 10). As can be seen, there are slight declines in degradation efficiency for GCN/CQD, GCN/rGO and GCN/CNT samples after four repeated runs, suggesting relatively good stabilities of those photocatalysts. Compared

to pristine GCN in the previous report, nanocarbon modification would improve the stability of GCN for SCP degradation [26]. Table 3. 4 shows that the specific surface area of GCN/CNS decreases from 34.8 to 23.4 m²/g after the four cycles of reaction while the pore volumes and average pore sizes have unobviously dropped, which would deactivate the catalysts. In terms of photocatalytic efficiency, the carbon catalysts are more favorable or superior to those conventional metal-based catalysts, despite that the stability needs to be improved.

3.5. Conclusions

To sum up, four typical nanocarbon materials with different morphologies were applied to modify GCN via the one-pot hydrothermal process and the composites demonstrated high photocatalytic activities in the degradation of various organics. The integration of all nanocarbon materials with the GCN would result in red shifts and stronger light absorption capabilities. In particular, the activity of GCN/CNS sample has been improved by a factor of 5 compared to the pure GCN. The outstanding activity can be attributed to the large number of active sites and the enhanced charge and mass transport abilities, owing to the optical property and chemical composition of GCN significantly modified by CNS. The electrochemical study reveals the critical roles of CNS in electrocatalysis of GCN for the increased electron and hole separation, which has been believed to increase the photocatalytic activity. Compared to other nanocarbon morphologies in nanotube, quantum dots and layered graphene oxides, the GCN composite with carbon nanospheres (CNS) gave the best performance in this particular application of organic photocatalytic degradation. This is probably due to the most favorably intimate contact or interaction between the GCN and the carbon nanospheres compared to others. Therefore, CNS modification of GCN provides a more feasible pathway for the development of highly efficient metal-free photocatalysts for more economic and environmental friendly solar energy applications.

References

1. Q. Liu, L. Zhou, J. Gao, S. Wang, L. Liu and S. Liu, Surface chemistry-dependent activity and comparative investigation on the enhanced photocatalytic performance of graphitic carbon nitride modified with various nanocarbons. *J. Colloid Interface Sci.*, 2020, 1(569), 12-21.
2. Q. Liu, X. Duan, H. Sun, Y. Wang, M. O. Tade and S. Wang, Size-Tailored Porous Spheres of Manganese Oxides for Catalytic Oxidation via Peroxymonosulfate Activation. *J. Phys. Chem. C*, 2016. 120(30), 16871-16878.
3. P. Sriprang, S. Wongnawa and O. Sirichote, Amorphous titanium dioxide as an adsorbent for dye polluted water and its recyclability. *J. Sol-Gel Sci. Technol.*, 2014. 71(1), 86-95.
4. G. Crini, Non-conventional low-cost adsorbents for dye removal: A review. *Bioresour. Technol.*, 2006. 97(9), 1061-1085.
5. H. Yan, J. Yang, G. Ma, G. Wu, X. Zong, Z. Lei, J. Shi and C. Li, Visible-light-driven hydrogen production with extremely high quantum efficiency on Pt–PdS/CdS photocatalyst. *J. Catal.*, 2009. 266(2), 165-168.
6. S. Le, T. Jiang, Y. Li, Q. Zhao, Y. Li, W. Fang and M. Gong, Highly efficient visible-light-driven mesoporous graphitic carbon nitride/ZnO nanocomposite photocatalysts. *Appl. Catal. B*, 2017. 200, 601-610.
7. V. Vaiano, O. Sacco, D. Sannino and P. Ciambelli, Nanostructured N-doped TiO₂ coated on glass spheres for the photocatalytic removal of organic dyes under UV or visible light irradiation. *Appl. Catal. B*, 2015. 170, 153-161.
8. V. Iliev, D. Tomova and L. Bilyarska, Promoting the oxidative removal rate of 2, 4-dichlorophenoxyacetic acid on gold-doped WO₃/TiO₂/reduced graphene oxide photocatalysts under UV light irradiation. *J. Photochem. Photobiol. A*, 2018. 351, 69-77.

9. H. Sun, G. Zhou, Y. Wang, A. Suvorova and S. Wang, A new metal-free carbon hybrid for enhanced photocatalysis. *ACS Appl. Mater. Interfaces*, 2014. 6(19), 16745-16754.
10. S. Liu, H. Sun, H. M. Ang, M. O. Tade and S. Wang, Integrated oxygen-doping and dye sensitization of graphitic carbon nitride for enhanced visible light photodegradation. *J. Colloid Interface Sci.*, 2016. 476, 193-199.
11. X.-H. Song, L. Feng, S.-L. Deng, S.-Y. Xie and L.-S. Zheng, Simultaneous Exfoliation and Modification of Graphitic Carbon Nitride Nanosheets. *Adv. Mater.*, 2017. 4(15), 1700339-1700347.
12. P. Tiong, H. O. Lintang, S. Endud and L. Yuliati, Improved interfacial charge transfer and visible light activity of reduced graphene oxide–graphitic carbon nitride photocatalysts. *RSC Adv.*, 2015. 5(114), 94029-94039.
13. L. Zhou, H. Zhang, H. Sun, S. Liu, M. O. Tade, S. Wang and W. Jin, Recent advances in non-metal modification of graphitic carbon nitride for photocatalysis: a historic review. *Catal. Sci. Technol.*, 2016. 6(19), 7002-7023.
14. L. Zhou, H. Zhang, X. Guo, H. Sun, S. Liu, M. O. Tade and S. Wang, Metal-free hybrids of graphitic carbon nitride and nanodiamonds for photoelectrochemical and photocatalytic applications. *J. Colloid Interface Sci.*, 2017. 493, 275-280.
15. Y.-X. Zhang, K. Li, Y.-X. Yu and W.-D. Zhang, Carbon nanotubes-modified graphitic carbon nitride photocatalysts with synergistic effect of nickel (II) sulfide and molybdenum (II) disulfide co-catalysts for more efficient H₂ evolution. *J. Colloid Interface Sci.*, 2018. 526, 374-383.
16. H. Li, R. Liu, W. Kong, J. Liu, Y. Liu, L. Zhou, X. Zhang, S.-T. Lee and Z. Kang, Carbon quantum dots with photo-generated proton property as efficient visible light controlled acid catalyst. *Nanoscale*, 2014. 6(2), 867-873.

17. Y. Guo, P. Yao, D. Zhu and C. Gu, A novel method for the development of a carbon quantum dot/carbon nitride hybrid photocatalyst that responds to infrared light irradiation. *J. Mater. Chem. A*, 2015. 3(25), 13189-13192.
18. K. Li, F.-Y. Su and W.-D. Zhang, Modification of g-C₃N₄ nanosheets by carbon quantum dots for highly efficient photocatalytic generation of hydrogen. *Appl. Surf. Sci.*, 2016. 375, 110-117.
19. Y.-X. Zhang and W.-D. Zhang, Ternary catalysts based on amino-functionalized carbon quantum dots, graphitic carbon nitride nanosheets and cobalt complex for efficient H₂ evolution under visible light irradiation. *Carbon*, 2019. 145, 488-500.
20. S. Hu, W. Zhang, J. Bai, G. Lu, L. Zhang and G. Wu, Construction of a 2D/2D g-C₃N₄/rGO hybrid heterojunction catalyst with outstanding charge separation ability and nitrogen photofixation performance via a surface protonation process. *RSC Adv.*, 2016. 6(31), 25695-25702.
21. H. Zhang, Y. Huang, S. Hu, Q. Huang, C. Wei, W. Zhang, W. Yang, P. Dong and A. Hao, Self-assembly of graphitic carbon nitride nanosheets–carbon nanotube composite for electrochemical simultaneous determination of catechol and hydroquinone. *Electrochim. Acta*, 2015. 176, 28-35.
22. H. Sun, G. Zhou, Y. Wang, A. Suvorova and S. Wang, A new metal-free carbon hybrid for enhanced photocatalysis. *ACS Appl. Mater. Interfaces*, 2014. 6(19), 16745-16754.
23. K. Li, X. Xie and W. D. Zhang, Photocatalysts based on g-C₃N₄-encapsulating carbon spheres with high visible light activity for photocatalytic hydrogen evolution. *Carbon*, 2016. 110, 356-366.
24. H. Li, R. Liu, Y. Liu, H. Huang, H. Yu, H. Ming, S. Lian, S. Lee and Z. Kang, Carbon quantum dots/Cu₂O composites with protruding nanostructures and their highly efficient (near) infrared photocatalytic behavior. *J. Mater. Chem.*, 2012. 22(34), 17470-17475.

25. W. S. Hummers and R. E. Offeman, Preparation of graphitic oxide. *J. Am. Chem. Soc.*, 1958. 80(6), 1334-1339.
26. S. Liu, J. Ke, H. Sun, J. Liu, M. O. Tade and S. Wang, Size dependence of uniformed carbon spheres in promoting graphitic carbon nitride toward enhanced photocatalysis. *Appl. Catal., B*, 2017. 204, 358-364.
27. H.-C. Hsu, I. Shown, H.-Y. Wei, Y.-C. Chang, H.-Y. Du, Y.-G. Lin, C.-A. Tseng, C.-H. Wang, L.-C. Chen, Y.-C. Lin and K.-H. Chen, Graphene oxide as a promising photocatalyst for CO₂ to methanol conversion. *Nanoscale*, 2012. 5(1), 262-268.
28. P. Qiu, J. Yao, H. Chen, F. Jiang and X. Xie, Enhanced visible-light photocatalytic decomposition of 2,4-dichlorophenoxyacetic acid over ZnIn₂S₄/g-C₃N₄ photocatalyst. *J. Hazard. Mater.*, 2016. 317, 158-168.
29. Y. Li, W. Ho, K. Lv, B. Zhu and S. C. Lee, Carbon vacancy-induced enhancement of the visible light-driven photocatalytic oxidation of NO over g-C₃N₄ nanosheets. *Appl. Surf. Sci.*, 2018. 430, 380-389.
30. T. Muhmood, M. A. Khan, M. Xia, W. Lei, F. Wang and Y. Ouyang, Enhanced photo-electrochemical, photo-degradation and charge separation ability of graphitic carbon nitride (g-C₃N₄) by self-type metal free heterojunction formation for antibiotic degradation. *J. Photochem. Photobiol., A*, 2017. 348, 118-124.
31. D. Jiang, L. Chen, J. Zhu, M. Chen, W. Shi and J. Xie, Novel pn heterojunction photocatalyst constructed by porous graphite-like C₃N₄ and nanostructured BiOI: facile synthesis and enhanced photocatalytic activity. *Dalton Trans.*, 2013. 42(44), 15726-15734.
32. C. Pu, J. Wan, E. Liu, Y. Yin, J. Li, Y. Ma, J. Fan and X. Hu, Two-dimensional porous architecture of protonated GCN and reduced graphene oxide via electrostatic self-assembly strategy for high photocatalytic hydrogen evolution under visible light. *Appl. Surf. Sci.*, 2017. 399, 139-150.

33. J. Chen, Y. Zhang, M. Zhang, B. Yao, Y. Li, L. Huang, C. Li, and G. Shi, Water-enhanced oxidation of graphite to graphene oxide with controlled species of oxygenated groups. *Chem. Sci.*, 2016. 7(3), 1874-1881.
34. S. Park, J. An, R. D. Piner, I. Jung, D. Yang, A. Velamakanni, S.T. Nguyen and R.S. Ruoff, Aqueous suspension and characterization of chemically modified graphene sheets. *Chem. Mater.*, 2008. 20(21), 6592-6594.
35. G. Rajender and P. K. Giri, Formation mechanism of graphene quantum dots and their edge state conversion probed by photoluminescence and Raman spectroscopy. *J. Mater. Chem. C*, 2016. 4(46), 10852-10865.
36. J.-P. Zou, L.-C. Wang, J. Luo, Y.-C. Nie, Q.-J. Xing, X.-B. Luo, H.-M. Du, S.-L. Luo and S. L. Suib, Synthesis and efficient visible light photocatalytic H₂ evolution of a metal-free g-C₃N₄/graphene quantum dots hybrid photocatalyst. *Appl. Catal. B*, 2016. 193, 103-109.
37. X. Duan, H. Sun, J. Kang, Y. Wang, S. Indrawirawan and S. Wang, Insights into heterogeneous catalysis of persulfate activation on dimensional-structured nanocarbons. *ACS Catal.*, 2015. 5(8), 4629-4636.
38. W.-J. Yin, H. Tang, S.-H. Wei, M.-M. Al-Jassim, J. Turner and Y. Yan, Band structure engineering of semiconductors for enhanced photoelectrochemical water splitting: the case of TiO₂. *Phys. Rev. B: Condens. Matter*, 2010. 82(4), 175-227.
39. H. Valdés and C. A. Zaror, Heterogeneous and homogeneous catalytic ozonation of benzothiazole promoted by activated carbon: kinetic approach. *Chemosphere*, 2006. 65(7), 1131-1136.
40. R. Qu, B. Xu, L. Meng, L. Wang and Z. Wang, Ozonation of indigo enhanced by carboxylated carbon nanotubes: performance optimization, degradation products, reaction mechanism and toxicity evaluation. *Water Res.*, 2015. 68, 316-327.

41. Y. Yuan, L. Zhang, J. Xing, M. I. B. Utama, X. Lu, K. Du, Y. Li, X. Hu, S. Wang, A. Genc, R. Dunin-Borkowski, J. Arbioldf and Q. Xiong, High-yield synthesis and optical properties of g-C₃N₄. *Nanoscale*, 2015. 7(29), 12343-12350.
42. M. S. Sam, H. O. Lintang, M. M. Sanagi , S. L. Lee and L. Yuliati, Mesoporous carbon nitride for adsorption and fluorescence sensor of N-nitrosopyrrolidine. *Spectrochim. Acta, Part A*, 2014. 124, 357-364.
43. J. Liu, J. Yan, H. Ji, Y. Xu, L. Huang , Y. Li, Y. Song, Q. Zhang, H. Xu and H. Li, Controlled synthesis of ordered mesoporous g-C₃N₄ with a confined space effect on its photocatalytic activity. *Mater. Sci. Semicond. Process.*, 2016. 46, 59-68.
44. J. T. B. T. Laboratories, I. M. Hill and N. Jersey, Absorption edge and internal electric fields in amorphous semiconductors. *Mater. Res. Bull.*, 1970. 5(8), 721-729.
45. V. N. Khabashesku, J. L. Zimmerman and J. L. Margrave, Powder Synthesis and Characterization of Amorphous Carbon Nitride. *Chem. Mater.*, 2000. 12(11), 3264-3270.
46. H. Sun and S. Wang, Research advances in the synthesis of nanocarbon-based photocatalysts and their applications for photocatalytic conversion of carbon dioxide to hydrocarbon fuels. *Energy Fuels*, 2014. 22-36.
47. X. Wei, Y. Wang, Y. Feng, X. Xie, X. Li and SenYang, Different adsorption-degradation behavior of methylene blue and Congo red in nanoceria/H₂ O₂ system under alkaline conditions. *Sci. Rep.*, 2019. 9(1), 1-10.
48. J. Kulkarni, R. Ravishankar, H. Nagabhushana, K. S. Anantharaju, R. B. Basavaraj, M. Sangeeta, H. P. Nagaswarupa and L. Renuka, Structural, Optical and Photocatalytic Properties of MgO/CuO *Nanocomposite* Prepared by a Solution Combustion Method. *Mater. Today: Process.*, 2017. 4(11), 11756-11763.
49. G. A. Snook, N. W. Duffy and A.G. Pandolfo, Evaluation of the effects of oxygen evolution on the capacity and cycle life of nickel hydroxide electrode materials. *J. Power Sources*, 2007. 168(2), 513-521.

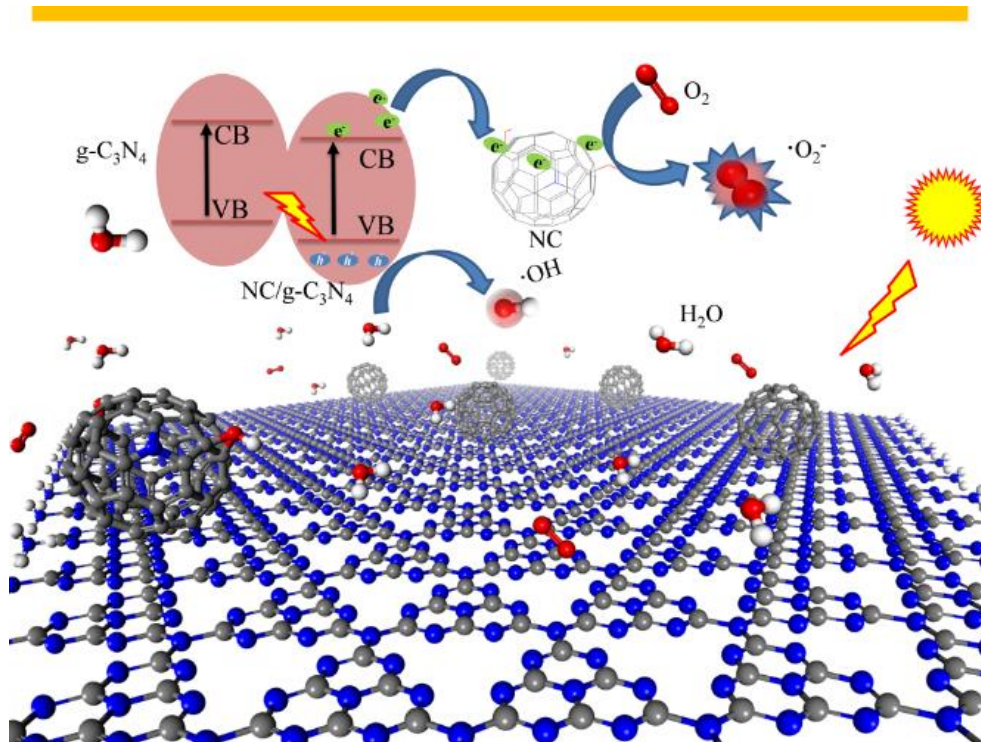
50. S. Maiti and B. Khatua, Electrochemical and electrical performances of cobalt chloride (CoCl_2) doped polyaniline (PANI)/graphene nanoplate (GNP) composite. RSC Adv., 2013. 3(31), 12874-12885.
51. Y. Bao and K. Chen, A novel Z-scheme visible light driven $\text{Cu}_2\text{O}/\text{Cu}/\text{g-C}_3\text{N}_4$ photocatalyst using metallic copper as a charge transfer mediator. Mol. Catal., 2017. 432, 187-195.
52. G. V. Buxton, C. L. Greenstock, w. P. Helman and A. B. Ross, Critical Review of rate constants for reactions of hydrated electrons, hydrogen atoms and hydroxyl radicals ($\cdot\text{OH}/\cdot\text{O}^-$ in Aqueous Solution. J. Phys. Chem. Ref. Data, 1988. 17(2), 513-886.
53. F. Dong, Z. Wang, Y. Li, W.-K. Ho and S. C. Lee, Immobilization of polymeric $\text{g-C}_3\text{N}_4$ on structured ceramic foam for efficient visible light photocatalytic air purification with real indoor illumination. Environ. Sci. Technol., 2014. 48(17), 10345.
54. C. Liu, F. Wang, J. Zhang, Ke Wang, Y. Qiu, Q. Liang and Z. Chen, Efficient Photoelectrochemical Water Splitting by $\text{g-C}_3\text{N}_4/\text{TiO}_2$ Nanotube Array Heterostructures. Nano-Micro Lett., 2018. 10(2), 1-13.

Every reasonable effort has been made to acknowledge the owners of copyright material. I would be pleased to hear from any copyright owner who has been omitted or incorrectly acknowledged.

Chapter 4. Nitrogen-doped Carbon Nanospheres Modified Graphitic Carbon Nitride for Enhanced Photocatalytic Performances

Abstract

Metals and metal oxides are widely used as photo/electro catalysts for environmental remediation. However, there are many issues related to these metal-based catalysts for practical applications, such as high cost and detrimental environmental impact due to metal leaching. Carbon-based catalysts have the potential to overcome these limitations. In this study, monodisperse nitrogen-doped carbon nanospheres (NC) were synthesized and loaded onto graphitic carbon nitride (g-C₃N₄, GCN) via a facile hydrothermal method for photocatalytic removal of sulfachloropyridazine (SCP). The prepared metal-free GCN-NC exhibited remarkably enhanced efficiency in SCP degradation. The nitrogen content in NC critically influences the physicochemical properties and performances of the resultant hybrids. The optimum nitrogen doping concentration was identified at 6.0 wt.%. The SCP removal rates can be improved by a factor of 4.7 and 3.2, under UV and visible lights, by the GCN-NC composite due to the enhanced charge mobility and visible light harvesting. The mechanism of the improved photocatalytic performance and band structure alternation were further investigated by density functional theory (DFT) calculations. The DFT results confirm the high capability of the GCN-NC hybrids to activate the electron-hole pairs by reducing the band-gap energy and efficiently separating electron/hole pairs. Superoxide and hydroxyl radicals are subsequently produced by the photogenerated electron/holes, leading to the efficient SCP removal.



The content of this chapter is published in *Nano-micro Lett.* 2020, 12, 24

4.1. Introduction

In recent decades, human being has enjoying the benefits of the technology development more than ever before in the human history. However, we are accompanied by sufferings from two issues: limited resources for raw materials and environmental pollution, one of which is water contamination. Some of the toxic pollutants are refractory to natural degradation, hence it is crucial to take stringent measures to battle the situation [1-3]. Sulfachloropyridazine (SCP) is one of the sulphonamides widely used against bacteria in aquaculture, animal husbandry and also in human medicine. The antibiotic exhibits high environmental mobility, presenting in both surface- and ground-waters. It is crucial to develop efficient technologies to remove recalcitrant SCP from polluted effluents. Currently, solar energy has been regarded as an abundant, clean and sustainable resource. Solar energy has attracted worldwide attention in many fields as an alternative supply to the conventional fossil fuel-based energy which produces the harmful emissions and impacts on human health and ecological systems [4]. For environmental remediation, metal-based catalysts like manganese [5], iron [6] or cobalt [7] have been applied, but they are costly and sometimes associated with metal leaching to secondary contamination [8]. Therefore metal-free catalyst materials have been highly recommended as “green” photo- or electro-catalysts [3, 9]. It has been reported that carbon materials as metal-free sustainable catalysts, such as graphene [10], graphene oxide [1, 10], carbon quantum dots [11], carbon nanotubes [12], and carbon nanospheres [9], can effectively promote photocatalytic reactions.

As a fascinating conjugated polymer, g-C₃N₄ (GCN) has become a new research hotspot and drawn broad interdisciplinary attention in solar energy conversion because of the excellent stability to photocorrosion and chemical corrosion, exceptionally high thermodynamic stability, nontoxicity, and low band-gap [13]. The polymer is composed of carbon and nitrogen, both of which are earth-abundant elements. Meanwhile

subsequent studies have shown that GCN based photocatalysts are effective for various applications, such as contaminant decompositions [14], hydrogen evolution reactions (HER) [15-17], oxygen evolution reactions (OER) [18], CO₂ reduction [19], bioimaging and electricity generation. Yet the low electrical conduction of the pristine GCN and the rapid photo-electron depletion cause the undesirable photon harvesting [20]. A variety of protocols involving heteroatom doping [21, 22], morphology modification [3, 23], hybrid copolymerization [24, 25], exfoliation [26] and co-catalysts have been employed to overcome these barriers and enhance the photocatalytic activity.

Among these methods, the modification by a carbon material [27] has become a hot focus, because of their potentials for enlarged specific area, good electronic conductivity and excellent rate of electron transfer [28-30]. In particular, our group has reported that size-tailored, uniformed carbon spheres can promote GCN toward enhanced photocatalysis [31]. Meanwhile, non-metal doping is demonstrated as an effective approach since the electronic structure and band gap would be changed dramatically via heteroatom doping [16, 32, 33]. Nitrogen doped carbonaceous nanomaterials are found to be able to expedite the migration of photoinduced electron-hole pairs and promote the generation of active sites during the photocatalytic reaction by forming delocalized p bonds [34-38].

Herein, we integrate uniform nitrogen doped carbon nanospheres (NC) with GCN to form NC/GCN composites via a one-step hydrothermal process. The mechanism of the enhancement of NC/GCN in terms of optical and electronic properties has been explored. We also employed density functional theory (DFT) calculations [39] to investigate the GCN band gap energy (E_g) variation with the introduction of carbon nanosphere or N-doping. This work provides a facile way to modulate the intrinsic electronic and band structure of GCN, and would lead to a simple and effective approach to synthesize an efficient NC/GCN photocatalyst via N doping.

4.2. Experimental

4.2.1 Materials

Melamine powder ($\geq 99.9\%$), resorcinol ($\geq 99.0\%$), formaldehyde (37% solution), 3-aminophenol ($\geq 99\%$), 4-amino-3-nitrophenol ($\geq 99\%$), aqueous ammonia (25% solution) and ethanol ($\geq 99.9\%$) were provided by Sigma-Aldrich and used as received without any further purification.

4.2.2 Synthesis of graphitic carbon nitride (GCN)

A conventional condensation method was employed to prepare carbon nitride utilizing melamine as the precursor. In a typical process, 10 g of melamine and 10 mL of methanol were added into a 20 mL crucible and well mixed by stirring. The crucible with a cover was then placed in an oven at 60 °C for 24 h to remove the methanol. Followed by transferring into a muffle furnace, the crucible was firstly heated up to 400 °C at a heating rate of 5 °C/min and kept at this temperature for 2 h. Subsequently, the furnace was heated to 520 °C at a rate of 10 °C/min and kept this temperature for another 2 h. When it was cooled down to room temperature, the resulting yellow powder was ground and denoted as GCN for further use.

4.2.3 Synthesis of carbon nanospheres (C) and nitrogen-doped carbon nanospheres (NC)

Monodisperse nitrogen-doped carbon nanospheres with diameter around 400 nm were synthesized. In a typical run, 0.5 mL of ammonia aqueous solution ($\text{NH}_3\text{H}_2\text{O}$) was added into 100 mL ethanol solution (volume ratio of ethanol and distilled water was 2:5) at room temperature. Then 2.0 g of 3-aminophenol was added into the solution under stirring for 0.5 h. Afterwards, 2.8 mL of 37 wt.% formaldehyde was dropwise-added continuously and kept stirring for 24 h. The obtained mixture was heated in an

oven at 100 °C for 24 h. The carbonation process was completed in a tube furnace using a rate of 1 °C /min up to 350 °C under N₂ flowing and dwelling for 2 h. After this, the temperature was increased to 700 °C at a rate of 1 °C/min and kept for 4 h to obtain the black powder and labelled as NC (5.4). As shown in Table 1, the nitrogen content of this sample was 5.4% by elemental analysis. During the preparation of NC, the volume proportion of ethanol and water was changed to 1:6, and a NC sample with nitrogen content of 6.0 wt% was obtained and denoted as NC (6.0). Similarly, NC (11.9) was synthesized by changing 3-aminophenol to 4-amino-3-nitrophenol. Control carbon nanospheres with a similar size were prepared by the method reported by Liu *et al.* [7] and labelled as C.

Table 4.1 Elemental analysis (weight percentage) of the nitrogen-doped carbon nanospheres

Sample	C%	N%	H%	O%
GCN	41.18	58.82	-	-
C	83.92	-	-	16.08
NC(5.4)	77.18	5.43	1.71	15.68
NC(6.0)	76.74	6.02	1.70	15.54
NC(11.9)	72.45	11.90	1.52	14.13

4.2.4 Preparation of GCN-NC and GCN-C

The GCN-NC and GCN-C hybrid photocatalysts were synthesized by a hydrothermal treatment using the prepared graphitic carbon nitride and nitrogen-doped carbon nanospheres as the precursors. Firstly, 0.05 g of NC or C spheres together with 0.95 g of pure GCN were put into 50 mL of water and stirred for 3 h with subsequent ultrasonication for 4 h at room temperature to generate well mixed suspensions. Secondly, the suspension was transferred into the 100 mL Teflon-lined autoclaves

which were then heated at 150 °C for 12 h. The autoclaves were cooled down to room temperature, and the obtained solids were washed thoroughly with ethanol and deionized water. After drying at 80 °C overnight, the obtained samples were denoted as GCN-NC(5.4), GCN-NC(6.0), GCN-NC(11.9) and GCN-C, respectively.

4.2.5 Characterizations

The crystal structure of the prepared samples was investigated by X-ray diffraction (D/Max-2500, Rigaku Corp) with a Cu K α radiation ($\lambda = 1.5406$ Å) at a scan rate of 0.05 °/s. The Brunauere-Emmette-Teller (BET) surface areas and the pore size distributions of the samples were measured by an automated gas adsorption–desorption analyzer (TriStar II Plus, Micromeritics, USA). Field emission scanning electron microscopy (FE-SEM) images of the samples were taken on Zeiss Neon 40EsB to analyze the morphology, size and textural properties of the as-prepared samples. The functional groups of the samples were evaluated by a Perkin-Elmer Fourier transform infrared spectroscopy (FTIR)-100 with a MIR detector. The surface chemical states were obtained by an X-ray photoelectron spectrometer on a Thermo Escalab 250 with an Al K α X-ray radiation source. The light absorption properties of photocatalysts were collected on a UV–visible diffuse reflectance spectra (DRS) spectrophotometer (JASCO V670) with an Ø60 mm integrating sphere and BaSO₄ as a reference material. Photoluminescence (PL) spectra were measured using a Hitachi F-4500 fluorescence spectrophotometer at room temperature. Electron paramagnetic resonance (EPR) experiments were performed on a Bruker EMX plus spectrometer (Germany) to analyze the generation of active radicals during the photocatalytic reactions. Electrochemical experiments were conducted on a Zennium electrochemical workstation in a conventional three-electrode cell with 0.2 M Na₂SO₄ solution as electrolyte, Hg/Hg₂Cl₂ as the reference electrode, and a platinum wire as the auxiliary electrode. Four on-off cycles were performed by turning on/off light for 30 s. Electrochemical impedance spectroscopy (EIS) was obtained under an open-circuited potential with signal

amplitude of 5 mV and frequency ranges from 10^6 to 10^{-1} Hz.

4.2.6 Photocatalytic activity testing

Photodegradation tests were carried out in a conical flask containing 200 mL (30 mg/L) SCP solution at 25 °C under CEL-LAX Xe lamp irradiations (UV cut-off filter < 400 nm and visible light cut-off filter 400–700 nm). The picture of the photocatalysis setup is shown in Fig. S3. The reaction system was placed 30 cm away from the light source. Firstly, 100 mg photocatalyst was put into SCP solution, which was positioned in a double-jacket cylindrical reactor with water cycling and constantly stirred at 400 rpm for 30 min to obtain the adsorption–desorption equilibrium. The water cycling was connected with a temperature controller. After that the photocatalytic degradation was triggered by switching on the light source. At regular intervals, 1 mL sample aliquot was withdrawn and passed through a 5 mL syringe filter unit (0.45 μ m pore) for analysis by high performance liquid chromatography (HPLC). The concentration was analyzed using the HPLC with an UV detector at wavelength of 270 nm. In the multi-cycle run experiment, the photocatalytic performance of composite catalyst is proceed continuously without recovery.

4.2.7 DFT calculations

The core electrons were treated by the ultra-soft pseudopotential, and the exchange and correlation effects were described by the Peidew-Burke-Ernzerhof (PBE) within generalized gradient approximation (GGA) [40]. In order to accurately describe the nonbonding van der Waals interaction along c-axis, the DFT+D method within the TS scheme was used in all calculations [41].

4.3 Results and Discussion

4.3.1 Physiochemical property of pre-pared samples

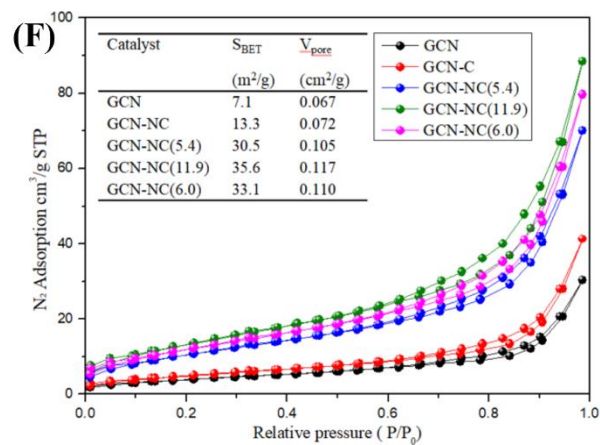
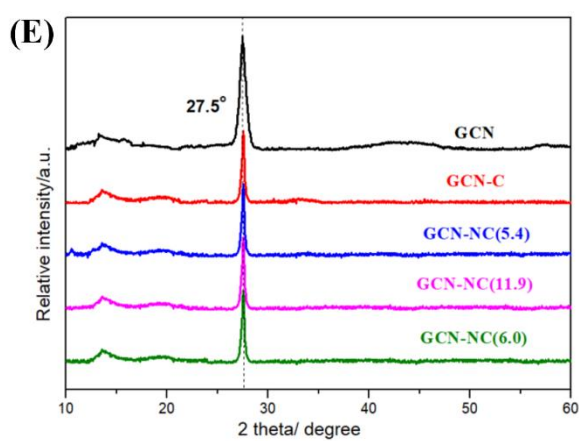
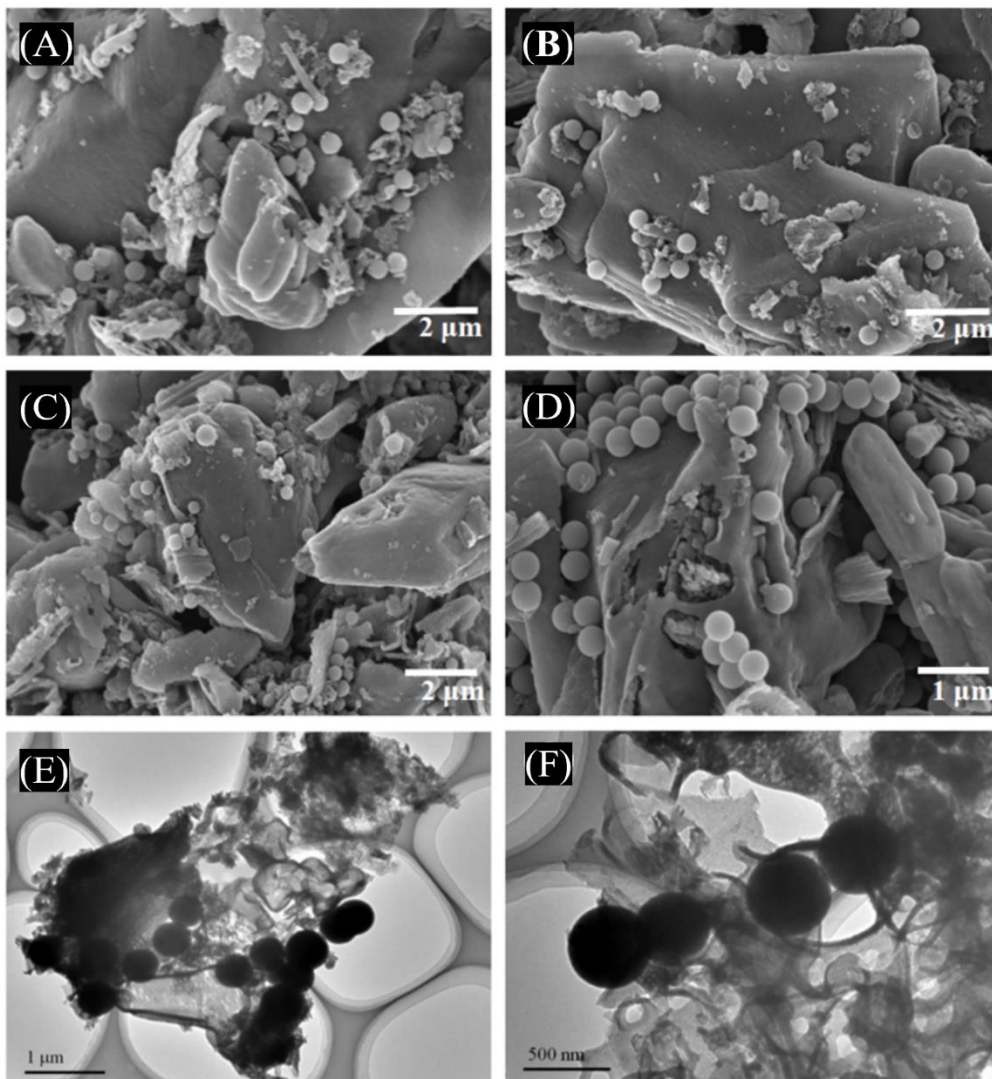


Fig. 4.1. (A) SEM images of GCN-C, (B) GCN-NC(5.4), (C) GCN-NC(11.9) and (D)GCN-NC(6.0). (E, F)TEM images of GCN-NC(6.0). (G) XRD patterns. (H) N₂ adsorption–desorption isotherms (f, inset: the textural properties) of samples

SEM images reveal the morphologies of the four GCN based composites. As presented in Fig. 4. 1(A-D), the GCN base shows a typical lamellar morphology, and 5 wt.% nitrogen-doped carbon nanospheres are closely attached onto the surface of layered GCN homogeneously. NC spheres with uniform diameters around 400 nm are found in GCN-NC(5.4), GCN-NC(11.9) and GCN-NC(6.0) composites (Fig. 4. 1(B-D)). From TEM images (Fig. 4. 1(E.F)), we can see these carbon nanospheres could be immobilized onto GCN via hydrothermal method, and the size of carbon sphere was 400 nm, which is suitable size to form strong interaction with GCN as observed previously [31]. X-ray diffraction (XRD) analysis (Fig. 1g) was performed to investigate the phase structure of the pristine GCN and hybrid GCN composite samples. The pristine GCN sample exhibits two characteristic reflections at 13.1° and 27.6 ° corresponding to the diffraction planes of (002) and (100), respectively [12]. The two peaks were found to be in good agreement with reported results, illustrating the successful synthesis of GCN with interplanar stacking fused aromatic rings and in-planar structure of triazine units. The main diffraction intensities of the GCN-NC composites are not substantially changed with the increase of nitrogen content in NC. It can be seen from Fig. 4. 2 that the FTIR spectra of pure GCN and carbon sphere loaded GCN composites show no noticeable difference. Peaks in the region of 3000-3500 cm⁻¹ originate from the adsorption of H₂O and CO₂ in the air. Several strong bands from 1200 to 1700 cm⁻¹ are found in the samples and the peaks at 1570 and 1630 cm⁻¹ were corresponding to the C=N stretching [42]. The detection of characteristic peaks of the GCN indicates that the GCN was successfully formed via thermal polymerization. N₂ adsorption and desorption isotherms of pristine GCN and GCN based composites were elucidated in Fig. 1h, which mirrors a type-IV adsorption behavior. The hysteresis

loops are H3 type with a mesoporous structure. GCN-NC(11.9) exhibited the largest surface area and pore volume, as illustrated in the inset table. The BET surface area of GNC-NC(6.0) was almost 5 times higher than GCN (33.1 vs 7.1 m²/g), thus GNC-NC(6.0) can provide more active sites to promote the adsorption of reactant, favourable for catalytic reaction [43].

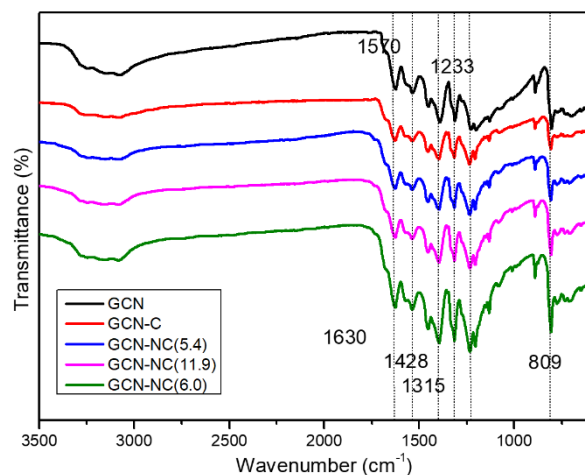


Fig. 4. 2 FTIR spectra of all GCN-based photocatalysts

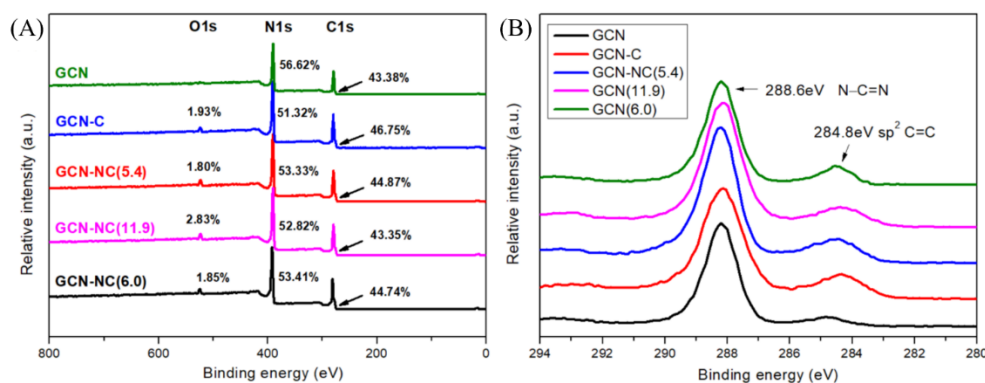


Fig. 4. 3 (A) XPS full survey and (B) C 1s spectra of GCN, GCN-C, GCN-NC(5.4), GCN-NC(11.9) and GCN-NC(6.0)

The chemical composition of GCN-NC nanocomposites was further investigated by X-ray photoelectron spectroscopy (XPS) in the region from 0 to 800 eV. The full survey shows two typical peaks for GCN with the corresponding content of 56.62% and 43.38% for N1s and C1s (Fig. 4. 3(A)), respectively. The surface oxygen contents of the

compounds are relatively low from 1.80% to 2.83%, possibly stemmed from the partial oxidation by O₂ and H₂O during the hydrothermal process. The high resolution narrow XPS scan spectra show two overlapping C1s peaks corresponding to the sp² bonded carbon (C-C/C=C) and the carbon adjacent with three N atoms (C-C=N) (Fig. 4. 3(B)) [44]. There was a small peak of sp² bonded carbon in pristine GCN since it is common to have adsorbed graphitic or amorphous carbon on the surface. However, this peak was stronger when carbon nanospheres loaded on GCN and the density of which decreased with the nitrogen content in carbon nanospheres. The position shift of C1s peak in these samples also implies the interaction between GCN and carbon nanosphere. Based on peak deconvolution, the ratio of N1s spectrum in the composite is described in Fig. 4. 4(A-E) and the relative amount of different nitrogen groups is summarized in Table 4.2. The N1s XPS spectrum is deconvoluted to four peaks. The one at 398.6 eV could be assigned to the sp² hybridized N bonded with two carbon atoms (C-N=C) and the dominant nitrogen species in the GCN with tris-triazine structure with the carbon. Spectrum at 399.5 eV can be assigned to the tertiary N (N bonded with three carbon atoms, N-(C)₃). The other two peaks at 400.8 eV and 397.7 eV correspond with the amino groups (C-NH) and N-graphene.

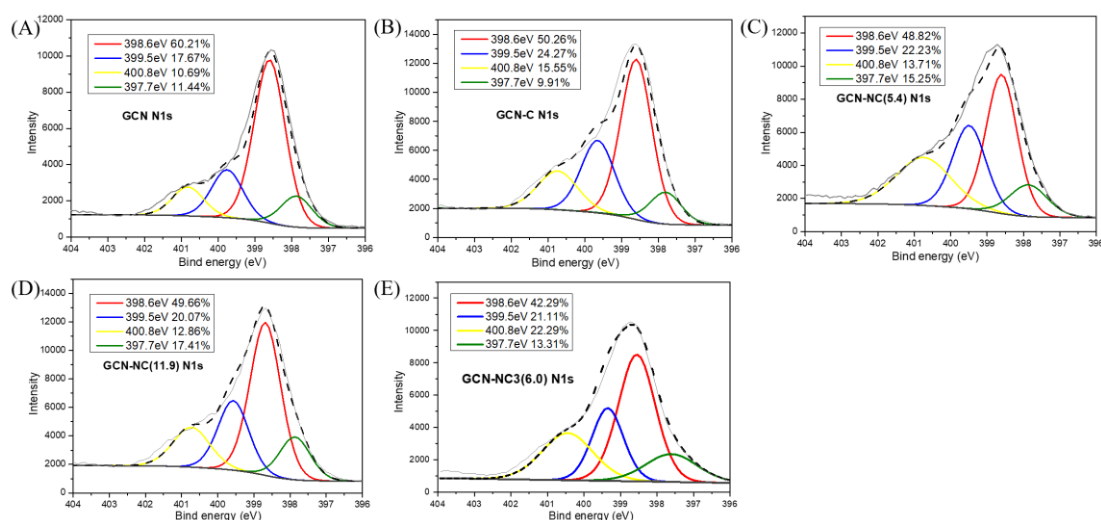


Fig. 4. 4. N1 XPS spectra of GCN(A), GCN-C(B), GCN-NC(5.4) (C), GCN-NC(11.9) (D) and GCN-NC(6.0) (E)

Table 4. 2. Total content and relative amount of different nitrogen groups on the surface of the catalysts

Sample	N content on the surface (at.%)	C-N=C	N-(C) ₃	C-NH	N-graphene
GCN	56.62	60.21	17.67	10.69	11.44
GCN-C	51.32	50.26	24.27	15.55	9.91
GCN-NC(5.4)	53.33	48.82	22.23	13.71	15.25
GCN-NC(11.9)	52.82	49.66	20.07	12.86	17.41
GCN-NC(6.0)	53.41	42.29	21.11	22.29	13.31

4.3.2 Photocatalytic property of pre-pared samples

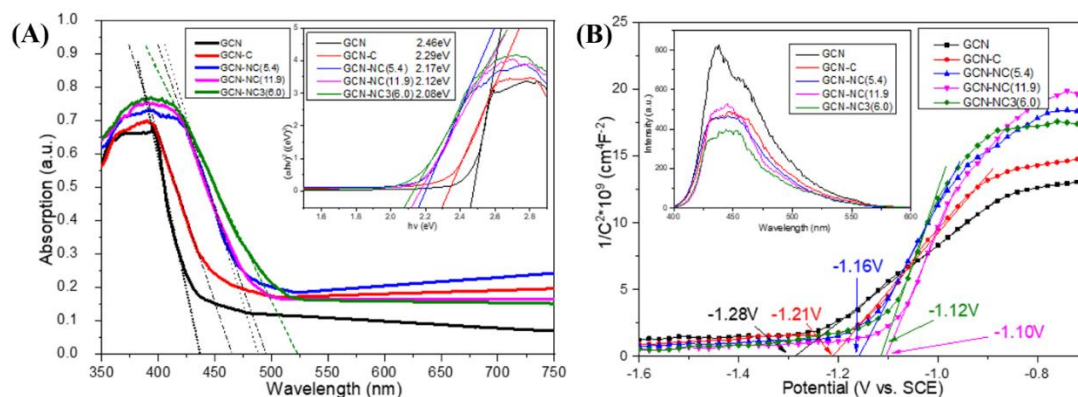


Fig. 4. 5. (A) UV-vis diffuse reflectance absorption and (B) Mott-Schottky of GCN and NC loaded GCN. The inset in (A) shows plots of $(\alpha h\nu)^2$ vs. photon energy ($h\nu$) for the band gap energy; the inset in (B) shows the photoluminescence spectra of the samples

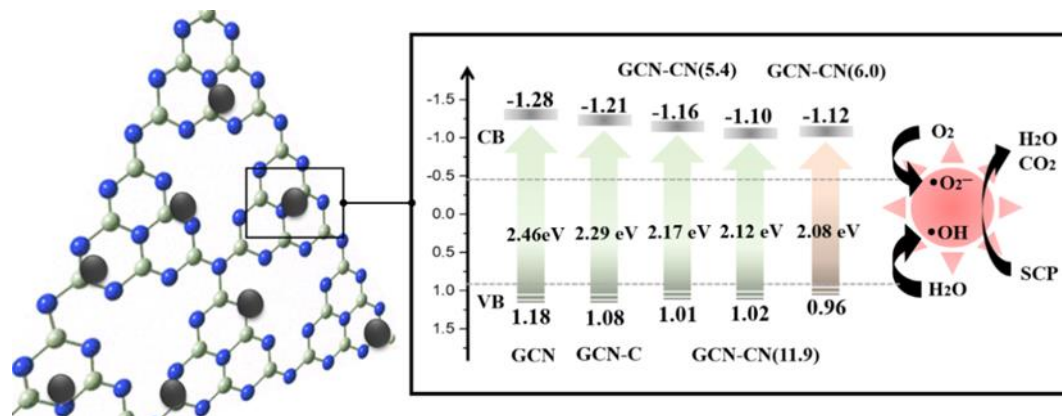
In Fig. 4. 5(A), the optical absorption abilities of pristine GCN and NC modified GCN samples were analyzed using UV-vis absorption spectroscopy. The GCN sample shows a typical feature of photosensitive semiconductor with an intrinsic characteristic absorption peak at 435 nm, corresponding to a band gap energy of 2.46 eV for photo-

excited electron, which is calculated based on the Kubelka–Munk formula as shown in the inset of Fig. 4. 5(A). Such observation is attributed to the lone pair electrons of nitrogen atom in valence band jumping into the π bonding electronic conduction band. The red-shift derived from hybridization can be observed, the absorption thresholds of GCN-C, GCN-NC(5.4), GCN-NC(11.9) and GCN-NC(6.0) were 463, 487, 491 and 520 nm, respectively, and the band gap energies were then evaluated to be 2.29, 2.17, 2.12 and 2.08 eV, respectively, which indeed reflect the changes at the interface with the integration of carbon spheres. Compared with GCN, carbon sphere and nitrogen doped carbon sphere have better visible light adsorption. Therefore, the absorptive capability of all composite materials was improved in the entire visible light region compared to pure GCN, especially for GCN-NC(6.0). The electrochemical Mott–Schottky plots were acquired to determine the energy levels, which features a typical n-type semiconductor in Fig. 4. 5(B). The conduction band potentials (CB) of GCN, GCN-C, GCN-NC(5.4), GCN-NC(11.9) and GCN-NC(6.0) were estimated to be -1.28, -1.21, -1.16, -1.10 and -1.12 eV, respectively. Accordingly, the valence band positions (VB) were then estimated according to Eq. (1):

$$E_g = E_{VC} - E_{VB} \quad (1)$$

The band structures of the samples are compared in Scheme 4.1. It can be seen that the introduction of NC onto GCN resulted in a negatively shift of VB position. The photodegradation efficiency can be partially determined by the separation rate of the photoinduced carriers on the composite materials. The accelerated charge carrier transfer of bare GCN, GCN-C, GCN-NC(5.4), GCN-NC(11.9) and GCN-NC(6.0) were exhibited through the PL-emission (inset in Fig. 4. 5(B)) under 320 nm exciting radiations. From 400 to 550 nm, the single luminescence peak of GCN was stronger than the hybrid photocatalysts, indicating that the composite structure provided a synergistic effect for GCN to separate the photoexcited carriers from the valence band. In particular, the recombination rate of photoinduced charges of GCN-NC(6.0) decreases more significantly, whereas the electron-hole recombination of GCN-C is

slightly higher. In addition, when the exciting light irradiated on the GCN-NC composites, the PL spectrum has a slight dislocation to 450 nm compared with that of the pure GCN sample at 440 nm, which might further signal the interaction between GCN and NC.



Scheme. 4.1. Proposed mechanism for photocatalytic process



Fig. 4. 6. photocatalysis setup

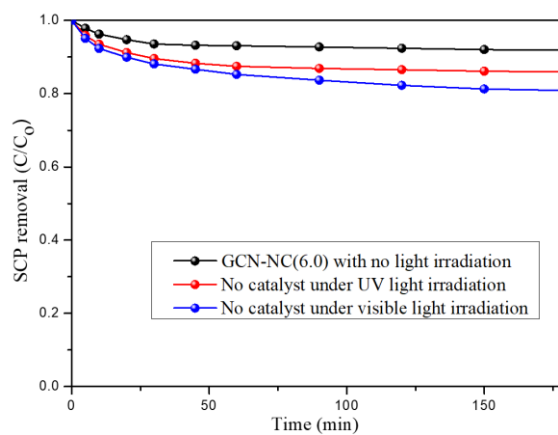


Fig. 4. 7. Control experiments

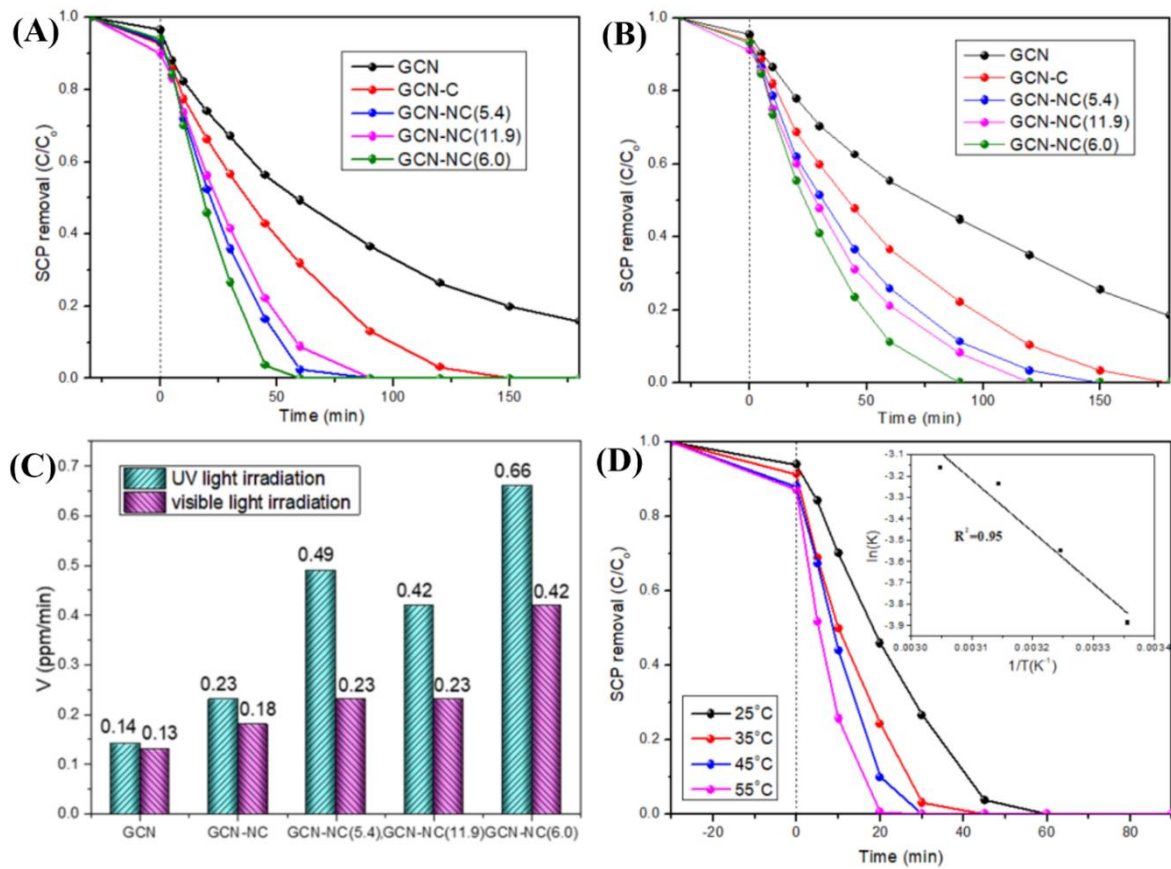


Fig. 4. 8. (A) Photocatalytic degradation of SCP over GCN, GCN-C, GCN-NC(5.4), GCN-NC(11.9) and GCN-NC(6.0) under UV light irradiation and (B) under visible light irradiation (C) Comparison of the degradation rate constants of GCN, GCN-C, GCN-NC(5.4), GCN-NC(11.9) and GCN-NC(6.0) photocatalysts under UV and visible light irradiations (D) the effect of temperature on degradation over GCN-NC(6.0)

The adsorption and photodegradation of SCP were carried out to evaluate the remediation performance of the prepared samples. Fig. 4. 7 shows control experiments of SCP adsorption on GCN-NC(6.0) and photolysis of SCP without catalyst. Only 8.2% of SCP were removed due to adsorption on GCN-NC(6.0), and SCP could hardly be degraded under both UV and visible light without a catalyst. The photocatalytic degradation results under UV light irradiations are shown in Fig. 4. 8(A). It is observed

that the composite photocatalysts had a higher adsorption rate than GCN in dark. GCN-NC(11.9) showed the best adsorption, which might be due to the largest specific surface area as revealed by BET analysis. As can be seen, SCP degradation reached 84% within 180 min by employing GCN, while the degradation efficiency of GCN-C was up to 100% in 150 min. GCN-NC(5.4) and GCN-NC(11.9) achieved complete degradation in 90 min. All of SCP was degraded by GCN-NC(6.0) within 60 min, manifesting that the hybrid photocatalysts can provide the best performance. The reaction rate constants of GCN-NC(6.0) was calculated to be 0.0205 min^{-1} , 4.36 times higher than GCN (0.0047 min^{-1}). The reaction rate constants of GCN-C, GCN-NC(5.4) and GCN-NC(11.9) were 0.0076 , 0.0154 and $0.0139 \text{ mg min}^{-1}$, respectively, under UV light irradiation (Fig. 4. 8(C)) based on the following pseudo-first-order kinetics.

$$\ln(C_0/C) = -kt \quad (2)$$

where C_0 is the concentration of the pollutant at the beginning of the reaction, C is the pollutant concentration at the time (t), k is the reaction rate constant. The calculated values of k and R^2 are listed in Table. S1. It is found in Fig. 4. 8(B) and Table 4.3 that the photocatalysts demonstrated a similar trend under visible light irradiations. GCN-NC(6.0) showed the highest photodegradation efficiency with complete SCP removal in 90 min, favorably to GCN-NC(11.9), GCN-NC(5.4) and GCN-C of 120, 150 and 180 min, respectively. While the pristine GCN exhibited a poor activity with 18% of SCP remained after 180 min. And the degradation rates were also fitted by the first order kinetics. GCN-NC(6.0) presented the best photodegradation with the reaction rate constants of 0.0139 min^{-1} , which is about 3.3 times higher than GCN (0.0042 min^{-1}). The reaction rate constants of GCN-C, GCN-NC(5.4) and GCN-NC(11.9) were 0.0061 , 0.0077 and 0.0078 min^{-1} , respectively. The observed less efficiency of GCN-C than GCN-NC in SCP photodegradation in Fig. 4. 8(A,B), illustrates that the nitrogen doped carbons are more favourable for charge transferring from GCN to adjacent carbon atoms, giving rise to positively charged sites (holes) to improve the photodegradation efficiency. It is interesting to note that the nitrogen content would impact the catalytic

performance in the photocatalytic reaction, but the catalyst with extra high N content would limit visible light absorption and reduce the conductivity, resulting in a lowered activity. Combining the elemental analysis and XPS in Tables 4. 1 and 4. 2, the solar activation did not show the same trend with the nitrogen content of the carbon spheres. The one with nitrogen content of 6.0% is more efficient than the others with 11.9% and 5.4%. However, the nitrogen should be at an appropriate level, otherwise too higher level of nitrogen would result in a lower degradation. SCP degradation within a temperature range of 35-55 °C was examined for GCN-NC(6.0) photocatalyst (Fig. 4. 8(D)). An enhanced trend can be observed with temperature elevation. GCN-NC(6.0) provided 100% SCP removal in 60, 45, 30 and 20 min when the reaction took place at 25, 35, 45 and 55 °C, respectively. The results suggest an endothermic reaction in this catalytic process. The kinetic rate constants are presented in Table 4. 3. The $\ln k$ against $1/T$ plotted in Fig. 4. 8(D) follows the Arrhenius equation and the obtained activation energy was 20.32 kJ/mol. Additionally, stability tests of the best photocatalyst were performed (Fig. 4. 9). SCP was decomposed in 90 min for the first run under visible light. For the subsequent two runs, GCN-NC(6.0) achieved 100% of SCP removal in 120 and 150 min. In the forth run, 92% degradation (Fig. 4.9 (A)). It is also revealed a decrease trend of degradation ability under UV light irradiations (Fig. 4.9 (B)). As seen in Fig. 4.10, the deposition of the intermediates on the surface of catalysts resulted in the blockage of surface reactive sites. The deactivation of the photocatalysts could be ascribed to the alteration of surface charges and the detachment of nitrogen-doped carbon nanospheres during the photocatalysis processes. The samples after recycle experiments were detected by XRD and Uv-vis measurements (Fig. 4.11). The results indicated that the morphology and optical property of N-CNT/mpg-C₃N₄-15 did not significantly change after four times cycles. Thus, the GCN-NC(6.0) materials could be reused in practical pollution treatment. The correlation between pH and photodegradation of antibiotics by GCN has been well documented by previous studies [45, 46]. As the pH value increases, the proportion of neutral SCP decreases and the proportion of negatively charged species increased, thus, justifying an increase in direct

photolysis with the increase in pH. On the other hand, an increase in pH can also lead to an increase in indirect photolysis, favouring the oxidation of the SCP due to the generation of highly reactive radicals.

Table 4.3. Kinetic parameters of SCP degradation on GCN-based photocatalysts

Irradiation	Catalyst	T	k	v	R ² of k	E _a	R ² of E _a
		(°C)	(min ⁻¹)	(mg/min)		(kJ/mol)	
UV	GCN	25	0.0047	0.141	0.84	-	-
	GCN-C	25	0.0076	0.228	0.84	-	-
	GCN-NC(5.4)	25	0.0154	0.493	0.88	-	-
	GCN-NC(11.9)	25	0.0139	0.417	0.87	-	-
	GCN-NC(6.0)	25	0.0205	0.656	0.92	20.32	0.95
	GCN-NC(6.0)	35	0.0287	0.861	0.85	-	-
	GCN-NC(6.0)	45	0.0392	1.254	0.87	-	-
	GCN-NC(6.0)	55	0.0423	1.269	0.81	-	-
Visible	GCN	25	0.0042	0.134	0.96		
	GCN-C	25	0.0061	0.183	0.94		
	GCN-NC(5.4)	25	0.0077	0.231	0.92		
	GCN-NC(11.9)	25	0.0078	0.234	0.90		
	GCN-NC(6.0)	25	0.0139	0.417	0.98		

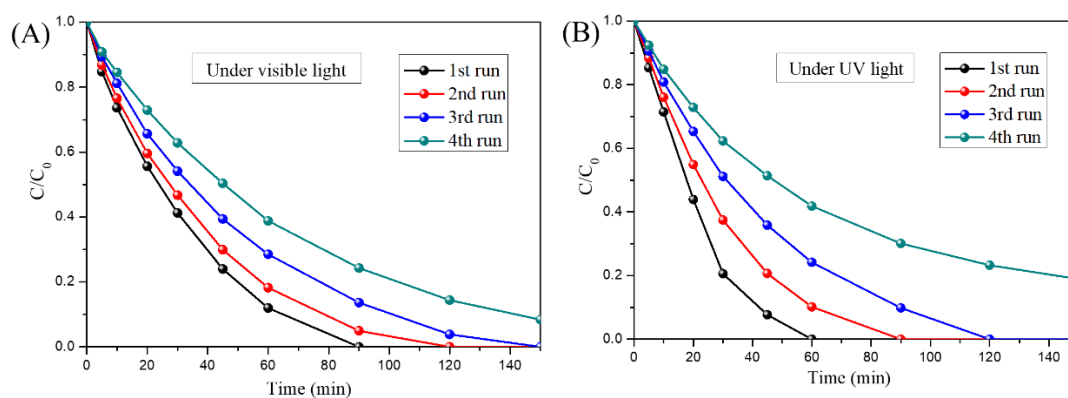


Fig. 4. 9. The stability evaluation of GCN-NC(6.0) under visible (A) and UV light (B)

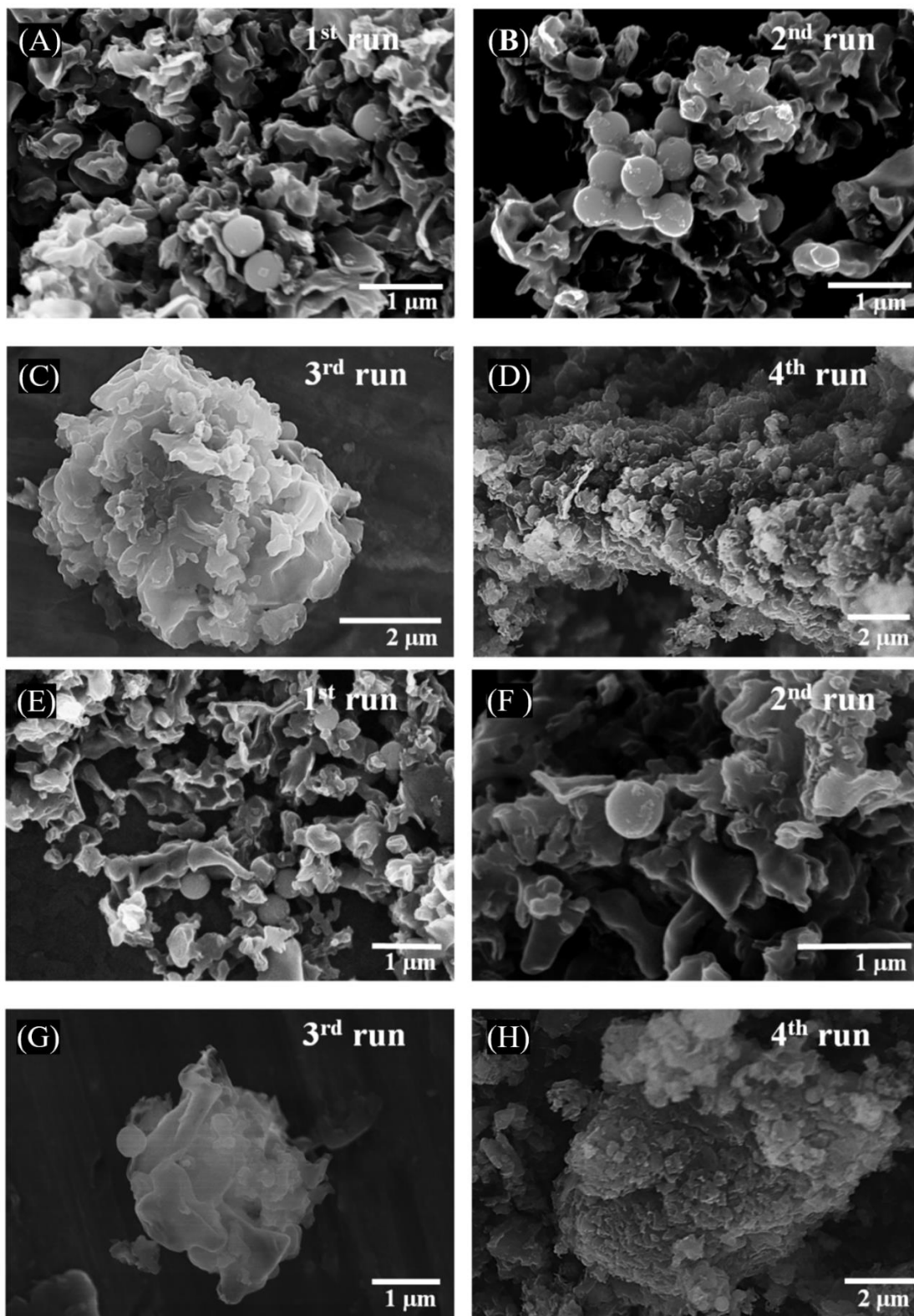


Fig. 4. 10. SEM image of GCN-NC(6.0) after the multiple runs under visible (A-D) and UV (E-H) light.

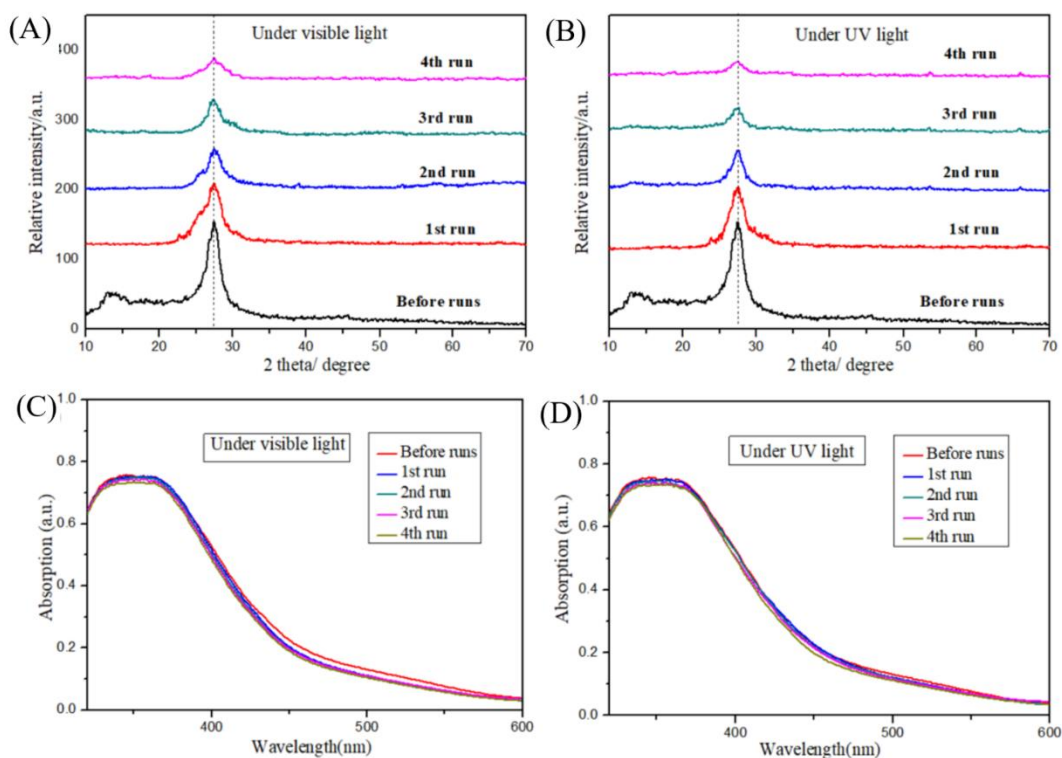


Fig. 4. 11. XRD patterns (A.B) and Uv-vis results (C.D) of GCN-NC(6.0) after the multiple runs under visible and UV light.

In Fig. 4.12(A), a comparison of the on/off photocurrent response of nitrogen-doped carbon decorated GCN under visible-light irradiations was studied. The photocurrent ascended until it reached a constant value with light on, then declined with light off, suggesting that these GCN-based samples were light-responsive materials. GCN produced a stable density of $1.8 \mu\text{A}/\text{cm}^2$ photocurrent, while all of the GCN-C, GCN-NC(5.4) and GCN-NC(11.9) enlarged the photocurrents to around $2.0 \mu\text{A}/\text{cm}^2$. GCN-NC(6.0) produced the biggest gap of photocurrent densities with the periodic irradiations, indicating that the lifetime of photogenerated carriers significantly increased. Initially, GCN-NC(6.0) had a photocurrent of $2.7 \mu\text{A}/\text{cm}^2$ but it decreased to $2.0 \mu\text{A}/\text{cm}^2$ at the fourth cycle. This distinguishable enhancement of photocurrent response reveals that introducing nitrogen-doped carbon spheres can accelerate the transport of the photoinduced carriers and the separation of photoexcited electron/hole pairs. To make further verification of the electrochemical properties, the EIS Nyquist

plots of the pristine GCN and nitrogen-doped carbon loaded GCN under visible light irradiations are recorded in Fig. 4.12(B). The smallest radius implied the fastest interfacial electron transfer. The Nyquist plot of GCN-NC(6.0) displayed a smaller arc radius EIS than other samples, suggesting that it possesses the lowest resistant barrier to electron transfer. All these results demonstrate that NC(6.0) can function as an efficient co-catalyst in the GCN-NC(6.0) composite to effectively reduce the charge recombination that favors for enhanced photocatalytic activity, which is in accordance with the PL spectra. Radical trapping experiments were carried out to differentiate the reactive oxygen species that play the key role in the photocatalytic process. Three radical scavengers, formate, tert-butyl alcohol and p-benzoquinone, were employed to quench photo-generated holes (h^+), hydroxyl radicals ($\bullet\text{OH}$) and superoxide radical ($\bullet\text{O}_2^-$), respectively. Fig. 4.12(C) illustrates that the removal rates of SCP were remarkably inhibited after the addition of quenchers and the decline rates follow an order of p-benzoquinone > tert-butyl alcohol > formate, testifying that photogenerated $\bullet\text{O}_2^-$ and $\bullet\text{OH}$ were the major species for SCP degradation. In order to verify the quenching results, EPR spectra were recorded using DMPO as the trapping agent [47], tert-butanol alcohol as $\bullet\text{OH}$ differentiation and p-benzoquinone as $\bullet\text{O}_2^-$ differentiation [48]. As displayed in Fig. 4.12(D), when the mixed suspension was irradiated by UV-visible light, the strong signals of spin-trapped $\bullet\text{OH}$ and $\bullet\text{O}_2^-$ would be detected, indicating that the reactive radicals play essential roles in this aqueous system. The two radicals produced by the activation of the photocatalyst under irradiations have been well-recognized to be responsible for the degradation of organics. Based on these results and analysis, the mechanism for photocatalytic degradation under UV and visible light irradiations is thus proposed and depicted in Scheme 1. It shows that the CB potential of NC modified GCN composites is more positive than pure GCN. The low photocatalytic activity of GCN is mainly attributed to the weak light absorbance caused by the wide band gap. Once the GCN is loaded with nitrogen-doped carbon, the degradation rate will be highly enhanced. The outstanding photoactivity of GCN-NC(6.0) originates from the appropriate N content and strong coupling between GCN

and NC, which provides a high concentration of active sites for fast charge carrier transport.

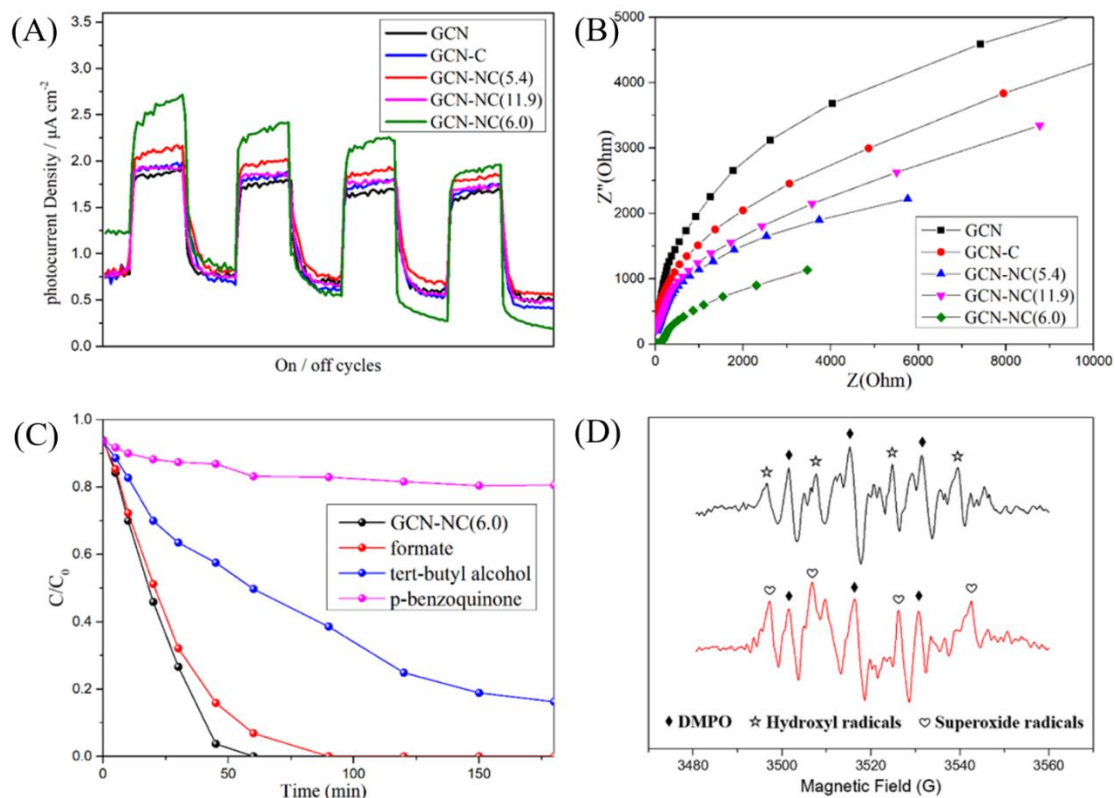


Fig. 4.12. (A) Transient photocurrent and (B) EIS curves of the GCN, GCN-C, GCN-NC(5.4), GCN-NC(11.9) and GCN-NC(6.0) in 0.1 M Na_2SO_4 solution (C) Photocatalytic activity of GCN-NC(6.0) for SCP degradation with radical scavengers (formate, tert-butyl alcohol and p-benzoquinone) under visible light irradiations (D) EPR spectra of GCN-NC(6.0) under UV-visible light irradiations with quenching of tert-butyl alcohol and p-benzoquinone

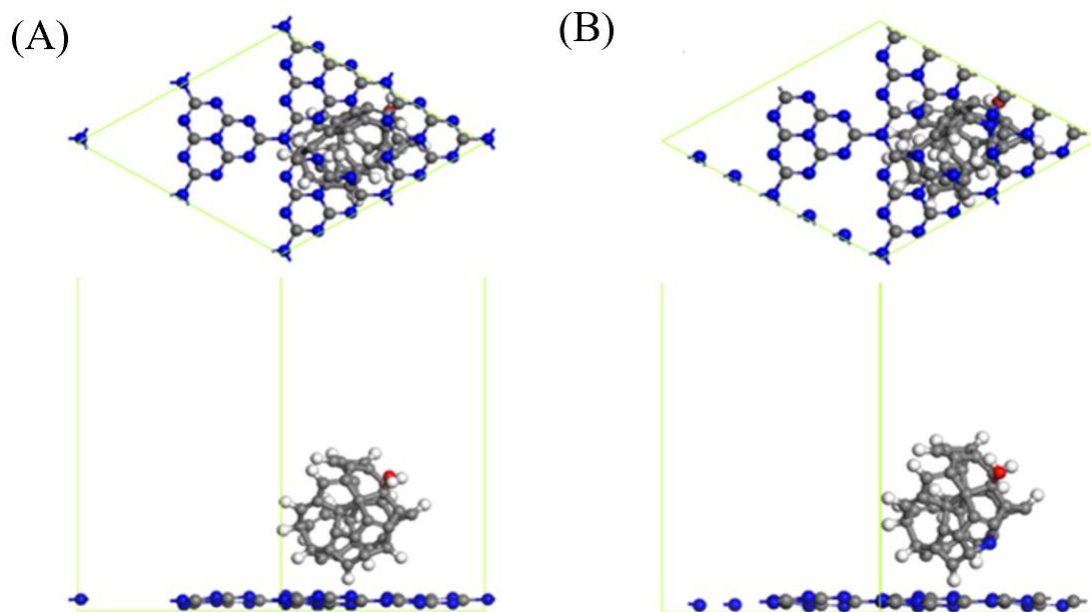


Fig. 4. 13. (A) The structure of GCN-C hybrid and (B) GCN-NC hybrid. In the simulation, a 2×2 supercell is taken, the grey, white, blue and red balls are standing for carbon, hydrogen, nitrogen and oxygen respectively

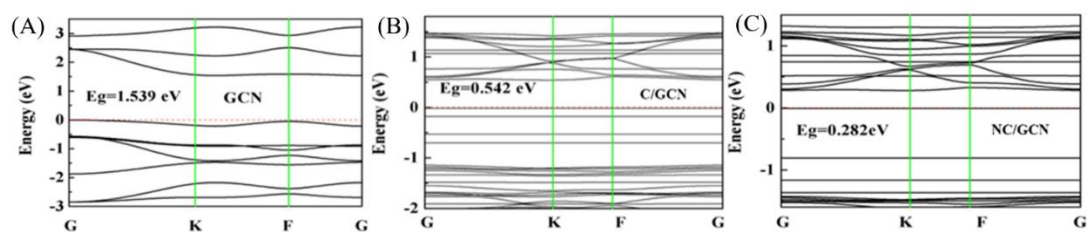


Fig. 4. 14. (A) The band structures of pristine GCN, (B) C/GCN and (C) NC/GCN systems, the red dash line at energy 0 is the position of Fermi level

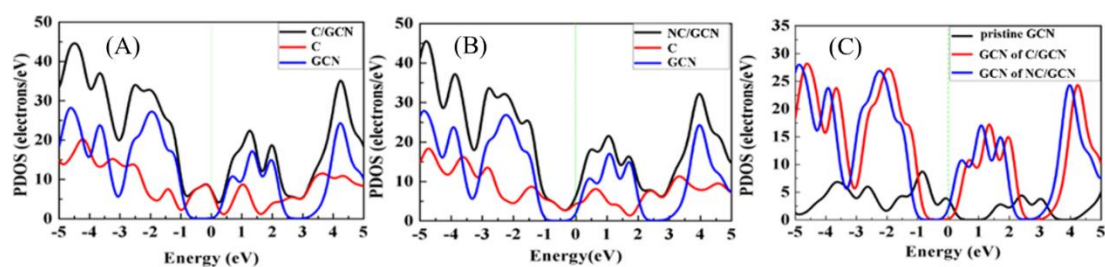


Fig. 4. 15. (A) The PDOS of C/GCN, (B) NC/GCN systems and (C) GCN in different

systems. The vertical dash lines are the position of the Fermi level

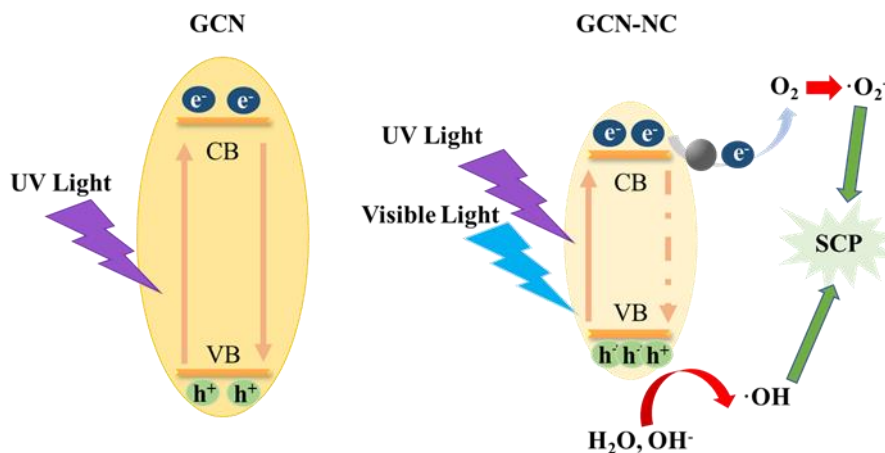


Fig. 4. 16. Mechanism scheme of GCN-NC in photocatalytic degradation of SCP

In general, photoactivity is largely dependent on the band edge positions of the photocatalyst. In DFT calculations, three-dimensional periodic boundary conditions were taken in the simulation. The simulation cell consists of a 2×2 g-C₃N₄ supercell with a vacuum width of 24 Å above the graphite like GCN layer to minimize the interlayer interaction. The k-point was set to $2 \times 2 \times 1$ when optimizing structures, and all atoms were allowed to relax. The density of states (DOS) were calculated with a net k-point grid of $4 \times 4 \times 1$. An energy cut off of 630 eV is used. For GCN-C, adsorption energy E_{ad} is determined by:

$$E_{ad} = E_{GCN-NC} - (E_C + E_{GCN}) \quad (3)$$

where E_{GCN-NC} , E_C and E_{GCN} are total energies of the GCN-C system, the isolate carbon nanosphere and GCN layer in the same slab, respectively. DFT calculation was performed to obtain a microscopic insight on how the complex GCN-NC acts as the best transition in photocatalysis. Given the possible adsorption configuration of carbon nanosphere in the GCN sheet, the energetic favorable configuration of carbon nanosphere should be located at the hollow site of GCN layer as shown in Fig. 4.13(A). It is noted that a hydroxyl group was attached on the outer sphere to mimic the

experimental conditions. The calculated charge transfer rates between the carbon nanosphere and GCN in the most stable structures of GCN-C and GCN-NC system are 0.06e and 0.04e, respectively. The distance between carbon nanosphere and GCN layer is 1.251 Å with adsorption energy of -0.54 eV, while those in nitrogen doping carbon nanosphere/g-C₃N₄ (NC/GCN) system are 1.289 Å and -1.45 eV, respectively. No chemical bond is observed in our simulation as shown in Fig. 4.13(B), and the carbon sphere still preferred to stay at the hollow site of the GCN layer. To better understand the photocatalytic properties of the composites, the band structures of pristine GCN, GCN-C and GCN-NC are shown in Fig. 4.14(A-C) for an in-depth analysis. Clearly, GCN has a band gap E_g of 1.53 eV, which agrees well with other reported calculation value of 1.54 eV using GGA functional [49]. After combining with carbon nanospheres, a remarkable decrease can be found in band gap to 0.54 eV, while the top of VB climbed to near the position of Fermi level. When introducing nitrogen into the carbon nanosphere, a further decrease in band gap can be observed, resulting in a direct band gap of 0.28 eV, with the bottom of CB dropping slightly and the top of VB nearly overlapping with the position of Fermi level, as shown in Fig. 4.15. To reveal the mechanism of the changes in GCN when composited with pristine carbon sphere and N-doped carbon nanosphere, the partial density of states (PDOS) calculations of GCN-C, GCN-NC hybrids and GCN in different systems were performed as presented in Fig. 4.16(A-C). As can be seen, the valence band maximum (VBM) of the PDOS of the whole systems was mainly contributed by the carbon nanosphere, while GCN made the greatest contribution to the CB bottom. After N-doping, the main features of the PDOS were maintained, except for the disappearance of the peak at -0.2 eV in carbon nanosphere and CB and VB of GCN changed toward the Fermi level especially. By comparing the PDOS of pristine GCN, GCN-C and GCN-NC systems (Fig. 4.16(C)), we infer the carbon nanospheres drastically reduce the band gap of GCN as the obvious changes were observed in GCN after loading nanospheres. A slight left shift was realized after introducing N into carbon nanospheres, which means that the CB moves downwards, consistent with the decrease in band gap of GCN-C material based on the

band structure calculation. It is found that the carbon nanosphere is physically adsorbed on the GCN layer with van der Waals interaction. The presence of carbon nanosphere can effectively reduce the band gap of GCN, and N-doping into carbon spheres would further reduce the band gap, improving the photocatalytic performance significantly.

Based on experimental and theoretical exploration, the photocatalytic mechanism of GCN-NC can be proposed as schematically shown in Fig. 4.17. During the hydrothermal process, nitrogen doped carbon nanospheres can be well integrated on GCN with strong interaction on the interface via Van der Waals force, which provide tunnels for fast interfacial electron transfer. The introduction of nitrogen doped carbon nanospheres can improve the absorption capability of visible light of pristine GCN thus the band gap and electronic structure have been favorably altered in the resultant catalyst composite. GCN-NC with narrow band gap can effectively absorb UV/visible light, promoting the generation of electron/hole pairs (right part of Fig. 4.17). Due to the strong affinity of N atoms, the generated electrons can be transferred by the nitrogen doped carbon spheres more efficiently than that by pure carbon spheres, limiting the electron/hole recombination rates. Although the nitrogen doping can improve the photocatalytic performance of composite materials, the nitrogen content should be controlled in an appropriate level otherwise overdosage would decrease the light absorption and defer the charge transfer. As shown in Fig. 4.17, the photogenerated electrons reduce the dissolved oxygen to superoxide radical ($\bullet\text{O}_2^-$) and holes lead to the production of hydroxyl radicals, both of which are effective to remove SCP. Based on reported intermediates of other sulphonamides degradation study, major oxidized products (OPs) of SCP are 3-Amino-6-chloropyridazine, 4-Aminobenzenesulfonic acid and hydroxylated SCP [50]. Sun et al. have demonstrated that the biodegradation of the OPs is enhanced, while toxicity of OPs is less compared to the parent SCP [51].

4.4. Conclusions

The atomic structure, chemical states and electronic properties of nitrogen-doped

carbon nanospheres (NC) on graphitic carbon nitride layer were characterized by SEM, XRD, FESEM, FT-IR, BET, UV-vis/DRS, XPS, EPR and EIS techniques. The absorption edges of GCN were extended to visible light region by the coupling of 6 wt.% nitrogen-doped carbon nanospheres with a similar size about 400 nm, while the effect of SCP degradation under visible light irradiations was affected by the nitrogen content. Among the tested samples, graphitic carbon nitride supported carbon nanospheres doped by 6 wt.% nitrogen exhibited the best catalytic efficiency for photodegradation of sulfachloropyridazine. Experimental results and DFT calculation imply that the carbon nanosphere is physically adsorbed on the GCN layer with van der Waals interaction. The presence of nitrogen-doped carbon nanospheres can significantly reduce the band gap of GCN, deferring the recombination rate of electron/hole pairs and thus improving the photocatalytic performance significantly. This study suggests that nitrogen-doped carbon and graphitic carbon nitride composite can be applied as a new class of metal-free photocatalysts not only for wastewater treatment but also for other applications.

References

1. Q. Liu, X. Duan, H. Sun, Y. Wang, M. O. Tade and S. Wang, Size-tailored porous spheres of manganese oxides for catalytic oxidation via peroxymonosulfate activation. *The J. Phys. Chem. C*, 2016. 120, 16871-16878.
2. L. Zhou, H. Zhang, H. Sun, S. Liu, M. O. Tade, S. Wang and W. Jin, Recent advances in non-metal modification of graphitic carbon nitride for photocatalysis: A historic review. *Catal. Sci. Technol.*, 2016. 6, 7002-7023.
3. K. P. Loh, Q. Bao, P. K. Ang and J. Yang. The chemistry of graphene. *J. Mater. Chem.*, 2010. 20, 2277-2289.
4. Y. Zhu, S. Murali, W. Cai, X. Li, J. W. Suk, J. R. Potts and R. S. Ruoff. Graphene and graphene oxide: Synthesis, properties, and applications. *Adv. Mater.*, 2010. 22, 3906-3924.
5. E. Saputra, H. Zhang, Q. Liu, H. Sun and S. Wang. Egg-shaped core/shell α - Mn_2O_3 @ α - MnO_2 as heterogeneous catalysts for decomposition of phenolics in aqueous solutions. *Chemosphere*, 2016. 159, 351-358.
6. Y. H. Seo, M. Sung, B. Kim, Y.-K. Oh, D. Y. Kim and J.-I. Han. Ferric chloride based downstream process for microalgae based biodiesel production. *Bioresour. Technol.*, 2015. 181, 143-147.
7. W. Liu, L. Cao, W. Cheng, Y. Cao, X. Liu, W. Zhang, X. Mou, L. Jin, X. Zheng, W. Che, Q. Liu, T. Yao and S. Wei. Frontispiece: Single-site active cobalt-based photocatalyst with a long carrier lifetime for spontaneous overall water splitting. *Angew Chem.*, 2017. 56, 9440-9445.
8. B. Ai, X. Duan, H. Sun, X. Qiu and S. Wang, Metal-free graphene-carbon nitride hybrids for photodegradation of organic pollutants in water. *Catal. Today*, 2015. 258, 668-675.

9. Y. Zhang, Y. Liu, W. Liu, X. Li and L. Mao. Synthesis of honeycomb-like mesoporous nitrogen-doped carbon nanospheres as pt catalyst supports for methanol oxidation in alkaline media. *Appl. Surf. Sci.*, 2017. 407, 64-71.
10. R. S. Weatherup, H. Amara, R. Blume, B. Dlubak, B. C. Bayer, M. Diarra, M. Bahri, A. Cabrero-Vilatela, S. Caneva, P. R. Kidambi, M.-B. Martin, C. Deranlot, P. Seneor, R. Schloegl, F. Ducastelle, C. Bichara and S. Hofmann. Interdependency of subsurface carbon distribution and graphene-catalyst interaction. *J. Am. Chem. Soc.*, 2014. 136, 13698-13708.
11. B. C. M. Martindale, G. A. M. Hutton, C. A. Caputo and E. Reisner. Solar hydrogen production using carbon quantum dots and a molecular nickel catalyst. *J. Am. Chem. Soc.*, 2015.137, 6018-6025.
12. X. C. Wang, K. Maeda, A. Thomas, K. Takanabe, G. Xin, J. Carlsson, K. Domen and M. Antonietti. A metal-free polymeric photocatalyst for hydrogen production from water under visible light. *Nat. Mater.*, 2009. 8, 76-80.
13. S. C. Yan, Z. S. Li and Z. G. Zou. Photodegradation performance of g-C₃N₄ fabricated by directly heating melamine. *Langmuir*, 2009. 25, 10397-10401.
14. J. He, H. Sun, S. Indrawirawan, X. Duan, M. Tade and S. Wang. Novel polyoxometalate@ g-C₃N₄ hybrid photocatalysts for degradation of dyes and phenolics. *J. Colloid Interface Sci.*, 2015. 456, 15-21.
15. Y. Zheng, J. Liu, J. Liang, M. Jaroniec and S. Qiao. Graphitic carbon nitride materials: controllable synthesis and applications in fuel cells and photocatalysis. *Energy Environ. Sci.*, 2012. 5, 6717-6731.
16. J. Chen, Z. Hong, Y. Chen, B. Lin and B. Gao. One-step synthesis of sulfur-doped and nitrogen-deficient g-C₃N₄ photocatalyst for enhanced hydrogen evolution under visible light. *Mater. Lett.*, 2015. 145,129-132.

17. P. Martín-Ramos, J. Martín-Gil, R. C. Dante, F. Vaquero, R. M. Navarro and J. L. G. Fierro. A simple approach to synthesize g- C₃N₄ with high visible light photoactivity for hydrogen production. *Int. J. Hydrogen Energy*, 2015. 40, 7273-7281.
18. J. Tian, Q. Liu, A. M. Asiri, K. A. Alamry and X. Sun. Ultrathin graphitic C₃N₄ nanosheets/graphene composites: Efficient organic electrocatalyst for oxygen evolution reaction. *Chem. Sus. Chem.*, 2014. 7, 2125-2130.
19. Z. Sun, H. Wang, Z. Wu and L. Wang. g-C₃N₄ based composite photocatalysts for photocatalytic CO₂ reduction. *Catal. Today*, 2017. 300, 160-172.
20. A. Y. Liu and M. L. Cohen. Structural properties and electronic structure of low-compressibility materials: β -Si₃N₄ and hypothetical β -C₃N₄. *Phys. Rev. B*, 1990. 41, 10727-10734.
21. J. Fang, H. Fan, M. Li and C. Long. Nitrogen self-doped graphitic carbon nitride as efficient visible light photocatalyst for hydrogen evolution. *J. Mater. Chem. A*, 2015. 3, 13819-13826.
22. S. W. Hu, L. W. Yang, Y. Tian, X. L. Wei, J. W. Ding, J. X. Zhong and P. K. Chu. Non-covalent doping of graphitic carbon nitride with ultrathin graphene oxide and molybdenum disulfide nanosheets: An effective binary heterojunction photocatalyst under visible light irradiation. *J. Colloid Interface Sci.*, 2014. 431, 42-49.
23. X. H. Song, L. Feng, S. L. Deng, S. Y. Xie and L. S. Zheng. Simultaneous exfoliation and modification of graphitic carbon nitride nanosheets. *Adv. Mater. Interfaces*, 2017. 4, 1700339.
24. G. Zhang, M. Zhang, X. Ye, X. Qiu, S. Lin and X. Wang. Iodine modified carbon nitride semiconductors as visible light photocatalysts for hydrogen evolution. *Adv. Mater.*, 2014. 26, 805-809.
25. Z. Lin and X. Wang. Nanostructure engineering and doping of conjugated carbon nitride semiconductors for hydrogen photosynthesis. *Angew Chem.*, 2013. 52, 1735-1738.

26. H. Sun, X. Zhou, H. Zhang and W. Tu. An efficient exfoliation method to obtain graphitic carbon nitride nanosheets with superior visible-light photocatalytic activity. *Int. J. Hydrogen Energy*, 2017. 42, 7930-7937.
27. S. Hu, W. Zhang, J. Bai, G. Lu, L. Zhang and G. Wu. Construction of a 2D/2D g-C₃N₄ /rGO hybrid heterojunction catalyst with outstanding charge separation ability and nitrogen photofixation performance via a surface protonation process. *RSC Adv.*, 2016. 6, 25695-25702.
28. R. C. Pawar, S. Kang, S. H. Ahn and C. S. Lee. Gold nanoparticle modified graphitic carbon nitride/multi-walled carbon nanotube (g-C₃N₄ /CNTs/Au) hybrid photocatalysts for effective water splitting and degradation. *RSC Adv.*, 2015. 5, 24281-24292.
29. G. Rajender, B. Choudhury and P. K. Giri. In situ decoration of plasmonic Au nanoparticles on graphene quantum dots-graphitic carbon nitride hybrid and evaluation of its visible light photocatalytic performance. *Nanotechnology*, 2017. 28, 395703.
30. Y. Sun, C. Li, Y. Xu, H. Bai, Z. Yao and G. Shi. Chemically converted graphene as substrate for immobilizing and enhancing the activity of a polymeric catalyst. *Chem. Commun*, 2010. 46, 4740-4742.
31. S. Liu, J. Ke, H. Sun, J. Liu, M. O. Tade and S. Wang. Size dependence of uniformed carbon spheres in promoting graphitic carbon nitride toward enhanced photocatalysis. *Appl. Catal. B: Environ*, 2017. 204, 358-364.
32. G. Dong, K. Zhao and L. Zhang. Carbon self-doping induced high electronic conductivity and photoreactivity of g-C₃N₄. *Chem. Commun*, 2012. 48, 6178-6180.
33. D. Gao, Y. Liu, P. Liu, M. Si and D. Xue. Atomically thin B doped g-C₃N₄ nanosheets: High-temperature ferromagnetism and calculated half-metallicity. *Sci. rep.*, 2016. 6, 35768-35776.

34. J. Cao, X. Yin, L. Wang, M. Guo, J. Xu and Z. Chen. Enhanced electrocatalytic activity of platinum nanoparticles supported on nitrogen-modified mesoporous carbons for methanol electrooxidation. *Int. J. Hydrogen Energy*, 2015. 40, 2971-2978.
35. J. Liu, Y. Song, H. Xu, X. Zhu, J. Lian, Y. Xu, Y. Zhao, L. Huang, H. Ji and H. Li. Non-metal photocatalyst nitrogen-doped carbon nanotubes modified mpg-C₃N₄: Facile synthesis and the enhanced visible-light photocatalytic activity. *J. Colloid Interface Sci.*, 2017. 494, 38-46.
36. L. Jia, D.H. Wang, Y.X. Huang, A.W. Xu and H.Q. Yu. Highly durable N-doped graphene/CdS nanocomposites with enhanced photocatalytic hydrogen evolution from water under visible light irradiation. *The J. Phys. Chem. C*, 2011. 115, 11466-11473.
37. G. Wang, Y. Sun, D. Li, H. W. Liang, R. Dong, X. Feng and K. Müllen. Controlled synthesis of N-doped carbon nanospheres with tailored mesopores through self-assembly of colloidal silica. *Angew Chem.*, 2015. 54, 15191-15196.
38. J. Fang, H. Fan, M. Li and C. Long. Nitrogen self-doped graphitic carbon nitride as efficient visible light photocatalyst for hydrogen evolution. *J. Mater. Chem. A*, 2015. 3, 13819-13826.
39. J. Clark Stewart, D. Segall Matthew, J. Pickard Chris, J. Hasnip Phil, I. J. Probert Matt and K. Refson, C. Payne Mike. First principles methods using CASTEP. *Zeitschrift für Kristallographie-Cryst. Mater*, 2005. 220, 567-570.
40. J. P. Perdew, A. Ruzsinszky, G. I. Csonka, O. A. Vydrov, G. E. Scuseria, L. A. Constantin, X. Zhou and K. Burke. Restoring the density-gradient expansion for exchange in solids and surfaces. *Phys. Rev. Lett.*, 2008. 100, 136406-136410.
41. A. Tkatchenko and M. Scheffler. Accurate molecular van der waals interactions from ground-state electron density and free-atom reference data. *Phys. Rev. Lett.*, 2009. 102, 073005.

42. Y. Zhou, L. Zhang, W. Huang, Q. Kong, X. Fan, M. Wang and J. Shi. N-doped graphitic carbon-incorporated g-C₃N₄ for remarkably enhanced photocatalytic H₂ evolution under visible light. *Carbon*, 2016. 99, 111-117.
43. C. Han, Y. Wang, Y. Lei, B. Wang, N. Wu, Q. Shi and Q. Li. In situ synthesis of graphitic- C₃N₄ nanosheet hybridized N-doped TiO₂ nanofibers for efficient photocatalytic H₂ production and degradation. *Nano Res.*, 2015. 8, 1199-1209.
44. P. Tiong, H. O. Lintang, S. Endud and L. Yuliati. Improved interfacial charge transfer and visible light activity of reduced graphene oxidegraphitic carbon nitride photocatalysts. *RSC Adv.*, 2015. 5, 94029-94039.
45. H. Wang, Y. Wu, M. Feng, W. Tu, T. Xiao, T. Xiong, H. Ang, X. Yuan and J. Chew. Visible-light-driven removal of tetracycline antibiotics and reclamation of hydrogen energy from natural water matrices and wastewater by polymeric carbon nitride foam. *Water Res.*, 2018. 144, 215-225.
46. M. Conde-Cid, D. Fernández-Calviño, J. C. Nóvoa-Muñoz, M. Arias-Estévez, M. Díaz-Raviña, A. Núñez-Delgado, M. J. Fernández-Sanjurjo and E. Álvarez-Rodríguez. Degradation of sulfadiazine, sulfachloropyridazine and sulfamethazine in aqueous media. *J. Environ. Manage.*, 2018. 228, 239-248.
47. L.Y. Zang, K. Stone and W. A. Pryor. Detection of free radicals in aqueous extracts of cigarette tar by electron spin resonance. *Free Radical Biol. and Med.*, 1995. 19, 161-167.
48. G. V. Buxton, C. L. Greenstock, W. P. Helman and A. B. Ross. Critical review of rate constants for reactions of hydrated electrons, hydrogen atoms and hydroxyl radicals ($\cdot\text{OH}/\cdot\text{O}^-$ in aqueous solution. *J. Phys. Chem. Ref. Data.*, 1988. 17, 513-886.

49. B. Jing, Z. Ao, Z. Teng, C. Wang, J. Yi and T. An. Density functional theory study on the effects of oxygen groups on band gap tuning of graphitic carbon nitrides for possible photocatalytic applications. *Sustainable Mater. Technol.*, 2018. 16, 12-22.
50. L. H. Hu, P. M. Flanders, P. L. Miller and T. J. Strathmann. Oxidation of sulfamethoxazole and related antimicrobial agents by TiO₂ photocatalysis. *Water Res.*, 2007. 41, 2612-2626.
51. X. Sun, M. Feng, S. Dong, Y. Qi, L. Sun, N. Nesnas and V. Sharma. Removal of sulfachloropyridazine by ferrate(VI): Kinetics, reaction pathways, biodegradation, and toxicity evaluation. *Chem. Eng. J.*, 2019. 372, 742-751.

Every reasonable effort has been made to acknowledge the owners of copyright material. I would be pleased to hear from any copyright owner who has been omitted or incorrectly acknowledged.

Chapter 5. Magnetic ZnO@Fe₃O₄ composite for self-generated H₂O₂ toward photo-Fenton-like oxidation of nitrophenol

Abstract

The present work focuses on the synthesis of a magnetically separable and stable catalyst for self-supplying H₂O₂ in photo-Fenton degradation of p-nitrophenol. Different from the most popular Fe₃O₄@ZnO core-shell structure, ZnO microflower cores were partially wrapped with Fe₃O₄ nanoparticles via a layer-by-layer self-assembly process. Several characterisation techniques were employed to investigate the crystal structure, morphology, surface chemistry and optical properties of the produced composites. The band gaps of the ZnO and Fe₃O₄ were considerably decreased from 3.05 and 2.60 to 2.35 eV after the assembly. The optimum Fe₃O₄ deposition layer number was found to be 5 for achieving 100% p-nitrophenol removal in 60 min. The degradation was triggered with in-situ photocatalytic formation of hydrogen peroxide over Fe₃O₄@ZnO. The exposed Fe₃O₄ nanoparticles provided Fe²⁺ and Fe³⁺ Fenton-active species for stable operation. We explored possible mechanisms of the enhanced photocatalysis by quenching and radical trapping experiments. The magnetic separation was also performed to recover and reuse the spent catalyst.

The content of this chapter is published in Compos. B. Eng. 2020, 200, 108345

5.1. Introduction

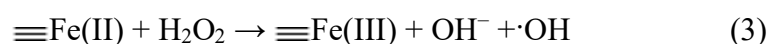
In recent decades, substantial quantities of wastewater containing organics with considerable toxicity were discharged by a multitude of chemical manufacturers, sewage disposal plants and textile factories to the ecosystem without proper treatments, which causes a series of terrible disasters to humans [1-4]. With high toxicity and high stability in the natural system, p-nitrophenol (p-NP) has caused emerging environmental issues and is listed as a priority controlled pollutant by various organizations [5, 6]. However, it is resistant to biological treatments and cannot be decomposed naturally, therefore arising an imperative requirement for sustainable and efficient remedies. The conversion from solar energy to chemical energies by photocatalysis has been believed as one of the most promising methods in p-NP treatment owing to non-selectivity, environmental-friendliness and low cost [7, 8].

Zinc oxide (ZnO) is a n-type semiconductor, which has attracted tremendous attention due to its remarkable physicochemical properties, easy availability, high chemical and photocorrosion stability, and environmental friendliness [9]. However, it is still a challenge to ensure sufficient photocatalytic activity of ZnO in practical applications due to the limited ability to work in UV region only and the unfavourably fast recombination of photogenerated electron-hole pairs [10]. For optimisation of the photocatalytic performance of ZnO, a variety of strategies have been attempted, including metal or non-metal doping [11, 12], dye sensitising [13], and semiconductor coupling [9, 14]. Many semiconductors, such as g-C₃N₄, CdS, AgBr, TiO₂, and Ag₂O, are introduced to improve the visible light photocatalytic activities for organic degradation compared with pristine ZnO [10, 12, 15-20]. Nanostructured Fe₃O₄ has attracted considerable attention because of a high surface-area-to-volume ratio and great catalytic activity in Fenton degradation of organic pollutants.

The difficulty in separation of photocatalysts from the reaction system for recycle and

reuse is becoming a serious drawback, which severely hinders their further applications. The conventional separation methods such as filtration and centrifugation are costly and tedious. According to previous studies, magnetic photocatalysts were synthesized to make the subsequent separation easier from reaction systems, thus solving the problem of recovery [21-23].

In most magnetite catalysed Fenton reaction, external H₂O₂ is provided and the dominant reactions on the iron oxide surface are presented below [24-27]:



Recently, in-situ generation of H₂O₂ at the catalytic site has been investigated to improve Fenton reagent efficiency and to avoid the potential hazards associated with the bulk H₂O₂ [28, 29]. It has been proven that H₂O₂ can be formed from photocatalytic processes at the ZnO/H₂O interface [30-32]. The application of hybrid nanoparticles of Fe₃O₄ and ZnO can result in enhanced photocatalytic activities and recoverability than pure ZnO [29, 33-35], but such efficiency is limited and subjected to particle size matching.

In this work, for the first time, we designed a partially wrapped ZnO with Fe₃O₄ (ZnO@Fe₃O₄) composite for efficient photo-Fenton degradation of organic contaminants via the improved light absorption, presence of abundant Fe²⁺/Fe³⁺ pairs and more importantly the self-generation of H₂O₂ to produce reactive oxygen species. For this purpose, a constant temperature (isothermal) aging approach was employed for flower-like ZnO synthesis. Fe₃O₄ nanopowder was prepared by a simple air oxidation method. The ZnO@Fe₃O₄ composites (ZFCMs) were obtained with a layer-by-layer (LBL) self-assembly method. The overall objectives of this research were to examine the photocatalytic degradation of p-NP in the presence of ZFCMs nanocomposites, understand the degradation kinetics, clarify the influence of various parameters on the

degradation, identify the dominant active species in the reactions and assess the reusability of the new nanocomposites.

5.2. Experimental

5.2.1. Materials

Analytical grade ferrous sulfate ($\text{FeSO}_4 \cdot 7\text{H}_2\text{O}$), NaOH, $\text{Zn}(\text{CH}_3\text{CO}_2)_2$, sodium dodecyl sulfate (SDS), H_2SO_4 , ethylenediaminetetracetic acid (EDTA), tert-butanol (TBA), p-benzoquinone (BZQ), tert-butanol, and p-nitrophenol (p-NP) were provided by Sigma-Aldrich and used as received without any further purification.

5.2.2. Preparation of Fe_3O_4 nano powder

Fe_3O_4 nano powder was synthesized using a simple air oxidation method. In a typical procedure, 0.027 g of $\text{FeSO}_4 \cdot 7\text{H}_2\text{O}$ was dissolved in 100 mL deionized water to make a 0.001 mol/L of Fe^{2+} solution, which was vigorously stirred at room temperature. Then, 6 mol/L NaOH solution was added gradually into the FeSO_4 solution until a pH value of 11.0 was reached. Afterwards, an air flow was introduced and the system was maintained at 25 °C for 1 h. After filtration and washing with deionized water and ethanol, the obtained Fe_3O_4 nano solids were dried in an oven at 70 °C for further uses.

5.2.3. Preparation of flower-like ZnO micro-powder

In preparation of ZnO microparticles, 20 mL of zinc acetate solution (1 mol/L) and 30 mL NaOH solution (4 mol/L) were mixed in a 100 mL volumetric flask. The mixture was then topped up with deionized water to make a 0.2 mol/L Zn^{2+} solution. Based on a constant-temperature aging method, the solution was placed in a water bath at 85 °C for 5 h to generate a well-mixed suspension. The obtained precipitate was thoroughly

washed with deionized water and ethanol and then dried at room temperature for 24 h to get flower-like ZnO.

5.2.4. Preparation of ZnO@Fe₃O₄ composites (ZFCMs)

ZFCMs were prepared by a layer-by-layer (L-B-L) self-assembly method. Briefly, 10 g of ZnO microparticles obtained from the previous experiment were dispersed in 20 mL of SDS (8 mol/L) solution in a 50 mL beaker to undertake surface modification. After continuously stirring at room temperature for 1 h, the mixed solution was filtered, washed and dried to generate negatively charged ZnO. After that, the surface modified ZnO was added into a 100 mL beaker with 50 mL of Fe₃O₄ suspension (7 g/L, pH = 4.8) and stirred at room temperature (25 °C) for 5 h. The obtained solids were filtered and washed thoroughly with ethanol. After drying in a vacuum oven at 70 °C for 6 h, the sample was denoted as ZFCM-1. The above process of SDS and Fe₃O₄ deposition was repeated in the same SDS and Fe₃O₄ solution to obtain other desired ZFCM-n with increasing Fe₃O₄ NPs percentage loading on the surface of ZnO microflower, where n is the deposited Fe₃O₄ layer number.

5.2.5. Characterisation techniques

The crystal structure of the prepared samples was investigated by a Bruker D8-ADVANCE X-ray diffractometer with Cu-K α radiation. The morphologies and element content of samples were measured by a scanning electron microscope (SEM Japan S-570) equipped with energy-dispersive X-ray spectroscopy (EDS, Kevex Sigma TM Quasar, USA). The functional groups of the samples were evaluated by a Bruker Tensor 27 Infrared spectrometer. The specific surface area of the iron oxides was determined by multipoint N₂-physisorption analysis using an automated gas adsorption–desorption analyser (TriStar II Plus, Micromeritics, USA). The light absorption properties of the

photocatalysts were collected on a UV–visible diffuse reflectance (DRS) spectrophotometer (JASCO V670) with an Ø60 mm integrating sphere and BaSO₄ as a reference material. Photoluminescence (PL) spectra were measured by a PerkinElmer LS55 luminescence spectrometer with a Xenon source at atmospheric temperature. Electron paramagnetic resonance (EPR) was measured using a Bruker EMXplus spectrometer. Photocurrent and Mott-Schottky curve measurements were accomplished on a Zennium workstation (Zahner, Germany) through a standard three electrode framework, in which Hg/Hg₂Cl₂ was applied as the reference electrode, a Pt wire as the counter electrode, and Na₂SO₄ solution (0.2 M, pH = 6.8) as an electrolyte. Five cycles were applied and the intermission for turning on/off light was 20 s.

5.2.6. Photocatalytic activity assessment

Photocatalytic performance of ZFCMs was investigated using 200 mL recalcitrant p-NP (7 mg) as the target pollutant in a photocatalytic reactor under a 100 W incandescent lamp (spectrum range 400 - 1700 nm). The initial pH was adjusted to 3 by utilising sulfuric acid. Afterwards, 50 mg catalyst was added in the reaction system. Prior to illumination, p-NP solutions containing the catalysts were sonicated and mechanically stirred at a constant rate in the dark for 5 h to obtain the adsorption/desorption equilibrium. The photocatalytic degradation was triggered by switching on the light source. An air flow was introduced in the reaction system subsequently. At a fixed interval, 10 mL of the suspension was taken from the reactor. After centrifugal treatment, the supernatant was collected and evaluated by a UV-vis spectrophotometer ($\lambda = 317$ nm) to measure the concentration. The degradation rate (DR) of p-NP was calculated according to the following equation:

$$DR = (1 - C_t/C_0) \times 100\% \quad [4]$$

Where, C_0 = initial concentration of p-NP, and C_t = concentration of p-NP at time t .

The concentration of H_2O_2 in the degradation solution was determined using a H_2O_2 -photometer (Lovibond ET-8600 Germany) at LED 528 nm.

5.3. Results and discussion

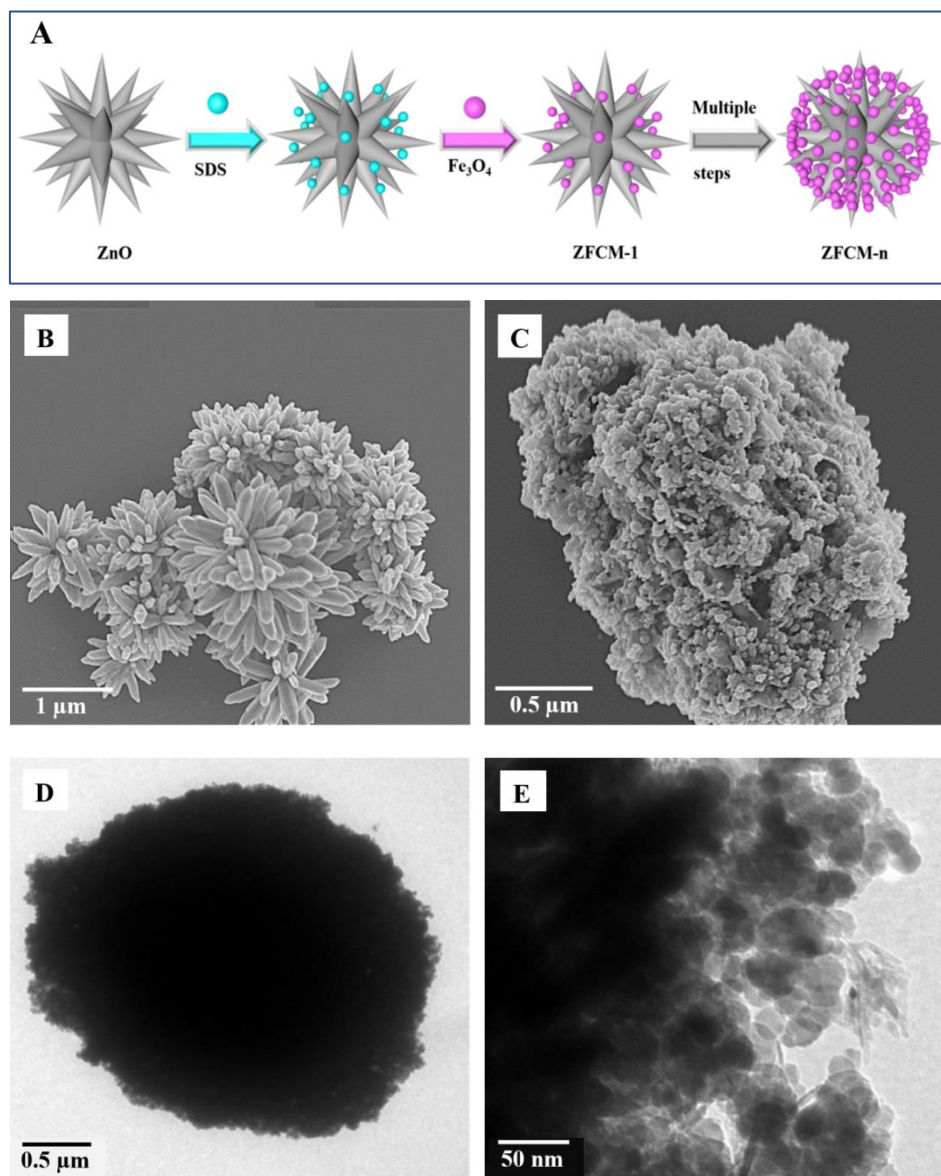


Fig. 5. 1 (A) Schematic illustration of ZnO@Fe₃O₄ composite formation via layer-by-layer deposition; SEM images of (B) ZnO and (C) ZFCM-5; (D, E) TEM images of ZFCM-5.

Highly oxygen-deficient flower-like ZnO was prepared by an isothermal aging approach. Fe₃O₄ NPs were prepared by air oxidation. As illustrated in Fig. 5. 1(A), novel ZnO@Fe₃O₄ composites were constructed by consecutive L-B-L adsorption of sodium dodecyl sulfate (SDS) micelles. In this study, the isoelectric points of ZnO and Fe₃O₄ were 9.5 and 7.2, respectively. The pH of the synthesis system was 4.8, so the positively charged surface of Fe₃O₄ and ZnO could be counterbalanced by anionic SDS to initiate the assembly. The formed ZnO has hexagonal pyramid tips with the edge length of ~ 1.5 μm (Fig. 5. 1(B)). Spherical Fe₃O₄ NPs were started to accumulate on ZnO surface with the increasing of coating layers. Additional L-B-L process led to more densely packed NPs on the surface of ZnO (Fig. 5. 2(A-F), ESI†). The ZFCM-5 had a relatively sealed core-shell structure in a size of 2.5-3.0 μm (Fig. 5. 1(C)). EDS results confirm that Fe content grew gradually with the increased Fe₃O₄ deposition cycles (Fig. 5. 3(A)).

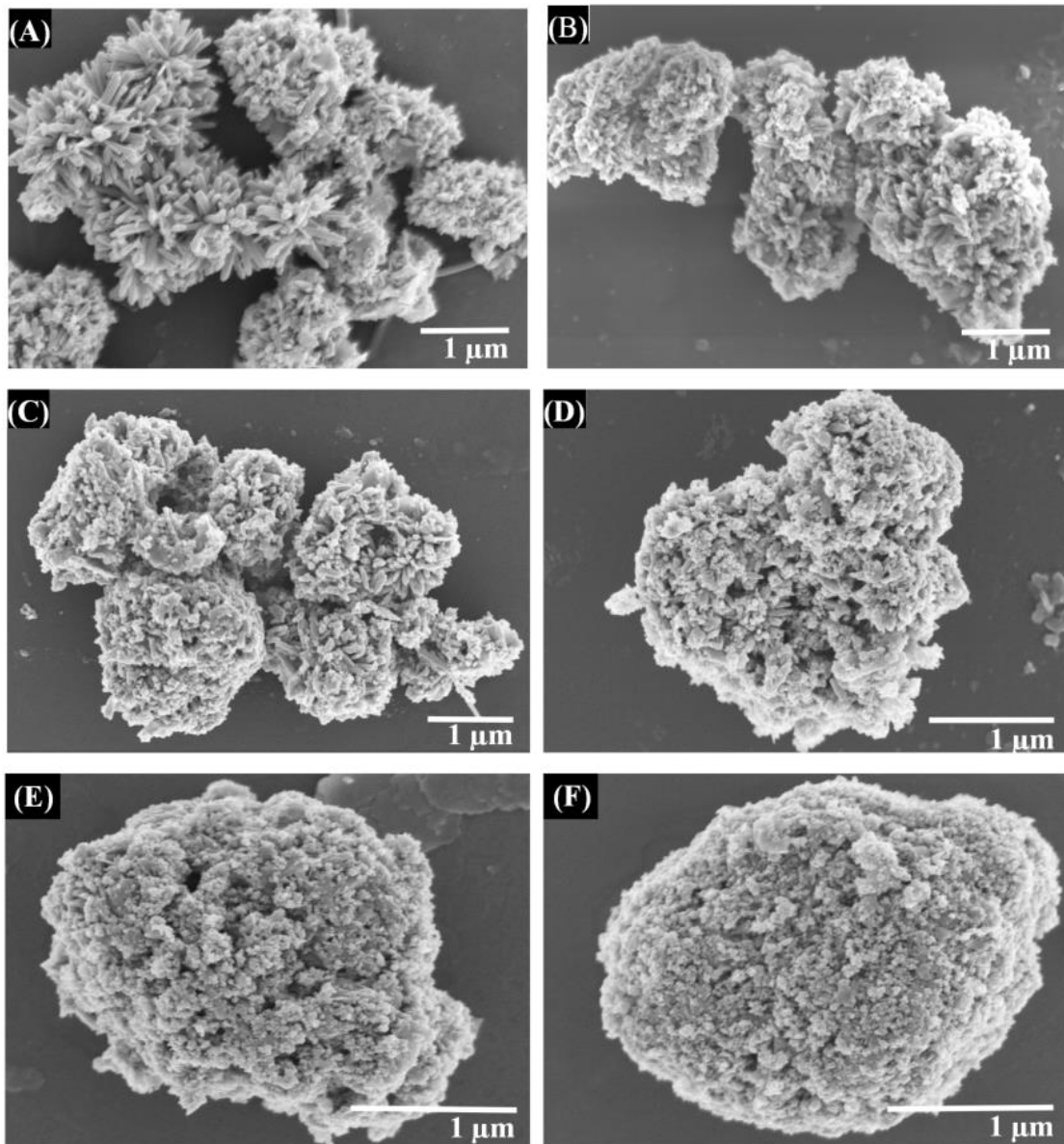


Fig. 5. 2. SEM images of (A) ZFCM-1, (B) ZFCM-2, (C) ZFCM-3, (D) ZFCM-4, (E) ZFCM-6, and (F) ZFCM-7.

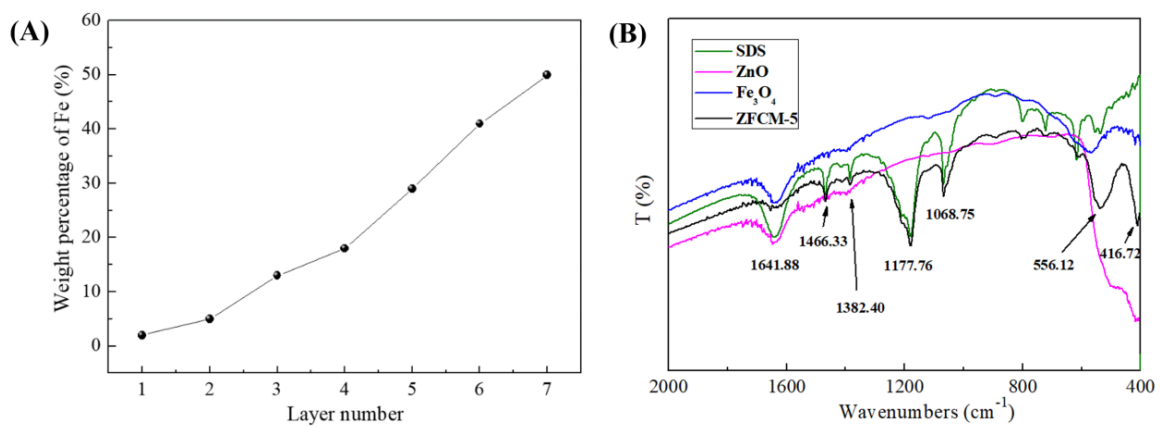


Fig. 5. 3. (A) The weight percentage of iron with different Fe_3O_4 layers in the composite. (B) FTIR spectra of SDS, ZnO, Fe_3O_4 and ZFCM-5

In Fig. 5. 4(A), sharp XRD peaks at 32.1° , 34.8° , 36.4° , 47.9° , 56.8° and 62.9° of ZFCM-5 could be assigned to the crystal planes of the (100), (002), (101), (102), (110) and (103) of ZnO (JCPDS 36-1451) [36]. Other peaks matched well with the planes of a face-centered cubic Fe_3O_4 structure (JCPDS 65-3107) [37]. Noticeably, the intensities of the diffraction peaks of ZnO in ZFCM-5 were reduced due to the core-shell structure. In FTIR spectra (Fig. 5. 3(B)), the adsorption bands at 1177.8 and 1068.8 cm^{-1} were due to the strong stretching vibrations of S=O/S-O in $-\text{OSO}_3$ groups and $-\text{CH}_2-$ chain in SDS. The bands at 1382.4 and 1466.3 cm^{-1} were assigned to the C-O and C=O stretch. An absorption peak at 416.7 cm^{-1} could be attributed to Zn-O [38]. Two obvious peaks at 556.1 and 1641.9 cm^{-1} corresponded to the bending vibrations of Fe-O bond and -OH groups [39], respectively. Both the XRD and FTIR results indicated that ZnO and Fe_3O_4 were held together by electrostatic interaction during the assembling process.

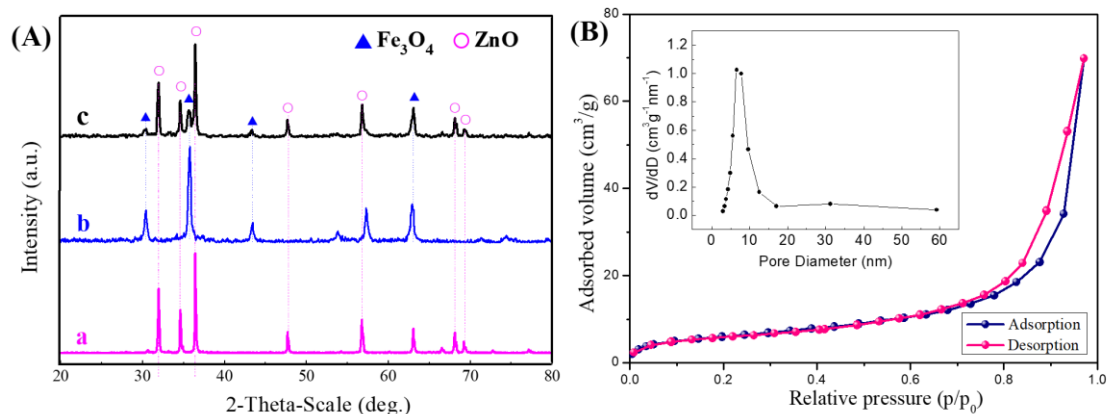


Fig. 5. 4. (A) XRD patterns; (B) N_2 adsorption-desorption isotherm and pore size distribution of ZFCM-5.

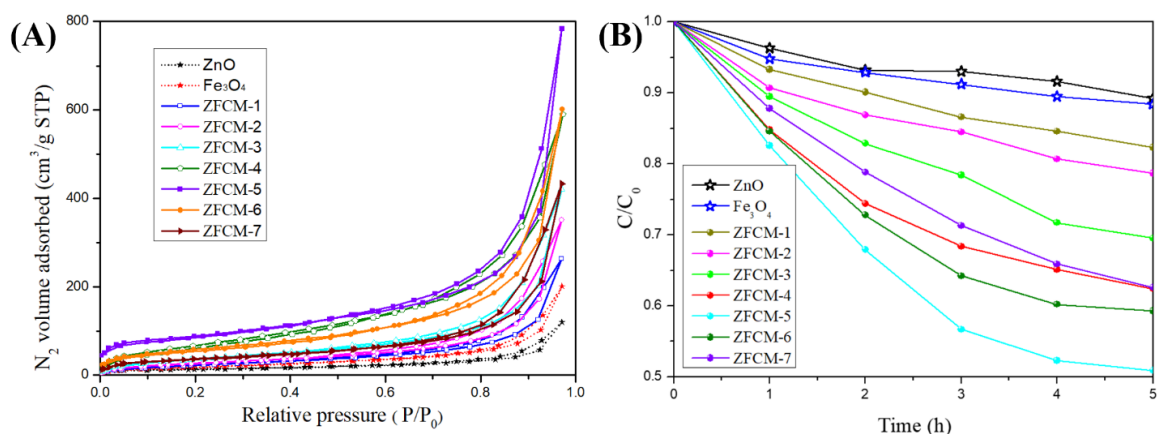


Fig. 5. 5. N_2 adsorption-desorption isotherms measurements (A) and p-nitrophenol adsorption curves (B).

To assess the textural properties of Fe_3O_4 and the composites, their nitrogen adsorption-desorption isotherms were acquired. As exhibited in Fig. 5. 5(A) and Table 5. 1, the BET specific surface areas of the composites increased with the attached Fe_3O_4 layer number from 1 to 5, ZFCM-5 displayed the highest surface area of $139 \text{ m}^2\text{g}^{-1}$, with $0.23 \text{ cm}^3 \text{ g}^{-1}$ of pore volume and a prevalent pore size of $\sim 8 \text{ nm}$ (Fig. 5. 4(B)). Therefore, the higher specific surface area and pore volume of the ZFCM-5 provide more active sites for a contact with contaminants, which is favourable to the photocatalytic activity. However, the BET surface areas of the samples declined with further compounding ($119 \text{ m}^2\text{g}^{-1}$ for ZFCM-6; $96.4 \text{ m}^2\text{g}^{-1}$ for ZFCM-7). In comparison with ZFCM-5, ZFCM-6 and ZFCM-7 showed lower pore volumes at 0.19 and $0.18 \text{ cm}^3 \text{ g}^{-1}$, respectively, due to more Fe_3O_4 particle deposition on the surface of the samples, which was arranged closely to fill the surface voids. The type IV isotherm with a distinct H3 hysteresis loop indicates the presence of significant mesopores.

Table 5. 1. Surface areas, pore volumes and adsorption parameters of as-prepared samples.

Samples	Surface areas ($\text{m}^2 \text{ g}^{-1}$)	Pore volumes	$\Gamma_{\max} \times 10^{-5}$ (mol g^{-1})	$K_a \times 10^4$ (L mol^{-1})	R^2
---------	---	--------------	--	---	-------

	(cm³ g⁻¹)				
ZnO	52.60	0.10	2.43	2.42	0.996
Fe₃O₄	63.68	0.09	2.56	2.50	0.996
ZFCM-1	70.56	0.12	2.63	2.65	0.994
ZFCM-2	80.02	0.15	2.78	2.78	0.997
ZFCM-3	94.51	0.17	3.02	2.98	0.995
ZFCM-4	115.34	0.19	3.18	3.11	0.997
ZFCM-5	138.99	0.23	3.47	3.18	0.994
ZFCM-6	119.60	0.19	3.30	3.07	0.997
ZFCM-7	96.38	0.18	3.19	3.02	0.995

The adsorption abilities of the ZFCMs samples were studied, which are in turn to evaluate the corresponding structure-effect relationship. As observed in Fig. 5. 5(B), the pristine ZnO and Fe₃O₄ samples presented poor p-NP adsorption efficiencies of 10.8% and 11.6%, respectively, after 5h in dark. For comparison, 17.7%, 21.3%, 30.5%, 37.6%, 49.1%, 40.7% and 37.4% removal of p-NP were observed by utilizing ZFCM-1, ZFCM-2, ZFCM-3, ZFCM-4, ZFCM-5, ZFCM-6 and ZFCM-7, respectively. The adsorption abilities are in accordance with the BET variations, which confirms the enhancement of adsorption ability by increasing the specific surface area via hybridization.

The isotherms are calculated to be well fitted with the linear form of the Langmuir isotherm model as expressed below:

$$\frac{C_e}{\Gamma} = \frac{1}{\Gamma_{max}} C_e + \frac{1}{K_L \Gamma_{max}}, \quad [5]$$

where C_e is concentration of adsorbate at equilibrium, Γ_{max} is the saturated adsorption capacity, and K_L is the adsorption equilibrium constant. In line with the highest value of Γ_{max} and K_L , ZFCM-5 exhibited the best adsorption of p-NP as shown in Fig. 5. 5(B).

The favourable adsorption of p-NP by ZFCM-5 was also confirmed by the separation factor R_L , which was a dimensionless constant calculated by equation [6].

$$R_L = \frac{1}{1+K_L C_0} \quad [6]$$

Where, K_L is the Langmuir constant (mg g^{-1}) and C_0 is initial concentration of adsorbate (mg g^{-1}). Fig. 5. 6(A)(inset) indicated that the affinity between p-NP and ZFCM-5 was stronger than that with either ZnO or Fe_3O_4 .

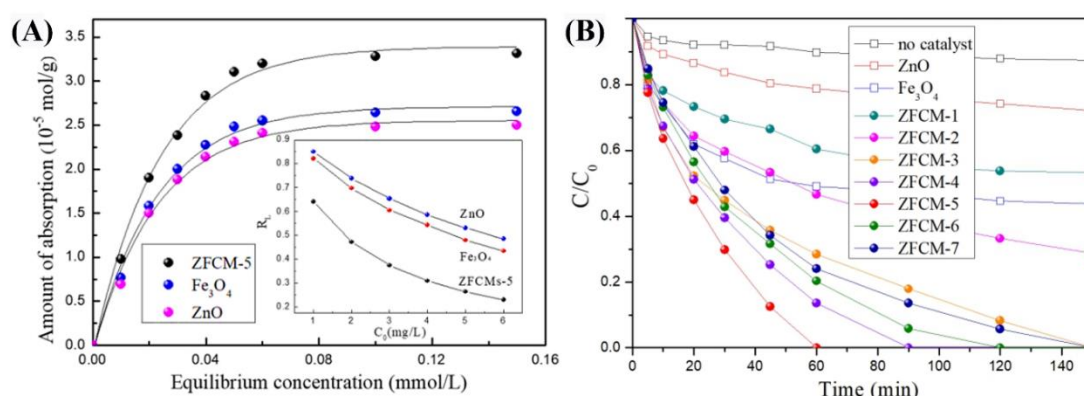


Fig. 5. 6. (A) Adsorption isotherms of p-NP at 25 °C on ZnO, Fe_3O_4 and ZFCM-5. Inset is the plot of R_L against initial concentration of p-NP; (B) Degradation rate of p-NP on different samples.

After reaching the adsorption-desorption-equilibrium in 5 h, the incandescent lamp was switched on to start the reaction. As shown in Fig. 5. 6(B), the self-photolysis of recalcitrant p-NP was less than 5% after 150 min irradiation. Pristine ZnO and Fe_3O_4 removed 28.0% and 56.3% of p-NP, respectively. In contrast, ZFCM-5 could degrade 100% of the pollutant in 60 min. Fig. 5. 7 shows the concentration of the detected H_2O_2 increased in the earlier stages of the reaction (0–15 min) which reached the highest value (197 $\mu\text{mol/L}$) at 15 min. With the photocatalytic reaction proceeding, the concentration of H_2O_2 decreased gradually, indicating the self-generated H_2O_2 was consumed by Fe^{2+} to form Fe^{3+} .

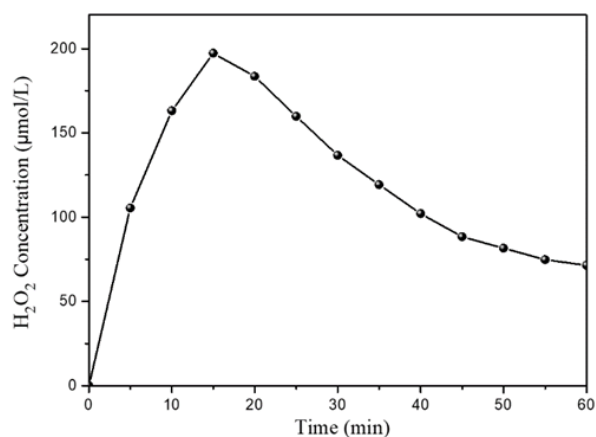


Fig. 5. 7. Changes of the H₂O₂ concentration with reaction time using ZFCM-5 as a catalyst under visible light irradiation.

In addition, reaction temperature is a key operating factor in photocatalysis. p-NP degradation was examined within a temperature range of 15 to 45 °C for ZFCM-5, and the results are shown in Fig. 5. 8. All of these reaction profiles were then fitted with the first order kinetics, and the kinetic rate constants are presented in Table 5. 2. As can be seen, the calculated reaction rate constants (k) were 0.0157, 0.0213, 0.0291 and 0.0320 min⁻¹ at 15, 25, 35 and 45 °C, respectively. By applying the Arrhenius equation (the inset of Fig. 5. 8), the activation energy (E_a) of the catalytic reaction for ZFCM-5 can be calculated as 18.5 kJ/mol.

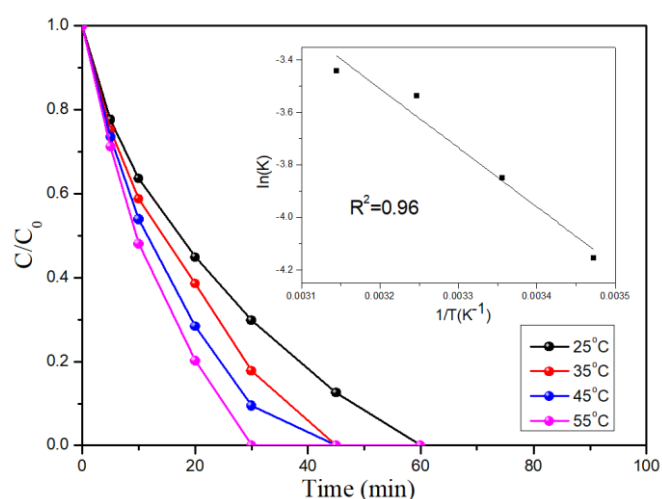


Fig. 5. 8. Effect of reaction temperature.

Table 5. 2 Kinetic parameters in p-nitrophenol degradation

Catalyst	T(°C)	k(min ⁻¹)	R ² of k	E _a (kJ mol ⁻¹)	R ² of E _a
ZFCM-5	15	0.0157	0.94	18.5	0.96
	25	0.0213	0.95		
	35	0.0291	0.96		
	45	0.0320	0.97		

ZFCM-5 presented the highest p-NP removal among the catalysts in Table 5. 3, compared to other reported values in the literature. In conventional Fenton-like heterogeneous p-NP degradation using pure Fe₃O₄ NPs, 620 mM external H₂O₂ was required to reach 95% removal with catalyst dosage and reaction duration 6 and 10 times as high as these of ZFCM-5, respectively [40].

Table 5. 3. Comparison of p-nitrophenol degradation on various catalysts.

Catalyst	C _{catalyst} (mg/L)	C _{p-NP} (mg/L)	Light condition	Time (min)	Degradation amount (%)	Ref.
ZnO@Fe₃O₄ (ZFCM-5)	250	35	100W lamp	60	100	This work
Fe₃O₄ + 620 mM H₂O₂	1500	35	No lamp	600	95	[40]
ZnO	5000	30	Solar light	190	100	[41]
Fe³⁺ - Doped ZnO	1000	20	400W lamp	300	75	[45]
Fe₃O₄@SiO₂ @ZnO	800	30	300W lamp	Hg 120	99	[7]
Fe₃O₄@ZnO	600	10	250W lamp	Hg 60	98.3	[46]
ZnO	600	10	250W lamp	Hg 60	91.6	[46]

In another study, 20 times more dosage of pristine ZnO was needed to degrade 100% p-NP in 190 min [41]. We hypothesize that the excellent performance of ZFCM-5 stems

from three factors: improved adsorption capacity by the interconnected mesopores, improved light absorption and e^-/h^+ transportation on Fe_3O_4 -ZnO heterojunction, and most predominantly the in-situ generation of H_2O_2 . More optical properties and band structure of ZnO, Fe_3O_4 and ZFCM-5 were probed to verify the reaction mechanism. The optical properties and band structures of ZnO, Fe_3O_4 and ZFCM-5 were investigated utilising UV-vis DRS, PL spectrum and room temperature Mott-Schottky analysis. As observed in Fig. 5. 9(A), the absorption spectrum of ZnO exhibited a steep edge at wavelength of around 325 nm, illustrating the main absorption in ultraviolet light region. While Fe_3O_4 revealed an extended absorption range, ZFCM-5 had an increased absorption at the wavelength ranging from 380 to 700 nm, mirroring the existence of the transition bands in ZFCM-5 composite. In general, alternation of light absorption is due to the impurities which result in more vacancies; these factors would further affect PL and photocatalytic properties.

UV-vis DRS were converted into absorbance via the Kubelka-Munk function, as shown in equation [7].

$$F(R) = \frac{(1 - R)^2}{2R} = \frac{K}{S} \quad [7]$$

Where, R is the diffuse reflectance, K is the absorption coefficient, and S is the scattering coefficient. The band gap energy values of ZnO, Fe_3O_4 , and ZFCM-5 samples are about 3.05, 2.60 and 2.35 eV, respectively. Hence, it is observed that the band gap of the assembled ZnO and Fe_3O_4 composite sample considerably decreased.

The accelerated transfer of charge carriers was investigated based on PL spectra (Fig. 5. 9(B)). As shown, when the exciting light at 370 nm irradiated on the composites, the intensity of single luminescence peak of ZFCM-5 dropped remarkably between 380 and 600 nm as compared with those of pristine ZnO and Fe_3O_4 . Such an observation can help explain that the presence of impurities can exert a synergistic effect on separation and capture efficiency of the holes photoexcited from the valance bands of ZnO and Fe_3O_4 , thereby inhibiting direct luminescent charge recombination. The

scattering effect of ZFCM-5 was also enhanced owing to an enlarged pore volume, which could provide more surface terminal sites for transfer and separation of the photoinduced holes. It is clear that the combination of Fe_3O_4 and ZnO can effectively inhibit the recombination of photo-generated electron-hole pairs, therefore improving the photocatalytic degradation performance [42-44].

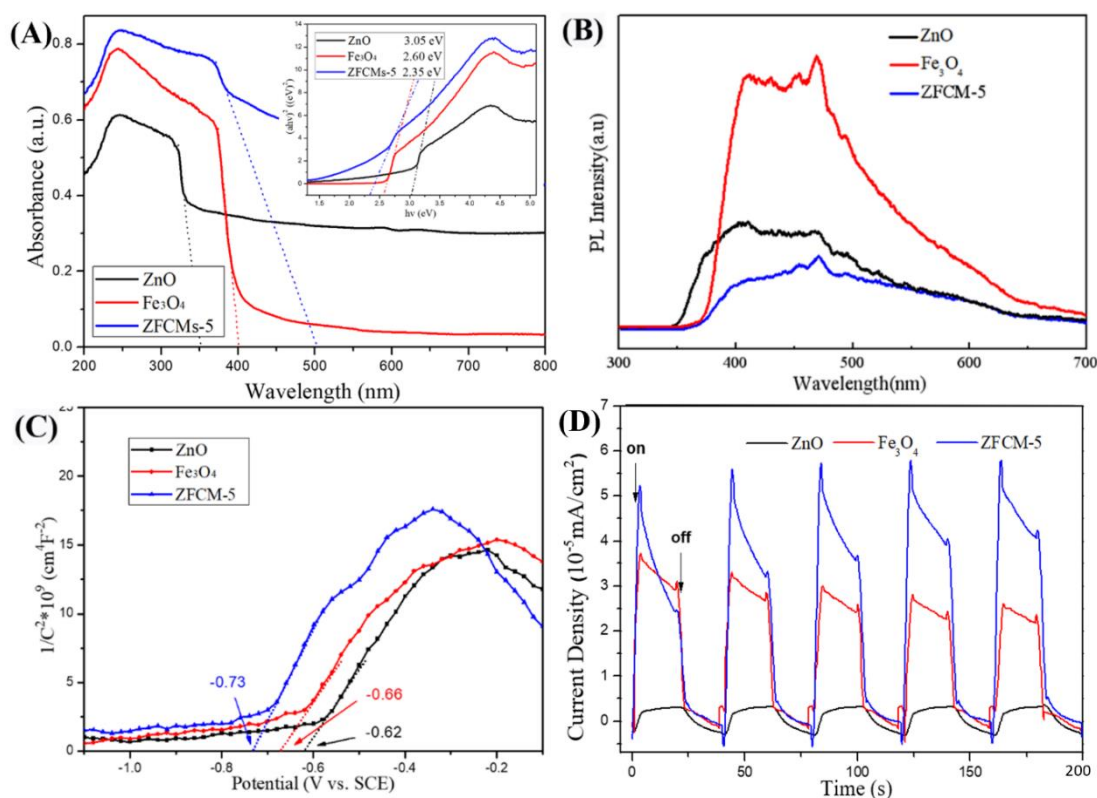
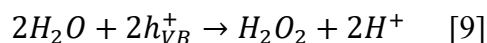
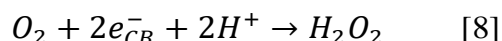


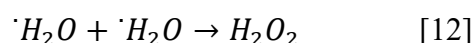
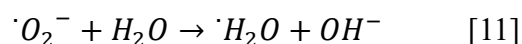
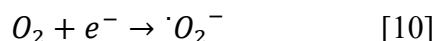
Fig. 5. 9. (A) UV-Vis diffuse reflectance spectra of the prepared samples, the inset shows the dependence of $(ah\nu)^2$ on photon energy ($h\nu$); (B) PL spectra; (C) Mott-Schottky plots; (D) Transient photocurrent responses.

As shown in Fig. 5. 9(C), the flat band potentials of ZnO, Fe_3O_4 and ZFCM-5 were determined by the Mott-Schottky plots as -0.62 , -0.66 and -0.73 V, respectively, revealing a smaller barrier for charge transfer in ZFCM-5. Similar observations were reported in Fe-doped ZnO. However, the doped ZnO could only degrade 75% p-NP with catalyst dosage, lamp power and reaction duration being 4, 4 and 5 times higher, respectively, than these of ZFCM-5 [45]. Apparently, there must be other mechanism involved in the degradation.

The generation of H₂O₂ over illuminated ZnO has been well explored as follows [17]:

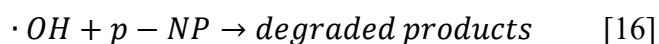
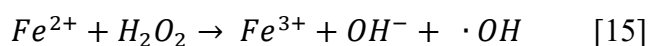
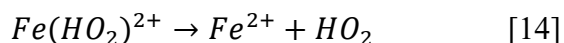


Even in the dark, H₂O₂ could be significantly produced from aqueous suspension of ZnO [47, 48]:



Prasanna proposed that nano ZnO had singly ionized oxygen vacancy, i.e., oxygen vacancy with one electron. Oxygen from the atmosphere could react with an electron from the ZnO surface to form a superoxide radical as shown in Equation 10. Superoxide then reacted with water to form hydroperoxyl radicals and radicals could recombine to form H₂O₂ (Equation 11 and 12).

It is reasonable to propose that the photo-Fenton degradation of p-NP involves the following reactions in our system.



In addition to providing Fe²⁺/Fe³⁺ for Fenton reaction, Fe₃O₄ showed strong absorption up to a wavelength of 400 nm as displayed in Fig. 5. 9(A). Hence, Fe₃O₄ might also act as a photocatalyst in addition to its function as the Fenton catalyst.

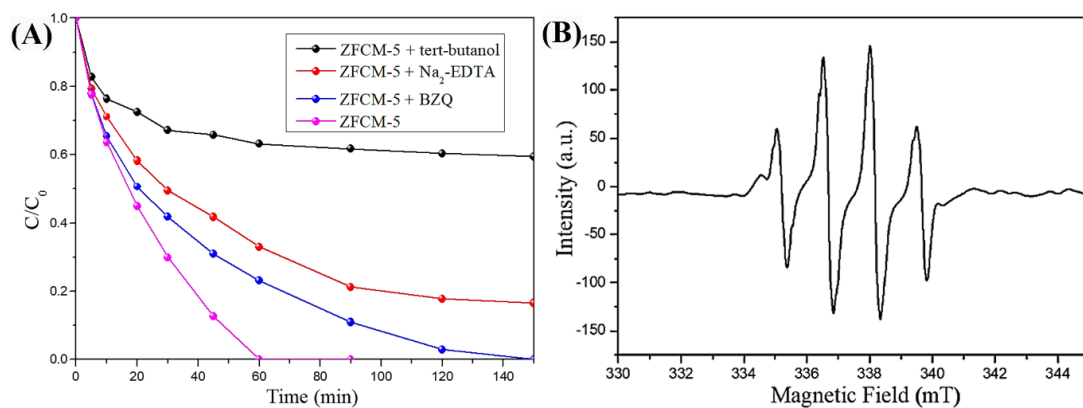


Fig. 5.10. (A) Reduced degradation efficiency of p-NP with the presence of hole and radical quenching agents. (B) EPR result of DMPO-•OH.

As shown in Fig. 5.10(A), hole and radical scavengers, BZQ (O_2^- scavenger), Na₂-EDTA (photo-generated h^+ scavenger), and tert-butanol (OH^\bullet scavenger), were employed to differentiate the major reactive oxygen species (ROS) in the degradation process [49-51]. The removal rates were remarkably inhibited by adding the quenchers and the quenching effect follows the order of tert-butanol > Na₂-EDTA > BZQ, suggesting that photo-Fenton generated OH^\bullet plays a key role for p-NP degradation. EPR spectra were recorded using DMPO as the trapping agent [52]. As displayed in Fig. 5.10(B), when the mixed suspension is irradiated by UV-visible light, the strong signals of spin-trapped OH^\bullet could be detected, confirming the primary role of OH^\bullet in this degradation system.

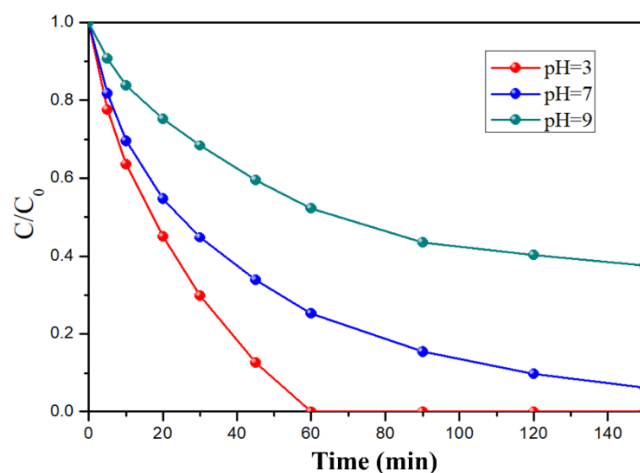


Fig. 5.11. Effect of pH values on p-nitrophenol degradation on ZFCM-5.

Degradation experiments were carried out at pH = 3, 7 and 9 (Fig. 5.11). ZFCM-5

showed the best performance at pH of 3. The result is in consistent with the general observation that a pH range of 2 - 4 is optimal for Fenton reactions [53, 54]. One reason is the oxidation potential of $\bullet\text{OH}$ decreases as the pH of the reaction mixture increases [53]. Another reason is the catalyst activity is reduced by the formation of Fe(II) complexes such as $[\text{Fe}(\text{II}) (\text{H}_2\text{O})_6]^{2+}$, which reacts more slowly with H_2O_2 [47].

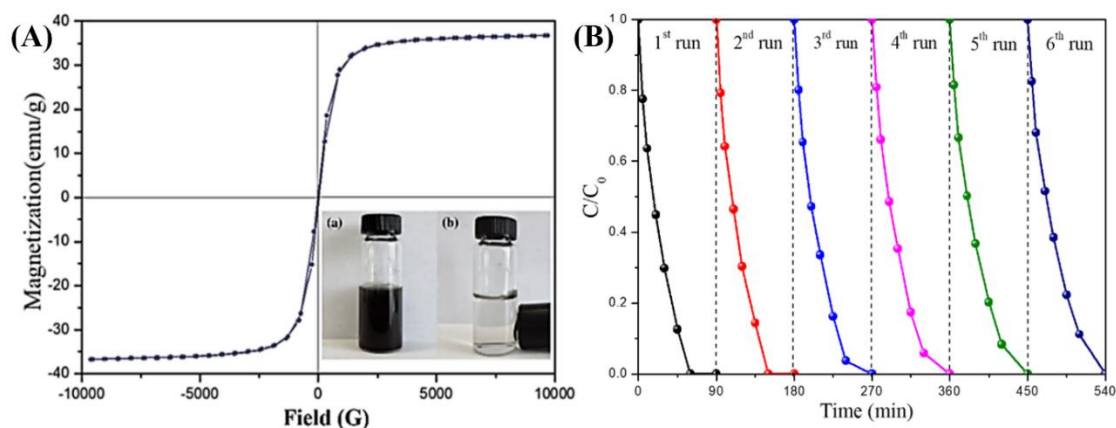
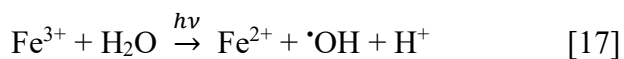


Fig. 5.12 (A) Magnetization curve of ZFCM-5 recorded at room temperature. The inset shows the suspension of ZFCM-5 (a) and separation of ZFCM-5 by an external magnetic field (b); (B) Recycle tests on ZFCM-5.

The magnetic behavior of ZFCM-5 was studied by room temperature VSM measurements. Fig. 5.12(A) exhibits that the saturation magnetization was 36.7 emu/g. The homogeneous dispersion of the ZFCM-5 microspheres could be separated quickly via an external magnet.

As the reusability of the catalyst is an important parameter in the photodegradation process, the repetitive use of ZFCM-5 was investigated under identical conditions. As shown in Fig. 5.12(B), after each run, the catalyst was separated from treated solution by magnetic separation. Results indicate that the ZFCM-5 photocatalyst could be reused effectively for at least six times without an obvious loss of activity, agreeing well with the stable photocurrent density in Fig. 5.9(D). The excellent reusability is attributed to the smart design of Fe_3O_4 shell. Under UV-vis irradiation, Fe (III) can be reduced to Fe

(II) as depicted in equation 17,



The Fe^{2+} can react with self-generated H_2O_2 to produce more $\cdot\text{OH}$ (equation 15) for p-NP decomposition.

5. 4. Conclusions

H_2O_2 consumption is the critical component of the operating costs in Fenton technology to treat highly polluted industrial effluents. It will be desirable to achieve in-situ generation of H_2O_2 at the catalytic sites, which will increase the reaction efficiency, reduce the process cost and avoid the potential hazards of the bulk H_2O_2 . This paper reports the intelligent layer-by-layer construction of $\text{ZnO@Fe}_3\text{O}_4$ composites for advanced oxidation of p-nitrophenol. In contrast to pure ZnO or Fe_3O_4 , the customized ZFCM-5 provides enhanced catalytic performance with 100% removal of p-nitrophenol in 60 min under visible light irradiation. The ZFCM-5 possesses a surface area of $139 \text{ m}^2\text{g}^{-1}$ and a pore volume of $0.23 \text{ cm}^3 \text{ g}^{-1}$. The mesoporous structure of ZFCM-5 offers more active sites for efficient adsorption of target organics. Meanwhile, from the photochemical characterisation, the band gap of ZFCM-5 was reduced to 2.35 eV, which leads to a remarkable visible-light-responsive photocatalyst. Furthermore, ZFCM-5 showed not only the phenomenon of superparamagnetism, but also the presence of abundant $\text{Fe}^{2+}/\text{Fe}^{3+}$ pairs for Fenton reaction. Most importantly, with the self-generated H_2O_2 , the composite outperformed conventional $\text{Fe}_3\text{O}_4/\text{H}_2\text{O}_2$ Fenton-like reagents and $\text{ZnO@SiO}_2@\text{Fe}_3\text{O}_4$ photocatalyst even when 6 (3.2)- and 10 (2)-fold less catalyst dosage and reaction time were used. The excellent reusability further endows the composite a promising candidate for sustainable wastewater treatment.

References

1. H. Karimi-Maleh, F. Karimi, S. Malekmohammadi, N. Zakariae, R. Esmaeili, S. Rostamnia, M. L. Yola, N. Atar, S. Movaghgharnezhad, S. Rajendran, A. Razmjou, Y. Orooji, S. Agarwal and V. K. Gupta, An amplified voltammetric sensor based on platinum nanoparticle/polyoxometalate/two-dimensional hexagonal boron nitride nanosheets composite and ionic liquid for determination of N-hydroxysuccinimide in water samples. *Mol. Liq.*, 2020. 310, 113185-113191.
2. H. Karimi-Maleh, B. G. Kumar, S. Rajendran, J. Qin, S. Vadivel, D. Durgalakshmi, F. Gracia, M. Soto-Moscoso, Y. Orooji and F. Karimi, Tuning of metal oxides photocatalytic performance using Ag nanoparticles integration. *J. Mol. Liq.*, 2020. 314, 113588-113598.
3. H. Karimi-Maleh, C. T. Fakude, N. Mabuba, G. M. Peleyeju and O. A. Arotiba, The determination of 2-phenylphenol in the presence of 4-chlorophenol using nano- Fe_3O_4 /ionic liquid paste electrode as an electrochemical sensor. *J. Colloid Interface Sci.*, 2019. 554, 603-610.
4. R. Chen, C. Yin, H. Liu and Y. Wei, Degradation of rhodamine B during the formation of Fe_3O_4 nanoparticles by air oxidation of $\text{Fe}(\text{OH})_2$. *J. Mol. Catal. A: Chem.*, 2015. 397, 114-119.
5. N. Alhokbany, T. Ahama, Ruksana, M. Naushad and S. Alshehri, AgNPs embedded N- doped highly porous carbon derived from chitosan based hydrogel as catalysts for the reduction of 4-nitrophenol. *Composites Part B*, 2019. 17315, 106950-106958.
6. A. Sangili, M. Annalakshmi, S.-M. Chen, P. Balasubramanian and M. Sundrarajan, Synthesis of silver nanoparticles decorated on core-shell structured tannic acid-coated iron oxide nanospheres for excellent electrochemical detection and efficient catalytic reduction of hazardous 4-nitrophenol. *Composites Part B*, 2019. 1621, 33-42.

7. Y. Qin, H. Zhang, Z. Tong, Z. Song and N. Chen, A facile synthesis of $\text{Fe}_3\text{O}_4@\text{SiO}_2@\text{ZnO}$ with superior photocatalytic performance of 4-nitrophenol. *J. Environ. Chem. Eng.*, 2017. 5, 2207-2213.
8. K. Liu, Y. Qin, Y. Muhammad, Y. Zhu, R. Tang, N. Chen, H. Shi, H. Zhang, Z. Tong and B. Yu, Effect of Fe_3O_4 content and microwave reaction time on the properties of $\text{Fe}_3\text{O}_4/\text{ZnO}$ magnetic nanoparticles. *J. Alloys Compd.*, 2019.781, 790-799.
9. K. M. Lee, C. W. Lai, K. S. Ngai and J. C. Juan, Recent developments of zinc oxide based photocatalyst in water treatment technology: A review. *Water Res.*, 2016. 88, 428-448.
10. H. Sun, S. Liu, S. Liu and S. Wang, A comparative study of reduced graphene oxide modified TiO_2 , ZnO and Ta_2O_5 in visible light photocatalytic/photochemical oxidation of methylene blue. *Appl. Catal., B*, 2014.146, 162-168.
11. S. Muthulingam, I.-H. Lee and P. Uthirakumar, Highly efficient degradation of dyes by carbon quantum dots/N-doped zinc oxide (CQD/N-ZnO) photocatalyst and its compatibility on three different commercial dyes under daylight. *J. Colloid Interface Sci.*, 2015. 455, 101-109.
12. F. I. A. Bakar, K. A. Birang, M. A. M. Adnan, J. A. Razak and S. Ismail, Formation of Cobalt Doped Zinc Oxide Photocatalyst for Methyl Orange Degradation. *Solid State Phenom.*, 2017. 264, 211-214.
13. H. H. Mohamed, I. Hammami, S. Akhtar and T. E. Youssef, Highly efficient Cu-phthalocyanine-sensitized ZnO hollow spheres for photocatalytic and antimicrobial applications. *Composites Part B*, 2019. 1761, 107314-107322.
14. Y. Huang, Y. Wei, J. Wu, C. Guo, M. Wang, S. Yin and T. Sato, Low temperature synthesis and photocatalytic properties of highly oriented $\text{ZnO}/\text{TiO}_{2-x}\text{N}_y$ coupled photocatalysts. *Appl. Catal., B*, 2012. 123, 9-17.
15. W. Muersha and G. S. P. Soylu, Effects of metal oxide semiconductors on the photocatalytic degradation of 4-nitrophenol. *J. Mol. Struct.*, 2018.1174, 96-102.

16. Y. He, Y. Wang, L. Zhang, B. Teng and M. Fan, High-efficiency conversion of CO₂ to fuel over ZnO/g-C₃N₄ photocatalyst. *Appl. Catal., B*, 2015.168-169, 1-8.
17. F. Xu, Y. Yuan, H. Han, D. Wu, Z. Gao and K. Jiang, Synthesis of ZnO/CdS hierarchical heterostructure with enhanced photocatalytic efficiency under nature sunlight. *Cryst. Eng. Comm.*, 2012. 14, 3615-3622.
18. Q. Zhang, C. Tian, A. Wu, Y. Hong, M. Li and H. Fu, In situ oxidation of Ag/ZnO by bromine water to prepare ternary Ag–AgBr/ZnO sunlight-derived photocatalyst. *J. Alloys Compd.* 2013. 563, 269-273.
19. Y. Koo, G. Littlejohn, B. Collins, Y. Yun, V. N. Shanov, M. Schulz, D. Pai and J. Sankar, Synthesis and characterization of Ag–TiO₂–CNT nanoparticle composites with high photocatalytic activity under artificial light. *Composites Part B*, 2014. 57, 105-111.
20. A. Kadam, R. Dhabbe, A. Gophane, and K. Garadka, Template free synthesis of ZnO/Ag₂O nanocomposites as a highly efficient visible active photocatalyst for detoxification of methyl orange. *J. Photochem. Photobiol., B*, 2016. 154, 24-33.
21. Y. Zhang, J. Li, N. Ma, Z. Meng and G. Sui, Processing cellulose@Fe₃O₄ into mechanical, magnetic and biodegradable synapse-like material. *Composites Part B*, 2019. 17715, 107432-107440.
22. R. Chen, G. Song and Y. Wei, Synthesis of variable-sized Fe₃O₄ nanocrystals by visible light irradiation at room temperature. *J. Phys. Chem. C*, 2010. 114, 13409-13413.
23. R. Chen, J. Cheng and Y. Wei, Preparation and magnetic properties of Fe₃O₄ microparticles with adjustable size and morphology. *J. Alloys. Compd.*, 2012. 520, 266-271.
24. M. Usman, P. Faure, C. Ruby and K. Hanna, Remediation of PAH-contaminated soils by magnetite catalyzed Fenton-like oxidation. *Appl. Catal., B*, 2012. 117, 10-17.

25. K. Hanna, T. Kone and G. Medjahdi, Synthesis of the mixed oxides of iron and quartz and their catalytic activities for the Fenton-like oxidation. *Catal. Comm.*, 2008. 9, 955-959.
26. X. Xue, K. Hanna, M. Abdelmoula and N. Deng, Adsorption and oxidation of PCP on the surface of magnetite: Kinetic experiments and spectroscopic investigations. *Appl. Catal., B*, 2009. 89, 432-440.
27. L. Hu, Z. Liu, C. He, P. Wang, S. Chen, J. Xu, J. Wu, H. Wang and H. Wang, Ferrous-oxalate-decorated polyphenylene sulfide fenton catalytic microfiber for methylene blue degradation. *Composites Part B*, 2019. 1761, 107220 -107228.
28. Y.-G. Zhang, L.-L. Ma, J.-L. Li and Y. Yu, In Situ Fenton Reagent Generated from TiO₂/Cu₂O Composite Film: a New Way to Utilize TiO₂ under Visible Light Irradiation. *Environ. Sci. Technol.*, 2007. 41, 6264-6269.
29. X. Zhang, J. Wu, G. Meng, X. Guo, C. Liu and Z. Liu, One-step synthesis of novel PANI-Fe₃O₄@ZnO core-shell microspheres: An efficient photocatalyst under visible light irradiation. *Appl. Surf. Sci.*, 2016. 366, 486-493.
30. A. J. Hoffman, E. R. Carraway and M. R. Hoffmann, Photocatalytic Production of H₂O₂ and Organic Peroxides on Quantum-Sized Semiconductor Colloids. *Technol.*, 1994. 28, 776-785.
31. B. Pal and M. Sharon, Photocatalytic formation of hydrogen peroxide over highly porous illuminated ZnO and TiO₂ thin film. *Toxicol. Environ. Chem.*, 2000. 78, 233-241.
32. X. Domènech, J. A. Ayllón and J. Peral, H₂O₂ Formation from photocatalytic processes at the ZnO/water interface. *Environ. Sci. Pollut. Res.*, 2001. 8, 285-287.
33. X. Feng, H. Guo, K. Patel, H. Zhou and X. Lou, High performance, recoverable Fe₃O₄-ZnO nanoparticles for enhanced photocatalytic degradation of phenol. *Chem. Eng. J.*, 2014. 244, 327-334.

34. M. Xu, Q. Li and H. Fan, Monodisperse nanostructured Fe₃O₄/ZnO microrods using for waste water treatment. *Adv. Powder Technol.*, 2014. 25, 1715-1720.
35. R. Y. Hong, S. Z. Zhang, G. Q. Di, H. Z. Li, Y. Zheng, J. Ding and D. G. Wei, Preparation, characterization and application of Fe₃O₄/ZnO core/shell magnetic nanoparticles. *Mater. Res. Bull.*, 2008. 43, 2457-2468.
36. R. Hong, T. Pan, J. Qian and H. Li, Synthesis and surface modification of ZnO nanoparticles. *Chem. Eng. J.*, 2006. 119, 71-81.
37. J. Feng, J. Mao, X. Wen and M. Tu, Ultrasonic-assisted in situ synthesis and characterization of superparamagnetic Fe₃O₄ nanoparticles. *J. Alloys. Compd.*, 201. 509, 9093-9097.
38. H. Liu, Y. Guo, N. Wang, B. Liu, Y. Zhang, H. Liu and R. Chen, Controllable synthesis and photocatalytic activity of ultrathin hematite nanosheets. *J. Alloys. Compd.*, 2019. 771, 343-349.
39. X. Liu, Z. Ma, J. Xing and H. Liu, Preparation and characterization of amino-silane modified superparamagnetic silica nanospheres. *J. Magn. Magn. Mater.*, 2004. 270, 1-6.
40. S.-P. Sun and A. T. Lemley, p-Nitrophenol degradation by a heterogeneous Fenton-like reaction on nano-magnetite: Process optimization, kinetics, and degradation pathways. *J. Mol. Catal. A: Chem.*, 2011. 349, 71-79.
41. M. Sugiyama, Z. Salehi, M. Tokumura and Y. Kawase, Photocatalytic degradation of p-nitrophenol by zinc oxide particles. *Water Sci. Technol.*, 2012. 65, 1882-1886.
42. H. Wu, H. L. Tan, C. Y. Toe, J. Scott, L. Wang, R. Amal and Y. H. Ng, Photocatalytic and Photoelectrochemical Systems: Similarities and Differences. *Adv. Mater.*, 2020. 32, 1904717- 1904788.
43. H. L. Tan, F. F. Abdi and Y. H. Ng, Heterogeneous photocatalysts: an overview of classic and modern approaches for optical, electronic, and charge dynamics evaluation.

Chem. Soc. Rev., 2019. 48, 1255-1271.

44. H. Wu, Z. Zheng, Y. Tang, N. Huang, R. Amal, H. N. Lim and Y. H. Ng, Pulsed electrodeposition of CdS on ZnO nanorods for highly sensitive photoelectrochemical sensing of copper (II) ions. *Sustain. Mater. Technol.*, 2018. 18, e00075-e00081.
45. E. Rokhsat and A. Khayatian, Enhanced photocatalytic activity of Fe doped ZnO hierarchical nanosheets on the degradation of p-nitrophenol under visible light. *Inorg. Nano-Met. Chem.*, 2018. 48, 203-209.
46. Y. Wu, T. He, W. Xu and Y. Li, Preparation and photocatalytic activity of magnetically separable Fe₃O₄@ZnO nanospheres. *J. Mater. Sci.-Mater. Electron.*, 2016. 27, 12155-12159.
47. X. Xu, D. Chen, Z. Yi, M. Jiang, L. Wang, Z. Zhou, X. Fan, Y. Wang and D. Hui, Antimicrobial Mechanism Based on H₂O₂ Generation at Oxygen Vacancies in ZnO Crystals. *Langmuir*, 2013. 29, 5573-5580.
48. V. L. Prasanna and R. Vijayaraghavan, Insight into the Mechanism of Antibacterial Activity of ZnO: Surface Defects Mediated Reactive Oxygen Species Even in the Dark. *Langmuir*, 2015. 31, 9155-9162.
49. X. Yang, H. Cui, Y. Li, J. Qin, R. Zhang and H. Tang, Fabrication of Ag₃PO₄-Graphene Composites with Highly Efficient and Stable Visible Light Photocatalytic Performance. *Acs Catal.*, 2013. 3, 363-369.
50. H. Cui, X. Yang, Q. Gao, H. Liu, Y. Li, H. Tang, R. Zhang, J. Qin and X. Yan, Facile synthesis of graphene oxide-enwrapped Ag₃PO₄ composites with highly efficient visible light photocatalytic performance. *Mater. Lett.*, 2013. 93, 28-31.
51. R. Chen, L. Yang, Y. Guo, W. Zheng, H. Liu and Y. Wei, Effect of p-nitrophenol degradation in aqueous dispersions of different crystallized goethites. *J. Mol. Catal. A: Chem.*, 2018. 353, 337-343.

52. L. Zang, K. Stone and W. Pryor, Detection of free radicals in aqueous extracts of cigarette tar by electron spin resonance. *Free Radical Biol. Med.*, 1995. 19, 161-167.
53. B. K. Mert, T. Yonar, M. Y. Kiliç and K. Kestioğlu, Pre-treatment studies on olive oil mill effluent using physicochemical, Fenton and Fenton-like oxidations processes. *J. Hazard. Mater.*, 2010. 174, 122-128.
54. A. M. F. M. Guedes, L. M. P. Madeira, R. A. R. Boaventura and C. A. V. Costa, Fenton oxidation of cork cooking wastewater—overall kinetic analysis. *Water Res.*, 2003. 37, 3061-3069.

Every reasonable effort has been made to acknowledge the owners of copyright material. I would be pleased to hear from any copyright owner who has been omitted or incorrectly acknowledged.

Chapter 6. MXene as non-metal charge mediator in 2D layered CdS@Ti₃C₂@TiO₂ composites with superior Z-scheme visible light-driven photocatalytic activity

Abstract

Exploitation of photocatalysts towards efficient organic pollutant degradation is highly desirable in the field of environmental remediation. Here, we report a rational synthesis of two-dimensional CdS@Ti₃C₂@TiO₂ nanohybrids by facile calcination and a subsequent hydrothermal process. The physico-chemical properties of CdS@Ti₃C₂@TiO₂ were investigated by a variety of characterization techniques. The effect of CdS loading on the photocatalytic performance was elucidated. When compared with Ti₃C₂ and Ti₃C₂@TiO₂, the optimal ternary nanostructures exhibited significantly enhanced visible light-driven ($\lambda \geq 420$ nm) degradation of sulfachloropyridazine, phenol and several typical dyes. The origin of improved photocatalytic performance mainly stems from the enhanced electron-hole separation efficiency. The charge carrier sinking function of Ti₃C₂ in this first time pre-fabricated three-phase Z-scheme catalyst was proposed based on UV-visible spectroscopy band gap calculation, photoluminescence measurement and photoelectrochemical analysis. The electron paramagnetic resonance assay verified that both superoxide ions and hydroxyl radicals played crucial roles in the removal of contaminants.

The content of this chapter is published in *Environ. Sci.: Nano*, 2019, 6, 3158

6.1 Introduction

In recent years, the growing interests in two-dimensional (2D) photocatalysts are driven by the apparent merits of cost-effective and environmentally benign routes for degradation of aqueous pollutants [1]. Especially, since the first synthesis of Ti_3C_2 by etching the Al atoms in layered Ti_3AlC_2 , MXene material has become one of the most promising candidates due to its high specific surface area, narrow band gap and fast electron transfer ability [2,3]. However, MXene is associated with the problem of fast charge recombination which considerably limits its practical use. To overcome this inherent problem, various methods have been developed, including stoichiometry engineering and coupling with other semiconductors. For example, based on density functional theory and the cluster expansion method, the $\text{Ti}_{2(1-x)}\text{Zr}_{2x}\text{CO}_2$ alloy with $x = 0.2778$ has been predicated to be the most promising water-splitting photocatalyst when compared with Ti_2CO_2 and Zr_2CO_2 [4]. A variety of semiconductors such as C_3N_4 , Fe_2O_3 and TiO_2 are coupled with MXene to form the heterojunction that promote photogenerated electron-hole separation and improve the light absorbance for photocatalytic reactions [5-7].

Besides bandgap alteration and co-catalyst introduction, another strategy to boost photocatalyst performance is the formation of a cascading junction (Z-scheme) structure [8]. Successful ternary Z-scheme photocatalysts often employ noble metals like Au and Ag, as the electron-transfer component [9-11]. A representative example is $\text{CdS@Au@C}_3\text{N}_4$ nanocomposite, where Au nanoparticles were designed to trap photoinduced conduction band (CB)-electrons of CdS and valence band (VB)-holes of C_3N_4 . As a result, the reduction and oxidation catalytic centres were maintained in C_3N_4 and CdS to minimize an undesirable back-reaction of photocatalytic products. Also, a larger overpotential was obtained due to a high conduction band minimum of C_3N_4 and a low valence band maximum of CdS [12,13]. To replace the prohibitively expensive metal nanoparticles, several promising noble metal-free electron mediators such as

$[\text{Co}(\text{bpy})_3]^{2+}/[\text{Co}(\text{bpy})_3]^{3+}$ (bpy=2, 2'-bipyridine) redox couple and reduced graphene oxide have been developed [14,15]. Most bare and terminated MXenes have very small bandgaps or possess metallic conductivity, which may make them a good substitute for noble metals. Nevertheless, reduced graphene oxide (rGO) is still widely used as solid electron mediators in the Z-scheme system, due to the difficulty in formation of intimate interfacial contact among multiple components imposed by the thick layer of MXene. Recently, in-situ growth of TiO_2 on the surface of multilayer Ti_3C_2 MXene has been realized by heating 2D Ti_3C_2 in air, hydrothermal process, or hydrolysis in the presence of tetrabutyl titanate [16]. These studies have paved the way for intimate coupling of TiO_2 on 2D- Ti_3C_2 nanosheet as evidenced by the Schottky junctions formation thus Ti_3C_2 could act as electron sinks through Schottky barrier electron-trapping [17,18].

In this work, a novel composite of CdS-MXene- TiO_2 was prepared for organic pollutant degradation. For this purpose, Ti_3C_2 was firstly calcified at 500 °C to get $\text{Ti}_3\text{C}_2@\text{TiO}_2$ with suitable band edge alignments for photogenerated electron to migrate from TiO_2 to Ti_3C_2 [18]. Afterwards, hydrothermally grown CdS were chosen for the third phase of Z-scheme catalyst due to its thermodynamically favourable energy levels. The rational construction of $\text{CdS}@\text{Ti}_3\text{C}_2@\text{TiO}_2$ displayed excellent photocatalytic activity and recycling stability. The possible relative charge transfer models and photocatalytic mechanisms for organic degradation have been explored. This work provide useful insights on MXene usage as a non-metal charge mediator in Z-scheme photocatalysis.

6.2. Material and Methods

6.2.1. Material preparation

6.2.1.1 Synthesis of layered Ti_3C_2

The multilayered Ti_3C_2 was fabricated by selectively exfoliating the Al layers from

Ti₃AlC₂ with HF (49 wt %) at 60 °C for 25 h while stirring. Then the solid was centrifuged, thoroughly rinsed with DI water, and dried at 60 °C in a vacuum oven overnight.

6.2.1.2 In-situ formation of Ti₃C₂@TiO₂

The obtained Ti₃C₂ powder was used to synthesize Ti₃C₂@TiO₂ via one-step calcination approach [19]. 1 g of Ti₃C₂ were firstly added into 100 ml NaOH (3 mol/L) solution and the mixture was kept in air at 60 °C for 24 h with constant stirring to form a homogeneous suspension. The resulting suspensions were centrifuged and dried at 60 °C in a vacuum oven overnight. Afterward, the treated product was calcined at 500 °C for 2 h in a muffle oven. The obtained black powder was labelled as Ti₃C₂@TiO₂.

6.2.1.3 Synthesis of CdS@Ti₃C₂@TiO₂

In a typical hybrid construction process, 0.5 g of Ti₃C₂@TiO₂ was firstly added into 100 mL CdCl₂ solution at 1, 2, 3 and 4 mol/L, respectively. Subsequently, Na₂S solution was added into the mixture dropwise at room temperature with constant stirring. Molar ratio of Na₂S to CdCl₂ was 1:1. The pH of solution containing Ti₃C₂@TiO₂, CdCl₂, and Na₂S was about 5.5. TiO₂ nanoparticle is usually positively charged at this pH value therefore Cd²⁺ should be adsorbed preferentially on negative MXene surface. Subsequently, more CdS nanoparticles were formed in tight connection with MXene. The obtained yellow colloidal precipitate was then transferred into a 120 mL Teflon-lined stainless steel autoclave and put into an oven for hydrothermal treatment at 200 °C for 6 h. After cooling, centrifugation and washing, the precipitate was dried at 85 °C in a vacuum oven overnight. The obtained samples were labelled as 1:1CTT, 2:1CTT, 3:1CTT and 4:1CTT, respectively.

6.2.2. Material characterizations

The phase composition was analysed by an X-ray diffractometer (XRD, Bruker D8 Advance) using Cu K α ($\lambda=0.15418$ nm) radiation at 40 kV and 15 mA. The morphology and microstructure of the prepared samples were revealed using field emission scanning electron microscope (FESEM, Japan S-570) equipped with an EDS (Kevex Sigma TM Quasar, USA). The Brunauer–Emmett–Teller (BET) specific surface areas of as-prepared samples were measured by N₂ adsorption–desorption isotherm with a Quantachrome NOVA touch LX4 apparatus (Quantachrome Instruments, South San Francisco, CA, USA). The chemical composition and bond were studied by X-ray photoelectron spectroscopy (XPS, ESCALAB 250, Thermo Fisher Scientific) with Al K α X-ray at 15 kV and 150 W. The optical properties of samples were investigated with UV–vis diffuse reflectance spectra (acquired by using UV–vis DRS, Hitachi U3010) and photoluminescence (PL) spectra was measured by a PerkinElmer LS55 luminescence spectrometer with a Xenon source at room temperature. The transient photocurrent response test was performed with CHI 760A electrochemical analyser (CHI, Shanghai) using a 300 W Xe lamp (cutting off $\lambda < 400$ nm) to produce visible light irradiation. A platinum wire and saturated Ag/AgCl electrode was used as the counter and reference electrode, respectively. To prepare working electrode, 5 mg samples were dispersed into 250 μ L mixture of ethanol and Nafion under ultrasonication. Then 30 μ l slurry was drop-coated onto the fluorine-doped tin oxide (FTO) glass substrate. The substrates were dried in an oven at 80 °C for 3 h. The photocurrent measurement was conducted in 0.5 M aqueous Na₂SO₄ solution at 0.8 V during on-off cycling of the visible light irradiation.

6.2.3. Photocatalytic activity evaluations

The performances of various photocatalysts were evaluated by the photodegradation of sulfachloropyridazine (SCP, 20 mg/L), methylene blue (MB, 20 mg/L), Rhodamine B

(RhB, 20 mg/L) and Phenol (20 mg/L) in water solution under visible light irradiations. Specifically, the designed amount of catalyst (0.05g) was dispersed in 200 mL of organic pollutant solutions which were poured into a 1 L cylindrical double jacketed glass reactor with a 25°C thermostatic water circulation system. Prior to irradiation, the suspensions were kept on stirring for 30 min to ensure the establishment of an adsorption equilibrium. The reactor was placed 30 cm away from the light source. The visible light source employed in this study has a light intensity of 300 mW/cm² and wavelength between 400–1050 nm. After the light was turned on, 3 mL of solution was extracted in regular intervals and transferred to centrifuge tubes followed by centrifugation at 13,000 rpm for 15 min to remove the solid particles. SCP and phenol concentrations were measured by using high performance liquid chromatography (HPLC, Thermo Scientific); MB and RhB solutions were analysed by a UV-vis spectrometer (Perkin-Elmer Lambda 900UV/Vis/NIR)

6.2.4. Reactive oxygen species (ROS) capturing experiment

The electron paramagnetic resonance (EPR) measurement was carried out using a Bruker EMX-10/12 spectrometer with a 9.866 GHz magnetic field. 5,5- dimethylpyrroline N-oxide (DMPO) spin-trapping EPR method was used to determine the generation of ROS in photocatalysis.

6.3. Results and discussion

6.3.1. Structures, morphologies and textural properties of as-prepared samples

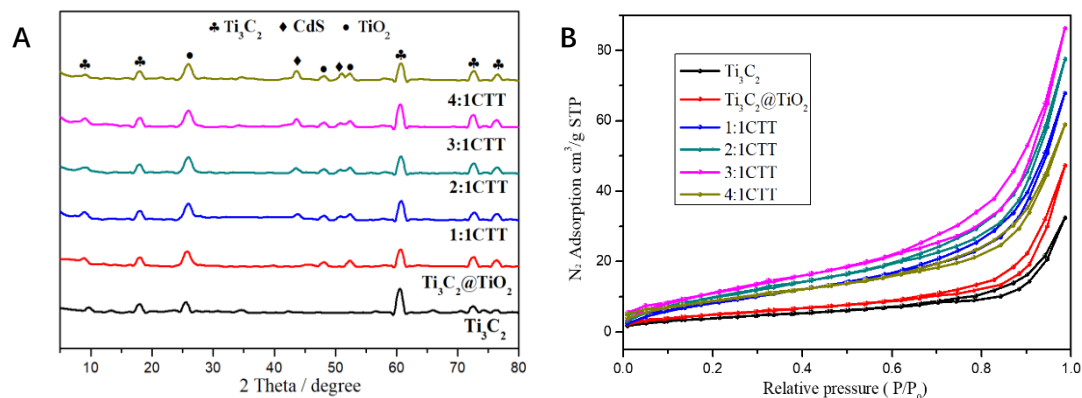


Fig. 6. 1. (A) XRD patterns and (B) nitrogen adsorption–desorption isotherms of Ti_3C_2 , $\text{Ti}_3\text{C}_2@\text{TiO}_2$, 1:1CTT, 2:1CTT, 3:1CTT and 4:1CTT.

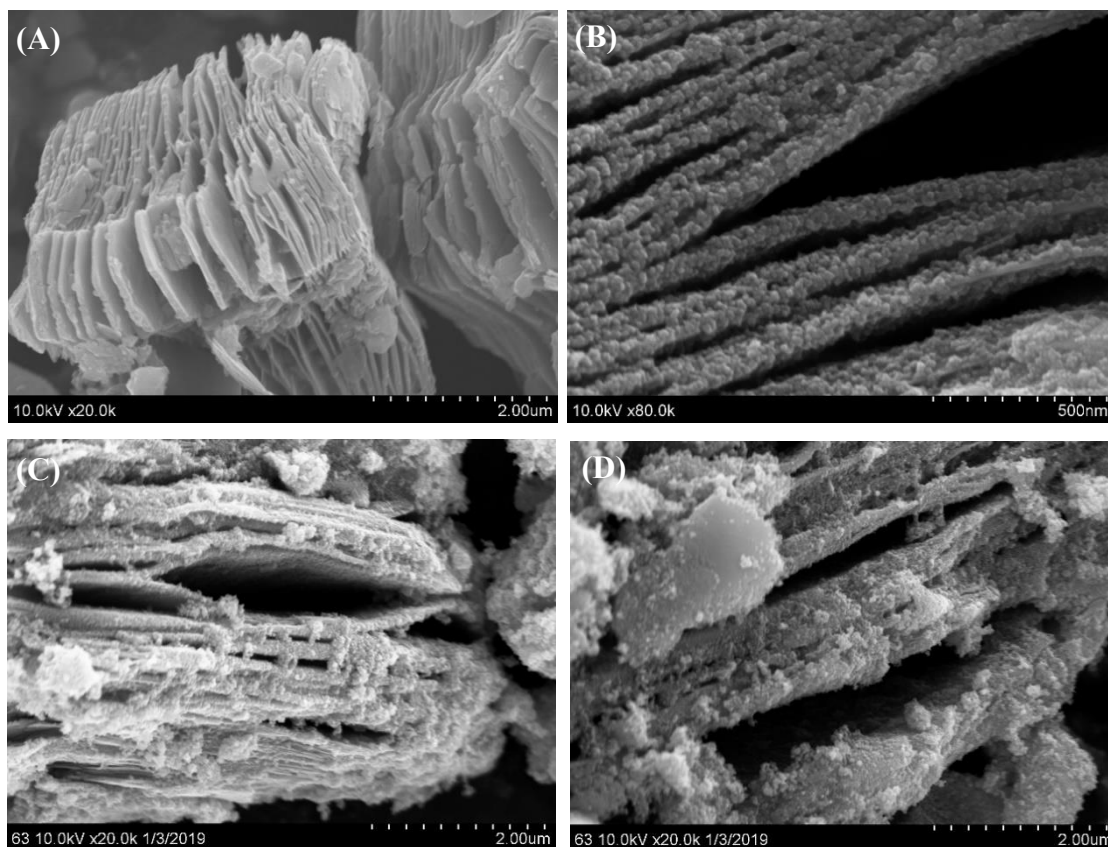
Fig. 6. 1(A) shows the X-ray diffraction patterns of the as-prepared Ti_3C_2 , $\text{Ti}_3\text{C}_2@\text{TiO}_2$, and CdS loaded $\text{Ti}_3\text{C}_2@\text{TiO}_2$. After HF etching, the intense peak at $2\theta \approx 39^\circ$ corresponding to the (104) diffraction of Ti_3AlC_2 disappeared [20]. Moreover, the (002) and (004) peaks of Ti_3AlC_2 shifted to lower 2θ values, indicating the removal of Al layers from the parent MAX [21]. Li et al. reported the synthesis of MXene $\text{Ti}_3\text{C}_2/\text{TiO}_2$ through simple calcination of Ti_3C_2 . Similarly, we obtained $\text{Ti}_3\text{C}_2/\text{TiO}_2$ hybrid as confirmed by the additional peaks at 2θ of 25.4° , 48.2° and 54.1° , which correspond to (101), (200) and (105) diffraction planes of anatase- TiO_2 [19]. The XRD results also verified the well crystallized CdS in the ternary composites. Peaks at $2\theta = 43.6, 51.9^\circ$ of (220) and (311) planes are assigned to cubic CdS [22].

Table. 6. 1. Structural properties and organic pollutant adsorption (in dark for 30 min) of different samples.

Samples	S_{BET} (m^2/g)	V_{pore} (cm^3/g)	Pore size (nm)	Adsorption (%)			
				SCP	MB	RhB	Phenol
Ti_3C_2	8.17	0.052	10	2.6	3.5	3.9	3.5
$\text{Ti}_3\text{C}_2@\text{TiO}_2$	16.83	0.073	20	4.4	3.3	5.7	4.3
1:1CTT	31.05	0.081	30-80	5.2	6.9	9.1	5.7

2:1CTT	42.38	0.119	30-80	8.7	8.1	11.8	7.5
3:1CTT	36.84	0.093	30-80	7.5	6.1	10.1	5.6
4:1CTT	25.16	0.075	30-80	5.4	6.1	8.1	5.0

The BET specific surface area (SSA) and pore size of the samples were evaluated by N₂ adsorption (Fig. 6. 1(B) and Table 6.1). In Fig. 6. 1(B), all samples display a H3 type hysteresis loop without a plateau at high P/P₀, indicating the multilayer structure with low degree of pore curvature. Compared with the Ti₃C₂ (8.17 m²/g), the SSA of Ti₃C₂@TiO₂ was increased to 16. 83 m²/g. The pore size also increased from 10 to 20 nm after calcination treatment. The hydrothermal process for CdS loading further improved the SSA of 1:1CTT because more nano-TiO₂ were formed and the maximum value of 42.38 m²/g was obtained for the 2:1CTT sample. As expected, 3:1CTT and 4:1CTT samples exhibited gradually decreasing SSA (36.84 and 25.16 m²/g) due to the blockage of CdS particles. These textural properties play important roles in organic molecule adsorption and degradation which will be discussed in the following sections.



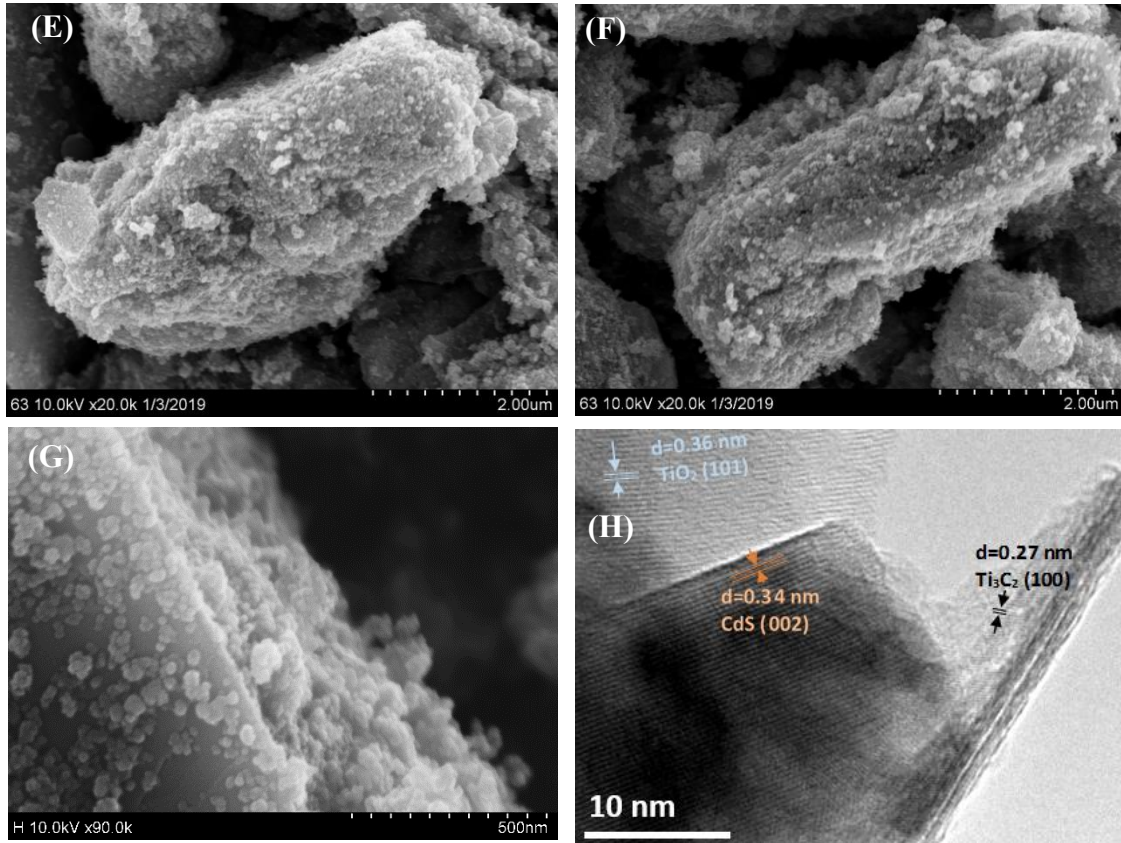


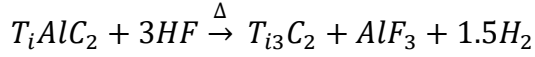
Fig. 6. 2. FESEM images of Ti_3C_2 (A), $Ti_3C_2@TiO_2$ (B), 1:1CTT (C), 2:1CTT (D), 3:1CTT (E) and 4:1CTT (F). Top view SEM and HRTEM images of the 2:1CTT sample are shown in (G) and (H), respectively.

Table 6. 2. Elemental analysis (weight percentage) of as-prepared samples.

Samples	Ti (at.%)	C (at.%)	O (at.%)	S (at.%)	Cd (at.%)
Ti_3C_2	83.78	13.54	2.68	-	-
$Ti_3C_2@TiO_2$	74.63	8.41	16.96	-	-
1:1CTT	62.54	7.23	13.22	3.81	13.20
2:1CTT	50.06	5.69	10.81	7.35	26.09
3:1CTT	37.52	4.03	8.12	11.39	38.94
4:1CTT	24.19	2.45	5.21	15.37	52.78

The morphological features and composition of the samples were further studied by FESEM, HRTEM, and EDX techniques. As shown in Fig. 6. 2(A), Ti_3AlC_2 was etched

into multilayered Ti_3C_2 with accordion-like structure. The spaces between 2D-nanosheets were caused by the release of H_2 during the exothermic reaction with HF [23]:



After air-calcination at 500 °C for 2h, the smooth surface of Ti_3C_2 became rough due to the in-situ transformation of MXene to TiO_2 (Fig. 6. 2(B)). The SEM images of $CdS@Ti_3C_2@TiO_2$ show that more particles are tightly attached on the surface of $Ti_3C_2@TiO_2$ (Fig. 6. 2(C-F)). This intimate coupling between CdS and MXene derived supporting co-catalyst may provide efficient interfacial photo-induced charge diffusion upon visible-light irradiation [24]. The EDX results in Table 6. 2 indicate that the content of CdS increased when the concentration of $CdCl_2/Na_2S$ changed from 1 to 4 mol/L. However, CdS particles in loose contact with $Ti_3C_2@TiO_2$ nanosheets are revealed in Fig. 6. 2(E, F). These particles occupied a considerably large volume of open spaces between the nanolayers thus leading to decreased BET surface area. Fig. 6. 2(G) is a representative top-view micrograph showing a few clusters of nanoparticles attached on the Ti_3C_2 sheets. In Fig. 6. 2(H), the clear lattice fringes of 0.36, 0.34 and 0.27 nm were attributed to the (101) planes of TiO_2 , (002) planes of CdS and (100) planes of Ti_3C_2 , respectively. The direct contact of CdS with Ti_3C_2 suggests that when the $CdCl_2$ solution was mixed with $Ti_3C_2@TiO_2$, the negative charges at the surface and edges of the MXene sheets can strongly attract Cd^{2+} and facilitate CdS nucleation and further growth. This hypothesis is also supported by the study of Low et al.. They found a lot of voids existed in between TiO_2 nanoparticles due to the production of CO_2 gas during the calcination process [18].

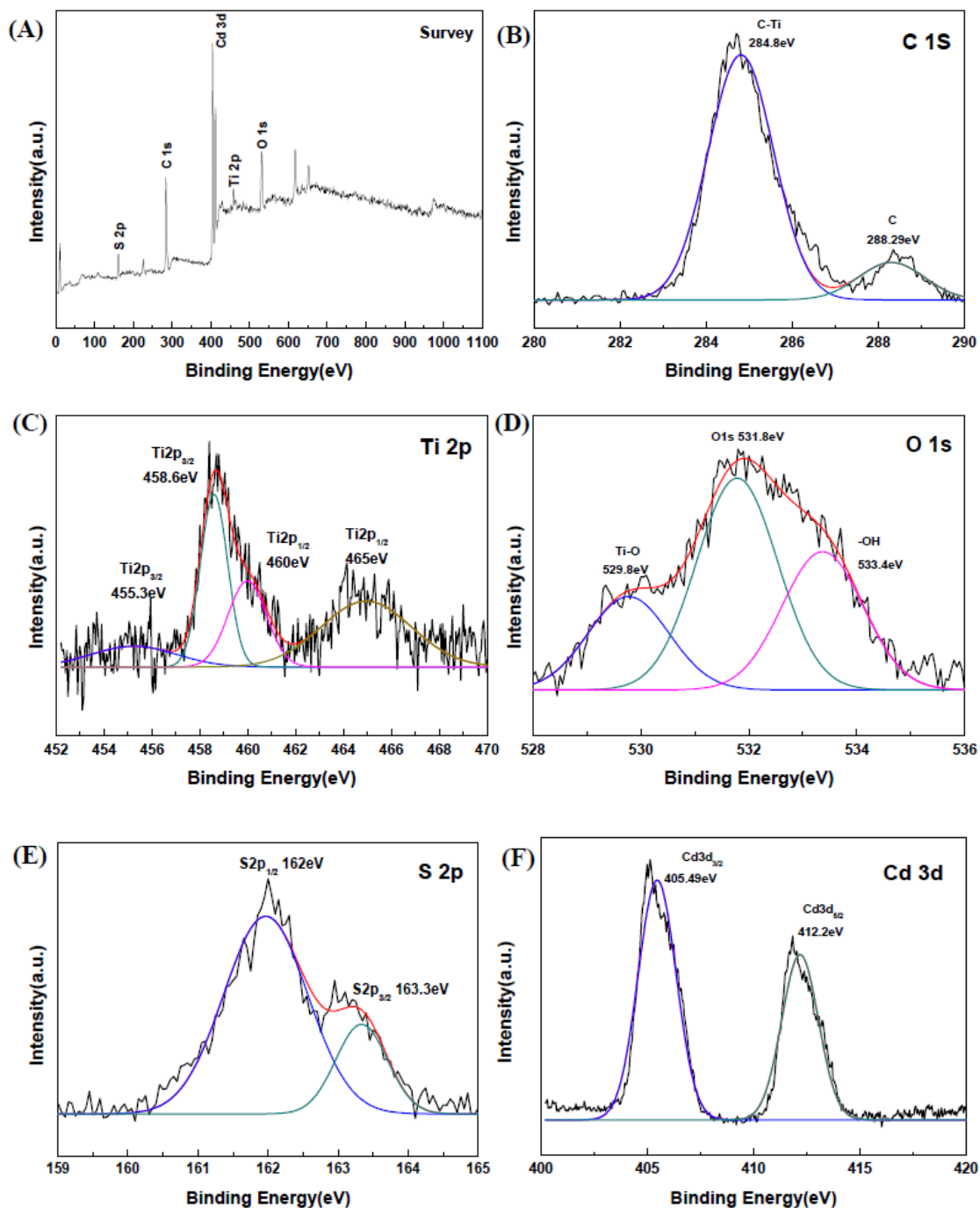


Fig. 6. 3. XPS survey spectrum (A), C1s (B), Ti2p (C), O1s (D), S2p (E) and Cd3d (F) spectra of the 2:1CTT sample.

In this study, XPS analysis was applied to investigate the formation of heterojunction on the 2:1CTT sample. The full XPS survey spectrum reveals the presence of carbon, oxygen, titanium, sulfur and cadmium elements (Fig. 6. 3(A)). In Fig. 6. 3(B), the C 1s peak at about 288.29 eV is attributed to sp²-hybridized carbon (C-O) and peak at

binding energies of around 284.8 eV correspond to the C-Ti on the surface of 2:1CTT. In addition, the C-Ti bond was further studied by high-resolution Ti 2p spectroscopy. As shown in Fig. 6. 3(C), the core levels at 460.0 eV and 465 eV are attributed to the lattice Ti–O bond in TiO₂ [25], while the peaks at 455.3 eV and 458.6 eV are assigned to the lattice Ti–C bond in Ti₃C₂ [26]. As displayed in Fig. 6. 3(D) for O1s, three peaks with binding energies centered at 533.4, 531.9 and 529.8 eV, are assigned to the bonding of -OH, O1s and Ti-O, respectively. For S2p XPS spectrum, after peak fitting, two peaks at 162 eV and 163.3 eV can be found in Fig. 6. 3(E), being ascribed to the S 2p_{1/2} and S 2p_{3/2} doublet of S 2p in CdS. Two peaks at 405.49 eV and 412.2 eV can be fit into Cd 3d_{3/2} and Cd 3d_{5/2}. These results confirmed the heterostructural generation on Ti₃C₂ nanosheets.

6.3.2. Organic pollutants removal studies

6.3.2.1 Adsorption of organic molecules

Owing to their large specific surface area, hydrophilic nature and abundant negatively charged terminal groups (–O and –OH), Ti₃C₂T_x family members have an enormous capacity for adsorbing a variety of environmental pollutants, including metal ions and organic dyes [27]. For example, the spontaneous intercalation of cations into 2D Ti₃C₂ layers has been exploited to adsorb and remove Ba²⁺ and radioactive Pd²⁺ from problematic water [28,29]. The adsorption mechanism of dyes on MXene is mainly electrostatic attraction therefore MXene matrix could take up more cationic methylene blue than anionic acid blue 80 [30].

In this study, the adsorptive removal percentage of MB, RhB, SCP and phenol were tested under dark conditions. As show in Table 6.1, the adsorption capacities of SCP and phenol onto all prepared samples are comparable to cationic MB and RhB. The 2:1CTT sample even accumulated more SCP than MB (8.7% vs 8.1%). These results imply that besides electrostatic attraction, the hydrogen-bonding interactions have also contributed to the adsorption of SCP and phenol on the surface of sorbents [31]. To

further enhance the pollutant removal percentage, photocatalytic degradation should be carried out.

6.3.2.2 Photocatalytic activity and reusability

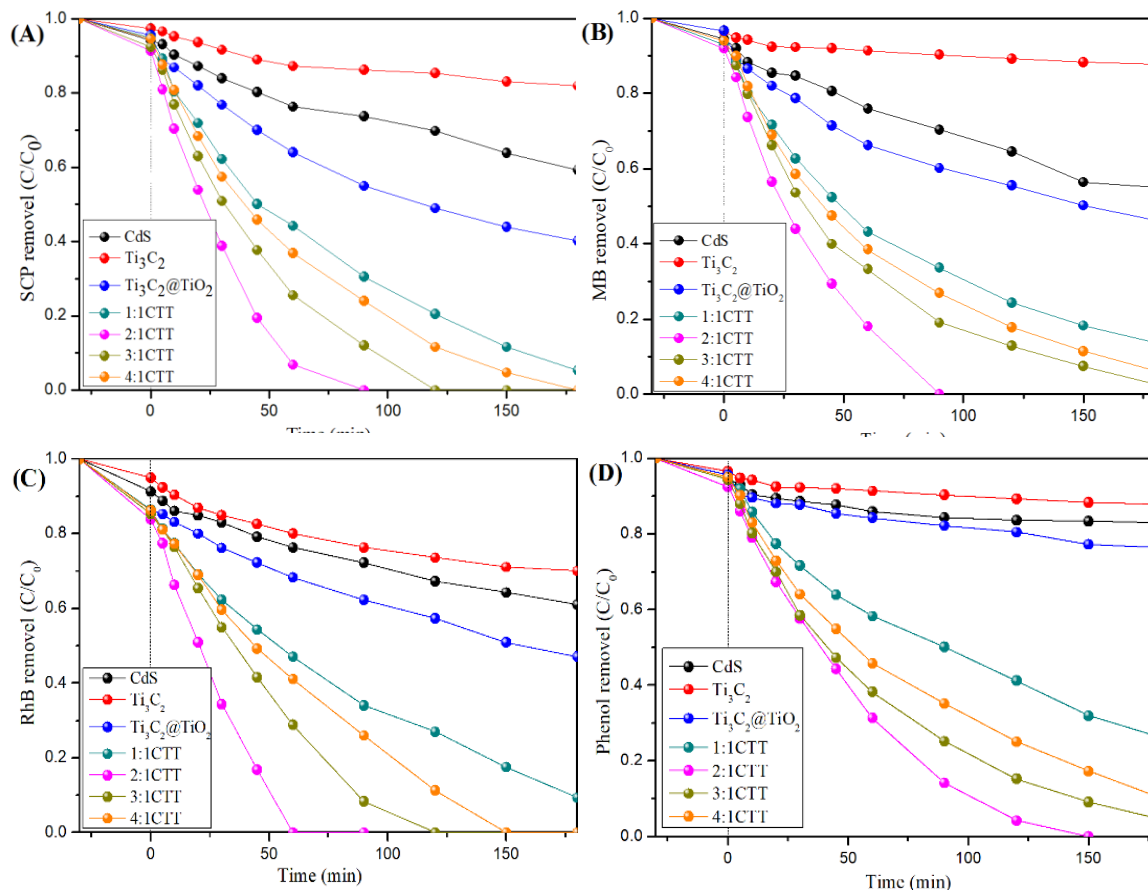


Fig. 6. 4. Degradation curves of sulfachloropyridazine (SCP, A), methylene blue (MB, B), rhodamine B (RhB, C) and Phenol (D).

At a temperature of 25 °C, the photo-degradation results of organic pollutants catalysed by the as-prepared samples under visible light are shown in Fig. 6. 4(A-D). Ti_3C_2 exhibited slightly positive effect on C/C_0 reduction. The best decolourization rate of RhB by Ti_3C_2 was 30% after 180 min irradiation. Similarly, plain CdS showed low activity and the best decolourization rate of MB was 48%. Although $\text{Ti}_3\text{C}_2@\text{TiO}_2$ displayed enhanced activity, all the CdS-loaded samples had much higher photocatalytic performance, implying that CdS is the predominant photoactive species

in the composites. The degradation behaviour was found to depend upon the amount of CdS present in the $\text{Ti}_3\text{C}_2@\text{TiO}_2$ matrix and follows the order of 2:1CTT > 3:1CTT > 4:1CTT > 1:1CTT. Complete removal of RhB, MB, SCP and phenol was achieved by employing 2:1CTT catalyst after 60, 88, 88 and 150 min reactions.

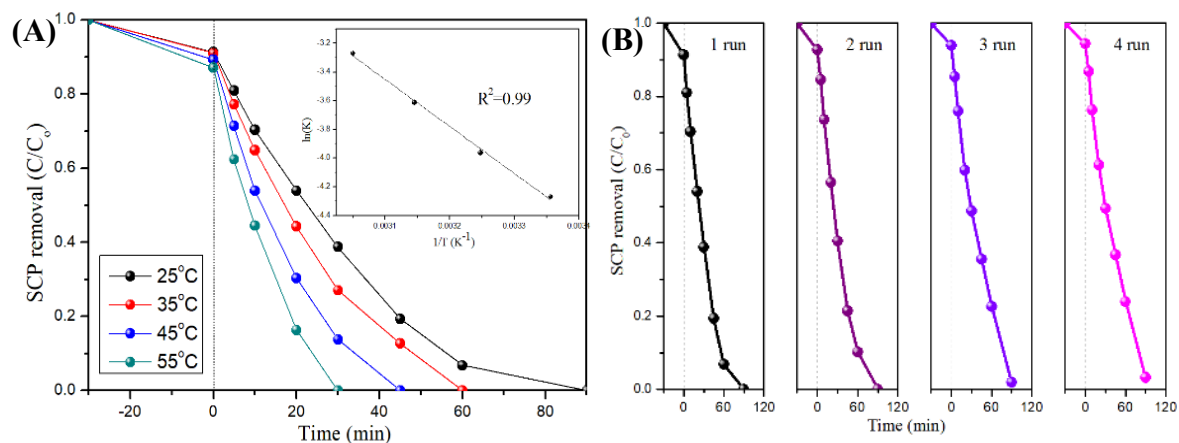


Fig. 6. 5. (A) Effect of reaction temperatures on SCP degradation and estimation of activation energy; and (B) Stability of 2:1CTT catalyst after subsequent reactions under identical conditions.

Table 6. 3. Kinetic parameters in organic degradation.

Catalyst	T (°C)	k (min ⁻¹)	R ² of k	E _a (kJ/mol)	R ² of E _a
2:1CTT	25	0.014	0.98	25.01	0.99
	35	0.019	0.97		
	45	0.027	0.98		
	55	0.038	0.98		

Fig. 6. 5 (A) reveals the effect of different reaction temperatures and the first-order kinetics fitting on SCP degradation by using 2:1CTT. According to Arrhenius equation, the reaction rate constants at 25, 35, 45 and 55 °C are calculated to be 0.014, 0.019, 0.027 and 0.038 min⁻¹, respectively. The activation energy of 2:1CTT are then computed to be 25.01 kJ/mol (Table 6. 3).

To evaluate the photostability of 2:1CTT, four successive cyclic SCP degradation tests under the same reaction conditions were performed (Fig. 6. 5(B)). No significant deterioration of activity was observed for 2:1CTT during four cycling tests.

6.3.3 Proposed photocatalytic degradation mechanism

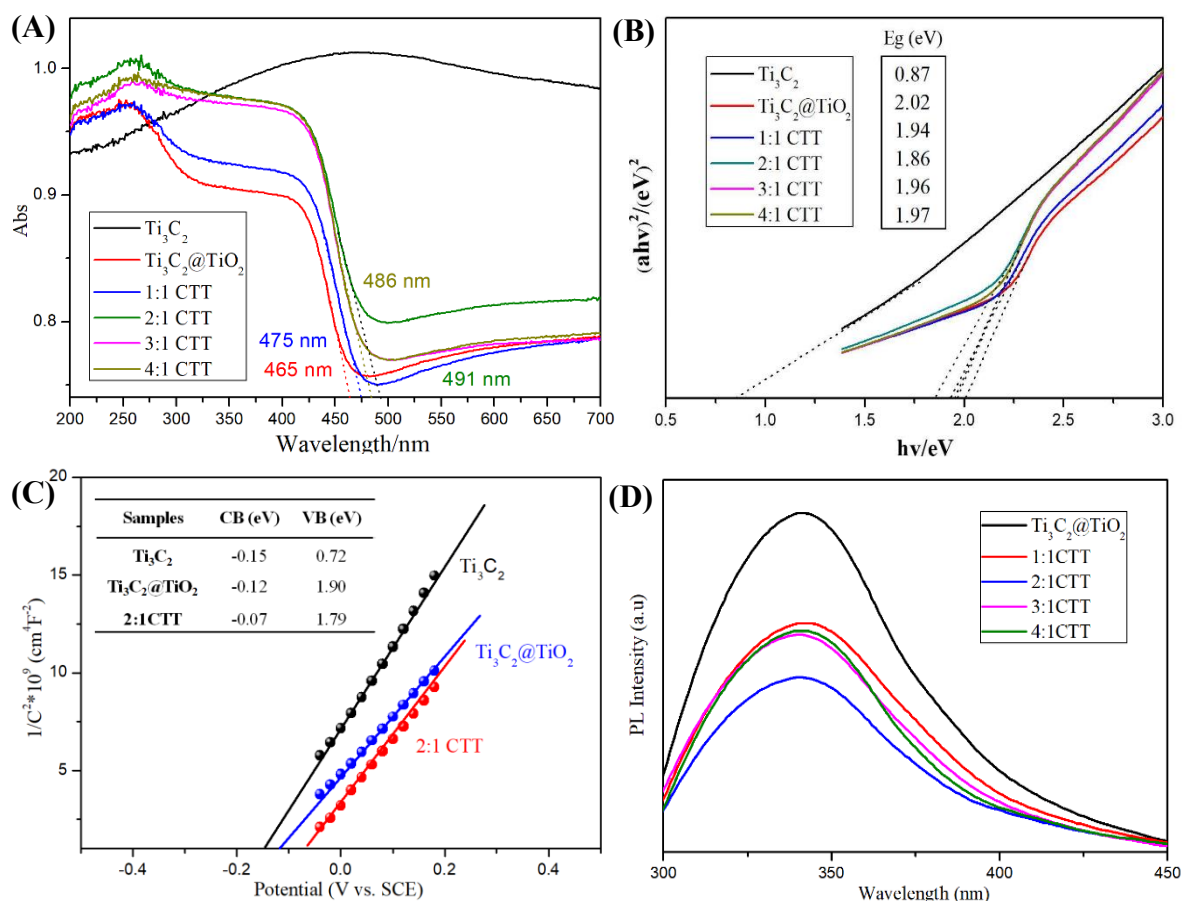


Fig. 6. (A) Diffuse reflectance UV-Vis spectra; (B) Plots of $(ah\nu)^2$ vs. photon energy ($h\nu$) for the band gap energy of Ti_3C_2 , $\text{Ti}_3\text{C}_2@\text{TiO}_2$, 1:1CTT, 2:1CTT, 3:1CTT and 4:1CTT. (C) Mott-Schottky measurements, the inset table shows the CB and VB of Ti_3C_2 , $\text{Ti}_3\text{C}_2@\text{TiO}_2$ and 2:1CTT and (D) PL spectra of $\text{Ti}_3\text{C}_2@\text{TiO}_2$, 1:1CTT, 2:1CTT, 3:1CTT and 4:1CTT.

It is well known that efficient light absorption and charge separation and transportation are important factors in photocatalytic activity. To understand the origin of performance

enhancement by 2:1CTT, the optical features of all samples were investigated in detail. Firstly, Fig. 6. 6(A) compares the UV-Vis diffuse reflectance spectra of Ti_3C_2 , $\text{Ti}_3\text{C}_2@\text{TiO}_2$, 1:1CTT, 2:1CTT, 3:1CTT and 4:1CTT. The light absorption of Ti_3C_2 was observed from 200 to 700 nm due to the black colour nature of MXene. After calcination, the $\text{Ti}_3\text{C}_2@\text{TiO}_2$ sample showed an absorption edge at about 465 nm, confirming a small portion of Ti_3C_2 was converted to TiO_2 [18]. The pure CdS has poor absorbance intensity in the region of 550 to 800 nm [32], while 1:1CTT, 2:1CTT, 3:1CTT and 4:1CTT displayed absorption edges at about 475, 491, and 486 nm, respectively [33]. These results indicate the higher capability of 2:1CTT in utilizing visible light. The bandgaps (Fig. 6. 6(B)) of these samples were estimated based on the Tauc plot and the following equation

$$(\alpha h\nu)^2 = A(h\nu - E_g)$$

where α , h , ν , A and E_g represent the absorption coefficient, Planck constant, light frequency, constant for direct transition and bandgap, respectively. The electronic properties of MXene family differ from metallic to semiconducting depending upon surface functional groups. In this study, the highly conductive Ti_3C_2 delivered the smallest bandgap of 0.87 eV which was in line with the results based on first-principle calculations [34]. The bandgaps of $\text{Ti}_3\text{C}_2@\text{TiO}_2$, 1:1CTT, 2:1CTT, 3:1CTT and 4:1CTT were estimated to be 2.02, 1.94, 1.86, 1.96 and 1.97 eV.

Secondly, Mott–Schottky relationships ($1/C^2$ vs E , (MS)) were identified by UV–vis DRS to determine the changes of band structure of Ti_3C_2 , $\text{Ti}_3\text{C}_2@\text{TiO}_2$ and 2:1CTT. As can be seen in Fig. 6. 6(C), all of the as-prepared catalysts are n-type semiconductor [35]. The conduction band energies (CB) are then estimated to be -0.15, -0.12 and 0.07 V for Ti_3C_2 , $\text{Ti}_3\text{C}_2@\text{TiO}_2$ and 2:1CTT, respectively. According to the above-mentioned band gap energies, the valence band (VB) of Ti_3C_2 , $\text{Ti}_3\text{C}_2@\text{TiO}_2$ and 2:1CTT are determined to be 0.72, 1.90 and 1.79 V, respectively.

The steady-state photoluminescence (PL) spectra of $\text{Ti}_3\text{C}_2@\text{TiO}_2$ and ternary

nanocomposites with different contents of CdS are recorded to study the separation and transfer process of photoinduced charge pairs. As shown in Fig. 6. 6(D), the samples are excited at 330 nm and exhibit emission peaks at round 340 nm. These PL emissions are caused by the energy relaxation from the electron-hole recombination. The high combining rate of electrons and holes results in high PL intensity. It is evident that 2:1CTT shows the weakest emission peak, testifying its enhanced charge separation efficiency.

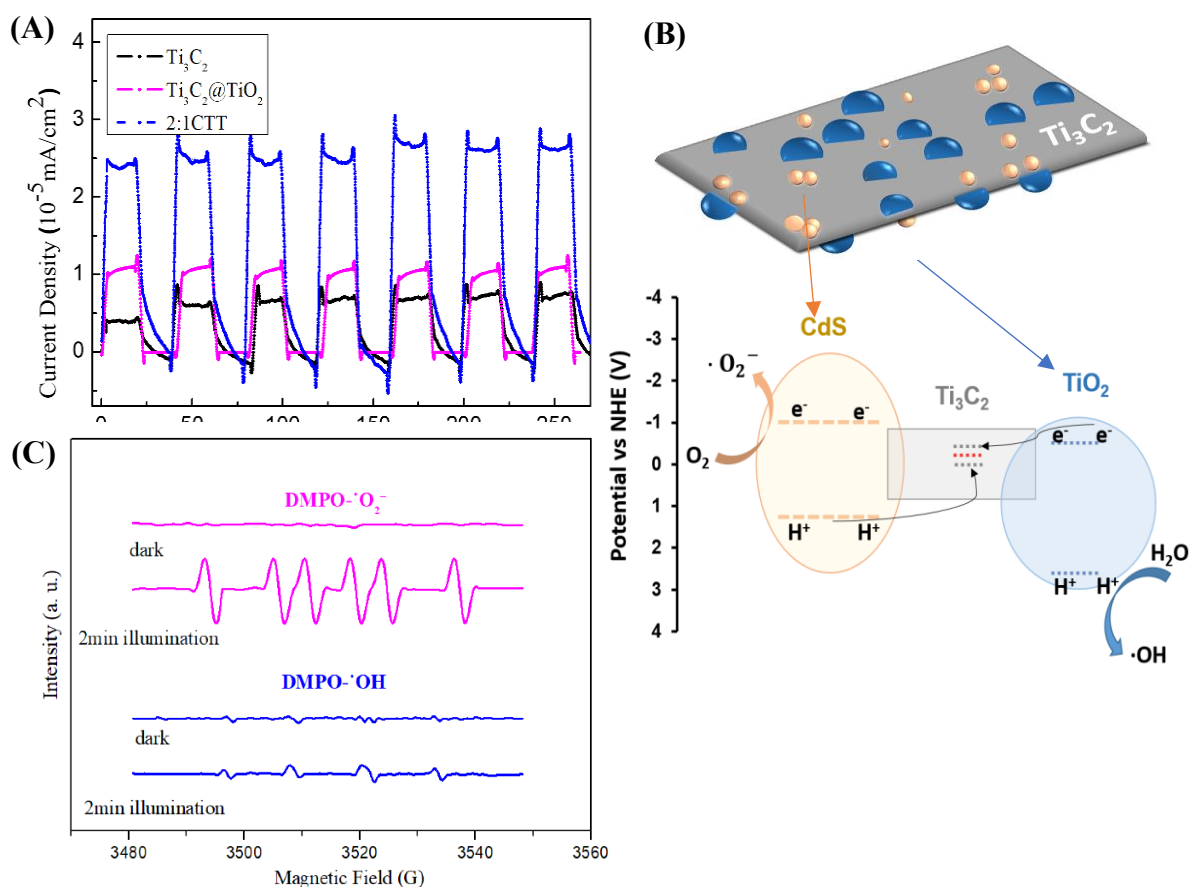


Fig. 6. 7. (A) Transient photocurrent responses of Ti_3C_2 , $Ti_3C_2@TiO_2$ and 2:1CTT, (B) Proposed composite and band gap structures and degradation mechanism of CdS loaded $Ti_3C_2@TiO_2$ photocatalyst, and (C) DMPO trapping EPR spectra for 2:1CTT sample to detect $\cdot OH$ and $\cdot O_2^-$.

To gain further insight into the charge separation and the electron transportation mechanisms in 2:1CTT, the transient photocurrent response tests were studied under

visible light irradiation with 20 s on/off cycles (Fig. 6. 7(A)). Again, 2:1CTT catalyst shows the highest photocurrent density of $0.025 \mu\text{A cm}^{-2}$ compared with Ti_3C_2 and $\text{Ti}_3\text{C}_2@\text{TiO}_2$, corresponding to the highest separation efficiency and the fastest electron transfer rate. In the transient photocurrent responses of Ti_3C_2 and 2:1CTT, a peak in the transient photocurrent is observed after light-on before a decay to the steady-state photocurrent level and a photocurrent decline tail is also observed after light-off. This phenomenon can be interpreted as the trap-mediated separation [36] with a slow electron detrapping rate in both Ti_3C_2 and 2:1CTT [37,38] as the positive photocurrent transient are associated with accumulation of holes in the electrode space charge layer under illumination [39]. The electron trap sites in Ti_3C_2 may be related to its unique energy level structure. In the ternary composite of 2:1CTT, Ti_3C_2 can work as the trap center, where the excited electrons on the CB of TiO_2 can combine with the photogenerated holes left on the VB of CdS through the Ti_3C_2 as a mediator. Thus, the photogenerated holes on the VB of TiO_2 can be accumulated rapidly, resulting in a high transient photocurrent. On the other hand, the light-on photocurrent peak and light-off decline tail are not clearly observed in the case of $\text{Ti}_3\text{C}_2@\text{TiO}_2$ and the photocurrent shows a slight increase with the light-on time. This result can be contributed to the Type I heterojunction between TiO_2 and Ti_3C_2 [36], where the photogenerated electrons and holes of TiO_2 would recombine on Ti_3C_2 . Due to the different charge transfer rates, it may take time to reach the equilibrium. Meanwhile, photocurrent responses maintain excellent stability after seven on/off cycles, indicating the catalyst can restrain photocorrosion, which is in accordance with the reusability results.

Reaction mechanisms for organic pollutants degradation over 2:1CTT catalyst is proposed based on above results and revealed in Fig. 6. 7(B). Ti_3C_2 layer might act as a charge transmission bridge to form the CdS- TiO_2 Z-scheme system [40]. The conduction band (CB) of TiO_2 (-0.25 V vs. NHE) is more negative than the conduction band level of Ti_3C_2 (-0.15 V), the photogenerated electrons can be easily wired to Ti_3C_2 due to its narrow band and carrier mobility. Moreover, the Schottky barrier formed at

the $\text{Ti}_3\text{C}_2/\text{TiO}_2$ interface could prevent the electrons from flowing back to TiO_2 [41]. On the other hand, the E_{CB} value of CdS was ~ -0.8 V vs. NHE [24,33], the potential of valence band E_{VB} was thus estimated to be 1.5 V vs. NHE. It is feasible for photogenerated holes to migrate to the valence band of Ti_3C_2 , leaving the photoelectrons in the conduction band of CdS. Therefore, the photocatalytic performance was enhanced due to the formation of Z-scheme heterostructure in the system, which facilitated the separation of e^-h^+ pairs. Moreover, the hybrids possessed a higher redox ability because the photogenerated e^- accumulated in the more negative CB of CdS and the photogenerated h^+ are located in the more positive VB of TiO_2 [42].

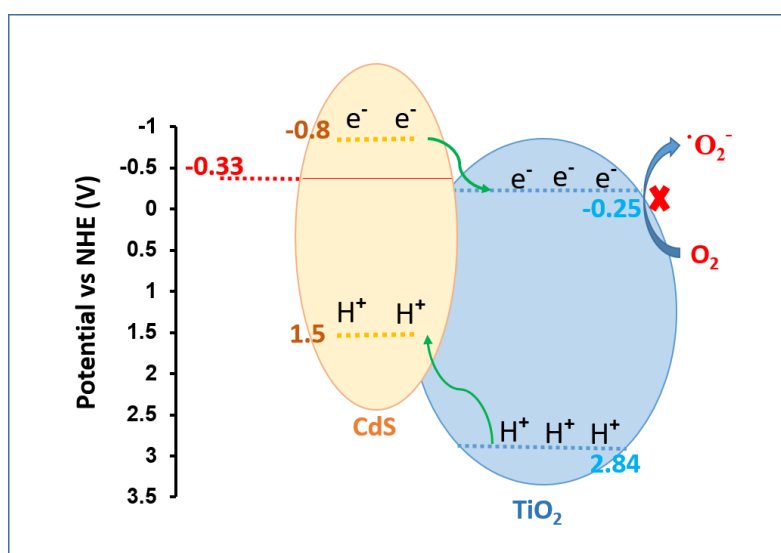


Fig. 6. 8. The photocatalytic mechanism of conventional Type-II CdS@TiO₂ heterojunction

The CB energy position of CdS is higher than the potential of superoxide radicals (-0.80 V vs -0.33 V), it is likely O_2 molecules can be reduced to O_2^- [43]. The holes on TiO_2 are positive enough (2.84 V vs NHE) to generate OH^\bullet from the solution ($E^\circ(\text{OH}^\bullet/\text{H}_2\text{O}) = 2.38$ V vs NHE) [44]. Both O_2^- and OH^\bullet can degrade MB, RhB, SPC and phenol non-specifically [45]. To verify this speculation, electron spin resonance (EPR) technique was employed by using 5,5-dimethyl-1-pyrroline *N*-oxide (DMPO) as the trapping agent. Considering that O_2^- is unstable in aqueous media, the EPR spectra of

DMPO- $\cdot\text{O}_2^-$ is recorded in methanol. In Fig. 7C, clearly, no signals of DMPO- $\cdot\text{OH}$ or DMPO- $\cdot\text{O}_2^-$ adducts can be detected in the dark. After 2 min illumination, the six characteristic peaks of the DMPO- $\cdot\text{O}_2^-$ adducts can be detected under light irradiation over the 2:1CTT photocatalyst [46]. Besides, the 1:2:2:1 signals of DMPO- $\cdot\text{OH}$ species can also be found under visible light irradiation [47]. These results directly prove that superoxide radicals and hydroxyl radicals play a dominant role in the efficient photodegradation of MB, RhB, SPC and phenol under visible light irradiation. Importantly, the detected $\cdot\text{O}_2^-$ further support the Z-scheme mechanism in this catalyst system. In case the CdS NPs are mainly attached on the TiO_2 NPs, the composite may follow the conventional Type-II heterojunction carriers transport rule as shown in Fig. 6.8. The photoinduced electrons (holes) tend to transfer from the CB (VB) of CdS to the CB (VB) of TiO_2 . However, the CB potential of TiO_2 was more positive (-0.25 V vs. NHE) than the standard redox potential of $\cdot\text{O}_2^- / \text{O}_2$ (-0.33 V vs. NHE) thus superoxide anion radical cannot be generated in this system [36].

6. 4. Conclusions

In summary, we have demonstrated a novel 2D-layered $\text{CdS}@ \text{Ti}_3\text{C}_2@ \text{TiO}_2$ hybrid synthesis via calcination and hydrothermal processes. The enhanced activity in degrading organic pollutants is attributed to the “sink” effect of MXene as well as the well matched band configuration of $\text{CdS}@ \text{Ti}_3\text{C}_2@ \text{TiO}_2$. The photoexcited charge carriers in the Z-scheme type composite are separated efficiently and subsequently produce free radicals $\cdot\text{O}_2^-$ and $\cdot\text{OH}$, which play important roles in oxidizing the aqueous contaminants. This work may open up new prospects for the application of low-cost MXene as efficient noble metal substitute in all solid Z-scheme photocatalysts. By combining with other co-catalysts, the system can generally be utilized in sustainable H_2 production and CO_2 reduction.

References

1. J. Low, S. Cao, J. Yu and S. Wageh, Two-dimensional layered composite photocatalysts, *Chem. Commun.*, 2014, 50, 10768-10777.
2. M. Naguib, M. Kurtoglu, V. Presser, J. Lu, J. Niu, M. Heon, L. Hultman, Y. Gogotsi and M. W. Barsoum, Two-dimensional nanocrystals produced by exfoliation of Ti_3AlC_2 , *Adv. Mater.* 2011, 23, 4248-4253.
3. J. Zhu, E. Ha, G. Zhao, Y. Zhou, D. Huang, G. Yue, L. Hu, N. Sun, Y. Wang, L. Lee, C. Xu, K. Wong, D. Astruc and P. Zhao, Recent advance in MXenes: A promising 2D material for catalysis, sensor and chemical adsorption, *Coord. Chem. Rev.*, 2017, 352, 306-327.
4. Z. Wong, T. Tan, S. Yang and G. Xu, Enhancing the photocatalytic performance of MXenes via stoichiometry engineering of their electronic and optical properties, *ACS Appl. Mater. Interfaces*, 2018, 10, 39879-39889.
5. Y. Sun, D. Jin, Y. Sun, X. Meng, Y. Gao, Y. Agnese, G. Chen and X. Wang, g- $\text{C}_3\text{N}_4/\text{Ti}_3\text{C}_2\text{T}_x$ (MXenes) composite with oxidized surface groups for efficient photocatalytic hydrogen evolution, *J. Mater. Chem. A*, 2018, 6, 9124-9131.
6. Q. Liu, L. Ai and J. Jiang, MXene-derived $\text{TiO}_2@C/g\text{-C}_3\text{N}_4$ heterojunctions for highly efficient nitrogen photofixation, *J. Mater. Chem. A*, 2018, 6, 4102-4110.
7. H. Zhang, M. Li, J. Cao, Q. Tang, P. Kang, C. Zhu and M. Ma, 2D $\alpha\text{-Fe}_2\text{O}_3$ doped Ti_3C_2 MXene composite with enhanced visible light photocatalytic activity for degradation of Rhodamine B, *Ceram. Int.*, 2018, 44, 19958-19962.
8. Handoko, S. Steinmann and Z. Seh, Theory-guided materials design: two-dimensional MXenes in electro- and photocatalysis, *Nanoscale Horiz.*, 2019, 4, 809-827.
9. H. Tada, T. Mitsui, T. Kiyonage, T. Akita and K. Tanaka, All-solid-state Z-scheme in CdS-Au-TiO_2 three-component nanojunction system, *Nat. Mater.*, 2006, 5, 782-786.
10. M. Ou, S. Wan, Q. Zhong, S. Zhang, Y. Song, L. Guo, W. Cai and Y. Xu, Hierarchical Z-scheme photocatalyst of $g\text{-C}_3\text{N}_4@Ag/\text{BiVO}_4(040)$ with enhanced

visible-light-induced photocatalytic oxidation performance, *App. Catal. B*, 2018, 221, 97-107.

11. H. Li, H. Yu, X. Quan, S. Chen and Y. Zhang, Uncovering the key role of the Fermi level of the electron mediator in a Z Scheme photocatalyst by detecting the charge transfer process of WO₃ metal-gC₃N₄ (Metal = Cu, Ag, Au), *ACS Appl. Mater. Interfaces*, 2016, 8, 2111-2119.

12. D. Zheng, C. Pang and X. Wang, The function-led design of Z-scheme photocatalytic systems based on hollow carbon nitride semiconductors, *Chem. Commun.*, 2015, 51, 17467-17470.

13. J. Jin, J. Yu, D. Guo, C. Cui and W. Ho, A hierarchical Z-Scheme CdS-WO₃ photocatalyst with enhanced CO₂ reduction activity, *Small*, 2015, 39, 5262-5271.

14. Y. Yuan, D. Chen, S. Yang, L. Yang, J. Wang, D. Cao, W. tu, Z. Yu and Z. Zou, Constructing noble-metal-free Z-scheme photocatalytic overall water splitting systems using MoS₂ nanosheet modified CdS as a H₂ evolution photocatalyst, *J. Mater. Chem. A*, 2017, 5, 21205-21213.

15. L. Kuai, Y. Zhou, W. Tu, P. Li, H. Li, Q. Xu, L. Tang, X. Wang, M. Xiao, M. Xiao and Z. Zou, Rational construction of a CdS/reduced graphene oxide/TiO₂ core-shell nanostructure as an all-solid-state Z-scheme system for CO₂ photoreduction into solar fuels, *RSC Adv.*, 2015, 5, 88409-88413.

16. J. Zhu, Y. Tang, C. Yang, F. Wang and M. Cao, Composites of TiO₂ nanoparticles deposited on Ti₃C₂ MXene nanosheets with enhanced electrochemical performance, *J. Electrochem. Soc.*, 2016, 163, 785-791.

17. H. Wang, R. Peng, Z. Hood, M. Naguib, S. Adhikari and Z. Wu, MXene-TiO₂ composites as novel photocatalysts for hydrogen production under visible light irradiation, *Chem. Sus. Chem.*, 2016, 9, 1490-1497.

18. J. Low, L. Zhang, T. Tong, B. Shen and J. Yu, TiO₂/MXene Ti₃C₂ composite with excellent photocatalytic CO₂ reduction activity, *J. Catal.*, 2018, 361, 255-266.

19. Y. Li, D. Zhang, X. Feng, Y. Liao, Q. Wen and Q. Xiang, Truncated octahedral bipyramidal TiO₂/Mxene Ti₃C₂ hybrids with enhanced photocatalytic H₂ production activity, *Nanoscale Adv.*, 2019, 1, 1812-1818.
20. X. Zhang, Y. Liu, S. Dong, Z. Ye and Y. Guo, One-step hydrothermal synthesis of a TiO₂-Ti₃C₂T_x nanocomposite with small sized TiO₂ nanoparticles, *Ceram. Int.*, 2017, 43, 11065-11070.
21. W. Yuan, L. Cheng, Y. Zhang, H. Wu, S. Lv, L. Chai and X. Guo, L. Zheng, 2D-layered carbon/ TiO₂ hybrids derived from Ti₃C₂ Mxenes for photocatalytic hydrogen evolution under visible light irradiation, *Adv. Mater. Interfaces*, 2017, 4, 1700577.
22. R. Chen, P. Wang, J. Chen, C. Wang and Y. Ao, Synergetic effect of MoS₂ and Mxene on the enhanced H₂ evolution performance of CdS under visible light irradiation, *Appl. Surf. Sci.*, 2019, 4, 7311-19.
23. M. Lukatskaya, O. Mashtalir, C. Ren, Y. Dall'Agnese, P. Rozier, P. Taberna, M. Naguib, P. Simon, M. Barsoum and Y. Gogotsi, Cation Intercalation and High Volumetric Capacitance of Two-Dimensional Titanium Carbide, *Science*, 2013, 341, 1502-1505.
24. J. Ran, G. Gao, F. Li, T. Ma, A. Du and S. Qiao, Ti₃C₂ MXene co-catalyst on metal sulfide photo-absorbers for enhanced visible-light photocatalytic hydrogen production, *Nat. Commun.*, 2017, 8, 13907.
25. L. Zheng, S. Han, H. Liu, P. Yu and X. Fang, Hierarchical MoS₂ nanosheet@ TiO₂ nanotube array composites with enhanced photocatalytic and photocurrent performances, *Small*, 2016, 12, 527-1536.
26. C. Peng, P. Wei, X. Li, Y. Liu, Y. Cao, H. Wang, H. Yu, F. Peng, L. Zhang, B. Zhang and K. Lv, High efficiency photocatalytic hydrogen production over ternary Cu/TiO₂@Ti₃C₂T_x enabled by low-work-function 2D titanium carbide, *Nano Energy*, 2018, 53, 97-107.
27. Y. Zhang, L. Wang, N. Zhang and Z. Zhou, Adsorptive environmental applications of MXene nanomaterials: a review, *RSC Adv.*, 2018, 8, 19895-19905.

28. Fard, G. McKay, R. Chamoun, T. Rhadfi, H. Preud'Homme and M. Atieh, Barium removal from synthetic natural and produced water using Mxene as two dimensional (2-D) nanosheet adsorbent, *Chem. Eng. Sci.*, 2017, 317, 331-342.
29. W. Mu, S. Du, X. Li, Q. Yu, H. Wei, Y. Yang and S. Peng, Removal of radioactive palladium based on novel 2D titanium carbides, *Chem. Eng. Sci.*, 2019, 358, 283-290.
30. W. Zheng, P. Zhang, W. Tian, X. Qin, Y. Zhang and Z. M. Sun, Alkali treated Ti_3C_2Tx MXenes and their dye adsorption performance, *Mater. Chem. Phys.*, 2018, 206, 270-276.
31. Y. Liu, X. Liu, W. Dong, L. Zhang, Q. Kong and W. Wan, Efficient adsorption of sulfamethazine onto modified activated carbon: a plausible adsorption mechanism, *Sci. Rep.*, 2017, 7, 12437-12449.
32. X. Xie, N. Zhang, Z. Tang, M. Anpo and Y. Xu, $Ti_3C_2T_x$ MXene as a Janus cocatalyst for concurrent promoted photoactivity and inhibited photocorrosion, *App. Catal. B*, 2018, 237, 43-49.
33. Z. Ai, Y. shao, B. Chang, B. Huang, Y. Wu and X. Hao, Effective orientation control of photogenerated carrier separation via rational design of a $Ti_3C_2 (TiO_2)@CdS/MoS_2$ photocatalytic system, *App. Catal. B*, 2019, 242, 202-208.
34. M. Khazaei, M. Arai, T. Sasaki, C. Chung, N. Venkataramanan, M. Estili, Y. Sakka and Y. Kawazoe, Novel electronic and magnetic properties of two-dimensional transition metal carbides and nitrides, *Adv. Funct. Mater.*, 2013, 23, 2185-2192.
35. D. Kong, The influence of fluoride on the physicochemical properties of anodic oxide films formed on titanium surfaces, *Langmuir*, 2008, 24, 5324-5331.
36. M. Wang, G. Tan, D. Zhang, B. Li, L. Lv, Y. Wang, H. Ren, X. Zhang, A. Xia and Y. Liu, Defect-mediated Z-scheme $BiO_{2-x}/Bi_2O_{2.75}$ photocatalyst for full spectrum solar-driven organic dyes degradation, *App. Catal. B*, 2019, 254, 98-112.
37. Z. Li, W. Wang, N. Greenham and C. McNeill, Influence of nanoparticle shape on charge transport and recombination in polymer/nanocrystal solar cells. *Phys. Chem. Chem. Phys.*, 2014, 16, 25684-25693.

38. F. Le Formal, K. Sivula and M. Gratzel, The transient photocurrent and photovoltage behavior of a hematite photoanode under working conditions and the influence of surface treatments, *J Phys. Chem. C*, 2012, 116, 26707-26720.
39. A. Tamirat, A. Dubale, W. Su, H. Chen and B. Hwang, Sequentially surface modified hematite enables lower applied bias photoelectrochemical water splitting, *Phys. Chem Chem Phys.*, 2017, 19, 20881-20890.
40. Y. He, L. Zhang, B. Teng and M. Fan, New application of Z-Scheme $\text{Ag}_3\text{PO}_4/\text{g-C}_3\text{N}_4$ composite in converting CO_2 to fuel, *Environ. Sci. Technol.*, 2015, 49, 649–656.
41. Shahzad, K. Rasool, M. Nawaz, W. Miran, J. Jang, M. Moztahida, K. Mahoud and D. Lee, Heterostructural $\text{TiO}_2/\text{Ti}_3\text{C}_2\text{T}_x$ (MXene) for photocatalytic degradation of antiepileptic drug carbamazepine, *Chem. Eng. Sci.*, 2018, 349, 748-755.
42. F. Deng, X. Lu, Y. Luo, J. Wang, W. Che, R. Yang, X. Luo, S. Luo and D. Dionysiou, Novel visible-light-driven direct Z-scheme $\text{CdS}/\text{CuInS}_2$ nanoplates for excellent photocatalytic degradation performance and highly-efficient Cr(VI) reduction, *Chem. Eng. Sci.*, 2019, 361, 1451-1461.
43. T. Zhou, G. Zhang, H. Zhang, H. Yang, P. Ma, X. Li, X. Qiu and G. Liu, Highly efficient visible-light-driven photocatalytic degradation of rhodamine B by a novel Z-scheme $\text{Ag}_3\text{PO}_4/\text{MIL-101}/\text{NiFe}_2\text{O}_4$ composite, *Catal. Sci. Technol.*, 2018, 8, 2402–2416.
44. Z. Ni, F. Dong, H. Huang and Y. Zhang, New insights into how Pd nanoparticles influence the photocatalytic oxidation and reduction ability of $\text{g-C}_3\text{N}_4$ nanosheets, *Catal. Sci. Technol.*, 2016, 6, 6448-6458.
45. Y. Chu, X. Tan, Z. Shen, P. Liu, N. Han, J. Kang, X. Duan, S. Wang, L. Liu and S. Liu, Efficient removal of organic and bacterial pollutants by $\text{Ag-La}_{0.8}\text{Ca}_{0.2}\text{Fe}_{0.94}\text{O}_{3-\delta}$ perovskite via catalytic peroxydisulfate activation, *J. Hazard. Mater.*, 2018, 356, 53-60.

46. Y. Zhang, N. Zhang, Z. Tang and Y. Xu, Transforming CdS into an efficient visible light photocatalyst for selective oxidation of saturated primary C–H bonds under ambient conditions, *Chem. Sci.*, 2012, 3, 2812-2822.
47. F. Song, H. Zhang, S. Wang, L. Liu, X. Tan and S. Liu, Atomic-level design of CoOH⁺–hydroxyapatite@C catalysts for superfast degradation of organics via peroxymonosulfate activation, *Chem. Commun.*, 2018, 54, 4919-4922.

Every reasonable effort has been made to acknowledge the owners of copyright material. I would be pleased to hear from any copyright owner who has been omitted or incorrectly acknowledged.

Chapter 7. Conclusions and Perspectives

7.1 Conclusions

To address the difficulty in treating organic refractory dyes in water, the project of this thesis was focusing on the synthesis and characterization of different types of novel hybrid photocatalysts. Results confirm the success of photocatalysts in improving both catalytic and adsorption efficiencies. In this thesis, general fabrication methods of novel photocatalytic materials and their recent applications in wastewater treatment are also discussed.

Specifically, carbon nitride based composite catalyst materials were synthesized by simple hydrothermal method, and the adsorptive and oxidative degradation of organic matters were evaluated. The influences of textural properties, surface compositions/chemical states, surface functional groups and light absorbance of the obtained materials were studied and discussed. The temperature, PH value and repeatability were tested during the reaction. Meanwhile, the mechanistic investigation inferred that the $\bullet\text{OH}$ and $\bullet\text{O}_2^-$ played a dominating role key role in improving the catalytic ability under the light excitation.

$\text{ZnO}@\text{Fe}_3\text{O}_4$ composite was synthesized by simple layer-by-layer method, and the catalytic effect on the degradation of organics was investigated. The mechanism of self-generated H_2O_2 was firstly studied by quenching and radical trapping experiments. Self-generated H_2O_2 was observed and identified as a key determinant of the reaction. In addition, the magnetic separation ability was also verified to reuse the spent catalyst efficiently.

MXene was also applied as an efficient charge mediator in the 2D layered catalyst, due to its high specific surface area, narrow band gap and fast electron transfer ability. The obtained composites revealed superior Z-scheme visible light-driven photocatalytic activity in organic degradation.

Different photocatalytic efficiencies and adsorption capacities from these developed catalysts are listed showed below:

7.1.1 Surface chemistry-dependent activity and comparative investigation on the enhanced photocatalytic performance of graphitic carbon nitride modified with various nanocarbons.

Four kinds of nanocarbon modified GCNs were synthesized via one-pot hydrothermal method and exhibited great activities in photocatalytic removal of various pollutants.

1. GCN was prepared by direct condensation of melamine, and four nanocarbons (CQD, rGO, CNT and CNS) were prepared through four different processes. Nanocarbon modified GCN hybrids were prepared through hydrothermal treatment.
2. From the BET and SCP adsorption results, it was found that open porous structure and relatively large surface area of GCN/rGO were beneficial to provide more active sites for organics adsorption. Combining the XPS with degradation results, increased catalytic oxidation activities could be observed by introducing C=O or COOH.
3. The integration of all nanocarbon materials with the GCN would result in red shifts and stronger light absorption capabilities, which illustrated that the introduction of carbon materials changed the energy level of original GCN and increased the optical properties of the catalysts.

4. The photocatalytic activities of the four hybrids were systematically evaluated in degradation of sulfachloropyridazine, methylene blue, methyl orange and Rhodamine B under artificial sunlight irradiation. It was also found that GCN/CNS presented the highest activity in all degradation systems.

5. Photocatalytic activation on GCN/CNS was investigated by in situ electron paramagnetic resonance (EPR). The in-depth mechanistic studies on the enhanced photoelectrochemical and photocatalytic performances were also conducted, which inferred that the $\bullet\text{OH}$ and $\bullet\text{O}_2^-$ played a pivotal role in photocatalytic process.

7.1.2 Nitrogen-doped Carbon Nanospheres Modified Graphitic Carbon Nitride for Enhanced Photocatalytic Performances.

1. Monodisperse nitrogen-doped carbon nanospheres (NC) were prepared and loaded onto graphitic carbon nitride (g-C₃N₄, GCN) via a facile hydrothermal method. The prepared metal-free GCN-NC exhibited remarkably enhanced efficiency in SCP degradation. The nitrogen content in NC exerted a great influence on the photocatalytic activity due to the physicochemical properties and performances of the resultant hybrids.

2. Through density functional theory (DFT) calculations, the mechanism of improved photocatalytic performance was studied. The GCN-NC hybrid showed an improved photocatalytic ability via reducing band gap energy and activating the effective separation of electron-hole pairs. Thereby, subsequent generation of superoxide and hydroxyl radicals could remove SCP effectively using light energy.

7.1.3 Efficient photo-Fenton oxidation of nitrophenol driven by self-generated H₂O₂ from ZnO@Fe₃O₄ composite.

1. ZnO@Fe₃O₄ was prepared using a layer-by-layer self-assembly process with ZnO microflower and wrapped with Fe₃O₄ nanoparticles with different deposition layers. The characterizations were revealed to investigate the crystal structure, morphology, surface chemistry and optical properties of the produced composites.
2. Band gaps of the samples were also studied, and the band gap energy values of ZnO, Fe₃O₄, and ZFCM-5 samples were calculated to 3.05, 2.60 and 2.35 eV, respectively. From the PL spectra, the peak of ZFCM-5 dropped remarkably compared with pristine ZnO and Fe₃O₄, illustrating the combination of Fe₃O₄ and ZnO could effectively inhibit the recombination of photo-generated electron-hole pairs, therefore improving activity.
3. The as-synthesized ZFCM-5 showed excellent p-NP degradation, due to in-situ photocatalytic formation of hydrogen peroxide over Fe₃O₄@ZnO. The mechanism of photocatalytic activation on ZFCM-5 was investigated by EPR, which suggested that photo-Fenton generated [•]OH played a key role during photocatalytic activation on ZFCM-5 and was determined to be the primary role in p-NP degradation.
4. The magnetic behavior and reusability tests were carried out to testify a good magnet separatable behavior and excellent reusability, which further endowed a promising candidate for sustainable wastewater treatment.

7.1.4 MXene as non-metal charge mediator in 2D layered CdS@Ti₃C₂@TiO₂ composites with superior Z-scheme visible light-driven photocatalytic activity.

1. Two-dimensional CdS@Ti₃C₂@TiO₂ nano hybrids were synthesized using a facile calcination and a subsequent hydrothermal process. The physico-chemical characterizations of the as-synthesized materials performed a tight attachment of CdS, Ti₃C₂ and TiO₂.

2. The photocatalytic activities of the CdS@Ti₃C₂@TiO₂ nano hybrids were elucidated in degradation of sulfachloropyridazine, phenol and several typical dyes. It was found that 2:1CTT presented an excellent activity.

3. The effect of Ti₃C₂ in this three-phase Z-scheme catalyst was proposed based on UV-visible spectroscopy band gap calculation, photoluminescence measurement and photoelectrochemical analysis. The EPR assay revealed that both superoxide ions and hydroxyl radicals contributed mainly to the organic degradation

4. Excellent stability of 2:1CTT catalyst was proved after subsequent reactions under identical conditions.

7.2 Perspectives for Future Research

Research for this project was focusing on synthesizing different types of photocatalysts for the degradation of organics such as sulfachloropyridazine, methylene blue, methyl orange and rhodamine B in water under UV/visible light irradiation. The data presented an excellent result in completely degrading the refractory pollutants in wastewater.

However, there are still some challenging issues on the material development which need to be investigated before putting into industrial applications. Based on the research results, the following future studies are recommended:

1. The photocatalytic experiments were carried out under artificial UV-visible light sources. Solar light should be encouraged to be applied in future works since it has a lower cost and possesses a greater practical application prospects.
2. To increase the efficiency of sewage treatment, further work can focus on the adsorption capacity and kinetics of the novel materials as adsorbents.
3. Further research should be performed to clarify the mechanisms during the reaction. The active sites and the reaction pathways between the catalysts and oxidants should be investigated utilizing simulation methods.
4. Future research in wastewater remediation can focus on industrial applications rather than experimental test in lab. It is highly recommended to realize large-scale industrialization in the end.
5. It is advised to design catalysts with ability to remove real industry pollutants consisting of multi-components from several persistent drugs including organics and inorganics.

APPENDIXI: ATTRIBUTION TABLES

Paper “Surface chemistry-dependent activity and comparative investigation on the enhanced photocatalytic performance of graphitic carbon nitride modified with various nanocarbons”. J. Colloid Interface Sci. 2020, 569,12-21.

Li Zhou, Jun Gao, Shaobin Wang*, Lihong Liu, Shaomin Liu*

Name	concepti on and design	Acquisitio n of data & method	Data conditioning & manipulation	Analysis & statistical method	Interpret ation & discussion	Final appr oval
Li Zhou	<input checked="" type="checkbox"/>	<input type="checkbox"/>	<input type="checkbox"/>	<input type="checkbox"/>	<input checked="" type="checkbox"/>	<input type="checkbox"/>
I acknowledge that these represent my contribution to the above research output. Sign:						
Jun Gao	<input type="checkbox"/>	<input type="checkbox"/>	<input type="checkbox"/>	<input type="checkbox"/>	<input checked="" type="checkbox"/>	<input type="checkbox"/>
I acknowledge that these represent my contribution to the above research output. Sign:						
Shaobi n Wang	<input checked="" type="checkbox"/>	<input type="checkbox"/>	<input type="checkbox"/>	<input type="checkbox"/>	<input checked="" type="checkbox"/>	<input checked="" type="checkbox"/>
I acknowledge that these represent my contribution to the above research output. Sign:						
Lihong Liu	<input type="checkbox"/>	<input type="checkbox"/>	<input type="checkbox"/>	<input checked="" type="checkbox"/>	<input checked="" type="checkbox"/>	<input type="checkbox"/>
I acknowledge that these represent my contribution to the above research output. Sign:						

Shaomin Liu	<input checked="" type="checkbox"/>	<input type="checkbox"/>	<input type="checkbox"/>	<input type="checkbox"/>	<input checked="" type="checkbox"/>	<input checked="" type="checkbox"/>
I acknowledge that these represent my contribution to the above research output.						
Sign:						

Paper “Nitrogen-doped Carbon Nanospheres Modified Graphitic Carbon Nitride for Enhanced Photocatalytic Performances”. *Nano-micro Lett.* 2020, 12, 24. Hao Tian, Zhenghua Dai, Hongqi Sun, Jian Liu, Zhimin Ao, Shaobin Wang*, Chen Han, Shaomin Liu*

Name	conception and design	Acquisition of data & method	Data conditioning & manipulation	Analysis & statistical method	Interpretation & discussion	Final approval
Hao Tian	<input type="checkbox"/>	<input checked="" type="checkbox"/>	<input checked="" type="checkbox"/>	<input type="checkbox"/>	<input type="checkbox"/>	<input type="checkbox"/>
I acknowledge that these represent my contribution to the above research output.						
Sign:						
Zhenghua Dai	<input type="checkbox"/>	<input checked="" type="checkbox"/>	<input checked="" type="checkbox"/>	<input type="checkbox"/>	<input type="checkbox"/>	<input type="checkbox"/>
I acknowledge that these represent my contribution to the above research output.						
Sign:						
Hongqi Sun	<input checked="" type="checkbox"/>	<input type="checkbox"/>	<input type="checkbox"/>	<input type="checkbox"/>	<input checked="" type="checkbox"/>	<input type="checkbox"/>
I acknowledge that these represent my contribution to the above research output.						
Sign:						

Jian Liu	<input checked="" type="checkbox"/>	<input checked="" type="checkbox"/>	<input type="checkbox"/>	<input type="checkbox"/>	<input checked="" type="checkbox"/>	<input type="checkbox"/>
I acknowledge that these represent my contribution to the above research output.						
Sign:						
Zhimin Ao	<input checked="" type="checkbox"/>	<input checked="" type="checkbox"/>	<input type="checkbox"/>	<input type="checkbox"/>	<input type="checkbox"/>	<input type="checkbox"/>
I acknowledge that these represent my contribution to the above research output.						
Sign:						
Shaobin Wang	<input checked="" type="checkbox"/>	<input type="checkbox"/>	<input type="checkbox"/>	<input type="checkbox"/>	<input checked="" type="checkbox"/>	<input checked="" type="checkbox"/>
I acknowledge that these represent my contribution to the above research output.						
Sign:						
Chen Han	<input type="checkbox"/>	<input type="checkbox"/>	<input type="checkbox"/>	<input checked="" type="checkbox"/>	<input checked="" type="checkbox"/>	<input type="checkbox"/>
I acknowledge that these represent my contribution to the above research output.						
Sign:						
Shaomin Liu	<input checked="" type="checkbox"/>	<input type="checkbox"/>	<input type="checkbox"/>	<input type="checkbox"/>	<input checked="" type="checkbox"/>	<input checked="" type="checkbox"/>
I acknowledge that these represent my contribution to the above research output.						
Sign:						

Paper “**Magnetic ZnO@Fe₃O₄ composite for self-generated H₂O₂ toward photo-Fenton-like oxidation of nitrophenol**”. Compos. B. Eng. 2020, 200, 108345. **Li Zhou, Lihong Liu***, Jiaquan Li, Shaobin Wang*, Hussein Znad, Shaomin Liu*

Name	concepti	Acquisitio	Data	Analysis	Interpret	Final
------	----------	------------	------	----------	-----------	-------

	on and design	n of data & method	conditioning & manipulation	& statistical method	ation & discussion	appr oval
Li Zhou	<input checked="" type="checkbox"/>	<input type="checkbox"/>	<input type="checkbox"/>	<input type="checkbox"/>	<input checked="" type="checkbox"/>	<input type="checkbox"/>
I acknowledge that these represent my contribution to the above research output. Sign:						
Lihong Liu	<input type="checkbox"/>	<input type="checkbox"/>	<input checked="" type="checkbox"/>	<input checked="" type="checkbox"/>	<input checked="" type="checkbox"/>	<input checked="" type="checkbox"/>
I acknowledge that these represent my contribution to the above research output. Sign:						
Jiaquan Li	<input type="checkbox"/>	<input type="checkbox"/>	<input checked="" type="checkbox"/>	<input type="checkbox"/>	<input checked="" type="checkbox"/>	<input type="checkbox"/>
I acknowledge that these represent my contribution to the above research output. Sign:						
Shaobi n Wang	<input checked="" type="checkbox"/>	<input type="checkbox"/>	<input type="checkbox"/>	<input type="checkbox"/>	<input checked="" type="checkbox"/>	<input checked="" type="checkbox"/>
I acknowledge that these represent my contribution to the above research output. Sign:						
Hussei n Znad	<input type="checkbox"/>	<input type="checkbox"/>	<input type="checkbox"/>	<input type="checkbox"/>	<input checked="" type="checkbox"/>	<input type="checkbox"/>
I acknowledge that these represent my contribution to the above research output. Sign:						
Shaomi n Liu	<input checked="" type="checkbox"/>	<input type="checkbox"/>	<input type="checkbox"/>	<input type="checkbox"/>	<input checked="" type="checkbox"/>	<input checked="" type="checkbox"/>
I acknowledge that these represent my contribution to the above research output. Sign:						

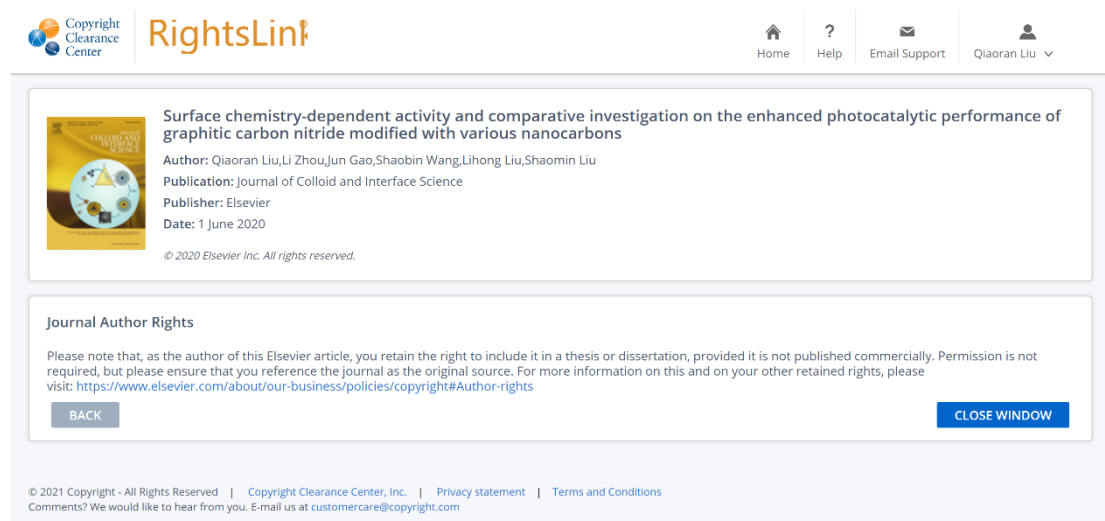
Paper “MXene as non-metal charge mediator in 2D layered CdS@Ti₃C₂@TiO₂ composites with superior Z-scheme visible light-driven photocatalytic activity”.
 Environ. Sci.: Nano, 2019, 6, 3158. Xiaoyao Tan, Shaobin Wang, Fang Ma, Hussin Znad, Zhangfeng Shen*, Lihong Liu* and Shaomin Liu*

Name	concepti on and design	Acquisitio n of data & method	Data conditioning & manipulation	Analysis & statistical method	Interpret ation & discussion	Final appr oval
Xiaoya o Tan	<input type="checkbox"/>	<input type="checkbox"/>	<input type="checkbox"/>	<input type="checkbox"/>	<input checked="" type="checkbox"/>	<input type="checkbox"/>
I acknowledge that these represent my contribution to the above research output. Sign:						
Shaobi n Wang	<input checked="" type="checkbox"/>	<input type="checkbox"/>	<input type="checkbox"/>	<input type="checkbox"/>	<input checked="" type="checkbox"/>	<input type="checkbox"/>
I acknowledge that these represent my contribution to the above research output. Sign:						
Fang Ma	<input checked="" type="checkbox"/>	<input type="checkbox"/>	<input type="checkbox"/>	<input type="checkbox"/>	<input checked="" type="checkbox"/>	<input type="checkbox"/>
I acknowledge that these represent my contribution to the above research output. Sign:						
Hussin Znad	<input type="checkbox"/>	<input type="checkbox"/>	<input type="checkbox"/>	<input type="checkbox"/>	<input checked="" type="checkbox"/>	<input type="checkbox"/>
I acknowledge that these represent my contribution to the above research output. Sign:						

Zhangf eng Shen	<input type="checkbox"/>	<input type="checkbox"/>	<input type="checkbox"/>	<input type="checkbox"/>	<input checked="" type="checkbox"/>	<input checked="" type="checkbox"/>
I acknowledge that these represent my contribution to the above research output. Sign:						
Lihong Liu	<input type="checkbox"/>	<input type="checkbox"/>	<input type="checkbox"/>	<input type="checkbox"/>	<input checked="" type="checkbox"/>	<input checked="" type="checkbox"/>
I acknowledge that these represent my contribution to the above research output. Sign:						
Shaomi n Liu	<input checked="" type="checkbox"/>	<input type="checkbox"/>	<input type="checkbox"/>	<input checked="" type="checkbox"/>	<input checked="" type="checkbox"/>	<input checked="" type="checkbox"/>
I acknowledge that these represent my contribution to the above research output. Sign:						

APPENDIX II: Copyright Permission Statements


- A. Chapter 3, reprinted with permission from “Qiaoran Liu, Li Zhou, Jun Gao, Shaobin Wang, Lihong Liu, Shaomin Liu, Surface chemistry-dependent activity and comparative investigation on the enhanced photocatalytic performance of graphitic carbon nitride modified with various nanocarbons. *J. Colloid Interface Sci.* 2020.”



The screenshot displays the RightsLink interface for a specific article. At the top left, the Copyright Clearance Center logo is visible. The main header includes the RightsLink logo and navigation links for Home, Help, Email Support, and the user profile Qiaoran Liu. The article details section includes a thumbnail of the journal cover, the title "Surface chemistry-dependent activity and comparative investigation on the enhanced photocatalytic performance of graphitic carbon nitride modified with various nanocarbons", the author list "Qiaoran Liu, Li Zhou, Jun Gao, Shaobin Wang, Lihong Liu, Shaomin Liu", the publication "Journal of Colloid and Interface Science", the publisher "Elsevier", and the date "1 June 2020". Below this, a "Journal Author Rights" section contains a disclaimer and a link to the full rights policy. At the bottom, there are "BACK" and "CLOSE WINDOW" buttons, and a footer with copyright information and contact details.

Copyright Clearance Center RightsLink

Home Help Email Support Qiaoran Liu

 Surface chemistry-dependent activity and comparative investigation on the enhanced photocatalytic performance of graphitic carbon nitride modified with various nanocarbons
Author: Qiaoran Liu, Li Zhou, Jun Gao, Shaobin Wang, Lihong Liu, Shaomin Liu
Publication: Journal of Colloid and Interface Science
Publisher: Elsevier
Date: 1 June 2020
© 2020 Elsevier Inc. All rights reserved.

Journal Author Rights

Please note that, as the author of this Elsevier article, you retain the right to include it in a thesis or dissertation, provided it is not published commercially. Permission is not required, but please ensure that you reference the journal as the original source. For more information on this and on your other retained rights, please visit: <https://www.elsevier.com/about/our-business/policies/copyright#Author-rights>

BACK CLOSE WINDOW

© 2021 Copyright - All Rights Reserved | Copyright Clearance Center, Inc. | Privacy statement | Terms and Conditions
Comments? We would like to hear from you. E-mail us at customer@copyright.com

B. Chapter 4, reprinted with permission from “Qiaoran Liu, Hao Tian, Zhenghua Dai, Hongqi Sun, Jian Liu, Zhimin Ao, Shaobin Wang, Chen Han, Shaomin Liu, Nitrogen-doped Carbon Nanospheres Modified Graphitic Carbon Nitride for Enhanced Photocatalytic Performances. *Nano-micro Lett.* 2020.”

Article | [Open Access](#) | Published: 17 January 2020

Nitrogen-doped Carbon Nanospheres-Modified Graphitic Carbon Nitride with Outstanding Photocatalytic Activity

[Qiaoran Liu](#), [Hao Tian](#), [Zhenghua Dai](#), [Hongqi Sun](#), [Jian Liu](#), [Zhimin Ao](#), [Shaobin Wang](#) , [Chen Han](#) & [Shaomin Liu](#) 

Nano-Micro Letters **12**, Article number: 24 (2020) | [Cite this article](#)

2825 Accesses | 10 Citations | 1 Altmetric | [Metrics](#)

Highlights

- Monodisperse nitrogen-doped carbon nanospheres were synthesized and loaded onto graphitic carbon nitride and the composites show outstanding photocatalytic activity.
- Improved sulfachloropyridazine degradation is consistent with density functional theory calculation.

Download PDF 

Sections

Figures

References

Highlights

Abstract

Introduction

Experimental

Results and Discussion

Conclusions


References

Acknowledgements

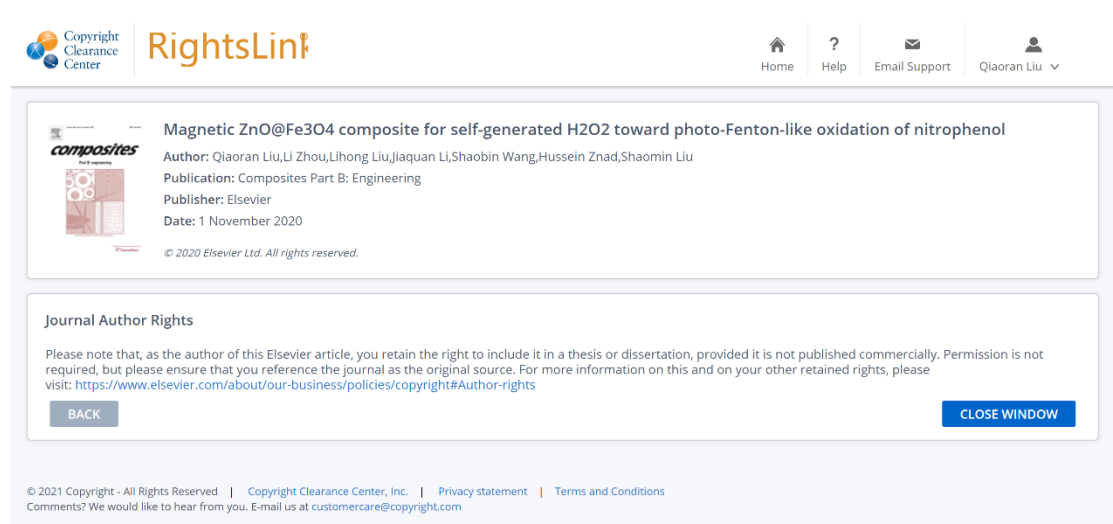
Author information

Electronic Supplementary Material

Rights and permissions

About this article 

C. Chapter 5, reprinted with permission from “Qiaoran Liu, Li Zhou, Lihong Liu, Jiaquan Li, Shaobin Wang, Hussein Znad, Shaomin Liu, Magnetic ZnO@Fe₃O₄ composite for self-generated H₂O₂ toward photo-Fenton-like oxidation of nitrophenol. *Compos. B. Eng.* 2020.”



The screenshot displays the RightsLink interface for a specific article. At the top left, the Copyright Clearance Center logo is visible. The main header area includes the RightsLink logo and navigation links for Home, Help, Email Support, and a user profile for Qiaoran Liu. The central content area features a thumbnail of the journal cover for 'Composites Part B: Engineering' and the following article details:

- Title:** Magnetic ZnO@Fe₃O₄ composite for self-generated H₂O₂ toward photo-Fenton-like oxidation of nitrophenol
- Author:** Qiaoran Liu, Li Zhou, Lihong Liu, Jiaquan Li, Shaobin Wang, Hussein Znad, Shaomin Liu
- Publication:** Composites Part B: Engineering
- Publisher:** Elsevier
- Date:** 1 November 2020

Below the article details, a section titled 'Journal Author Rights' contains a disclaimer: 'Please note that, as the author of this Elsevier article, you retain the right to include it in a thesis or dissertation, provided it is not published commercially. Permission is not required, but please ensure that you reference the journal as the original source. For more information on this and on your other retained rights, please visit: <https://www.elsevier.com/about/our-business/policies/copyright#Author-rights>'. At the bottom of this section are 'BACK' and 'CLOSE WINDOW' buttons. The footer of the interface includes copyright information: '© 2021 Copyright - All Rights Reserved | Copyright Clearance Center, Inc. | Privacy statement | Terms and Conditions' and a contact email: 'Comments? We would like to hear from you. E-mail us at customercare@copyright.com'.

D. Chapter 6, reprinted with permission from “Qiaoran Liu, Xiaoyao Tan, Shaobin Wang, Fang Ma, Hussin Znad, Zhangfeng Shen, Lihong Liu, Shaomin Liu, MXene as non-metal charge mediator in 2D layered CdS@Ti₃C₂@TiO₂ composites with superior Z-scheme visible light-driven photocatalytic activity. *Environ. Sci.: Nano*, 2019.”

Issue 10, 2019
Previous Article
Next Article

From the journal:
Environmental Science: Nano

MXene as a non-metal charge mediator in 2D layered CdS@Ti₃C₂@TiO₂ composites with superior Z-scheme visible light-driven photocatalytic activity†

[Qiaoran Liu](#)^a, [Xiaoyao Tan](#)^b, [Shaobin Wang](#)^c, [Fang Ma](#)^c, [Hussin Znad](#)^a, [Zhangfeng Shen](#)^{a,d}, [Lihong Liu](#)^{e,f} and [Shaomin Liu](#)^{g,h}

[Author affiliations](#)

Abstract

Exploitation of photocatalysts towards efficient organic pollutant degradation is highly desirable in the field of environmental remediation. Here, we report a rational synthesis of two-dimensional CdS@Ti₃C₂@TiO₂ nano-hybrids by facile calcination and a subsequent hydrothermal process. The physico-chemical properties of CdS@Ti₃C₂@TiO₂ were investigated by a variety of characterization techniques. The effect of CdS loading on the photocatalytic performance was elucidated. When compared with Ti₃C₂ and Ti₃C₂@TiO₂, the optimal ternary nanostructures exhibited significantly enhanced visible light-driven (λ ≥ 420 nm) degradation of sulfachloropyridazine, phenol and several typical dyes. The origin of improved photocatalytic performance mainly stems from the enhanced electron-hole separation efficiency. The charge carrier sinking function of Ti₃C₂ in this first time pre-fabricated three-phase Z-scheme catalyst was proposed based on UV-visible spectroscopy band gap calculation, photoluminescence measurement and photoelectrochemical analysis. The electron paramagnetic resonance assay verified that both superoxide ions and hydroxyl radicals played crucial roles in the removal of contaminants.

About
Cited by
Related

MXene as a non-metal charge mediator in 2D layered CdS@Ti₃C₂@TiO₂ composites with superior Z-scheme visible light-driven photocatalytic activity

Q. Liu, X. Tan, S. Wang, F. Ma, H. Znad, Z. Shen, L. Liu and S. Liu, *Environ. Sci.: Nano*, 2019, 6, 3158
DOI: 10.1039/C9EN00567F

If you are not the author of this article and you wish to reproduce material from it in a third party non-RSC publication you must [formally request permission](#) using Copyright Clearance Center. Go to our [Instructions for using Copyright Clearance Center page](#) for details.

Authors contributing to RSC publications (journal articles, books or book chapters) do not need to formally request permission to reproduce material contained in this article provided that the correct acknowledgement is given with the reproduced material.

Reproduced material should be attributed as follows:

- For reproduction of material from NJC:
Reproduced from Ref. XX with permission from the Centre National de la Recherche Scientifique (CNRS) and The Royal Society of Chemistry.
- For reproduction of material from PCCP:
Reproduced from Ref. XX with permission from the PCCP Owner Societies.
- For reproduction of material from PPS:
Reproduced from Ref. XX with permission from the European Society for Photobiology, the European Photochemistry Association, and The Royal Society of Chemistry.
- For reproduction of material from all other RSC journals and books: